Analysis and modeling of ex-vessel underwater cooling processes of debris bed and molten corium pool in interaction with concrete

Analyse et modélisation des processus de refroidissement sous eau des lits de débris et des bains de corium en interaction avec le béton

par

Alejandro VILLARREAL LARRAURI

Une thèse en vue de l'obtention du

DOCTORAT DE L'UNIVERSITÉ DE LORRAINE

Spécialité: Mécanique et Energétique

Ecole doctorale:

Sciences et Ingénierie des Molécules, des Produits, des Procédés, et de l'Énergie (SIMPPÉ)

Soutenue le 10 Mars 2020 devant le jury composé par:

Président :	Jérôme BELLETTRE	LTeN, Université de Nantes, CNRS
Rapporteurs :	Nathalie MARIE	CEA (DEN/CAD/DER/SESI/DIR)
	Jérôme BELLETTRE	LTeN, Université de Nantes, CNRS
Directeur de Thèse :	Michel GRADECK	LEMTA, Université de Lorraine, CNRS
Co-directeur de Thèse :	Nicolas RIMBERT	LEMTA, Université de Lorraine, CNRS
Examinateurs :	Pascal PILUSO	CEA (DEN/CAD/DER/SESI/DIR)
	Irina PANFILOVA	LEMTA, Université de Lorraine, CNRS
Membre invité(Encadrant):	Renaud MEIGNEN	IRSN (PSN-RES/SAG)

Laboratoire Énergies et Mécanique Théorique et Appliquée(LEMTA) — UMR 7563
Laboratoire d'Étude de la Physique du Corium (LEPC) — IRSN/PSN-RES/SAG/LEPC

En honor a mi tata, que en paz descanse.

Acknowledgements

First and foremost I would like to express my most profound acknowledgment and thankfulness towards Nathalie Marie and Jérôme Belletre for accepting both being part of my Ph.D. committee, and the quite probably exhausting task of going through my manuscript, a part of which I sent over as a Christmas present (I'm sorry). Having said that, I would also like to extend the same recognition to Pascal Piluso, and Irina Panfilova for accepting to be part of my Ph.D. committee. I feel fortunate and honored to have counted with the presence of each of the illustrious experts of such diverse fields as part of my Ph.D. committee. In the same tone, I feel privileged to have received my Ph.D. degree from them.

I'd also like to express my deepest appreciation and admiration towards Michel Gradeck and Nicolas Rimbert, whose involvement throughout as my Ph.D. directors was crucial. Regardless of the physical distance from which we worked at, their contributions, challenging questions, and their overall willingness to help me during this intense process were absolutely necessary for me. Their calm demeanor, availability, and their amiability is something I treasured and can objectively say I'm lucky to have counted on. The innate constant drive for academic rigor and scientific soundness of both Michel and Nicolas has left a profound and surely long-lasting desire to reach a level of professionalism that could (hopefully) one day compare to the one I found in them.

It'll be hard for me to forget the feeling I had when my tutor Renaud Meignen informed me he had chosen me for this project. It'll be equally difficult to forget the amount of help I received from his part. If I get the chance to continue my dream of pursuing a career in the nuclear sector is by all means largely thanks to the small amount of the overwhelmingly vast knowledge Renaud has which I was able to absorb. The amount of time and energy he willingly invested has earned him my everlasting admiration and respect. His incomparable expertise in the difficult subject of my thesis project was from the beginning a key to all, if any, amount of accomplished success. Any amount of pleasantries I could muster would fall short for the real value of having Renaud as my tutor. Simply put, without him and his patience, I would not have succeeded in completing my Ph.D.

I know the number of people and the reasons for which I have to thank them for is rather quite large, but I'll try to keep it short. I'm afraid it'll be inevitable for me to forget to mention someone, for which I apologize in advance.

I'll start with the permanent members of my lab who made me feel welcomed and comfortable to work in an environment I was not used to. I'll like to thank: Marie-Claire (during her time) and Caroline for their help with my many, and constant, questions of all the administrative procedures and more; Jean-Marc for his patience and for taking the time to travel and assist my Ph.D. defense; Libuse for her time and for her kindness when helping me with MC3D; Alain for his time and help with my MCCI and MEDICIS queries; Florian, Laure and everyone else that happily and without any such obligation lent their time to answer any question I asked them; Laurent, Patrick, Laure, Vincent, Claude, Olivia, François, Letitia, and all the people of not only the LEPC but the LETR that with their kindness and friendliness (and occasional croissants during their birthdays) made my work life wholesome and quite enjoyable. Special thanks to Stéphane Picchi for his availability to discuss all MC3D related problems I encountered, and for the quite enjoyable talks we had. Special thanks to Guillaume Astier for his never-ending help with

MC3D and because without him I would have probably not be able to play football, a crucial de-stress activity throughout these 3 years. I'd also like to thank the rest of the members of CS whom with I'd had the chance to share office building and inevitably some noise and croissants as well.

To continue I'd like to thank the friends I met in the lab during these past 3 years specially Shambhavi Nandan whom I've had the pleasure of sharing lab from even before the start of the Ph.D., Ignacio whom I had the absolute pleasure of sharing an office with, and Julie-Anne (intentionally excluded from the above permanent LEPC list) whom I'd not only shared office for a while when she was still a post-doc but who's help with MC3D during the first part of my Ph.D. was essential for my work. Thanks to Ankita, Ali, Adrien, Juliana, Linkai, Miloud, Míriam, Mathilde, Mirco, Nitendra, Noé, Tsvetoslav, and all the rest of the Ph.D's, post-docs and interns whose day to day in and out of office camaraderie I'll always cherish. Almost reaching the end, I'd like to thank the friends I made, or had made, outside my lab without which I'd would not have endured through these 3 years. Special thanks to Guillaume Brochard, whom I shared a house with from before the start of my Ph.D. and who's presence made my life in France so much easier and whom I'll always thank for the enthusiasm he transmitted to me through his love for science. Thanks to Piotr, Juan Pablo, Bernardo, Francisco, Felipe, Elias, Jorge, Julio, and many others for their friendship.

Finally, I could not conclude without thanking the people who reside within my heart: my corazona Elisabetta Caschera, my brother Antonio, my sister Areli, my parents Gabriela and Antonio, the rest of my family, and the great friends I left behind in my home country. Through the hardest of times, it was their love and their support that helped me find the motivation, and their encouragement that kept me focused. It was their belief in me that pushed me to find the quite crucial belief in myself. If I arrived to where I did, It is because of them.

Con mucho cariño y aprecio, gracias a todos =) .

Sommaire

En cas d'accident grave avec fusion du cœur, le magma surchauffé constitué d'acier et de combustible fondu, appelé corium (T> 2 500 K), peut menacer l'intégrité de la cuve du réacteur, puis du bâtiment de confinement, si le refroidissement du corium n'est pas assuré. La capacité de refroidissement en situation hors-cuve, par l'injection d'eau et pénétration de celle-ci dans le corium en surface supérieure, est étudiée pour deux configurations attendues : le lit de particules et bain de corium. La seconde configuration est liée à la situation d'interaction corium-béton (ICB) où une croute se forme en face supérieure en contact avec l'eau, puis est soumise à une fracturation à cause des effets thermiques dans cette croute. L'enjeu est de caractériser l'efficacité d'une éventuelle pénétration de l'eau dans la croute. La première configuration peut intervenir en particulier dans deux situations suite à une fragmentation du corium dans l'eau : lors de l'éjection hors de la cuve, ou suite à des périodes d'éjection à travers la croute en phase d'ICB par entrainement du corium par des gaz issus de l'ablation du béton. Les phénomènes de pénétration de l'eau dans le corium sont examinés par une analyse approfondie des résultats des expériences disponibles, par la mise au point d'un modèle analytique 1D et par la modification et l'utilisation du code de thermohydraulique multiphasique multi-fluides (CMFD) MC3D.

L'analyse 1D permet de mieux comprendre les détails de l'écoulement diphasique dans la matrice poreuse et conduit à proposer un model simplifié de pénétration de l'eau, avec des relations correspondantes applicables pour les deux configurations d'intérêt. Par ailleurs, le développement et l'impact d'instabilités au front de pénétration sont étudiés avec des simulations 2D avec MC3D, illustrant le rôle important de la température initiale du lit et sa perméabilité sur la vitesse de pénétration du front, et sur l'apparition des instabilités. Le modèle analytique est alors étendu à une configuration à deux zones (une zone soumise à un écoulement diphasique en contre-courant et une zone monophasique dans laquelle la vapeur surchauffe traverse) pour analyser plus en détail l'impact des hétérogénéités de progression du front sur les flux thermiques extraits. Le mécanisme de pénétration de l'eau dans les croutes est discuté. L'analyse indique de forts effets de bords sur les processus de fracturation dans les essais SSWICS (Argonne Nat. Lab.), dédiés à ce phénomène. Les conclusions des travaux précédents sur l'efficacité du phénomène ne peuvent dès lors être confirmées du fait des fortes incertitudes sur les processus de fracturation, très sensibles aux propriétés mécaniques du corium, très mal caractérisées.

Finalement, les modèles sont appliqués aux situations réelles impliquant la présence de la puissance résiduelle. Pour les lits de débris, les flux extraits et les capacités de refroidissement sont moindres qu'avec l'utilisation du critère simplifié de « flux d'assèchement ».

Mots-clés: Corium, Interaction Corium-Beton, MCFD, SSWICS, Lit debris, Water Ingression

Abstract

In the case of a hypothetical nuclear severe accident with partial or extensive core meltdown, the superheated magma made of molten steel and fuel, called corium (T $>$ 2500K), may threaten the integrity of the reactor pressure vessel and subsequently the reactor containment building, if long-term corium coolability is not assured. The coolability by water injection and successive water penetration into the corium through the upper surface is analyzed for two expected configurations: particle bed, and corium pool overlaying the concrete. The second configuration is linked to the situation of Molten Corium-Concrete Interaction (MCCI), where a crust is formed in the upper corium surface when it comes into contact with water and is later subjected to thermal stresses that lead to its fracturing. The challenge is to characterize the effectiveness of extracting heat by the possible water penetration into the crust. The first configuration can be expected in two different situations: melt fragmentation coming from the rupture of the reactor pressure vessel and expulsion of the corium, or during melt eruption episodes through the corium crust during MCCI via corium entrainment by the concrete decomposition gases. The phenomena linked to the water penetration into the corium for these two configurations are examined through an in-depth analysis of the available experimental results, by the development of an analytical model and finally through the modification and use of the Computational Multi-Fluid Dynamics (CMFD) code MC3D.

One dimensional analysis conducts to a better understanding of the minutia of the two-phase countercurrent flow through the porous media and leads the proposal of a simplified heat flux model for the water penetration with corresponding relations applicable for both configurations of interest. Furthermore, the development and the impact of penetrating front instability are studied with the help of 2D MC3D simulations, which show important effects of the initial temperature and the permeability of the corium configuration on the penetration front velocity and appearance of the instabilities. The analytical model is extended to a pseudo-two-dimensional two-zone configuration (with one zone subjected to a two-phase countercurrent flow and another through which monophasic superheated vapor flows) to analyze in greater detail the impact of the penetrating front heterogeneity over the extracted heat flux. The mechanism of water penetration through a fractured crust is revisited. The analysis indicates strong border effects in the SSWICS tests (Argonne National Laboratories) dedicated to the study of this phenomenon. The conclusions of precedent studies on the efficiency of the phenomena could not, therefore, be confirmed due to important uncertainties over the process of fracturing, overly sensitive to the mechanical properties of corium, which in turn are not properly characterized.

Finally, the models, and simulations, are applied to real accidental scenarios, including the presence of residual power. For the debris bed, the extracted heat flux, and the cooling capabilities are less than those found using the simplified dry-out heat flux criteria.

Keywords: Corium, Molten Corium-Concrete Interaction, MCFD, SSWICS, Debris bed, Water Ingression

Contents

Chapter 1
Introduction/Context/Phenomenology

Chapter 2
Literature Review

Chapter 3
Preliminary Analysis of Top-Reflooding

Chapter 4
One-dimensional Analysis

Chapter 5
Two-dimensional Effects

Chapter 6
Conclusions and Perspectives

List of Figures

List of Tables

Symbols

Symbol	Description	Units	Page(s)
α	Local-averaged vapor saturation	-	63
α_{th}	Thermal diffusivity of crust material	$\frac{m^2}{s}$	65
β	Linear expansion coefficient of the material	$\frac{1}{K}$	72
$\varLambda_c$	Capillary length	m	123
c_p	Heat capacity of the material	$\frac{J}{kg \cdot K}$	77
d_p	Sautrer mean diameter of the debris bed particles	m	63
$\varDelta T$	Temperature difference from initial debris bed temperature, T_0, and saturation temperature, T_{sat}	K	131
E	Young modulus of a material	$\frac{kg}{m \cdot s^2}$	73
ε	Porosity, or void fraction of the porous media	-	63
η	Absolute passability of the porous media	m	63
$\eta_{r,i}$	Relative passability of the porous media, function of the vapor saturation (α)	-	63
$f_{2\phi}$	Horizontal surface fraction of the two-zone debris bed occupied by a two-phase counter-current flow configuration (quenched portion)	-	162
F_{lv}	Interfacial (liquid-vapor) friction pressure drop	$\frac{kg}{m^2 \cdot s^2}$	63
G_{cr}	Fracture energy density of the material	$\frac{J}{m^2}$	73
h_{fs}	Latent heat of fusion	$\frac{J}{kg}$	77
h_{lv}	Latent heat of vaporization	$\frac{J}{kg}$	116
j_i	Superficial velocity of phase "i"	$\frac{m}{s}$	63
κ	Absolute permeability of the porous media	m^2	62
$\kappa_{r,i}$	Relative permeability of the porous media, function of the vapor saturation (α)	-	63
λ_{cr}	Thermal conductivity of crust material	$\frac{W}{m \cdot K}$	76
μ_i	Dynamic viscosity of phase "i"	$\frac{kg}{m \cdot s}$	63
ϕ	Heat flux, either extracted or imposed by the volumetric power over a certain height	$\frac{W}{m^2}$	116
ϕ_{do}	Dry-out heat flux, debris bed power at which some part of the bed just becomes dry	$\frac{W}{m^2}$	70
$\frac{\delta P_i}{\delta z}$	Pressure drop of phase "i" with respect to z	$\frac{kg}{m^2 \cdot s^2}$	63
$\frac{\delta P_c}{\delta z}$	Capillary pressure drop with respect to z	$\frac{kg}{m^2 \cdot s^2}$	63
ρ_i	Density of phase "i"	$\frac{kg}{m^3}$	63
σ_{lv}	Liquid-vapor surface tension at saturation temperature	$\frac{N}{m}$	63

Symbol	Description	Units	Page(s)
σ_{cr}	Tensile strength of the crust material	$\frac{kg}{m \cdot s^2}$	73
T_{crack}	Cracking temperature of the material	K	76
T_{melt}	Melting temperature of the material	K	146
T_{sol}	Solidification temperature of the material	K	77
u_i	Cooling front velocity in the regime "i" (λ for laminar, τ for inertial, or mix for mixt)	$\frac{m}{s}$	131
X_{H_2O}	Fraction of the liquid mass in the unsteady front that is used to partially fill the pores bellow the front	-	131

Superscripts

Symbol	Description
P	Unsteady

Subscripts

Symbol	Description
2ϕ	Two-phase zone in two-zone configuration
cr	Crust material
l	Liquid phase
T_0	Dry zone in two-zone configuration
v	Vapor phase
λ	Laminar regime
mix	Mix laminar-inertial regime
τ	Inertial (turbulent) regime

Glossary

Acronym	Description	Page(s)
ACE	Advanced Containment Experiments	49
ANL	Argonne National Laboratories	40
ASTEC	Accident Source Term Evaluation Code	30
BWR	Boiling Water Reactor	7
CCI	Core-Concrete Interaction experimental program	49, 58, 97
CHF	Critical Heat Flux	28
CMFD	Computational Multi-Phase Fluid Dynamics	80
DCH	Direct Containment Heating	17
DHF	Dry-out Heat Flux	31
EDF	Électricité de Francee	23
EPR	European Pressurized Reactor (or Evolutionary Power Reactor)	20
ERVC	External Reactor Vessel Cooling	24
FCI	Fuel-Coolant Interaction	12
HPME	High-Pressure Melt Ejection	17
IAEA	International Atomic Energy Agency	4
IVR	In-Vessel Retention	24
LCS	Limestone-common sand	22
LOCA	Loss-of-coolant Accident	10
LOOP	Loss-of-Offsite Power	8
MACE	Melt Attack Coolability Experiments	49
MC3D	Multi-Component 3D	30
MCCI	Molten Corium-Concrete Interaction	15
MW_e	MW electric	25
NPP	Nuclear Power Plant	4
PEARL	Programme Expérimental Analytique sur le Renoyage de Lits de débris	31
PSA	Probabilistic Safety Analysis	8
PWR	Pressurized Water Reactor	5
RPV	Reactor Pressure Vessel	5
SAM	Severe Accident Management	24
SAMG	Severe Accident Management Guidelines	18
SMR	Small Modular Reactor	2
SOAR	State of The Art Report	47
SSWICS	Small-Scale Water Ingression and Crust Strength	29
TEPCO	Tokyo Electric Power Company	7
TMI	Three Mile Island	5

Résumé

En cas d'accident grave, comme ceux survenus sur les centrales nucléaires de Three-Miles Island (1979), Tchernobyl (1986) et Fukushima (2011), la fusion partielle ou complète du cœur entraîne la formation d'un magma surchauffé (T> 2500 K) où des réactions de fission perdurent; ce magma est communément appelé "corium". Le corium est constitué du combustible, du matériau des crayons combustibles (alliage de zirconium) et autres matériaux présents au sein du cœur du réacteur (barres de commande de réacteur nucléaire, matériaux provenant de la cuve). La production de puissance résiduelle continue, provenant principalement de la chaleur générée par la fission, et sa température initiale élevée, pourraient menacer l'intégrité du réacteur.

Si la capacité de refroidissement du corium n'est pas assurée tout au long du scénario accidentel, cela peut entraîner la rupture des barrières de confinement, conduisant finalement au rejet de matières radioactives dans l'environnement. La progression accidentelle dépend considérablement du scénario. Cependant, généralement et dans un premier temps, la cuve sous pression des réacteurs (RPV par ses sigles en anglais, qui est le récipient épais où le réacteur lui-même est logé) est attaquée thermiquement. En cas de défaillance du RPV, le corium s'écoulera à l'extérieur et entrera en contact avec le béton du bâtiment de confinement du réacteur. Bien que différentes stratégies existent en fonction de la conception du réacteur, de ses caractéristiques et des réglementations imposées par les régulateurs de sûreté, deux stratégies distinctes existent dans le but de refroidir le corium et d'arrêter sa progression accidentelle.

La première stratégie, communément appelée stratégie de rétention en cuve (IVR par ses sigles en anglais), consiste en un refroidissement externe de la cuve du réacteur (ERVC par ses sigles en anglais) par inondation d'eau. Normalement un système d'eau spécifique dédié à ce propos est mis en place dans le réacteur. Le système est conçu pour inonder, au moins partiellement, une partie du bâtiment de confinement du réacteur pour refroidir le corium à travers la cuve. L'objectif de la stratégie IVR est de conserver l'intégrité ou au moins d'augmenter la probabilité de survie du RPV en cas d'accident grave.

La seconde stratégie, appelée la stratégie de stabilité du corium hors cuve, consiste à laisser le RPV fondre de sorte que le corium se propage vers l'extérieur dans un compartiment désigné, généralement dans le puit de cuve du réacteur, et potentiellement les compartiments annexes du bâtiment réacteur, augmentant ainsi la surface d'étalement disponible pour le corium. Augmenter la surface d'échange du corium permet de le refroidir davantage en le recouvrant d'eau une fois qu'il s'est complètement répandu. Dans le cas des réacteurs français, l'exploitant (EDF) a choisi de suivre la stratégie hors cuve.

Dans ce travail, la capacité de refroidissement en situation hors-cuve (seconde stratégie) et la pénétration d'eau (phénomène dit de water ingression en anglais) dans le corium à travers la surface supérieure de celui-ci est analysée dans deux cas: lit de particules et bain de corium (potentiellement avec une croûte solidifiée). La première configuration peut être produite suite à une fragmentation du corium dans l'eau: lors de son éjection de la cuve suite à la rupture de la cuve sous pression du réacteur, ou suite à des

épisodes d'éjection à travers la croûte du bain de corium en phase d'interaction corium-béton (ICB), due à l'entraînement de corium liquide par les gaz de décomposition du béton. Cette deuxième configuration est liée à une situation ICB où une croûte se forme à la surface supérieure du corium lorsqu'elle entre en contact avec l'eau et est ensuite soumise à des contraintes thermiques qui conduisent à sa fracturation. L'enjeu est de caractériser l'efficacité de l'extraction de chaleur par la possible pénétration d'eau dans la croûte.

Les phénomènes liés à la pénétration de l'eau dans le corium pour ces deux configurations sont examinés à travers une analyse approfondie des résultats expérimentaux disponibles, par le développement d'un modèle analytique et enfin par la modification et l'utilisation du code de thermohydraulique multiphasique multi-fluides (CMFD) MC3D.

À la suite d'une revue bibliographique approfondie, présenté dans le chapitre 2, certaines questions ouvertes liées aux configurations d'intérêt ont été identifiées. Parmi celles-ci, dans le cas d'un lit de débris de particules, l'importance des effets des conditions de température initiales sur la capacité de refroidissement a été mise en évidence. Malgré la grande quantité de programmes de recherche qui ont eu lieu concernant la capacité de refroidissement des lits de débris, la plupart des expériences ont été menées dans des conditions de régime permanent, et non dans des cas transitoires, plus contraignantes, conditions qui auraient lieu dans certaines phases d'un scenario accidentel réel. La plupart de ces investigations a été initiée d'un lit de débris de particules initialement refroidi où une puissance résiduelle progressive a été imposée jusqu'à trouver la limite où le lit de particules devient sec. Plusieurs modèles simplifiés de flux de chaleur d'assèchement ont été développés dans le passé, mettant en évidence les mécanismes qui régissent le point d'équilibre où l'eau et la vapeur (produite par d'eau qui traverse dans le lit de particules) extraient la quantité maximale de chaleur. Cette situation a été prise comme référence pour étudier la capacité de refroidissement dans des scénarios accidentels. Néanmoins, la dépendance du mécanisme, l'évolution du schéma de pénétration de l'eau et ses effets sur la capacité à extraire la chaleur n'ont pas été explorés. Au cours de ces travaux, la représentativité des modèles développés pour cette configuration particulière a été explorée.

Tout d'abord, dans le chapitre 3, une série des simulations préliminaires pour étudier la première configuration ont été fait, ou les résultats ont souligné des questions à répondre. Aussi dans cette chapitre, une réinterprétation des analyse SSWICS a été réalisé.

Dans le chapitre 4, un modèle unidimensionnel, à l'état stationnaire, a été construit pour différents régimes d'écoulement afin d'étudier les paramètres impliqués dans la mécanique des fluides de deux phases fluides en contrecourant. Les régimes d'écoulement ont été explorés sur l'ensemble de la gamme de tailles de particules attendues dans ce contexte d'un accident grave hors-cuve. Une extension ultérieure du modèle a également été faite pour étudier un état instable où l'eau percole à travers le lit de débris.

Les effets capillaires dans le lit de débris de particules ont également été discutés. Dans ce cas, il est essentiel de souligner qu'une carence dans les modèles disponibles pour évaluer ces effets capillaires a été constatée. Plus précisément, les formulations disponibles ont été développées dans un contexte de régime permanent, et une extrapolation en dehors de leur domaine de validité n'a pas été jugée appropriée. Les résultats du modèle ont été comparés aux quelques résultats expérimentaux disponibles. En complément, des simulations unidimensionnelles ont été réalisées avec le code MC3D. Les tendances dominantes trouvées dans les résultats expérimentaux ont été bien reproduites par le modèle et les simulations et sont dans la marge d'incertitude expérimentale. Les résultats du modèle développé et des simulations ont donc permis de mieux comprendre les mécanismes qui conduisent à un équilibre entre les phases fluides.

Par ailleurs, dans le chapitre 5 le modèle unidimensionnel a été étendu pour tendre vers un modèle pseudo-bidimensionnel. Plus précisément, il a été étendu à un modèle à deux zones, chaque zone étant unidimensionnelle. Dans ce cas, les résultats montrent qu'une situation en régime permanent avec une puissance résiduelle n'est pas susceptible d'être stable par nature. Néanmoins, les résultats (pour cette configuration) ont montré une dépendance critique du point d'équilibre entre les phases fluides sur les conditions initiales. Cela a permis l'extrapolation à une gamme différentes de scénarios accidentels spécifiques.

D'autres évaluations des schémas d'écoulement d'eau dans un lit des particules chaudes ont été effectuées avec des simulations bidimensionnelles MC3D dans la section 5.2.3 et la section 5.2.4. Pour un lit de débris constitué de particules dans une gamme de taille et une température de particules initiales particulières, les simulations bidimensionnelles ont montré qu'un schéma des instabilités particuliers s'est développé. Il a été constaté que des chemins d'eau préférentiels (les instabilités) étaient favorisés pour une gamme de tailles spécifiques de particules de lit de débris et de températures initiales, alors qu'ils étaient inexistants dans d'autres cas. En général, pour les particules plus petites et les températures plus élevées, les instabilités n'apparaissent pas. Ces instabilités inhibent les capacités d'extraction de chaleur et, dans certains cas, rendent le lit de débris instable, entraînant sa refusion. En d'autres termes, pour certaines conditions initiales, le flux de chaleur extrait et les capacités de refroidissement sont inférieurs à ceux trouvés en utilisant les critères simplifiés de flux de chaleur d'assèchement dans la configuration du lit de débris.

L'extrapolation du modèle pour étudier la stabilité thermique des lits de particules avec l'inclusion des effets de puissance résiduelle dans une configuration de pénétration instable a conduit à proposer deux critères simples sur lesquels la stabilité du lit de débris pourrait être évaluée. Premièrement, un critère thermique qui dicte la hauteur maximale du lit de débris pouvant être éteint par percolation de l'eau en fonction du diamètre des particules, de la température initiale et de la puissance résiduelle. Deuxièmement, un critère hydro-dynamique qui estime la hauteur maximale de corium dont la puissance résiduelle pourrait être logée à travers un lit de débris superposé déjà trempé également soumis à une puissance résiduelle. En utilisant ces critères, il a été constaté que pour les petites particules et la puissance résiduelle moyenne, le premier critère est le limitant, tandis que pour les grosses particules, c'est le second.

Pour le phénomène lié à la deuxième configuration d'intérêt (la croûte de corium fracturée), c'est-à-dire le phénomène généralement appelé « water ingression » dans le cadre du MCCI, encore moins de résultats expérimentaux ont pu être trouvés dans la littérature. Accompagnant ces quelques expériences (celles réalisées dans le cadre du programme SSWICS), il y a un manque de consensus dans l'interprétation du phénomène, rendant encore plus difficile la compréhension de la dynamique gouvernante. Ces expériences ont été réalisées avec des matériaux prototypes de corium à différentes concentrations de béton afin de simuler différentes étapes de la progression accidentelle. L'objectif de ces expériences était de pouvoir développer un modèle simplifié pour évaluer différentes situations accidentelles en fonction du contenu en béton dans le mélange de corium.

L'étude du modèle développé dans le cadre de ces expériences a révélé des faiblesses dans les hypothèses sur lesquelles le modèle a été construit. En outre, la poursuite d'une approche paramétrique pour ajuster les données de ces expériences a conduit à une mauvaise identification du phénomène dans les cas où aucune preuve claire n'a été trouvée. En d'autres termes, seules certaines de ces expériences ont montré des preuves du phénomène en cours. De plus, le plateau expérimental qui a servi de preuve de ce phénomène de « water ingression » n'était pas continu, diminuant rapidement le flux de chaleur extrait après un temps spécifique. Aucune explication de cette chute n'a été trouvée. En outre, il existe des hétérogénéités considérables dans la morphologie des fractures mises en évidence dans l'analyse des images post mortem disponibles. La réinterprétation de ces expériences SSWICS a mis en évidence une limite absolue sur laquelle le phénomène ne jouerait plus de rôle.

Les principes du mécanisme de fracture ont été explorés d'un point de vue théorique dans la section 2.4. Une méthode potentielle pour le développement d'un modèle définitif a été discutée. Néanmoins, un manque de propriétés matérielles fondamentales nécessaires au développement d'un modèle approprié a été constaté. L'application du modèle avec les propriétés actuelles a entraîné un écart entre les mesures expérimentales (dans les expériences SSWICS) et la perméabilité attendue de la croûte fracturée résultant du model. Plusieurs sources possibles de cette divergence, comme la forte dépendance des propriétés des matériaux par rapport à la température, ou les hétérogénéités possibles de la perméabilité mesurée en raison des limites physiques de la section d'essai expérimentale ont été discutées.

Dans la section 4.3, une extension du modèle unidimensionnel développé avec l'identification de plusieurs relations de perméabilité relative spécialement formulées pour un contexte de milieu poreux fracturé a été réalisée. L'application du modèle à la perméabilité mesurée expérimentalement et la comparaison des résultats de flux de chaleur extraits montrent que seules les expériences avec la preuve d'un plateau peuvent être interprétées comme ayant été soumises au phénomène du « water ingression ». Ensuite, une légère modification du code MC3D (l'inclusion des formulations de perméabilité relative identifiée pour ce contexte, et l'inclusion de la conduction thermique à travers la croûte) a permis d'effectuer quelques simulations unidimensionnelles. Les résultats de ces simulations, avec le modèle et les mesures expérimentales, ont confirmé l'existence d'une limite où le phénomène est actif. En d'autres termes, l'efficacité du phénomène d'injection d'eau pour extraire la chaleur à travers un écoulement d'eau à contre-courant percolant à travers la croûte de corium fracturée a été jugée inférieure à la chaleur qui pourrait être extraite par conduction à travers ladite croûte. De plus, les simulations montrent que la chute du flux de chaleur après le plateau est liée à la libération de l'énergie stockée dans le matériau isolant de la section d'essai une fois que le front d'avancement d'eau a atteint le bas de la section d'essai.

Dans la section 5.2.6 des simulations MC3D bidimensionnelles ont été réalisées pour étudier les schémas de pénétration de l'eau et leurs effets sur le flux de chaleur extrait. Ces simulations reproduisent mieux les résultats expérimentaux en termes de durée du plateau de flux thermique lié au phénomène du « water ingression ». Des simulations bidimensionnelles hétérogènes, avec une perméabilité plus importante dans une zone, réalisées pour imiter la fracturation plus importante dans une zone identifiée dans les images, tout en conservant la perméabilité globale mesurée, montrent clairement que l'eau a tendance à pénétrer principalement à travers la zone de perméabilité supérieure. En d'autres termes, les résultats de ces simulations montrent à quel point le phénomène est sensible aux hétérogénéités bidimensionnelles. À leur tour, cette sensibilité met en évidence les difficultés d'extrapolation de ces résultats à des scénarios de cas réels avec des précision dues aux effet d'échelle et limitations physiques qu'entrainent la taille de la section d'essai.

Au total, les phénomènes impliqués dans la capacité de refroidissement d'un scénario de corium "ex-vessel" sous MCCI ont été analysés. Plusieurs facteurs restrictifs ont été mis en évidence, et les limites sur lesquelles un phénomène comme le « water ingression » est actif ont été décrites. Les effets de la puissance résiduelle sur la capacité de refroidissement des configurations étudiées ont été explorés. Enfin, le besoin de plusieurs données expérimentales vitales a été mis en lumière, et plusieurs perspectives ont été énumérées pour la suite du travail.

Chapter 1

Introduction/Context/Phenomenology

Contents

It may come to no surprise that the current society is more dependent on energy than ever before. A simple glance at figure 1.1 will provide a clear and drastic trend of increasing energy consumption per capita, plotted as the green curve. In addition, recognizing the fact that the average access to electricity worldwide is still on the rise (as shown in the red dashed curve), it is easily arguable to expect that worldwide total energy consumption over the next few decades will continue rising. Furthermore, if both the energy needed to pursue industrialization in developing regions of the world and the decarbonization of non-electricity sectors (transport, for example) are also taken into account, the need for an increase in energy production becomes undeniable.

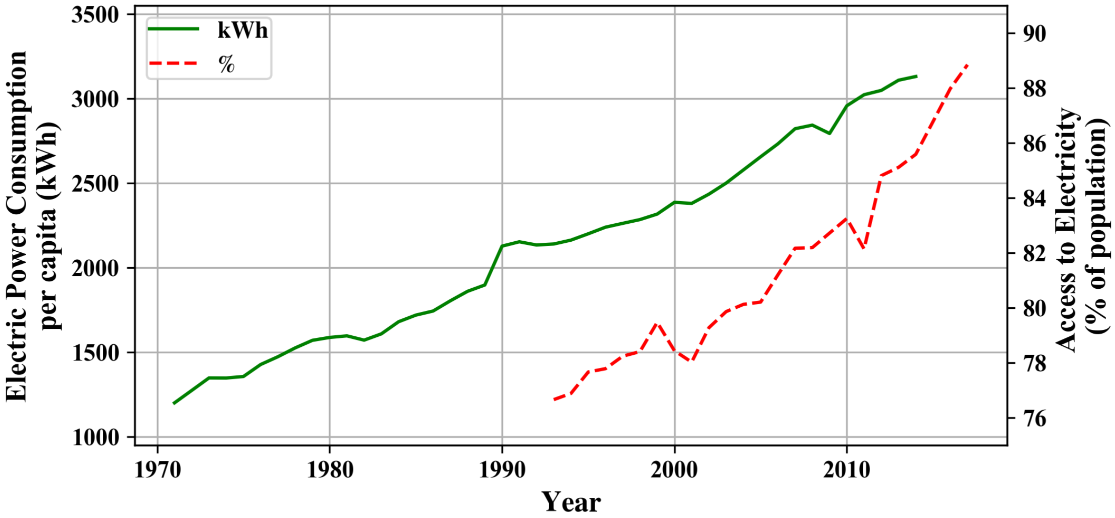

Figure 1.1 – Average world electricity consumption per capita and availability

Data taken from: The World Bank:World Bank Open Data [1]

This increase in energy production must imperatively come from reliable/robust energy sources which at the same time thwart, or at least curtail, the damage to the environment while also guaranteeing that it will keep up with the demand. This last is not currently the case. As can be seen in figure 1.2, there is and has historically been a large percentage of the electricity produced from sources that do not minimize the damage to the environment, such as those coming from coal, oil, and gas. This figure shows a slight growth after 2010 in electricity generated via natural gas, and coal, mainly offsetting the efforts made by increasing the generation via renewable sources.

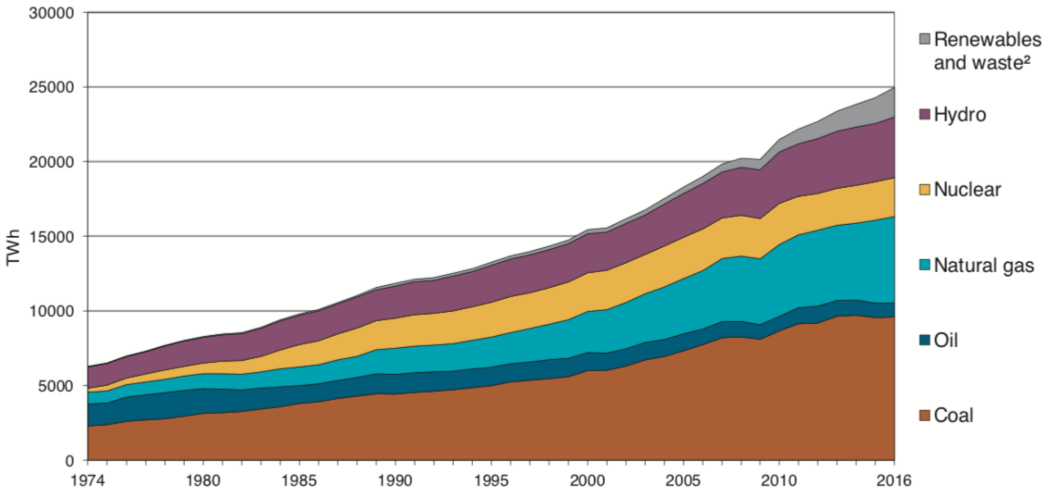

Figure 1.2 – Time evolution of electricity generation by technology

Taken from: [2]

It may be argued that nuclear energy is a viable, logical alternative to provide carbon-free energy on a large scale. Nevertheless, the never-ending debate of the possible consequences, costs, and benefits of nuclear energy present often contradicting points of view concerning the effectiveness of nuclear energy as a tool to reduce greenhouse gas emissions. To exemplify, some authors comparing the same regional scenarios in Asian countries have found opposing conclusions such as Park et al. [3, p.559] who states that "it is economically infeasible for renewable energy to be the sole method of low-carbon energy generation in Korea." whilst others like Sovacool [4, p.369] conclude that "electricity demand in an Asia facing climate change should promote the rapid expansion of renewable technologies and a more limited use of nuclear power."

Other authors come to firm conclusions such as Hong et al. [5, p.451] who state that "for effective climate-change mitigation, a high penetration of nuclear in association with a nationally appropriate mix of renewables achieves far superior cost and land effectiveness compared to a renewables-only future to reduce emissions", and Siqueira et al. [6, p.24] who concludes that "from a global perspective...only high-investment scenarios in nuclear power plants could contribute more effectively to non-CO_2 emissions", amongst other arguments in favor of nuclear energy [7], [8], [9]. On the other hand, authors such as Sovacool & Ramana [10] affirm that the future of nuclear reactors is not realistic and go as far as to say that novel concepts such as the Small Modular Reactors (SMRs) are based on fantasies. Jin & Kim [11, p.464] claim that "nuclear energy does not contribute to carbon reduction unlike renewable energy", or Kyne & Bolin [12, p.13] argue that the nuclear industry in general "raise a suite of justice issues including distributive, procedural, recognition and inter-generational justice issues", amongst many other claiming nuclear energy's benefits do not out-weight the costs [13], [14], [15].

Others take a more moderate stance, such as Augutis et al. [16], who establishes that an optimal energy mix in terms of energy security is a hybrid one that includes a large amount of nuclear energy, whilst Petrescu et al. [17] asserts that nuclear energy could serve as a buffer for renewable energies.

A more pragmatic approach would imply that local country-by-country or region-by-region energy mix should be analyzed by not only the projected energy demand-cost-emission comparison but also including critical factors such as energy security, energy independence, energy efficiency, amongst other factors. In any case, to approach a general global scenario without the inclusion of new and essential considerations of nuclear power plants would be both incomplete and unrealistic. It is clear that the urgency of fighting against climate change has left little to no time to ponder upon the vast portfolio of options to conclusively and adequately discard some of them. For this reason, consistent efforts towards informing the public and working towards the acceptance of the technology should be of utmost importance since authors such as Kim et al. [18], Zhou & Zhang [19] and Sun & Zhu [20] suggest that nuclear power generation is significantly related to public acceptance or rejection. As Parsons et al. [7] state, "we are running out of time...it is time to take a fresh look at the role that nuclear energy can play in decarbonizing the world's energy system" and conclude "renewable and nuclear energies are not mutually exclusive, but complementary". The more time it takes to act, the less effective any of the solutions to counterbalance the damage will be.

Having established that it is not only logical but crucial to include new nuclear energy projects in the future energy mix to be able to attain the current emission objectives to counterbalance climate change damage effectively, it is of central importance to aboard the current challenges that nuclear energy faces. Amongst the primary sources of unrest that tend to classify nuclear energy as a bad option for the world, a relatively large part of the criticism can be summarized into three main points of frailty: 1) Nuclear waste, 2) Dependency on nuclear fuel reserves (disponibility of Uranium), and 3) possibly most importantly, Nuclear safety.

The problem of nuclear waste is an on-going research field, and whilst there is no definite solution, some countries have already developed their strategy. For example, in Finland, a deep-waste repository is set to open as soon as 2020, which would store spent fuel without reprocessing [21]. On the other hand, the French strategy, as to date, is to reprocess the spent fuel and vitrify final unprocessable waste to further store in a deep-waste repository [22], [23]. Further research of this and similar concepts is on-going, but will not be further discussed in this work.

For the dependency of nuclear fuel on uranium, many promising concepts involve other sources of fissile material such as the thorium-based reactors that could utilize thorium as fuel, which is a much more readily available material compared to uranium [24], [25]. Furthermore, other reactor concepts including, but not limited to, fast-breeder reactors, can also be used in the future to profit from the nuclear spent fuel itself as a source of energy further increasing the availability of nuclear energy sources [26], [27], [28], [29], [30]. As before, the concepts tackling the nuclear fuel problem will not be further developed here.

This leaves the issue of nuclear safety. This particular concern can and has been tackled in multiple ways with varying foci. This work will focus on the specific context of the worst-case scenario, which queries the resilience of nuclear reactors to severe accidents. Even if other types of accidents may occur in a nuclear reactor, the uttermost damaging and thus, most feared sequence of events is that of a severe nuclear accident that would surpass the designed countermeasures. Hereafter, an overview of the history, accidental progression, and phenomenology involved in severe accidents.

1.1 Severe accidents

1.1.1 Brief historical review

The International Atomic Energy Agency (IAEA) defines a severe accident as "an accident involving core degradation (typically with core melting)" [31, p.2]. Since the postulation of the concepts that would eventually lead to the design and further construction of the first nuclear reactors, there has always been the looming possibility of accelerated uncontrolled scenarios. Due to the nature of the physical processes governing nuclear fission, severe accidents can result in dangerous human-made highly-radioactive materials.

Even if the presence of long-lived radioactive elements in human-made objects can be objectively linked to the first documented use of uranium (even if inadvertently) as found in the colored-glass of certain parts of a Roman mural glass mosaic[1] near Naples around the year 79 A.D. [33], the creation of highly-radioactive materials has been an object of recent history. Starting from the actual discovery/identification of uranium in the mineral pitchblende (now called Uraninite) by Martin Heinrich Klaproth in 1789, to the construction and operation of the first nuclear reactor by Enrico Fermi in 1942, 150 years of scientific advancement occurred passing through monumental events such as the discovery of ionizing radiation by Wilhelm Conrad Röntgen in 1895, the correct identification of radioactivity as a spontaneous event by Ernest Rutherford in 1902, the discovery of the neutron in 1932 by Sir James Chadwick and the almost simultaneous description of fission mechanisms (which in turn confirmed of Einstein's energy-mass equivalence) by Lise Meitner & Otto Robert Frisch, and Otto Hahn & Fritz Strassmann in 1939.

It took humankind 150 years to go from rock to reactor. However, only ten years transpired between the first operation of Enrico Fermi's "nuclear pile" and the first severe accident, where within twenty seconds the reactor core underwent partial meltdown. This first severe accident took place in the 30 MW NRX heavy-water research reactor in Ontario, Canada, on December 12, 1952. What started as a series of operator mistakes and system failures leading to an incorrect withdrawal of a control rod, finished in fuel rod melting and reactor core damage [34]. Whilst this was not the first time large amounts of radiation were received by humans, it was the first accident that incurred into mitigating measures in the form of removal of the damaged reactor [2] and further decontamination and burial of the reactor tank [38].

---

[1] Interestingly enough, it may be argued that a possible source for the uranium found in the mural may be linked to the infamous eruption at mount Vesuvius on 79 A.D. since, as Avanzinelli et al. [32] state, there is evidence of uranium excess at Mount Vesuvius linked to volcanic eruptions.

[2] Curious fact: The 39th president of the U.S.A., James Earl Carter Jr., was an active part in the efforts to dismantle the damaged core and absorbed the 1952's maximum yearly allowance of radiation in 90 seconds [35, p.54], which according to Adams [36] was equivalent to 150 milliSieverts. For comparison, as reported in [37, p.64], the average recorded dose that a liquidator received after the 1986 nuclear disaster in Chernobyl was of 170 milliSieverts.

Looking at the subsequent severe accidents, as listed in Sovacool [4, pp.393-400] and explained by Sehgal [39, pp.5-10], it is noted that it took four more severe accidents (Windscale 1957, again Chalk River in 1958, Simi Valley in 1959, and Idaho Falls in 1961), several international conferences (such as the 1955 Geneva Conference, which was the first gathering of nuclear reactor scientists from East and West, and the 1956 New York International Conference on the Peaceful Uses of Atomic Energy), and a series of papers, studies, and reports (such as the WASH-740 [40], TID-14844 [41]) before the first thorough document providing decisive and comprehensive views in the field of nuclear safety was published in 1964 as averred by Tanguy [42]. As a result of the continuous research, and the knowledge coming from a series of reports of the different accidents occurring during the 1960s-1970s, and after the dissolution of the U.S. Atomic Energy Commission in 1974 and the creation of the U.S. Nuclear Regulatory Commission (NRC) the same year, in 1975 the first full assessment of accident risks in U.S. commercial nuclear power plants was made by a commission of scientists under Rasmussen [43]. This famous publication (also known as the "Rasmussen Report", or more commonly as the "WASH-1400" report) considered different scenarios and series of events that could take place in a large Nuclear Power Plant (NPP) and quantified, with the resources available at the time of publication, the probability of their occurrence, and their consequences.

Despite the advancements of the state of knowledge concerning the 1952 severe accident, four years after the publication of the WASH-1400 report, the first of the three major nuclear disasters in human history occurred at the Three Mile Island (TMI) reactor 2, a Pressurized Water Reactor (PWR), located near Harrisburg, Pennsylvania on March 28, 1979.As presented by Sehgal [39, pp.28-32], Corey [44], Högberg [45], Marksberry et al. [46], Thomsen [47], Tolman et al. [48], and Rempe et al. [49] the accident started by loss of feed-water which caused the steam generators to dry-up. This, in turn, led to a series of events where the water temperature and the pressure in the reactor core rose.

The continuous rise of pressure forced an automatic shutdown of the reactor core and the turbines, and the further manual activation of a release valve. Following the unfortunate failure in the valve closing, the reactor pressure continued decreasing, and the water continued to flow out of the vessel. Due to the drop in pressure, the continued heat generation from the core, and the high temperature of the water, there was a large steam generation inside the vessel even after the automatic activation of the emergency core cooling system, which began injecting water back inside the vessel. The vapor inside the core impeded the water in the pressurizer to descend into the core, giving misleading information to operators about the water level inside the core, which led to them shutting down the emergency core cooling system. The continued loss of flow and failure in closing the release valve until later in the event sequence led to the vapor quantity inside the core to continue to grow until the main reactor coolant pumps were eventually forced to shut down (to avoid cavitation in the vapor filled pumps). The further descent of the water level inside the core led to core uncovering, which in turn conduced to fuel overheating, then to zirconium oxidation (which added further heat) and finally into core meltdown. Further actions taken by the operators restored control of the situation to them, but the damage was done, and the molten core partially relocated to the bottom of the Reactor Pressure Vessel (RPV) where it remained, as shown in figure 1.3. This molten core material, which is composed mainly of molten fuel and fuel rods/assemblies, fission products, and reactor core structural elements, is commonly known as corium.

The second, and perhaps the most infamous, major nuclear disaster occurred at the Chernobyl NPP reactor 4 (RBMK reactor design, which is a soviet water-cooled channel-type reactor with graphite as

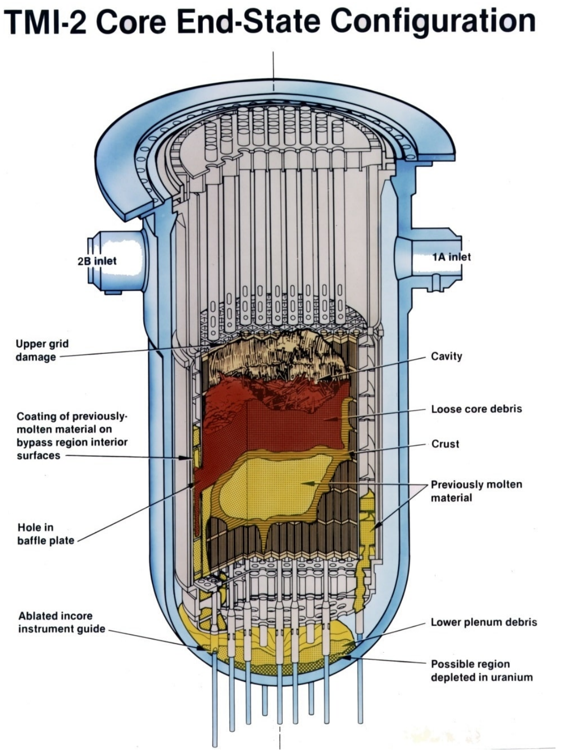

Figure 1.3 – TMI-2 core end-state configuration showing the relocation and accumulation of molten material inside the RPV

Taken from: [46, p.12]

moderator) located in Pripyat, Ukraine on April 26, 1986. Differing from what happened at TMI 7 years before, the events that led to the disaster are more complex since the reactor was not operating in normal conditions. It is also important to point out that the reactors at TMI and Chernobyl are largely different, hence a direct comparison of the sequence of events would be incomplete without the explanations of the overlying physics, design, and technological differences between the two. This last will not be addressed at length, but rather some important features will be pointed out. Amongst the essential differences, a notable one is that the design of the Chernobyl reactor building had a critical flaw in the shape of not having containment building on the upper part of the reactor. In other words, the reactor housed in a standard industrial building (not particularly well reinforced), had a proper concrete containment only at the bottom part of the core.

As previously stated, the reactor was not operating in normal conditions. The operators were performing a test of the turbines' efficiency to extract heat in the case of loss of power supply and the shutting down of emergency cooling systems. This required the reactor to be at low power, however, as Kortov & Ustyantsev [50, p.13] point out, "constructional and physical characteristics of RBMK-1000 reactor did not allow the staff to effectively control its work at such low capacity". The bad handling of the control rods during the test and the conditions of the reactor led to a loss of control of the reactor power, which prompted the operators to use the emergency shutdown rods. This rods also had a design flaw, which caused an initial surge in reactivity and further-flung the reactor out of control which led to power surge (of a factor of 100 times nominal power), instantaneous vapor generation, and finally explosion that destroyed the reactor core and the industrial building it was housed in, launching radioactive material into the surroundings as evidenced in figure 1.4. The mitigation of the accidental consequences involved active measures from soviet workers. As the molten reactor core continued its path through specific pathways, as can be seen in the figures 1.5 and 1.6, a significant effort took place to drain a particular part of the reactor building due to the inherent fear of a further violent steam explosion that would be triggered by the contact of migrating molten core and the water contained in the lower parts of the building [39, pp.33-43], [37], [45].

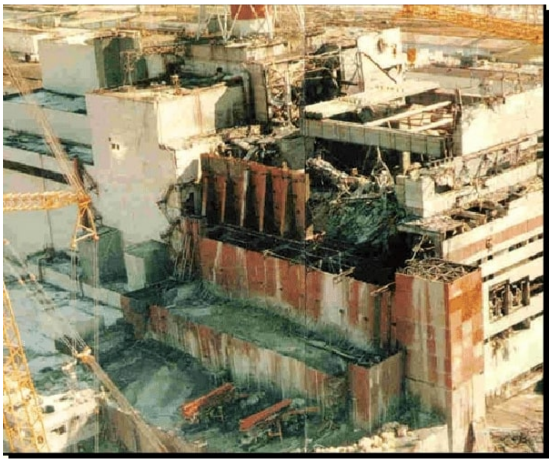

Figure 1.4 – Chernobyl reactor 4 building after the 1986 accident

Taken from: [51]

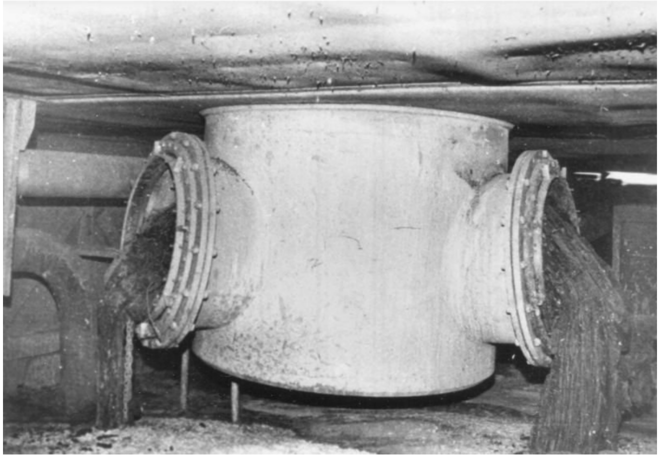

Figure 1.5 – Chernobyl corium flowing out a valve

Taken from: [52]

Figure 1.6 – Chernobyl corium found underneath the reactor, also known as the “elephants foot”, in a steam distribution corridor in 1996

Taken from: [52]

Twenty-five more years passed until the most recent, and first multi-reactor, nuclear disaster came to pass. This time it occurred at the Fukushima Dai-ichi NPP in reactors 1,2,3, and 4 Boiling Water Reactors (BWRs) (a light-water reactor designed to produce steam directly inside the RPV) located in Õkuma, Fukushima prefecture, Japan on March 11-15, 2011. Unlike the previous disasters, the one that transpired in Fukushima Dai-ichi has its roots in a 9.1 Richter scale earthquake close to the plant that led to a

∼14 meters tsunami that flooded the plant. Similar to Chernobyl, the plant had some fatal flaws. The anti-tsunami barrier was only 5.5 meters high (after being further expanded by the Fukushima NPP operator, Tokyo Electric Power Company (TEPCO), following a 2009 re-assessment of risks, which placed the tsunami height at 5.4-6.1 meters [53, p.11]). Nevertheless, as Synolakis & Kânoğlu [54, p.9] point out, TEPCO ignored other studies which predicted that tsunami heights of 8.4 to 10.2 meters would be probable in the region. Additionally, the plant design placed the emergency diesel generators in the basement of the buildings, and logically when the tsunami over-boarded the barriers, they were the first rooms to flood.

Despite the reactors in operation (units 1, 2, and 3) having been properly shut down when the earthquake was detected, the situation quickly turned grim. The earthquake induced a Loss-of-Offsite Power (LOOP), and the emergency diesel generators turned on immediately. Approximately 40 minutes later, the tsunami reached the NPP, and flooded the emergency generators of units 1-5. Thanks to a difference in location, and an extra redundant air-cooled generator (3 total emergency generators instead of 2 as for units 1-5), the emergency generators of unit 6 functioned adequately even after the tsunami made its way through the plant. This generator feed electrical energy to both unit 5 and unit 6 (which were not in operation at the time) allowed the proper de-escalation and further steering of the reactors into safety [53, p.3]. The unit 4 reactor had no fuel in the core as it was in the re-fuelling process. For the other units (1-3), the prolonged loss of cooling power led first to a decrease in the water levels inside the core, then to core uncovering, core degradation, and final core meltdown. The elevated temperatures to which the fuel and the reactor components were subjected also led to a high hydrogen production coming from the oxidation reaction of the zircaloy in the fuel cladding. This, in conjunction with reduced containment volume of the BWR (a particularity of the design which is partly due to the fact of the significantly lower pressure at which the reactors operate, in comparison to a PWR, ∼ 76 and 150-160 atm respectively) led to the final hydrogen explosion that destroyed the reactor buildings, as seen in figure 1.7. The explosion also led to the spread out of the radioactive fission product gasses that were vented to the containment buildings.

It is important to note that comparing with the Chernobyl nuclear disaster, the nature of the observed explosions is largely different. In Chernobyl, it was a vapor explosion inside the core, whilst in Fukushima, it was a hydrogen explosion in the containment building. In general terms, the accidental progression was relatively the same for the four units that underwent the hydrogen explosion, differing mainly in time. Unit 1 was ultimately destroyed the 12^{th} of March, whilst unit 2 was destroyed the 14^{th} of March, and finally units 3 and 4[3] were destroyed the following day [53], [54], [55], [56], [57]. The mitigating efforts continued after the explosions, and the cooling of the reactors was first done via sea-water, and further reestablished after electrical power normalized. Nevertheless, the core meltdown and temporary lack of cooling led to the relocation of the material outside the RPV. To this date, on-going efforts to localize, quantify, and characterize the corium are being pursued by TEPCO. Figures 1.8 and 1.9 show the latest updates, which evidence the relocation of the corium and the apparent morphology of some of the debris that has been found so far in one of the three units were debris has been found outside the RPV.

---

[3] It is important to clarify that the explosion in unit 4 is attributed to hydrogen coming from unit 3 due to a leak in piping connecting both buildings, as unit 4 had no fuel in the core.

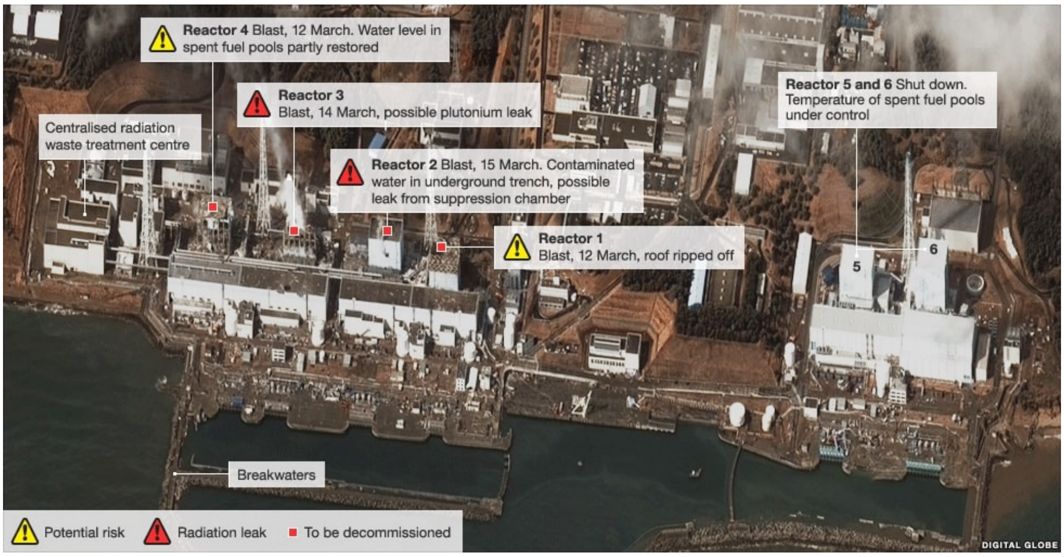

Figure 1.7 – Fukushima NPP areal view after the disaster. Note: The image has mislabeled the reactor 4 blast, which happened the 14^{th} of March not the 12^{th}.

Taken from: [58]

Figure 1.8 – Possible corium relocation into the primary containment vessel in Fukushima Dai-ichi unit 2

Taken from: [59]

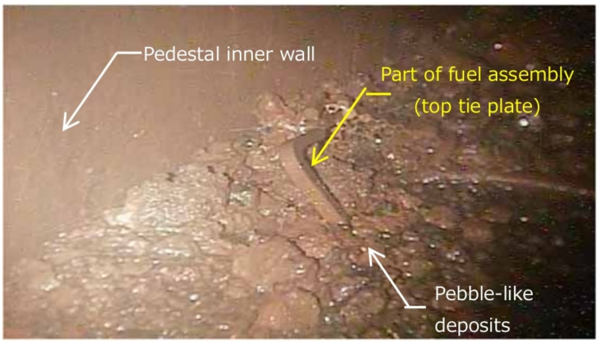

Figure 1.9 – Possible corium "pebble-like" deposits in the primary containment vessel in Fukushima Dai-ichi unit 2

Taken from: [60]

1.1.2 Accidental progression

Severe accidents are typically identified through "a combination of probabilistic methods, deterministic methods and sound engineering judgement" performed for each distinct plant and design [61, p.3]. The well-developed tools of the Probabilistic Safety Analysis (PSA) approach serve as a starting base to discern, classify, and quantify the risks of the impact of different failures in a modern NPP. Taking into account that as Domaratzki et al. [62, p.3] state "most accidents in nuclear power plants...will result in zero plant damage and zero radiological impact on members of the general public", it is of utmost importance to identify and understand the causes and consequences of the series of events that could lead to an accident that would result in plant damage and/or radiological consequences to the public. As in other industrial accidental analysis methodologies, it is vital to identify the events that give way to the accidental progression, otherwise known as initiating events.

1.1.2.1 Initiating events

The International Atomic Energy Agency [63] classifies the initiating events in two distinct groups: internal and external hazards. Internal hazards are defined as "hardware failures in the plant or maloperation of plant hardware through human errors or due to man-machine interface problems", whilst external hazards are defined as "events originating outside the NPP that create extreme environments common to several plant systems." [63, p.8]

Evidenced in both TMI and Chernobyl, several distinct internal events can lead to a severe accident with core meltdown. As presented by International Atomic Energy Agency [63, pp.18-19] "the internal initiating events may be looked upon as consisting of three main categories" non-exhaustively listed hereafter:

1. Loss-of-coolant Accident (LOCA) defined as primary system breaches of different sizes resulting in loss of primary coolant, e.g.:
    - pipe breaks (or ruptures) of different sizes, or
    - opening and failure to re-close of valves.
2. Transients defined as events that induce disturbances in nominal plant operation without loss of primary coolant, e.g.:
    - reactivity incursion (leading to abrupt power rise),
    - perturbation of feed-water flow, or
    - turbine/condenser failure.
3. Common cause initiators defined as events that require reactor shutdown and disable multiple plant control systems, e.g.:

- loss-of-offsite power, or
- loss of DC power.

On the other hand, external initiating events, as the one that led to the Fukushima disaster, can include, but are not limited to [63, pp.105]:

1. Natural, e.g.:
    - earthquakes,
    - forest fires,
    - floods, or
    - extreme winds.
2. Human, e.g.:
    - internal fires,
    - chemical releases,
    - airplane crashes, or
    - planned weaponized attacks.

As Blandford & May [64, p.p] summarize "in the case of Three Mile Island and Chernobyl, the initiating events that caused the accident were internal events and were exacerbated by human error. In the case of Fukushima, the initiating event was an external event in the form of an earthquake and subsequent tsunami".

Nevertheless, a rather common postulated initiating event used in severe accident scenario analysis that could lead to core degradation is the so-called LOCA. These types of accidents "range from a failure of a small (2-inch diameter) to a large (20-inch diameter) pipe", including pipes in the primary circuit [62, p.4]. Joyce [65, p.336] rightly states that "in such an event, due to the pressure in the primary circuit...the coolant would be lost...very rapidly from the reactor vessel along with a very rapid rate of depressurization." The reduced coolant in the reactor core would, in turn, reduce the capacity of the system to extract the heat from the core region.

1.1.2.2 Core degradation

The lack of cooling in the core would lead to some parts of the reactor core to uncover and be subjected to a high rise in temperature. The rise in temperature would, in turn, result in the thermal degradation of the fuel rods. The rise in temperature would also induce specific chemical reactions that could introduce additional energy, hence promoting the degradation of the situation, such as the zirconium oxidation (the main component of the fuel rods containing the fuel pellets). This situation could be further aggravated by the mechanical failure that would be induced and/or enhanced by the melting/degradation of some parts of the fuel rod/assembly. The loss of mechanical stability, which could be attributed to mechanical stresses between the interior and exterior regions of the degraded core, and/or interactions between degraded material and core wall [48] would result in migration of material to the lower part of the RPV, also called the lower-plenum or lower-head.

As in TMI, some actions can be taken by the operators that could limit or stop the further progression of the accident, such as high-pressure water injection into the vessel from the reactor's safety systems. Nevertheless, depending on the nature of the scenario, water injection could actually be counterproductive. In particular, reflooding could re-induce strong oxidation, i.e., substantial energy input and massive hydrogen generation. Furthermore, as per Thomsen [47, p.11], the core can also be "shattered by the quenching, resulting in collapse of the fuel elements into a debris bed". In other words, both the heat generation from the corium and the quenching of the same could lead to its fragmentation and facilitate relocation. Moreover, the large quantity of hydrogen production and an increase in reactor coolant system pressure further detriment the already unfavorable conditions.

Corium relocation to the lower plenum was evidenced in the TMI accident as shown in figure 1.3, where it was found that 62 tons of corium, around 45% of the core, ended up in the bottom of the reactor pressure vessel [45, p.270]. As seen in the lower part of figure 1.10, different parts of the degraded core were also found in different forms. Broken fuel rods, intact fuel pellets, parts of rod assemblies were found on top of a corium debris bed [66].

In theory, there could be a highly energetic water-corium interaction, also called Fuel-Coolant Interaction (FCI) (further discussed in section 1.1.2.6), inside the RPV during the stage of molten corium relocation towards the lower head, as there may be water remaining there. FCI could lead to aggressive vapor production and further steam explosion. Indeed, in the WASH-1400 report [43], this event was referred to as the α-mode of failure. It was presumed that the steam explosion would lead to a failure of the upper vessel lid (failure of the bolts), which, in turn, would allow some debris to hit the containment wall. After intense research work in the 1990s, such an event is nowadays considered as very improbable. More recently, in the OECD SERENA-2 program on steam explosion, Basu & Ginsberg [67] concluded that the lower head vessel failure itself is also quite unlikely. In addition, the existing experimental data converge towards the indication that the triggering of a steam explosion is very unlikely if the water temperature is at saturation, as should be the case here. Thus it is commonly accepted that a vessel failure following an FCI is mostly improbable.

Figure 1.10 – Panoramic view showing the corium migration and the morphology of the rubble bed and core periphery inside TMI-2 reactor vessel

Taken from: [46, p.30]

Nevertheless, although not explosive, the FCI will induce fragmentation of the melt, which may lead to the formation of a debris bed. However, it is estimated that the fragmentation is incomplete and that rapidly a molten pool may form in the lower head. If the heat extraction cannot accommodate the residual heat and the sensible heat of the molten material, the continuous degradation of the reactor fuel/elements would lead to an accumulation of molten material in the lower part of the vessel as represented schematically in figure 1.11. Intensive research on the behavior of the melt in the lower head is currently on-going, namely within the IVMR project, which is a European Commission project under the Horizon2020 framework [68].

The situation is further complicated by the complex and numerous thermodynamical and chemical interactions among the corium components. In particular, the metals that have not been oxidized, coming either from the fuel cladding (mainly zirconium), either from the molten internal structures as well as the vessel itself (stainless steel), will separate from the oxidized materials as they are not miscible. The evolution of the corium pool and its possible stratification will then strongly depend on the composition. The schematized situation pictured in figure 1.11 is probably somewhat simplified, with a significant probability of the evolution of the presence of a high-density metal (including uranium) layer at the bottom (not mentioning the axisymmetry).

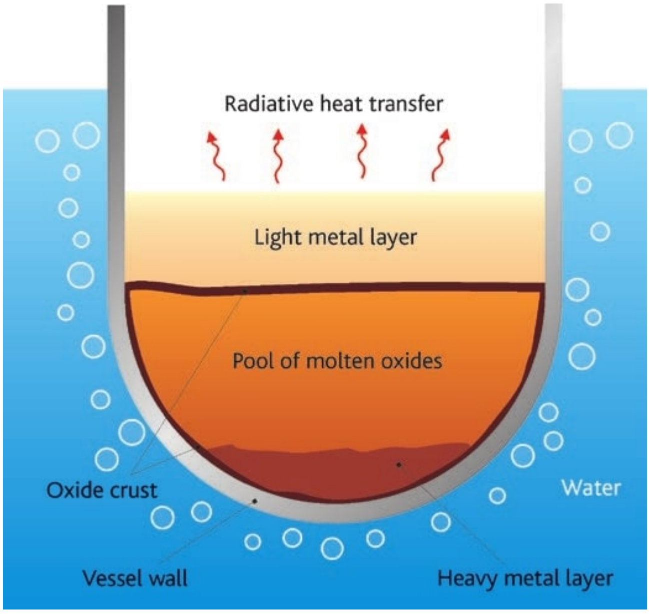

Figure 1.11 – Lower-plenum multi-layer corium scheme showing the possible stratification of corium forming a light metal layer on top and a heavy metal layer on the bottom of the RPV

Taken from: [69, p.232]

1.1.2.3 Hydrogen explosion

The accumulation of hydrogen all along the accident is unfavorable for the integrity of the containment building due to the likelihood of combustion when it interacts with the pre-existing oxygen. Hydrogen explosions have been reported in all three of the most severe accidents, including TMI-2 where with an estimated average volumetric hydrogen concentration of 7.9 % the pressure spike produced in the explosion was of around 2.9 bars without any significant consequence to the containment's wall integrity [70, p.41].

Although hydrogen explosions are by far not exclusive to the nuclear industry, considering that there is extensive literature boarding the topic, the scenarios and conditions intrinsic to severe accidents in NPPs lead to important specificities. Effects of scale, safety-systems measures, and configuration of the different components may hinder, or enhance, the conditions necessary for hydrogen explosion, exemplified in figure 1.12 where the limits of both the hydrogen flammability and explosion are plotted at different temperature and pressure conditions. For this and more, the evaluation of the hydrogen risk is complex and unique for each different plant design.

This hydrogen risk would be present throughout the entire accidental scenario as long as there are the right quantities of oxygen and hydrogen in the atmosphere. Due to the large volume of the PWR containment building, there can be different hydrogen distribution scenarios depending on the mixing dynamics of the atmosphere present at that time. The distribution and migration of the hydrogen would then influence the risk since heterogeneous concentrations could lead to a local accumulation and enhance the danger to the adjoining structures, hence leading to a localized building failure. The evolution of the concentration depends not only on the dynamics of hydrogen generation but also on the use of the safety systems.

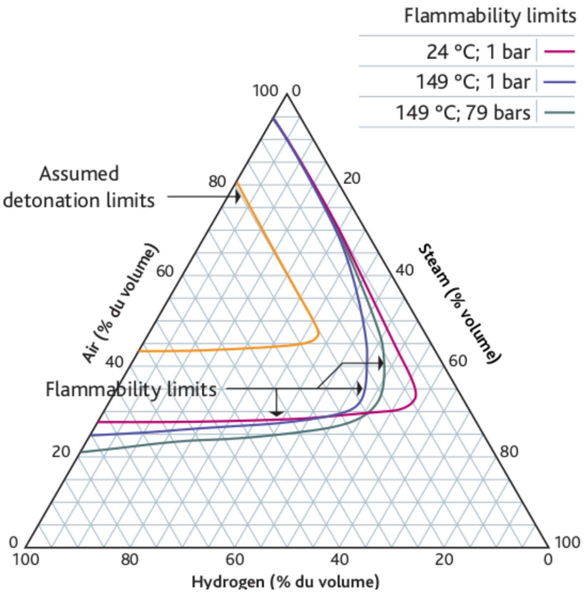

Figure 1.12 – Hydrogen flammability/explosion limits as a function of air-steam-hydrogen concentration

Taken from: [69, p.162]

First of all, especially after Fukushima, all modern NPPs include specific devices to reduce the hydrogen concentration, such as catalytic recombiners designed to transform hydrogen into water via reaction with oxygen [39], [69], [70]. This may be considered as a sufficient strategy to limit the explosion to acceptable bounds. Nevertheless, these systems reduce the concentration within a certain time scale, and they cannot accommodate rapidly to fast and massive hydrogen production (following, for example, a reflooding action). Case in point, the Containment Spray System, which is a water aspersion system designed to condensate water vapor in the containment building with the primary purpose of reducing the containment building pressure, may lead to an increase in hydrogen concentration due to steam condensation.

In any case, the intricate mechanisms that would affect the hydrogen concentration limit the manageability of the severe accident, and could be affected by mass flux (both vapor and hydrogen) from other severe accident phenomenology, including the Molten Corium-Concrete Interaction (MCCI).

1.1.2.4 Vessel failure

If the integrity of the RPV becomes compromised, a breach in the reactor vessel would appear, as seen in figures 1.13 and 1.14. The failure mechanism and its dependency on the materials and thermal processes have been studied [71], [72]. Obviously, the vessel failure characteristics will strongly depend on the actual scenario inside the vessel. As stated by Sehgal et al. [72, 51], the failure would most probably occur in the lateral region of the RPV. Furthermore, Wang & Cheng [73, p.1] assert that "the main failure mechanism of in-vessel corium retention through external reactor vessel cooling (IVR-ERVC) happens when the local heat flux through reactor pressure vessel (PRV) wall exceeds the critical heat flux (CHF)". This is due to the so-called "focusing effect", which arises from stratification in the corium pool, where the lower density metallic contents rise, leading to a concentration of the heat flux at the interface between the upper metal layer and the vessel wall. It may be noted that this leads to heat fluxes of the order of 1 to 2 $\frac{MW}{m^2}$, which have to be accommodated by the vessel. In fact, this entails a sharp reduction of the wall thickness, through its melting down to a few centimeters. This point is the major weakness of the management strategies relying on the retention of the melt inside the RPV by external cooling through specific actions and devices. The determination of the actual wall thickness during the accident and the minimum one to assure vessel "integrity" are not easy tasks.

The vessel failure dynamics itself, including fracture propagation, is also a complicated issue. Some experiments of the LHF/OLHF program [74], [75] showed a nearly complete "unzipping" of the lower head, figure 1.13, whilst other show a more localized vessel fracture as seen in the EC-FOREVER test experiment shown in figure 1.14. In turn, the characteristics and dynamics of the melt discharge will be affected by the mechanism and size of the break. In other words, the RPV failure could lead either to a relatively limited discharge of the melt and subsequent discharge episodes, either to a massive initial corium discharge. At the current state of knowledge, almost all situations are considered for the analyses of the subsequent events of the corium progression.

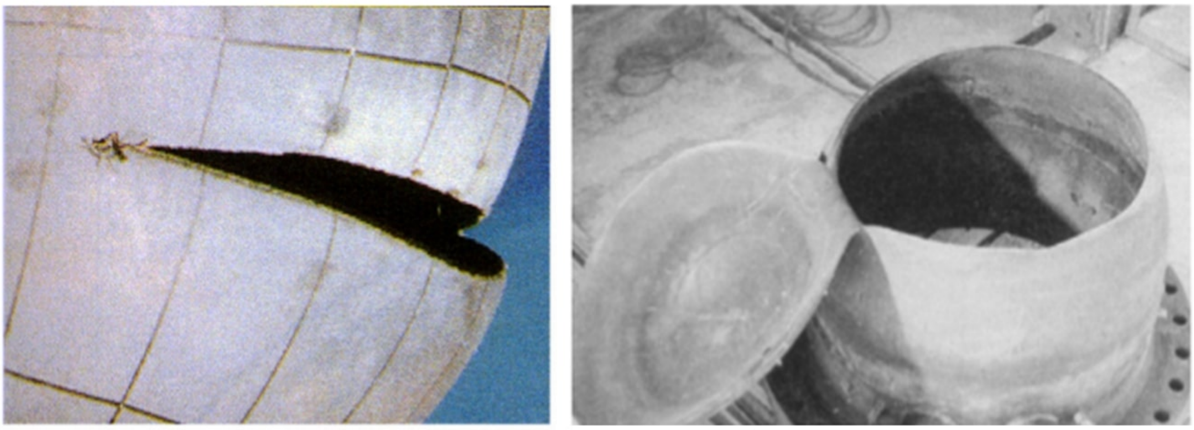

Figure 1.13 – LHF 3 test with a large vessel failure (left) and LHF 5 test with almost complete circumferential unzipping of the vessel (right) from the LHF experimental research program on RPV failure behaviour

Taken from: [74]

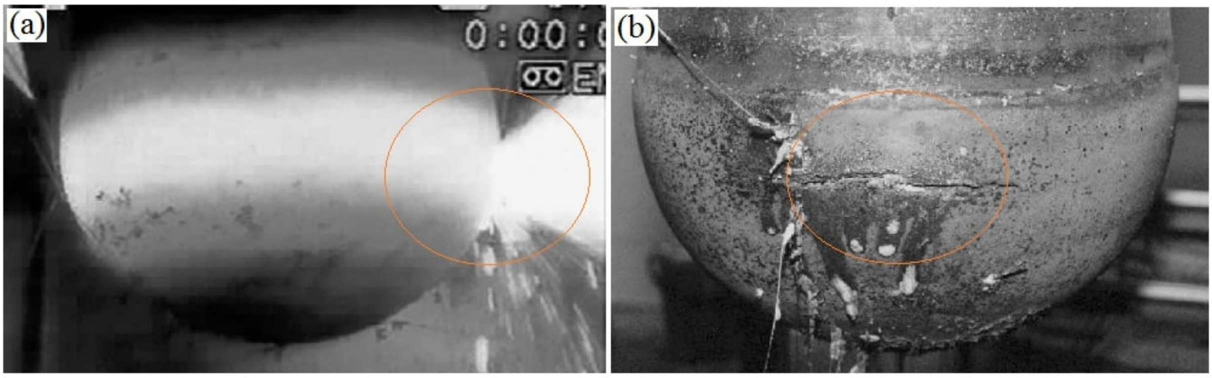

Figure 1.14 – Lower head failure during the test (left) and post-mortem failure configuration (right) from a test in the EC-FOREVER platform designed to study the possible failure modes for the in-vessel retention strategy

Taken from: [71, p.353]

1.1.2.5 High-pressure melt ejection/direct containment heating

In the case of reactor vessel failure, the corium contained inside the RPV can be violently expelled if there is a significant pressure difference between the inside of the RPV and the containment building as depicted in figure 1.15. This event is in general called High-Pressure Melt Ejection (HPME). Nevertheless, the less explicit expression of Direct Containment Heating (DCH) is now generally preferred. DCH has been studied mostly in the absence of water in the pit, or with minimal amounts. In the presence of water, the related studies are embedded in those related to FCI (see section 1.1.2.6). The high pressure will induce a high melt ejection velocity, leading to a fine fragmentation of the corium and spread of the particles into the containment building. The term DCH comes from the fact that the small particles will release their heat very rapidly, which will induce the containment's pressurization. Alongside the corium discharge, an important quantity of gases, such as vapor and hydrogen, would also be released into the containment building. However, the most dangerous aspect of DCH is the induced fast and almost complete oxidation [76]. The experiments also tend to indicate that the hydrogen produced will almost entirely burn, along with the one initially present.

Thus, the DCH risk is mostly associated with the following parameters:

- the vessel pressure,
- the amount of unoxidized melt, particularly zirconium, and
- the presence of pre-existing hydrogen in the containment.

IRSN could take benefit of the DISCO experiments [76] to evaluate the dispersion of the melt and evaluate the risk of DCH for the french fleet of PWRs and the future EPR reactor, [70], [77] with the MC3D code.

Taking into consideration the various uncertainties, the range of critical vessel pressure to avoid DCH is 20-30 bars for the existing fleet (900, 1300, and 1400 MWe) and a notably lower 5-10 bars for the EPR, due to its smaller reactor pit volume. Furthermore, the mechanical load exerted on the RPV, coming from the thrust generated by unloading of the RPV and the increased pressure in the reactor pit, may dislodge the RPV posing a severe threat to the integrity of the containment building [69, pp.146-148]. Nevertheless, recent studies at IRSN (not published) tend to indicate that, whilst the risk of vessel detachment is real at high vessel pressure, the risk of vessel "flight" and contact with the containment is quite minimal.

The study of the impact of the presence or absence of water at the moment of the HPME adds a considerable degree of difficulty. The dynamics of material transport, coupled with the generation of vapor, induce secondary effects. Amongst-which, an undesirable one would be the further pressurization of the containment building that could be expected from the vapor generation, linked to the evaporation by the cooling of the corium particles. Nevertheless, the presence of water can both inhibit the oxidation, hydrogen combustion, and extract heat from the corium (hence reducing the effects of the heating of gasses and further oxidation) [70].

The highly complex phenomena involved in this phase have led the NPP operators to modify the Severe Accident Management Guidelines (SAMG) to avoid the risk of HPME. As postulated by Jacquemain et al. [69, p.74], "direct containment heating is prevented by reducing the possibility of a high-pressure core melt. This ultimately involves intentionally reducing the pressure in the RCS so that the pressure in the vessel is below 15 or 20 bar (order of magnitude) when it is breached".

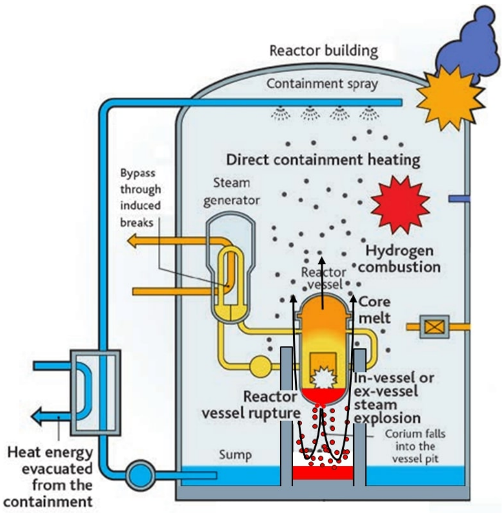

Figure 1.15 – High-pressure melt ejection/direct containment heating scheme depicting the corium fragmentation, relocation and possible RPV movement induced by the pressurized corium unloading

Adapted from: [69, p.147]

1.1.2.6 Fuel-coolant interaction/steam explosion

If the core melt relocates in a region containing liquid water either in the vessel or in the pit, figure 1.16, the molten material and the water will enter in a complex thermal-chemical-hydrodynamical interaction called fuel–coolant interaction [72], [78], [79]. The first (expected) result is the fragmentation and dispersion of the melt in the water that may form, depending on the conditions, a coolable particle bed. The length scale of the fragmented debris (drops) will be of the order of some few millimeters [80], [81], [82]. If the fragmentation is not complete and/or if melt drops are not sufficiently cooled to solidify, the melt will spread underwater. This stage is called the premixing of the fuel–coolant interaction. However, the flow during the premixing stage might also enter a critical phase and further destabilize to produce an energetic event called steam explosion, which may endanger the containment integrity. As already discussed, the risk posed by an in-vessel steam explosion to the containment integrity is now considered acceptable. However, the analysis resulting from the SERENA-2 project (in particular) could not rule out the risk for the ex-vessel case due to the low capacity of the concrete wall to accommodate the strong pressurization. Indeed, an explosion in the reactor pit may induce huge pressure spikes (some hundreds of bars), which despite their small duration (some tens of milliseconds), may strongly damage the internal structures and the containment itself.

The triggering phase of a steam explosion may occur under several mechanisms and cannot yet be predicted for practical situations. Then, particularly in reactor accident analysis, it still has to be considered as a stochastic event.

The complexity of the evaluation of FCI comes first from the turbulent mixing processes of the hot melt at a temperature of about 2500-3000 K in water. It may be sufficient to say that even in the most straightforward situation of a cold liquid, fluid dispersion in another cold fluid is still not fully characterized and understood.

Furthermore, several different physical phenomena additionally complexify the overall interaction. Firstly, the boiling of the water strongly influences the vapor film and its stability, hence adding complexity. Second, as the melt is cooled, it may solidify, which could influence the stability of the melt-drop and result in fragmentation. Last but not least, for the premixing, the oxidation of metals has some major effects including the production of hydrogen, i.e., a non-condensable gas in the mixture, the addition of energy to the melt by the reaction heat (particularly with zirconium), and the modification of the melt composition and thus its physical and thermodynamical properties.

The explosion phase itself has long appeared as some kind of mystery, and the understanding is slowly emerging from the on-going research. Since Board et al. [83], it is admitted that the phenomenon is analog to a detonation. The traveling pressure shock induces a fine fragmentation, which induces a fast release of heat, and then the build-up of the shock itself (up to some steady situation). The problem is the understanding and the description of the phenomena occurring at the micro-scales, high temperatures, and tremendous pressures. It may be highlighted that the quite chaotic evolution of knowledge, together with important confronting positions from different experts, does not facilitate the comprehension of the intricate phenomena.

In France, IRSN, CEA and the University of Lorraine are involved in a research project called ICE (for corium-water interaction in french), co-funded by EDF, AREVA and French government (ANR projet) with the goal of resolving the remaining issues and propose coherent modeling in the MC3D code [84].

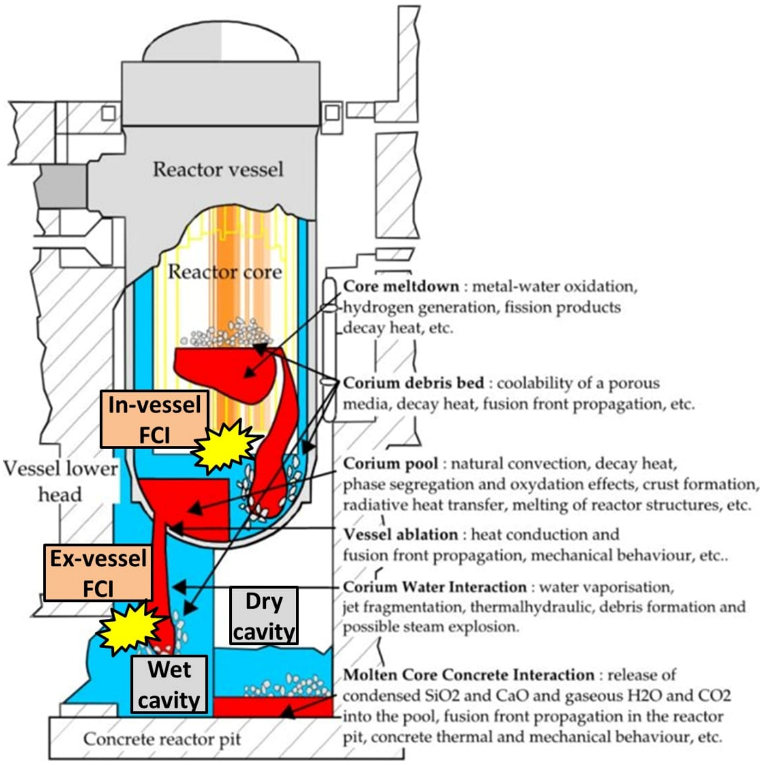

Figure 1.16 – In-Vessel and Ex-vessel corium propagation scheme and possible FCI configurations in PWRs showing the possibility of having an FCI both inside and outside the RPV

Adapted from: [85, p.3]

Steam explosion in the reactor pit is at the origin of the major differences amongst the 3rd generation nuclear reactors. Some of them are based on the idea that the vessel can be cooled externally by water, and that the explosion risk is acceptable, on a probabilistic point of view. Others, including the EPR, are based on the fact that, despite possible small probability, the explosion may induce a direct and early failure of the containment, the consequences of which cannot be accepted. This will be discussed more in detail in section 1.2.

1.1.2.7 Molten corium-concrete interaction (MCCI)

If the corium that is expelled out of the RPV does not undergo a vapor explosion (as would be expected for a dry cavity scenario) it would reach the lower part of the reactor building [4] and come into contact with the concrete. Nevertheless, when the corium comes into contact with the concrete, plenty of questions arise. During this MCCI heat transfer from the high-temperature radioactive corium to the overlaying layer (air/water) competes with the thermal attack of the concrete. With respect to this competition, the concern is the stability of the containment building, which is the last physical barrier available to contain the possible release of radioactive materials to the environment. The challenge lies in evaluating the capabilities of heat extraction by the overlaying water/air layer since "the residual heat...within the

---

[4] In some cases, such as in the European Pressurized Reactor (or Evolutionary Power Reactor) (EPR), the reactor design may include a special surface or compartment designed to contain an eventual corium spread.

corium...cannot be removed by conduction via the basemat due to its thickness and the very low thermal conductivity of concrete" as stated by Jacquemain et al. [69, p.200]. The complex interlinked behavior of the materials involved can result in a number of different configurations that may favor or hinder heat extraction. Figure 1.17 depicts such expected configuration enclosing some of the different processes that may take place during an MCCI, which include: concrete ablation, crust formation at the interfaces, gas bubbling through the corium pool, crust fracturing, water percolation through the crust, gas-driven melt eruptions, metals oxidation, layer stratification, amongst others.

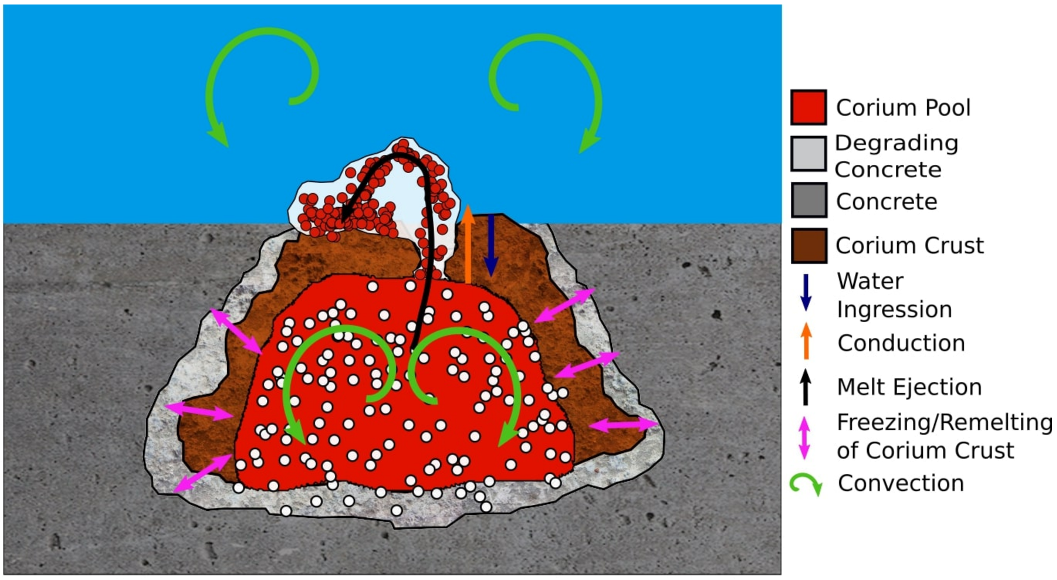

Figure 1.17 – MCCI diagram with heath exchange mechanisms and observed physical phenomena

The onset of such interaction would occur once the corium coming from the reactor vessel relocates on top of the corresponding concrete surface (basemat for reactors without core catcher or core catcher for advanced reactors such as the EPR). At the interfaces between the corium and the concrete, the heat dissipation to the concrete leads to a temperature rise, until reaching a temperature between the concrete's solidus temperature and the corium's liquidus temperature. This last derives into concrete degradation where, recalling that as Xotta et al. [86, p.86] state concrete "is a highly heterogeneous material and its composite behavior is exceedingly complex", it decomposes, and its components begin to incorporate into the corium pool. A set of reactions summarizing the decomposition process, widely utilized in the context of nuclear severe accidents [87] [88], is presented here after:

- 30–105 °C: escape of free water (not bonded). All free water is evaporated by 120 °C.
- 110–170 °C: decomposition of some of the cements components i.e. gypsum ($\mathrm{CaSO_4 * 2H_2O}$) via a double endothermic reaction, ettringite ($\mathrm{wCaO_4 * xAl_2O_3 * yCaSO_4 * zH_2O}$), and loss of water from carboaluminate hydrates

$$CaSO_4 * 2H_2O(s) \Longrightarrow CaSO_4 * 0.5H_2O(s) + 1.5H_2O(g) \tag{1.1}$$

$$CaSO_4 * 0.5H_2O(s) \Longrightarrow CaSO_4III(s) + 0.5H_2O(g) \tag{1.2}$$

- 180-300 °C: decomposition of the CaO-SiO_2-H_2O and carboaluminate hydrates takes place
- 450-550 °C: dehydroxilation of the portlandite (calcium hydroxide)

$$Ca(OH)_2 \Longrightarrow CaO + H_2O(g) \tag{1.3}$$

- 573 °C: $\alpha \rightarrow \beta$ transformation of quartz aggregates
- 700-900 °C: de-carbonation of calcium carbonate

$$CaCO_3 \Longrightarrow CaO + CO_2(g) \tag{1.4}$$

- 1100-1250 °C: Concrete ablation, taking "the formation of a liquid concrete layer as the reference transition, the effective melting temperature generally corresponds to the temperature at which 30 – 50 vol % is liquid" [89, p. 41]. Table 1.1 shows the liquidus and solidus temperature (below which everything is considered to be solid) of different concrete types.

Table 1.1 – Solidus and liquidus temperatures, and density for different types of concrete

	Siliceous	**Limestone-common sand (LCS)**	**Limestone**
Solidus Temperature (°C)	1130	1120	1220
Liquidus Temperature (°C)	1250	1295	2305
Density $\left(\frac{\mathbf{kg}}{\mathbf{m^3}}\right)$	2360	2290	2300

*Liquidus and solidus temperatures are hard to define since concrete is a mixture of different components with a wide range of different properties. Values here presented are taken from both experimental results and multi-phase, multi-component chemical equilibrium calculations using Gibbs free energy minimization procedure taken from [69] [90]

The dynamics of the concrete decomposition, and further incorporation to the corium pool, may vary largely with different types of concrete. Further adding complexity to the problem, the change of thermo-physical properties of the mix may also induce phase-change reactions at this interface, where a part of the pool may become solid at the interface. In other words, there may be a simultaneous process of concrete ablation, and solidification of corium into a crust [87]. At the other boundary, between the corium and the atmosphere (water or air), the temperature gradient also leads to the formation of a crust, whose permeability and intrinsic characteristics depend on the composition of the molten corium pool at the time of formation and the amount, and nature, of the concrete which has been incorporated within the corium. As corium from the melt solidifies, it shrinks, inducing series of defects that give rise to the morphology of the crust. This crust is further deformed during the transient by thermal or mechanical stresses through which a network of fissures, pores, holes, amongst others, may form. This upper crust may differ from the crust at the concrete-corium interface since it forms away from the concrete decomposition front, and at a different time, hence from a corium pool with a different composition.

Between these two boundaries, in the corium pool, complex interlinked phenomena condition the dynamics of the mixing and the heat transfer from it towards the boundaries. Gases coming from the concrete decomposition reactions rise through the pool and escape through the upper-crust. Nevertheless, the definite pathway the gases take to traverse the crust is not entirely clear. Up to an extent, again, depending on the nature of the corium and concrete, some gases may pass directly through certain pathways created within the crust and entrain an amount of corium with them. This last would result in corium being entrained from the pool through the crust, otherwise known as melt eruptions, which can draw similitude from underwater volcanic hornitos (rootless lava spatter cones). The corium expelled through the crust can be ejected in "violent" intermittent episodes, or semi-continuous extrusions, again drawing similitude from volcanic hornitos. In some cases where the corium may be ejected with a high velocity, it would first fragment to then settle down on top of the crust and form the so-called debris beds, whilst in others the molten material may simply extrude through the exit channel and drip down. As stated by Robb [91, p.5], "the melt eruption phenomenon has a number of beneficial impacts on melt coolability" since it extracts melt material from the pool hence enhancing the overall heat extraction from it. Nevertheless, the way the corium is expelled and the final state of the deposed materials raises several questions upon the stability of the newly formed layer and the existing crust.

Since all the different mechanisms depend on the time when they take place, and the point in the accidental scenario, a classification is often used to divide the MCCI into three main phases, as presented by Sehgal [39, p.370] :

- Short-term agitated phase with high heat flux (towards interfaces) and high gas sparging rate (superficial gas velocity of few tens $\frac{cm}{s}$) with low concrete mass content in the melt.
- Medium-term phase with high heat flux with increasing concrete mass content in the melt, hence altered melt properties. Superficial gas rise velocity is in the order of a few $\frac{cm}{s}$.
- Long-term phase with high concrete mass content in the melt with low heat transfer to the interfaces and highly viscous melt. The superficial gas velocity is around, or lower than, 1 $\frac{cm}{s}$.

The importance of understanding the different mechanisms governing each phase is reflected in the industry's recurrent effort in expanding the knowledge by pursuing both experimental programs and theoretical investigations. Furthermore, the knowledge gathered in the past decades has also led to the development of different severe accident management strategies fitted for each different type of reactor and plant design. Hereafter, in section 1.2, a non-exhaustive summary of the strategies used, with a particular focus of the strategy adopted by French operator Électricité de Francee (EDF).

1.2 Severe accidents mitigation strategy in France

As Hermsmeyer et al. [92, p.13] state, "the Fukushima accidents highlighted that both the in-depth understanding of such sequences and the development or improvement of adequate Severe Accident Management (SAM) measures are essential in order to increase further the safety of the Nuclear Power Plants (NPPs) operated in Europe". In fact, the need was already recognized before the accident with the emergence of the concept of "3rd generation" reactors, the main characteristics of which is taking into account in the design safety systems for severe accident mitigation. Multiple projects have been pursued to fulfill this need, which led to the proposal of reactors like the EPR in France and the AP-600/1000 in the USA. Thus, finally, the Fukushima accident mainly highlighted and reinforced this need rather than imposing it on new reactors. In contrast, this series of accidents pointed the attention on the existing reactors of which most needed significant improvements or demonstrations of their ability to stand a severe accident in acceptable conditions, i.e., limited radioactive emission to the environment.

Although the specific design of the Severe Accident Management (SAM) strategy varies with the plant type, and the reactor nominal power, two distinct strategies can be followed, related to the location where the melt can be stabilized: in the vessel, or out of the vessel. Whatever the strategy, the last barrier, i.e., containment building, must remain intact or, at least, with preserved capabilities of retention of the radioactive materials.

In general terms, the In-Vessel Retention (IVR) strategy, sometimes called In-Vessel Melt Retention strategy (IVMR), consists in External Reactor Vessel Cooling (ERVC) by flooding with a dedicated water system, at least partially, a part of the reactor containment building, such as the reactor vessel cavity (space between the RPV and the reactor pit) for the PWR and dry-well for the BWR [93]. The goal of the IVR strategy is to retain the integrity or at least increase the probability of the survival of the RPV in case of a severe accident. It may be highlighted then that this strategy relies on a probabilistic assessment.

Several reactor designs, such as the PWR AP600, AP1000, standard APR1400, HPR1000, and CAP1400, have adopted the IVR strategy from the design of the reactors, whilst others have retrofitted the necessary measures to follow the strategy [94], [95]. It is essential to point out that there is no definite strategy to follow for any reactor design. The specific country's guidelines may dictate the strategy, and the final decision lies with the company that operates the reactor. In addition, one same type of reactor may also follow different strategies, as evidenced in the difference between the standard and the European version of the APR1400 reactor. The former uses IVR, whilst the latter will have an ex-vessel core catcher [94, pp.107-108].

Generally, as explained by Fichot et al. [96, p.1], safety margins have been proved for reactors with a power lower than 600 MWe, whilst for reactors with a power closer to 1000 MWe and higher "it is not possible to completely exclude the possibility of vessel failure, leading to the energetic interaction of corium with water and a possible early containment failure". Unresolved adverse effects have led to an increased risk of vapor explosion, hence a reduced safety margin for the RPV failure [97]. This has led some countries, including France, to adopt an ex-vessel core melt stabilization strategy for the existing reactors as well as for the new ones.

The ex-vessel corium melt stability strategy consists of corium spreading into a designated compartment, generally into the reactor pit, and potential annexing reactor building compartments hence enhancing the available spreading surface, to further cool it by covering the corium with water once it is spread [39]. This strategy has been adopted for several PWR designs such as the System 80+ (originally designed by Combustion Engineering, now merged with Westinghouse Electric Company), the European Pressurized Reactor (or Evolutionary Power Reactor) (EPR), some of the VVER-1000 (V-428, V-428M, V-446, V-412), the VVER-1200, Westinghouse's WH 4LP, the European APR1400, and all the French PWRs operated by EDF [94], [98].

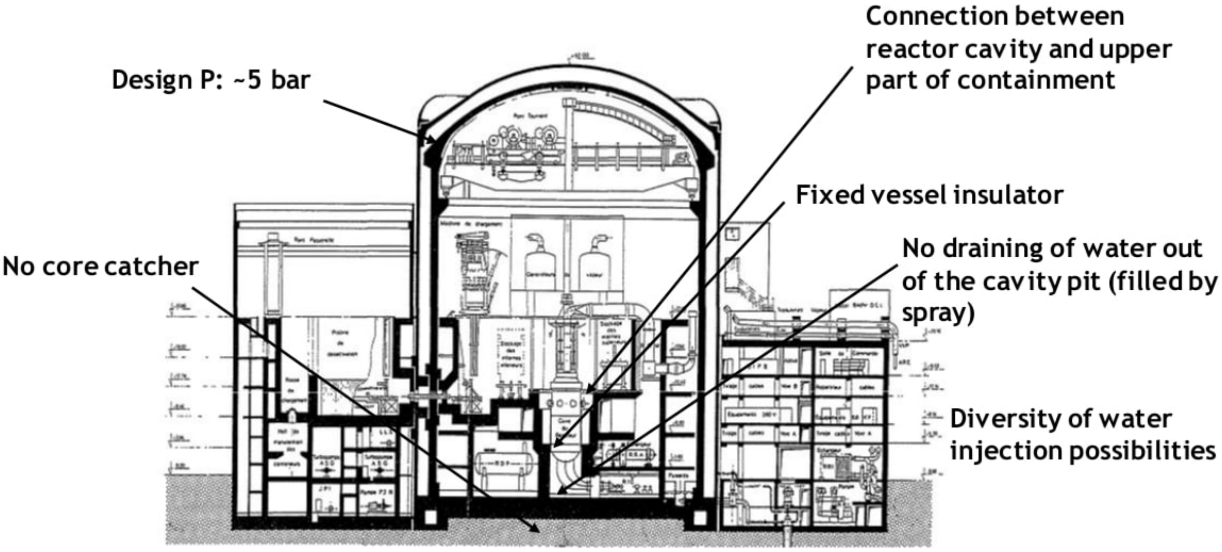

Figure 1.18 – French NPPs building scheme showing the designed large dry containment. 900 MWe series: single containment with liner 1300 & 1450 MWe series: double containment

Taken from: [99]

The EPR reactor has been designed explicitly for this purpose, with a dedicated spreading chamber and a dedicated source of water. Regarding the back-fitting of existing reactors, several problems arise, the first one being finding an adequate spreading surface. The second problem is to preserve a large amount of water, through a dedicated (new) reservoir. Nevertheless, the assurance of the containment building integrity does not depend solely on the available spreading surface and cooling source.

The problem comes from the understanding and modeling of the interlinked MCCI phenomena, including the interaction with water being added from the top. As will be discussed hereafter, among the possible phenomena for cooling the melt by the water, the phenomenon of melt ejection, that seems the most efficient in stabilizing the corium, is mainly linked to a type of concrete and particularly its content of gas, or, more appropriately, its capabilities to release gases (CO_2, vapor, etc.). As seen in table 1.2, this is not the case for a large part of the French NPP's, leaving the coolability of the corium to the more restrictive phenomenon of water ingression and debris bed coolability. An unquenched progression of the MCCI could lead to a failure of the reactor containment building. This last is one of the main reasons that the analysis of the efficiency of top-flooding of the corium pool to cool and stabilize it, as part of an ex-vessel containment strategy, represents high safety stakes.

France currently has 58 PWRs in operation in 19 different NPPs. It is important to note that all of the operating french reactors are a variation of the general PWR design, hence having a strong similarity amongst most NPPs. All of the reactors currently operating in France can be classified as three different iterations of the PWR design that can be grouped as: 4 1450 MW electric (MW_e) units, 20 1300 MWe units, and 34 900 MWe units. This, in turn, facilitates the studies and analysis of the plants, and the implementation of the developed SAM strategy.

The reactor pit, which is the concrete cylindrical structure which supports the RPV, has variable dimensions depending on the specific NPP. The French reactor pit dimensions vary[5] as shown in figure 1.19, with a total horizontal surface, also known as the reactor basemat, between 28-37 m^2 (including extra surface bellow piping underneath the RPV) [100].

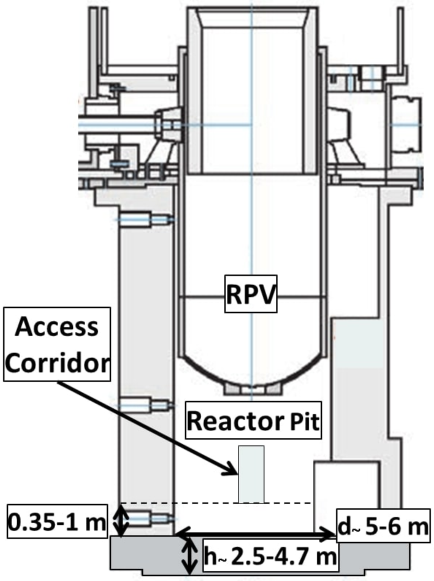

Figure 1.19 – Reactor pit diagram with dimensions from french NPP's

Adapted from: [69, p.151]

The concrete of the NPP comes typically from local or regional quarries, hence varying in composition. The concrete composition of the basemat for the 58 reactors in France is largely different, as can be seen in table 1.2, which in turn will influence the presence or absence of phenomena aiding the coolability of the corium. As mentioned before, and further discussed in section 2.2, some of the French reactors, especially those with a high silicon content, may be limited to the appearance of only some of the MCCI phenomena, hence be limited to lower heat extraction capabilities.

---

[5] The reactor pit thickness (h) of the Fessenheim NPP is only 1.5 meters comparing to the 2.5-4.7 meters of the other French NPPs. The access corridor for the 1300 MWe reactors in the Flamanville, Paluel, and Saint Alban NPPs is at ground level.

Table 1.2 – Main components for french NPP containment building concrete

Name	**Power**	**Concrete component in mass %**					
of NPP	MW_e	SiO_2	CaO	MgO	Al_2O_3	H_2O	CO_2
Bugey	900	34.30	36.62	0.40	2.33	5.66	20.70
Fessenheim*	900	67.36	17.76	0.47	2.16	5.66	6.59
Blayais	900	79.91	11.67	0.00	2.42	5.66	0.35
Dampierre	900	79.15	12.13	0.00	2.44	5.66	0.62
Gravelines 1-4	900	43.41	30.19	1.61	2.40	5.66	16.73
Gravelines 5-6	900	24.97	39.53	2.47	2.41	5.66	24.95
Tricastin	900	68.63	17.65	0.00	2.19	5.66	5.86
Chinon	900	78.29	12.41	0.19	2.46	5.66	1.00
Cruas	900	68.48	17.79	0.00	2.23	5.66	5.85
St Laurent des Eau	900	79.74	11.74	0.00	2.40	5.66	0.46
Flamanville	1300	80.87	10.87	0.00	2.24	5.66	0.36
Paluel	1300	72.89	15.36	0.00	2.26	5.66	3.84
Saint Alban	1300	67.87	17.81	0.28	2.23	5.66	6.15
Belleville	1300	80.92	10.76	0.00	2.19	5.66	0.47
Cattenom	1300	65.36	14.21	4.52	2.21	5.66	8.04
Golfech	1300	78.21	12.33	0.00	2.23	5.66	1.57
Nogent sur Seine	1300	78.18	12.36	0.00	2.23	5.66	1.57
Penly	1300	51.75	26.38	0.62	2.19	5.66	13.41
Chooz B	1450	29.44	35.70	3.18	2.07	5.66	23.94
Civeaux	1450	N.A.	N.A.	N.A.	N.A.	N.A.	N.A.

* This NPP has an abnormal reactor pit depth of only 1.5m N.A Not Available

Reproduced from: [100]

1.3 Open issues on corium coolability

The strategies for ultimately stabilizing the corium and mitigating the radioactive releases rely mainly on the analysis related to the coolability of the corium. Although numerous studies have been carried out with respect to different phenomena and configurations of corium coolability, several open, or at least uncertain, issues remain, in particular regarding the direct coolability of the corium with water addition on the top.

As will be highlighted in the next sections, the support of experimental facilities that lack full representativity of the prototypical condition in an accidental scenario gives rise to substantial uncertainties or even some misunderstanding. Thus, the models also lack full validation, and their use for safety studies requires proper consideration with attention to the related uncertainties.

1.3.1 Particle bed

Amongst the open questions inscribed in the context of ex-vessel corium coolability, a rather important one envelops the minutia surrounding the formation and evolution of the particle bed, whether they may come from the jet fragmentation following a RPV failure or an episode of melt ejections during a MCCI.

In particular, it is of great interest to determine the maximal amount of heat that can be extracted by the coolant in a heterogeneous or homogeneous porous media and its dependency on its characteristics. As will be discussed in section 2.1.1, this has been extensively studied in steady-state conditions parting from a fully flooded debris bed. Particle bed coolability is indeed currently an issue particularly important for the cases of the recent BWR's, also often referred to as "Nordic BWR's", where the vessel stands at a high elevation and cannot be cooled externally by simple means, whereas the deep pit is flooded.

A number of experimental programs have been launched (e.g., DEBRIS in Germany [101], COOLOCE in Finland [102], or POMECO in Sweden [103]) with the aim to determine the maximum heat flux that can be extracted in various conditions and possible particle bed geometries. However, these programs only investigate the situation with initially flooded (cold) beds, a situation that, for most cases, is probably quite unlikely.

Most studies and models have neglected the importance of the debris bed's initial conditions, which are expected to be created at high temperatures and with a high residual power, which can be inferred by observing figure 1.20. In the case of the French 900 MW$_e$ PWR, the residual power to be extracted during the initial state of the accident, is in the order of 20 to 30 MW corresponding to 240-370 $\frac{W}{kg_U}$ [69]. This last is shown in figure 1.20 which plots the residual power of a French 900 MWe PWR as a function of the time calculated using eq.(3-70c) in [104, p.66], here shown as:

$$P_{res} = P_0 \cdot 0.066 \left[\left(\tau - \tau_s\right)^{-0.2} - \tau^{-0.2} \right] \tag{1.5}$$

with P_{res} and P_0 being total fission power decay heat rate and the nominal power, and τ, and τ_s being the time and the time after reactor SCRAM respectively In it, the red and green dashed curves plot the residual power generated if the reactor is stopped one year or ten days after the reactor start-up.

The coolability of this initially dry-hot particle bed with residual power generation is uncertain vis-à-vis the thermohydraulics, the dynamics of the water penetrating the bed, and the stability of the layer with the expected set of initial conditions.

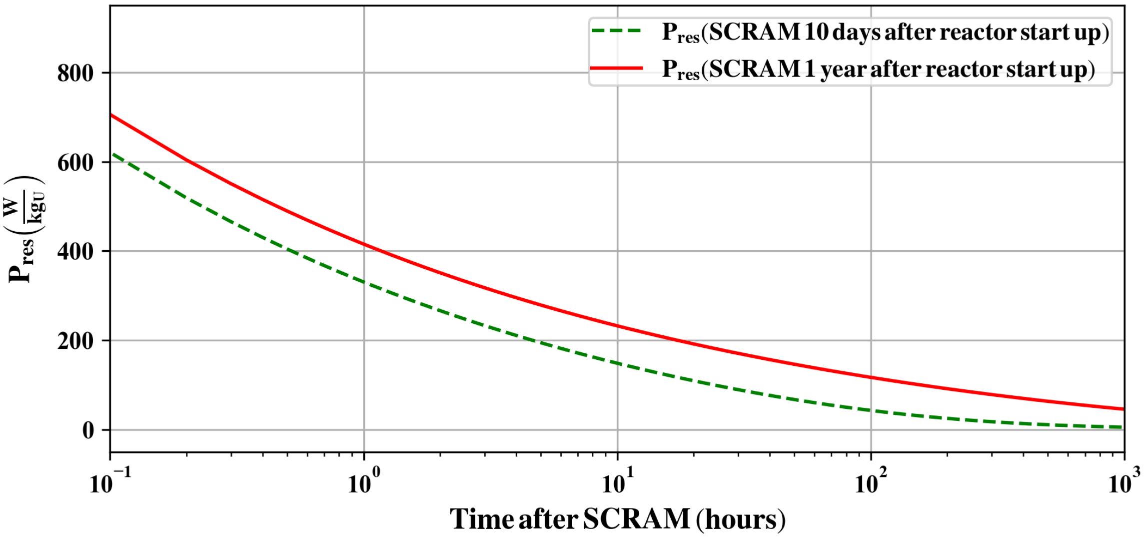

Figure 1.20 – Typical PWR residual power as a function of time after reactor shutdown (SCRAM) evaluated at two distinct times after reactor start-up calculated using eq. (1.5)

One first objective of this work is to characterize the analogy among the so-called Critical Heat Flux (CHF) and the effective heat flux that can be extracted during the penetration of water in the debris bed. There will be a competition between the heat extraction through the water penetration and temperature rise of the bed due to the residual power. Even if the bed is potentially coolable, the time to do it might lead to a second remelting of the debris bed.

It is also pertinent to recall the uncertainties related to the formation of the bed itself, i.e., the debris size and shape. These will influence the characteristics of the debris bed, namely the porosity, permeability (characteristic surface), and the passability (characteristic length scale).

In the present work, these characteristics will be considered as parameters. However, it is interesting to estimate a range of typical values for the sake of parametric analysis.

Regarding the case of debris beds following a jet fragmentation, experiments as FARO [105] or TROI [106] tend to maximize the possible debris mean size by about 3 mm, nevertheless resulting in poly-disperse debris sizes. However, in reactor conditions, due to larger scales, in particular for the BWR's, smaller particle size of about 1 mm might as well be expected. If the debris is well solidified, a somewhat porous bed is expected. Measurements in experiments like FARO and TROI give values of the order of 50-60 %, i.e., noticeably larger than the 40 % in debris beds made of round balls. However, local porosities might drop to much lower values if the solidification is partial.

The characteristics of the debris bed resulting from melt ejection remain elusive as it was not possible to find any related data in the literature. From the CCI experiments, only visual information, from images, is available. Debris seems to be in the order of some millimeters, thus are deemed quite coolable. In contrast, the porosity distribution was found (visually) to be very variable, potentially with considerable agglomeration and reduced porosity in certain areas of the debris bed. However, it may be emphasized that, regarding the melt ejection situation, an absence of coolability will not necessarily signify the failure of the strategy since the ejection itself is probably an efficient cooling mechanism, even if this cooling is not complete, and if the debris rapidly remelt.

1.3.2 Water ingression

Even fewer experiments have been performed to examine the mechanisms of water ingression (indeed, only the Small-Scale Water Ingression and Crust Strength (SSWICS) series). Additionally, a consensual interpretation of the results has not been reached. The limits upon which the material composing the crust would allow the development of fractures, which would translate to an increase of heat removal, are unresolved. The dependency of the material composition of this layer, and the under-laying physical processes governing these phenomena, are also dubious. Lastly, the validity of extrapolations of the modeling techniques and mathematical expressions, used in the context of porous media, towards water ingression is questionable.

1.4 Objectives of the thesis

The objectives of this work are:

- To help deepen the comprehension of the physical phenomena that govern the top-flooding of debris beds or fractured media using available data from dedicated experiments, Multi-Component 3D (MC3D) simulations, and by developing a dedicated analytical model. Of particular interest will be the case of water ingression. A first purpose of the present work is to readdress the SSWICS tests in order to improve the understanding and interpretation.
- Evaluate the impact of the residual power and extrapolate the identified phenomenology to an accidental scenario with reactor scale, again with the particular interest in the case of water ingression
- Provide alternative/complementary model for MCCI module in the Accident Source Term Evaluation Code (ASTEC) code (MEDICIS) dedicated to the study of MCCI.

Chapter 2

Literature Review

Contents

In this chapter, the observed phenomenology, main experimental results, models, and available constitutive laws for two particular expected, and observed, configurations will be discussed. The two configurations, namely debris bed and fractured crust, can be described as porous media layers formed by the solidification, or partial solidification, of the corium during different stages of a severe accident.

The first part of the chapter will cover the observed phenomenology related to debris bed cooling. An overall review of the studies related to the so-called Critical Heat Flux (CHF), which is, in fact, more appropriately a Dry-out Heat Flux (DHF), i.e., the maximum heat flux that can be introduced in the porous medium before a local dry zone appears, will be presented. Afterward, a short description of the experimental efforts for the reflooding of initially dry debris beds will be discussed. A brief point concerning the case of bottom flooding, which is currently investigated at IRSN, with the PEARL (for analytical, experimental program concerning debris bed reflooding in french) experimental platform with heterogeneous debris bed will be made. Subsequently, the discussion will continue via a presentation of the few experiments investigating the top reflooding of hot debris bed. Following a quick point respecting the recent top reflooding experiments performed in the PEARL facility will be presented and discussed. Finally, a brief discussion of water flow instabilities or water fingering in porous media will be approached.

In the second part, a short general description of the observed MCCI phenomenology will be given. Although only the water ingression phenomenon is investigated in this work, it is important to have a global view of the corium-concrete interaction to understand the phenomenon better. A specific attention will be given to the SSWICS experiments.

In the third part, the major constitutive laws and available models used in the following chapters will be recalled. The main available frictional laws and their range of applicability will be recalled. When the porosity and permeability are very small, the effects of capillarity are expected. However, as will be discussed, capillarity is far from being a well-characterized phenomenon when applied to debris bed. In the particular case of interest here of reflooding of hot debris beds or fractured medium, this is even more problematic as no readily available model, or data could be found in the literature for transient, heat-generating, and/or including phase-change situations. The simplifying hypotheses used later on will then be discussed. This will lead to the presentation of some conventional models for CHF/DH. In contrast, the configuration of the top reflooding of an initially dry hot bed does not seem to have received attention from the modeling point of view. Many works and analyses have been proposed regarding the evaluation of the critical heat flux in already flooded cold beds. However, rather strangely, the equivalence between the two situations is never discussed.

Regarding water ingression, the question of the mechanisms of fracture appearance in a cooling medium will be presented in the fourth part. After-which, two available complete models will be briefly discussed.

The final part of this literature review will comprise a brief description of the models of interest of the computer code MC3D-PREMIX, used in this work. Some examples of recent calculations for the analysis of bottom flooding will be presented. The modification done for the purpose of the present work will be briefly exposed.

2.1 Observed phenomenology related to debris bed coolability

2.1.1 Critical heat flux in flooded debris bed

The maximum quantity of heat a heated surface can transfer to an overlaying volatile fluid has been studied long before Nukiyama [107] first presented his findings. As the author explains, the heat exchange between the heated surface and the fluid increases with increasing temperature up until a certain point, after which the heat exchange decreases and the temperature of the heated material start to increase rapidly, with the possibility to re-melt. As defined by Celata & Mariani [108, p.5] "the term Critical Heat Flux (CHF) indicates an abrupt worsening of the heat transfer between a heating wall and a coolant fluid". Other terms such as departure from nucleate boiling, liquid film dry-out, annular film dry-out, dry-out, burnout, boiling crisis, boiling transition are also used. In the particular domain of porous media, the term critical heat flux sometimes is referred to as Dry-out Heat Flux (DHF) and often is used interchangeably. During this work a clear distinction will be made where CHF will be considered as the maximal amount of heat extracted by unit of horizontal surface allowed by the hydrodynamics of the system, whereas as Lipinski [109, p.3] defines for debris beds, DHF is "the bed power at which some part of the bed just becomes dry". As will be seen, it does not come for a local maximum heat flux between the debris surface and the coolant, but a maximum heat that can be transported via the two-phase flow. In the particular configurations of porous media to be discussed in the present work (dry-superheated heat-generating debris bed and fractured crust), it is somewhat unclear whether it is possible, and under which conditions, to sustain a steady heat exchange beyond CHF point.

A significant number of experiments have been carried out in the past concerning the boiling and DHF, in flooded particle beds under different conditions. As Lipinski [109] summarizes, before 1982, only accounting for volume-heated beds, over 250 measurements, and at least 15 models were made. These studies aimed to understand the dependency of DHF to several parameters such as the size of the particles, the material of the particles, the height of the bed, the mode of the water injection, the temperature of the water, the configuration of the debris bed, the heating mechanism, amongst others. Most of these studies consisted in a cylindrical test section, shown in figure 2.1, filled up to a certain height with metallic, or oxide, particles (steel, copper, UO_2) with a broad range of diameters (0.3-16 mm for steel particles) upon which a particular power was imposed, and step-wise increased until dry-out occurred. The heating techniques varied amongst the different authors, some of which introduced the power by electrically heating electrolytes dissolved in the liquid, or used a heating plate at the bottom of the bed, whilst others used inductive heating to heat all the particles volumetrically. For the current analysis, only volumetrically heated beds will be taken into account. In the studies, the different authors made diverse and sometimes contradictory remarks. Amongst them Lipinski summarized the following conclusions from different authors in [109]:

- Gabor et al. [110], Trenberth & Stevens [111] observed a decrease in DHF as the debris bed thickness increased whilst Dhir & Catton [112] reported the contrary (for bed above 50 millimeters in height).
- Keowen & Catton [113] described the debris bed as fluidized, meaning that there was high mobility of the particles in the liquid/vapor mixture, and Dhir & Catton [112] reported at least a part of the particle bed, notable in the topmost part, was fluidized. Nevertheless, authors like Lipinski & Rivard [114] state that a "debris bed cannot be fluidized by its vapor flow".
- Rivard [115] observed stable steady-state dry zones at powers slightly above initial DHF (using sodium-cooled UO_2 fission-heated beds), further stating that the dry zones appear at bed bottom. Other, such as Trenberth & Stevens [111] suggest the contrary, observing a dry-out location that increased with increasing bed thickness.

All in all, the studies showed that the process is highly complex and wholly dependent on the initial conditions and configuration of the particle beds. Despite the previous, it can be stated that the overall process is governed by the liquid-vapor, counter-current flow in the bed. Some examples of the test section and its similarities are presented in figure 2.1.

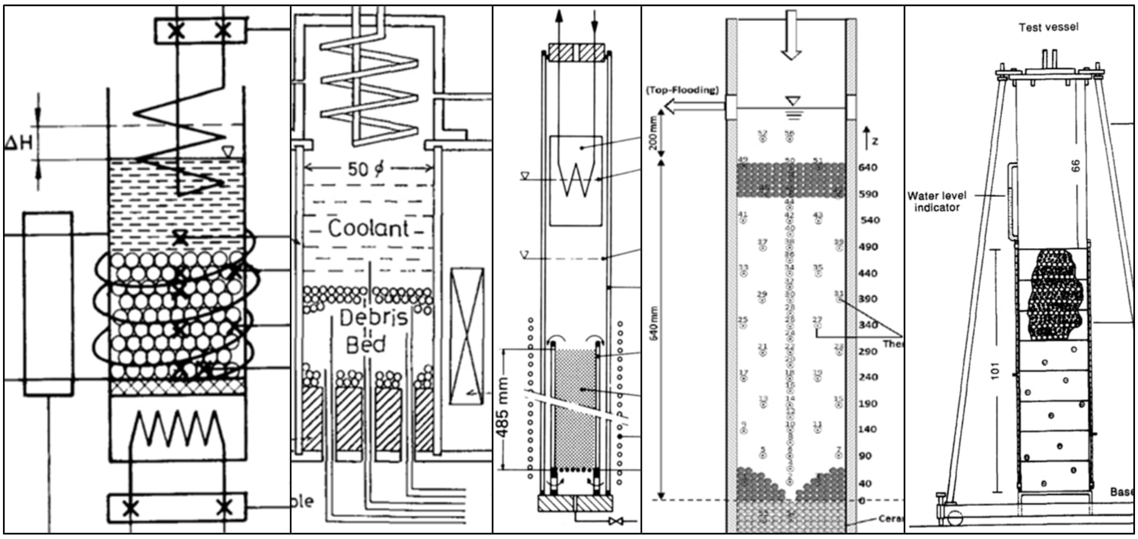

Figure 2.1 – DHF experimental test sections from Barleon et al. [116], Miyazaki et al. [117], Hofmann [118], Rashid [119], Hu & Theofanous [120] showing a similar cylindrical geometry and varying heating techniques

Taken from: [116], [118], [119], [120], [121]

Some analytical models, presented in section 2.3.3, were produced based on the data coming from these type of experiments which reproduce with good agreement, experimental data.

Figure 2.2 plots the dry-out heat-flux measured during the experiments with a similar configuration (cylindrical test section, atmospheric pressure, water injection from the top, initially flooded debris bed, injected water temperature at/close to saturation temperature, steel particles, similar debris bed height, etc.) as a function of the permeability. The results come from Hofmann [118], Miyazaki et al. [117], Barleon et al. [116], Atkhen & Berthoud [122], Squarer et al. [123], Trenberth & Stevens [111], Gabor et al. [110], Keowen & Catton [113], Dhir & Catton [112], Takasuo [124], amongst other taken from Lipinski [109] (Barleon & Werle, Gabor et al., Somerton et al., Squarer & Peoples, Sowa). The debris bed heights ranged from 0.02 m to 0.64 m with a mean of 0.15 m. The large scatter of experimental result is in general attributed to the fact that, in such conditions, the actual characteristics of the debris bed, notably the permeability, are often uncertain, as they may be modified by the flow forces themselves (small particles may move at the top section of the bed and modify the configuration, with the apparition of preferential channels, hence increasing the dry-out heat flux [117]). At low values of bed height, this last may drastically modify the initial conditions, giving rise to a larger experimental scatter.

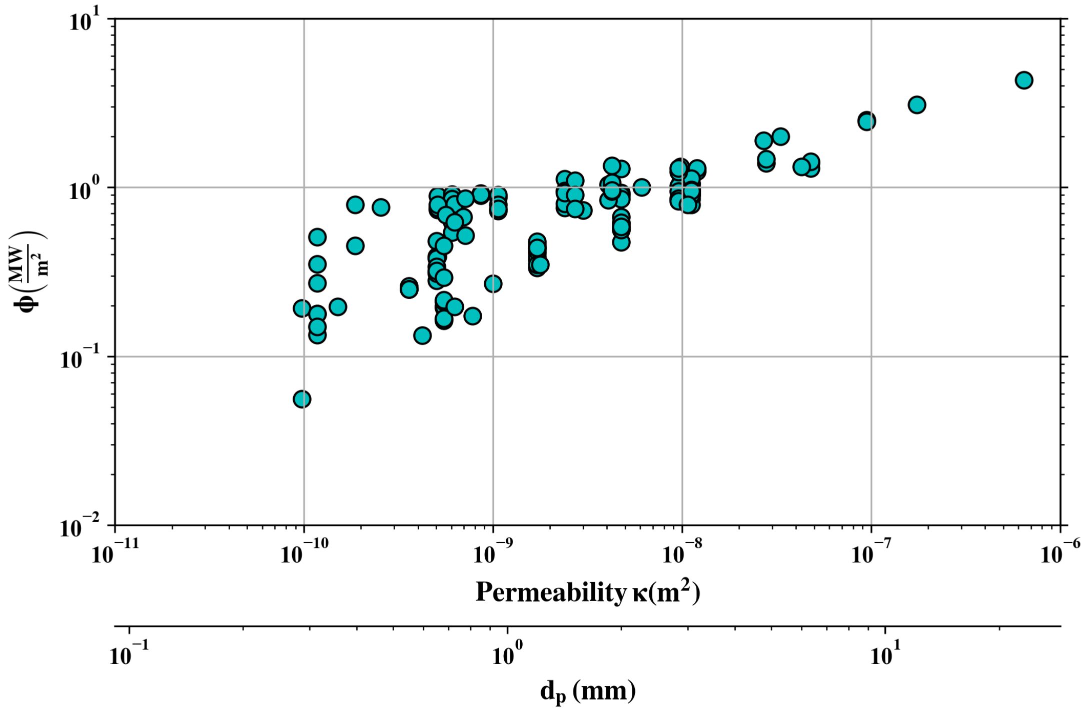

Figure 2.2 – DHF as a function of permeability from experimental data with different size particles and debris bed thickness [102], [109], [112], [116], [117], [118], [122], [123], [125], [126]

2.1.2 Bottom reflooding

The most natural way to cool a constituted debris bed is to inject water on the top. Nevertheless, during a severe accident, a debris bed might form in the vessel within the core, as illustrated by the TMI-2 accident. In such conditions, the question of the coolability of such debris bed is posed if a water injection system is readily available. The particularity of the problem is delimited by the heterogeneity of the debris characteristics and the presence of a bypass, constituted by the regions of the core still intact or weakly damaged. To investigate this situation, IRSN has launched a series of large scale reflooding experiments, recently conducted in the experimental platform PEARL [127], [128]. The facility has been designed to perform the reflooding of large debris bed (inner diameter of 540 mm, h = 500 mm and 500 kg of steel and quartz beads of diameter from 2 to 8 mm, see figure 2.3) in a pressurized containment. The steel part of the bed is heated by means of an induction system, whereas quartz beads are used to simulate the bypass.

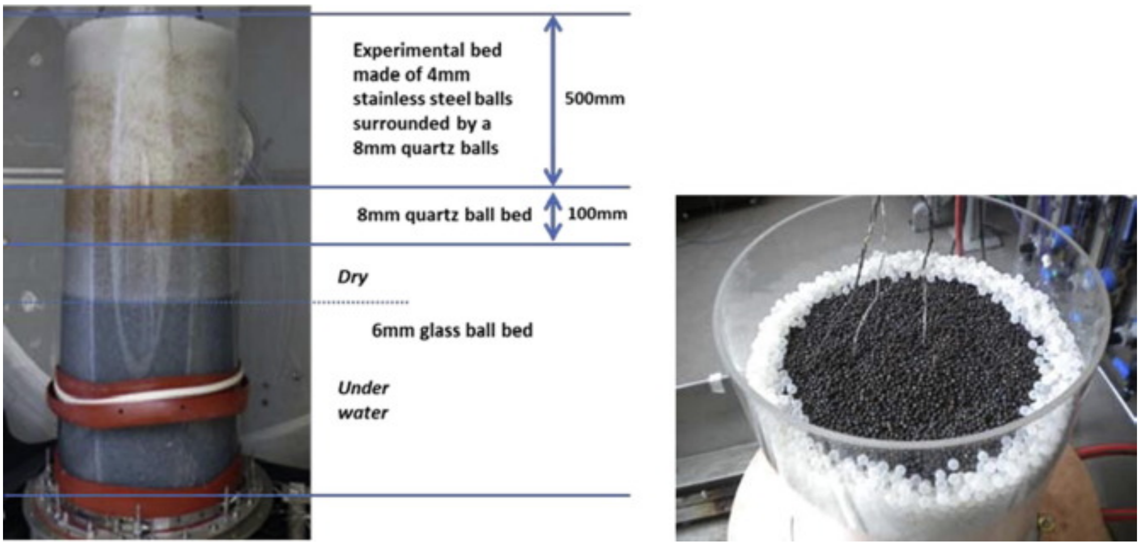

Figure 2.3 – PEARL test section and top view of the debris bed surrounded by the bypass

Taken from [128]

Different sets of experiments have been done to study the effects of the pressure, water injection flow rate, debris bed configuration, beads diameters, debris bed temperature, and others. As the flow rate is imposed, the main result regards the deviation of this flow in the bypass. If the deviation is too important, then the core cannot be reflooded and cooled. A noticeable deviation was observed when increasing the core temperature and decreasing the diameter of the beads. The deviation towards the bypass decreases when the pressure is increased.

Examples of calculation with MC3D are given in section 2.5. It can be concluded that, due to the imposed flow rate, bottom flooding does not present a particular issue regarding modeling, except for some specific configurations with heating obstacles or compact regions inside the debris bed.

2.1.3 Top reflooding

2.1.3.1 Ginsberg experiments

The experiments conducted by Ginsberg between 1982-1984 in Brookhaven National Laboratory were designed to characterize the thermohydraulic behaviors of packed beds of super-heated spheres being quenched in the top reflooding configuration. The experimental parameters studied during these tests were mainly the bed height, the particle diameter, and the initial temperature of the particle bed. The spheres composing the particle bed where made from stainless steel (302/304) spherical particles, and four sizes were used: 0.89, 3.18, 6.35, and 12.7 mm. The height determined the total mass of the particle bed, and it was 15 and 20 kilograms for a bed height of either 0.3 or 0.4 meters, respectively. A summary of the different iterations of the experiments is presented in table 2.1. The particle bed was itself housed in a pre-heated stainless steel cylindrical vessel of 0.1082 meters of inner diameter, 1.219 meters long, and a wall thickness of 3.05 millimeters. Most of the experiments took place in the TS1 experimental test section, whilst the experiments for the smallest particles ($d_p = 0.89mm$) took place in the test section TS2. The main difference is the way the particles were heated. In TS1, the particles were first heated in an oven above the test section. Once the desired temperature was reached, the spheres were allowed to fall onto the test section, and after a small settling period, water was injected from the top whilst thermocouples, pressure transducers, and a flow-meter monitored the progression of the quench front. The thermocouples, located at different axial positions, measured the progression of the quench front, the flow-meter measured the amount of vapor produced during the quenching process, whilst the pressure transducer monitored the pressure fluctuations above the debris bed hence identifying the beginning and the end of the boiling within the vessel [129]. In TS2, the particles were heated by hot air that passed through the already posed particle bed rather than in the oven, whilst the measurements were made by the same type of equipment. All the tests were conducted at atmospheric pressure and with an injected water temperature of 100 °C. These experiments were not heated during the quenching phase. Both sections are shown in figure 2.4.

Table 2.1 – Ginsbergs tests matrix

d_p (mm)	**0.89**	**3.18**	**6.35**		**12.7**	
Bed Height (m)	0.4	0.3	0.3	0.4	0.3	0.4
Initial Temperature T_0 (K)	581-798	532-913	532-791	776-785	560-829	785-789
ε (-)	0.403	0.401	0.375		0.410	
Experimental Test Section	TS2	TS1				

Reproduced from: [130]

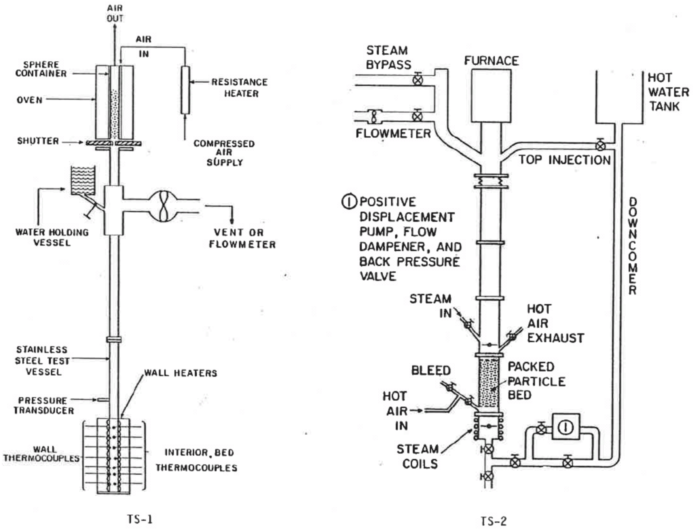

Figure 2.4 – Ginsberg's TS1 and TS2 experimental tests sections

Taken from: [130]

Figure 2.5 shows the results of early test runs [129]. The left part of the figure plots two experiments with the same bed height, with varying temperatures. In the right, three different experiments with the same initial temperature T_0 and varying bed height. From the figure 2.5, it is clear that the dependency on the bed height is negligible, whilst the effect of the temperature governs the quenching. Nevertheless, it is important to note two things. First, the legends of the figure seem somewhat confusing since they do not correspond to the expected behaviors. As can be seen in the left part of the figure 2.5, the legend suggests that the lower temperature experiment, marked with a "+", was quenched slower than the high-temperature experiment marked with a "x". In the document, [129], as it was found in its online source, a notice reads, "Portions of this report are ineligible. It has been reproduced from the best available copy...". Hence, it seems plausible that these legends are misleading due to an error during its reproduction. Second, the experimental results here presented do not appear in Ginsberg's latter work [130], which seem to indicate that these results were either preliminary or were made in a configuration of the test section that differs with those found in his 1986 report. Both the difference in bed height and the identification number given to the experiments (in the worked dubbed "run") seem to indicate this too.

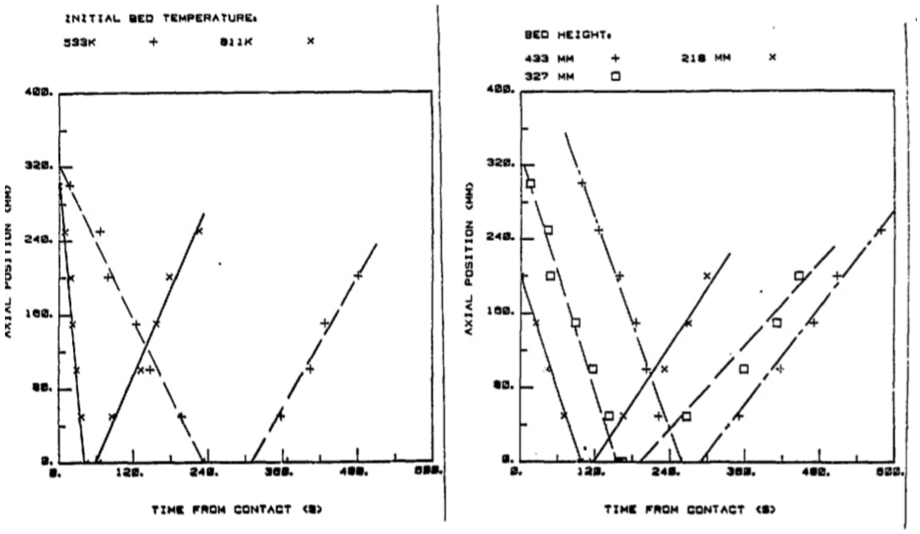

Figure 2.5 – Ginsberg's experimental results: Effects of bed temperature and height on front progressions with d_p=3 mm. Left: different temperatures with debris beds with the same height=327mm; Right: different bed heights with the same initial temperature T_0=800 K

Taken from: [129]

Figure 2.6 plots the quenching front velocity of different experimental tests with the same initial conditions with the exception of the initial temperature found in [130]. In it, it can be clearly seen the influence of the temperature in the quenching front velocity. The higher the initial bed temperature, the slower the quenching front.

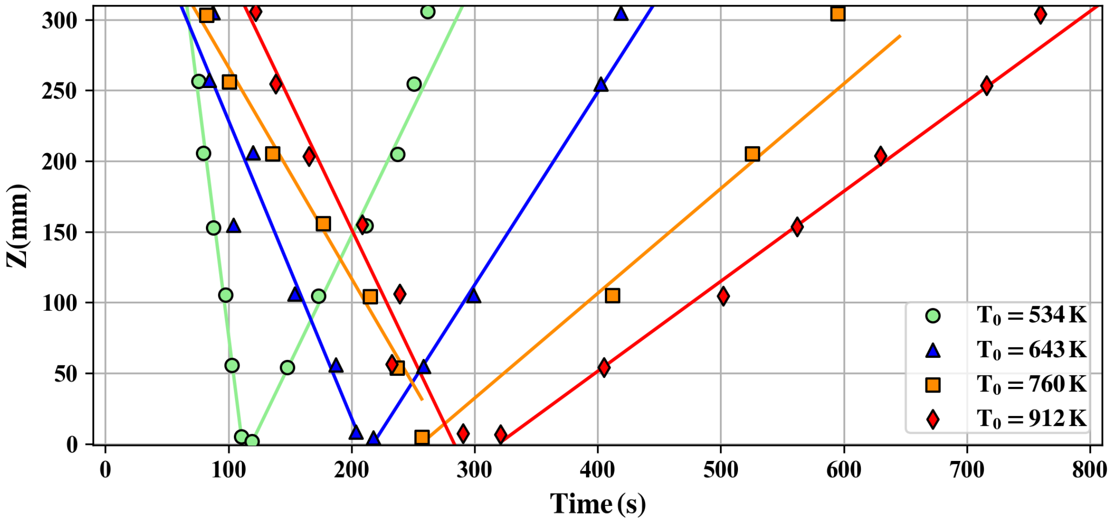

Figure 2.6 – Ginsberg's experimental quench front results: Effects of bed temperature with d_p=3.18 mm, h=0.4 m, and ε=0.401 with different temperatures T_0

Results taken from: [130]

Figure 2.7 shows the results of experiments with a similar initial temperature, with varying particle diameter. There is a drastic decrease in quenching front velocity with decreasing particle diameter.

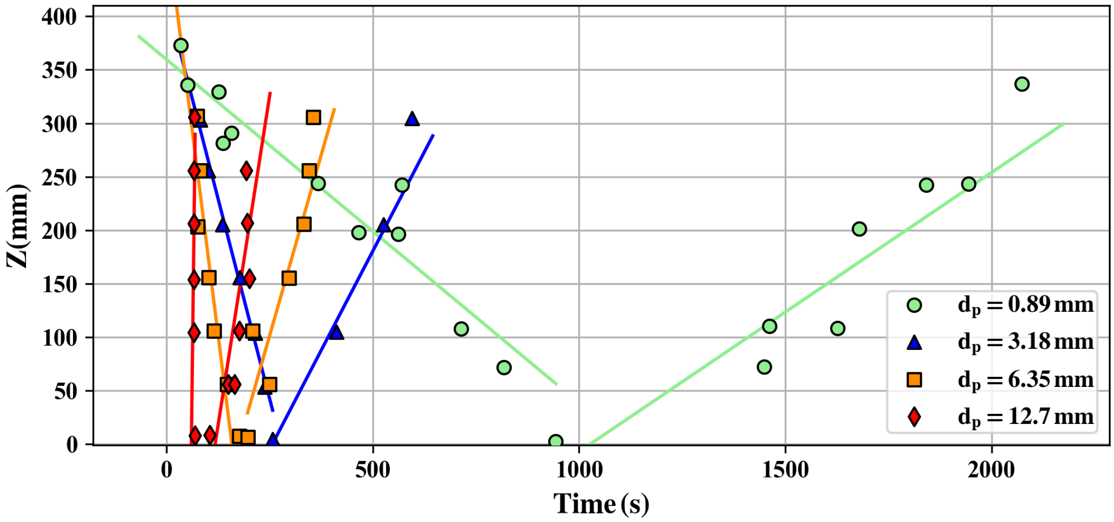

Figure 2.7 – Ginsberg's experimental results for quenching front velocity with similar initial temperature T_0=798, 760, 790, 829 K with d_p=0.89, 3.18, 6.35 and 12.7 mm respectively. Front velocity was obtained by following the axial thermocouples position at which a temperature close to T_{sat} was attained.

Results taken from: [130]

Regardless of the work, Ginsberg clearly indicates that the quenching of the debris bed takes place in two stages. In the first one, the water penetrates the debris bed through channels in a "downward" quench front where the water that penetrates evaporates and the vapor rises through (figure 2.8 left side). Once the water reaches the bottom of the debris bed (and if the geometrical configuration allows it), the water begins to rise through the lower part of the debris bed in an "upward" quench front (figure 2.8 right side).

Interestingly enough, as pointed out by Ginsberg, the heat flux remains relatively constant throughout the two stages.

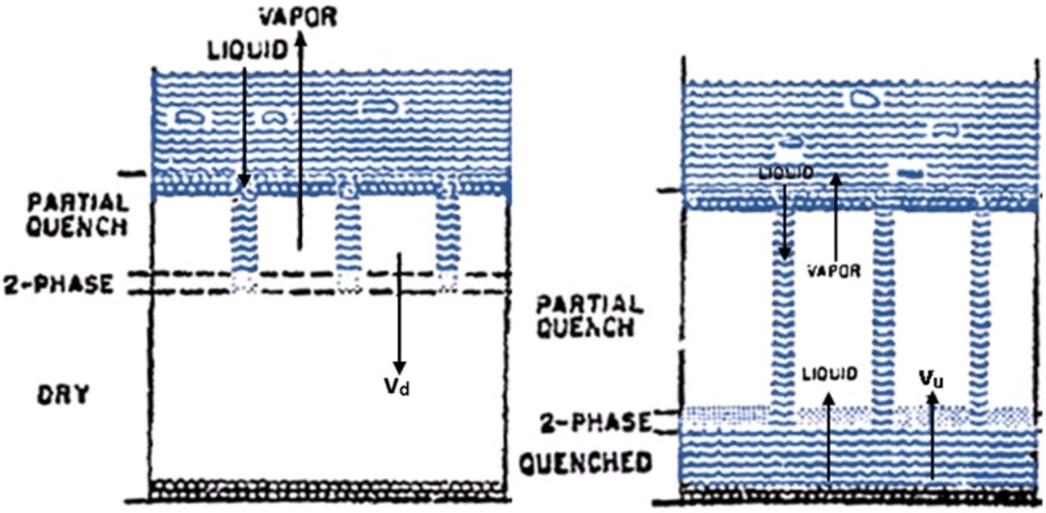

Figure 2.8 – Ginsberg's two stages quenching scheme

Reproduced from: [131, p.2]

Ginsberg also measured the extracted heat flux by measuring the vapor flow rate out of the test section, plotted in figure 2.9 as a function of the temperature for the beds composed of the different sized particles. The figure shows how the extracted heat flux for the same size of particles does not seem to depend on the initial temperature of the debris bed for small particle diameter, whilst a slight tendency can be observed with large particles. Nevertheless, even the small tendency might as well be a product of the experimental uncertainty.

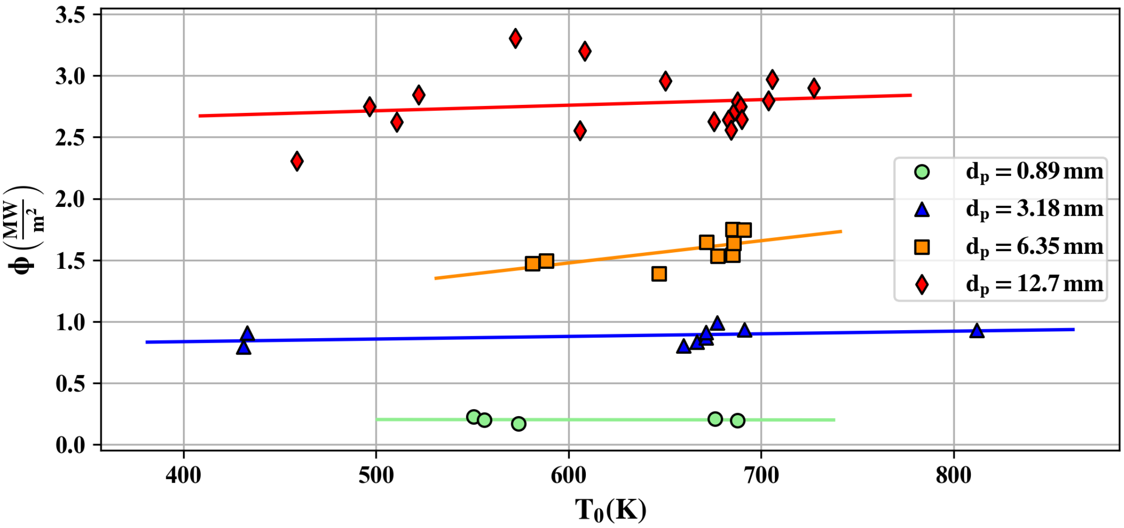

Figure 2.9 – Ginsberg's experimental quench front results: Extracted heat flux as a function of T_0 for different d_p showing a fit from the experimental data shown as the colored curves.

Reproduced from: [130, p.84]

2.1.3.2 Cho experiments

Cho et al. [132] also conducted top reflooding experiments in 1984 at an experimental facility located in Argonne National Laboratories (ANL). The experiments aimed to study the effects of different characteristics of a particle bed such as the injected water temperature, the initial bed temperature, the material of the particles, among others, on the pattern of water penetration into a hot particle bed.

Figure 2.10 shows a schematic representation of the experimental apparatus, which consisted of a cylindrical steel tank 0.15 m in inner diameter, and 2.8 meters tall. In it, the particle bed was 0.75 meters in height and consisted of stainless steel or alumina particles of 3.1 millimeters in diameter. The particles were heated externally via resistance heaters that were turned off once the desired initial conditions were reached. After that, the water resting on a reservoir located on the top part of the test section was released. The evolution of the temperature was measured via axial thermocouples along the central axis and two sets of radial thermocouples at 0.25 and 0.50 meters above the bed bottom.

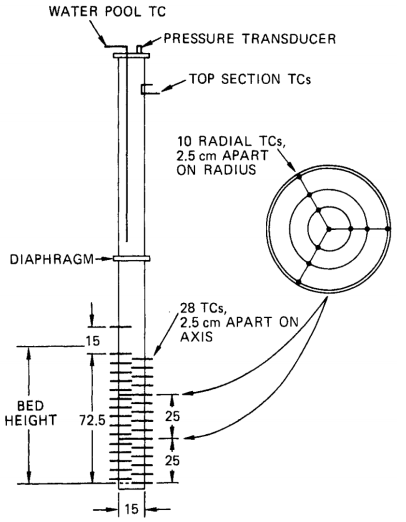

Figure 2.10 – Schematic of the test section used in Cho et al. study showing thermocouple locations and test section dimensions (all dimensions are in centimeters)

Taken from: [132, p.24]

Although several tests with different conditions were made, only one was made with the temperature of the injected water at saturation temperature. The initial bed temperature of this test was 500 °C. Figure 2.11 plots the evolution of the quench front, whereas in Ginsberg's tests, the downward front advances linearly. Figure 2.12 shows the axial and radial temperature measurements. The numbers represent the temperature measured, in °C, for all the 28 axial thermocouples (spaced 2.5 centimeters apart along the central axis) and the two sets of radial thermocouples at 4 different times.

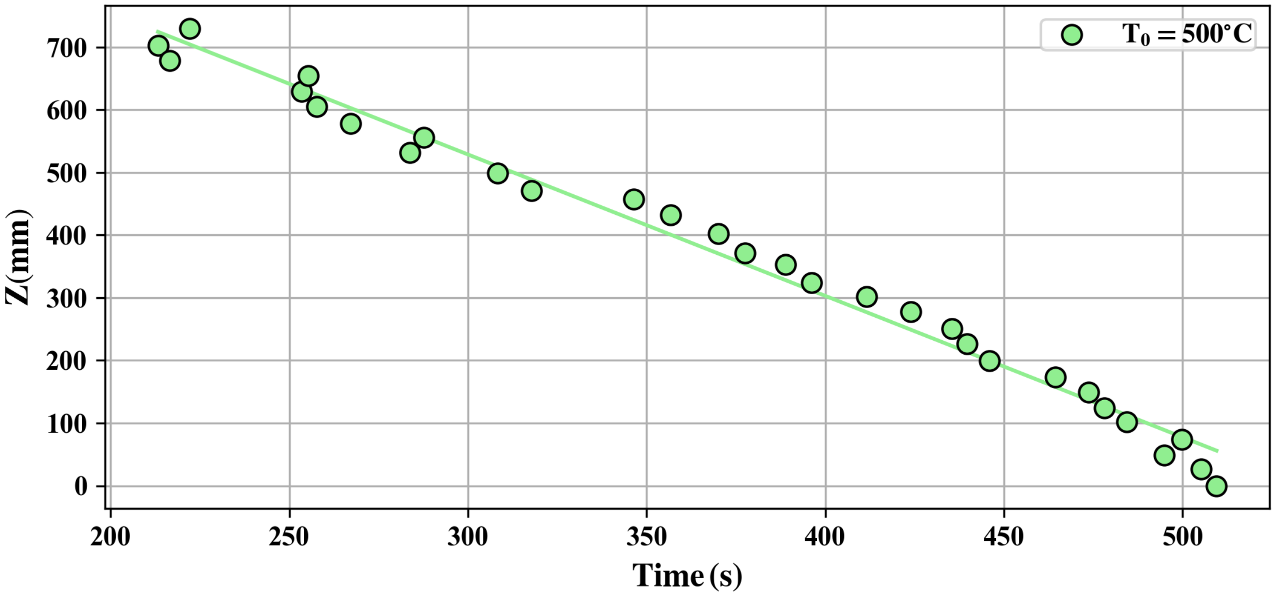

Figure 2.11 – Cho et al. experimental results for quenching front velocity with d_p=3.1 mm, H=0.75 m, water at saturation temperature, and T_0=500 °C. Time t∼220 marks the beginning of the water injection on the top. Front velocity was obtained by following the axial thermocouples position at which a temperature close to T_{sat} was attained.

Reproduced from: [133, p.995]

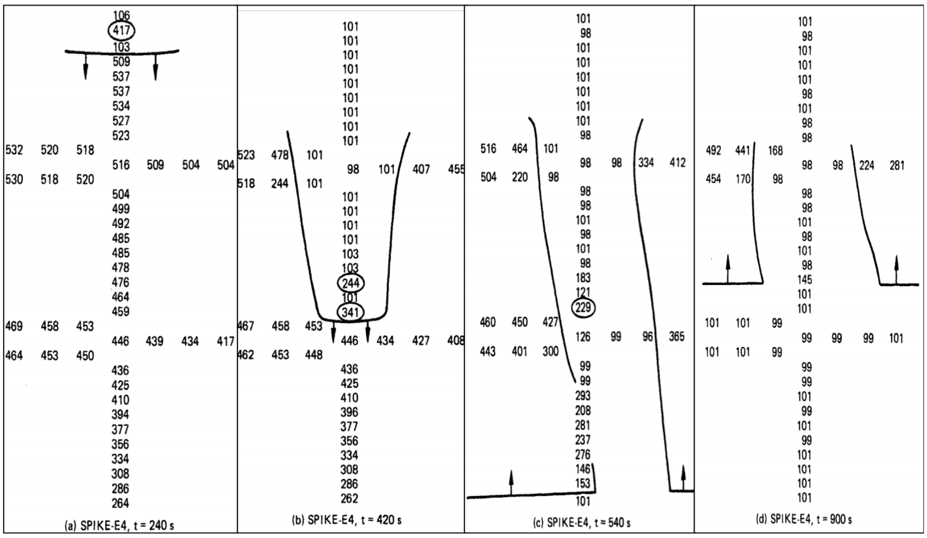

Figure 2.12 – Water penetration pattern given by the thermocouples measures for Cho et al. experiment with water injection temperature of 100°C

Reproduced from: [132, p.26]

Cho et al. [132, p.23] states, "the pattern of water penetration was found to be complicated due to the formation of dry pockets and channels." Depicted in figure 2.13 is Cho et al. further description of the water penetration as a single column through the central region. As can be seen, the temperatures in the central lower region are lower from the beginning of the experiment. The two sets of radial thermocouples (at 25 and 50 cm above the bed bottom) also show the heterogeneity of the temperature distribution. The uppermost set of radial thermocouples shows a difference of 30 °C from one side, whilst the lower set of thermocouples shows a more significant difference of 50 °C. It may be possible that both the axial and radial temperature heterogeneity favored the penetrating pattern observed. Evidence of this can be seen in figure 2.12 how the "central" single column of penetrating water deviates slightly to the side of the particle bed with the initial lowest temperature in the radial position. In other words, the pattern found in the experiment may be simply a result of the initial temperature distribution discrepancies, where an initial central penetrating water channel might have been accentuated, suppressing the appearance of other channels.

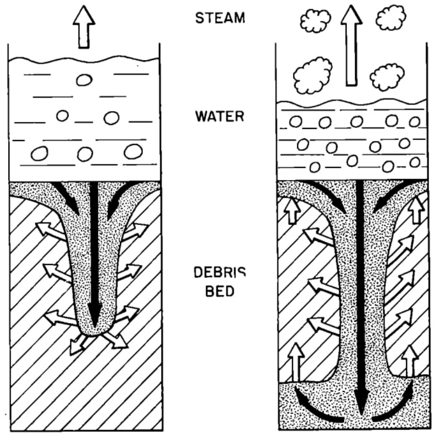

Fig. 2. Water Penetration Pattern;
(a) Downward Penetration
(b) Back-fill

Figure 2.13 – Cho et al. two stages quenching scheme

Reproduced from: [133, p.994]

2.1.3.3 PEARL experiments

In a series of unpublished experimental tests, the IRSN has studied the coolability and dynamics of a heterogeneous initially hot debris bed with power input in the top reflooding configuration in the PEARL test section. As for the bottom flooding experiments, the heterogeneity comes in the form of a lateral bypass with different material and diameter that favor the flow of both liquid and vapor coming from the debris bed. These top reflooding tests were carried out in a set of different initial conditions that varied initial bed temperature, pressure, water inflow rate, the pressure, and the thickness of the bypass section. The experimental results (video and thermocouples) show qualitatively 3 different cooling phases. At first, once the water starts to fall on top of the bed, it tends to penetrate by the bypass. The extracted heat flux corresponds to the quenching of the top and bypass layer of quartz spheres, whilst the penetration in the bed remains minimal. During this phase, an overlying water pool begins to form, supported by the out-coming vapor flux, and the resistance the hot debris bed represents to the water flow.

Once the bypass is more or less quenched, water begins to penetrate parts of the debris bed. During this phase, the vapor flux is mainly transported outside the debris bed through the bypass, hence inverting the tendency and drying the bypass. Again, it is possible to observe preferential channels, although its evolution is hard to follow since the path followed by the water is clearly three-dimensional in nature. Nevertheless, it is clear some parts of the bed remain at high temperatures whilst at the same height, other radial parts of the bed are quenched. The water-pool height during this phase is more significant.

The final stage begins when the out-coming vapor flux is no longer enough to support the overlaying water pool, and the water in at least one of the preferential channels inside the bed reaches the bottom. This stage is linked to an overall quenching of the debris bed, where there are still dry super-heated unquenched zones inside the debris bed, but a significant portion is quenched. The water-pool drains mainly through the bypass, again inverting the tendency of the vapor to escape through the bypass. Once the water pool is drained, quenching of the dry-zones continues rather slowly since all the water injected has the tendency of mainly entering the already quenched zones, and the bypass.

The experimental tests were stopped before complete quenching of the bed was observed due to safety precautions linked to the water reservoir level.

Some preliminary MC3D simulations show the same qualitative behavior, with a first penetration through the bypass, a subsequent drying of the bypass and bed quenching with preferential channels, and a final abrupt draining of the water pool through the bypass. Further simulations with the different bypass conditions need to be performed for a complete analysis. Nevertheless, the evidence for the water penetration phases, the extracted heat flux, and the observed preferential channels again support the importance of considering the penetration configuration/pattern.

2.1.4 Water flow instabilities and water fingering

The observed configurations discussed previously regarding the heterogeneity of the penetration front are not exclusive to debris beds, or fractured crust. In fact, the basic configuration of one fluid overlaying another will induce a specific pattern of motion between the fluids depending on their characteristics and relative positions. For the particular case of a denser fluid overlying a less dense one, the stability of the displacement of both has been studied for the better part of the last century. Although the phenomena had been observed before in varying contexts and industries, amongst the first experimental efforts to relate the flow pattern, and the conditions that lead to unstable flow in porous media, were presented by Hill [134], which studied the displacement of sugar liquors by water in granular bone charcoal. Further theoretical and experimental efforts followed by Saffman & Taylor [135], where they presented a stability analysis of viscous liquid displacement patterns and experimental results in configurations analogous to porous media (through the flow in a Hele-Shaw cell). It is important to note that this stability analysis of Saffman-Taylor consisted of a flow configuration of two regions of single-phase flow. Their analysis of the moving front between two immiscible fluids via the introduction of wave-like perturbances lead to some stability criterion, eq. (2.1) and approximate characteristic wavelengths. The onset of the instabilities has been since historically linked to the difference in viscosity between the fluids.

$$\varepsilon u > \frac{(\rho_l - \rho_v)\, g\kappa}{(\mu_l - \mu_v)} \tag{2.1}$$

At the same time Chuoke et al. [136] performed a similar analysis and arrived to a criterion of the same form here expressed as:

$$\varepsilon u > \frac{(\rho_l - \rho_v)\, g\kappa}{\left(\frac{\mu_l}{\kappa_{r,l}} - \frac{\mu_v}{\kappa_{r,v}}\right)} \tag{2.2}$$

Nevertheless, as Homsy [137, p.271] states, the term "viscous fingering", referring to the displacement of fluid in porous media has been coined since most cases, but not all, it is the viscosity variations between the phases that drive the instability. The mechanism is more likely gravity-driven in some configurations, like the ones of interest for this work. Moreover, the criteria presented are based on viscous flow, whereas some debris bed configuration may diverge from fully laminar (viscous dominant) flow, and inertial effects may begin to modify the velocity, hence rendering these criteria not entirely adequate. Regardless, the instability has still been observed even in configurations where the inertial effects play a non-negligible role, hence eq. (2.2) may be used only as a first-order approximation.

Gravity-driven fluid displacement has been more generally called gravity-driven unsaturated flow, water fingering, water invasion, or likewise, wetting front instability, or infiltration front instability. As presented by Cueto-Felgueroso & Juanes [138] "rather than a compact infiltration front, the flow is often unstable, and the water invasion takes the form of preferential paths (fingers)". Amongst the first to include the concepts of multiphase flow, unsaturated flow, were Parlange & Hill [139]. Experimental data, like the one of Glass et al. [140], further confirmed that indeed water fingering was a multiphase flow phenomenon. Figure 2.14 plots the evolution of the water content as a function of the time (each of the four images plots the state at different times). It is evident how the initial perturbations, shown in the leftmost image, evolve into preferential unsaturated (two-phase) water channels. What is less evident is the evolution of said channels; since in the rightmost image, it can be seen that one of the fingers has split into two smaller ones.

In a later publication, Glass & Nicholl [141] reviews a set of different experiments, including heterogeneity in the permeability of the porous media and the influence of different configurations, injection flow rates, and porous media. The authors conclude that whilst linear analysis implies specific criteria for the occurrence of gravity fingering, the assumptions inherent to the linear analysis are limiting concerning real field conditions. In other words, the applicability of the linear stability analysis to real porous media, including the heterogeneity, may not be entirely representative. Nevertheless, some insights into the stability of the phenomena in the simplified configurations were presented. In general, for the simplified configuration similar to the one of interest of this work (top reflooding), both gravity and viscous forces act as destabilizing forces.

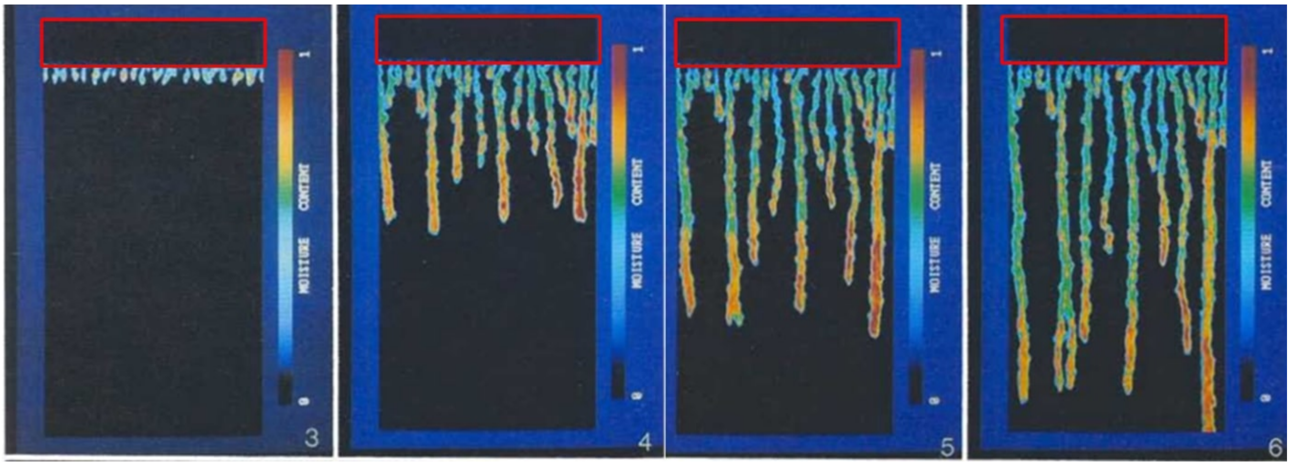

Figure 2.14 – Evolution of the moisture content, represented with different colors, in a 50cm by 90cm silica sand porous media at four different times. Top layer in red box had lower permeability and was used to control the water flowing into the bottom layer, the "test section". The value of the permeability, κ, can be calculated with the data presented in [142] and are $\sim 1.38\times10^{-11}m^2$, and $\sim 3.85\times10^{-10}m^2$ for the top layer and bottom layer respectively, with ε=0.42.

Adapted from: [143]

As presented by DiCarlo [144], other experimental results, such as some field tests shown in figures 2.15 and 2.16 evidence no instability were theory predicted there should be. Figure 2.15 shows the profile of the water penetration observed at different times with the aid of different colors dye injected with the water at different times. Figure 2.16 plots the infiltration front into dry sand at different times showing no evidence of water fingers. The author explained how the instability could instead be linked to what is called the "saturation overshoot". Figure 2.17 shows how the water saturation in the fingers remains relatively constant until arriving at the front, where accumulation is observed. In fact, this last can also be observed in the rightmost image in figure 2.14, where throughout the water fingers, a relatively constant water saturation was observed, whereas in the front a higher saturation was measured. The author further explains how recent investigations tend to link this saturation overshoot as an indispensable mechanism to observe the instabilities. Furthermore, he concludes that the stability of gravity-driven flow remains unsolved and that multiphase flow modeling and further development of numerical models may lead to unraveling the physical insights that would dictate stability or lack off. Amongst such numerical models, Cueto-Felgueroso & Juanes [145], Nieber [146] have produced interesting results.

In general, the linear stability analysis has yet to produce conclusive remarks on the stability of water fingering. This limits the availability of correlations that would prove helpful in the analysis related to the context of interest in this work. Furthermore, the effects of the elevated temperatures of the porous media, and the evaporation at the front and along the water fingers further distances the configuration of interest in this work from the simple configurations upon which the commonly called Saffman-Taylor instabilities are valid, or have been verified.

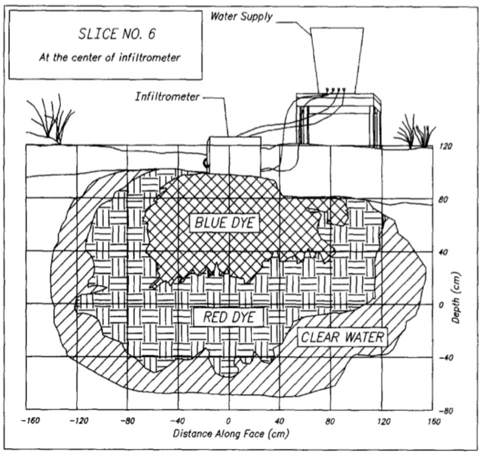

Figure 2.15 – Glass et al. field experiment in complicated alluvial deposit. Water infiltration front showing no evidence of water fingering instabilities where theory predicted fingering to occur.

Taken from: [141, p.146]

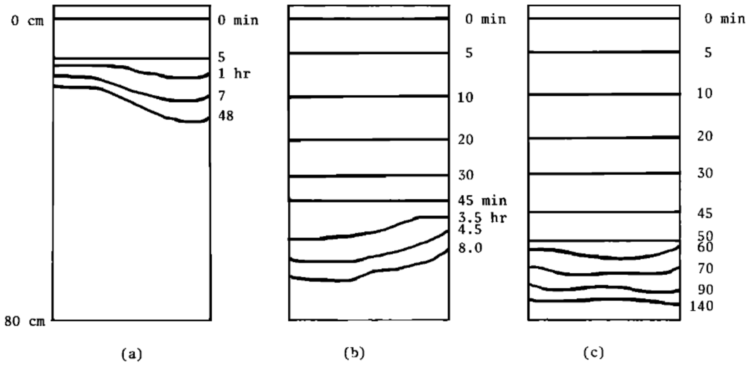

Figure 2.16 – Diment & Watson experimental results on wetting front patterns during redistribution in dry fine sand following infiltration at different times showing no fingering instabilities where theory predicted fingering to occur.

Taken from: [147, p.982]

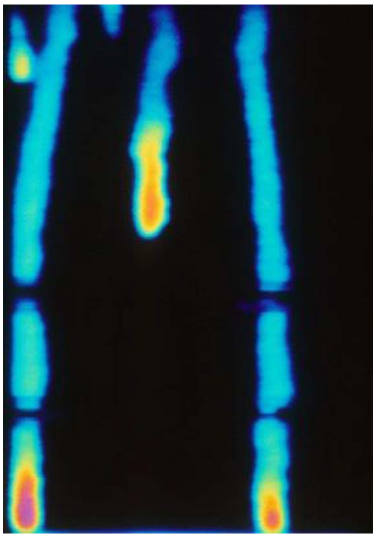

Figure 2.17 – Preferential flow paths showing a saturation overshoot, liquid accumulation (hotter colors) in the tail of the water fingers.

Taken from [144, p.4535]

2.2 Observed phenomenology of MCCI

MCCI is a complex interaction involving various intricated phenomena, for most related to the large number of present components. Hereafter a non-exhaustive summary of the key phenomenological observations made during past research programs, based on the OECD State of The Art Report (SOAR) [89].

2.2.1 Concrete ablation

Obviously, the first observed phenomenon when a scorching molten material comes into contact with a concrete floor or wall is the ablation of the concrete. As presented in section 1.1.2.7, it is reminded that the decomposition of the concrete starts rapidly beyond the saturation temperature. Some chemical reaction (decarbonization) occurs at a temperature of about 800 K, which leads to further degradation and release of the carbon oxide gases. Finally, the residual components are melting at temperatures around 1500 K. It is highlighted that the decomposition path is still the subject of research, particularly the so-called "ablation" temperature, which may be understood as the temperature where the concrete loses all mechanical properties and starts to be mixed with the corium.

Evidently, things are more complicated than in this simplified scheme. First, the concrete is not a homogeneous material. It contains, in particular, some large gravels with distinct properties, and these "likely subsist" for some time in the corium melt, before being fully incorporated (fully melted). Second, the real concretes contain significant portions of metals, particularly irons (mainly coming from the stainless steel of several components and iron rebars). The addition of a large amount of metals all along the ablation should have a substantial impact on the melt's coolability.

Not taking into account the presence of non-oxidized metal, the melting of the concrete leads to the incorporation of silicon and calcium oxides, with additions of the fewer amount of aluminum and magnesium oxides, into the corium, which is initially a composition of uranium, zirconium, with the addition of steel oxides. The new mixtures have very different thermo-physical properties (as shown in figure 2.18), which will lead to various impacts on the phenomenology.

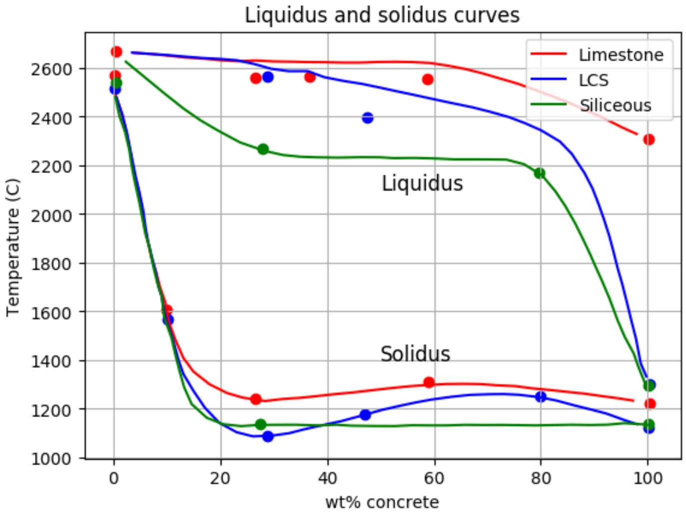

Figure 2.18 – Impact of the amount of incorporated concrete into a UO_2/ZrO_2 (1.6:1 mole ratio) corium on the solidius and liquidus temperatures

Reproduced from: [148]

First of all, they will induce a sharp reduction of the solidus temperature, i.e., on the "solidification' temperature. It is essential to state that this last concept is far from being well characterized, hence during this work, it will be taken simply as the temperature below which the corium has mechanical properties close to those of solids. The incorporation of concrete into the corium will, in any case, have a stabilizing effect by lowering its solidification temperature, since heat is best released when the corium is molten (due to convection effects). Furthermore, the density of the incoming materials is about half the initial corium one. This vast difference may induce a stratification of the melt, the light oxides (coming from the concrete) being on top of the heavy ones (uranium, zirconium), with a potentially broad impact on the coolability. A possible effect of the stratification of the melt may be the change in concentration of the residual power (present within the initial corium components) due to the migration of components with a high content of fission products. The release of the ablation gases will have an opposite effect from stratification. Thanks to the mixing induced by the gas traversing the melt, the result regarding its homogeneity may then differ strongly as a function of the concrete initial composition and nature with time. The change in conductivity is rather minor and has probably only small effects. In contrast, it is well known that the viscosity of the added components is strongly larger than of those of the initial corium (which viscosity is rather small). This should have a strong impact on the overall phenomenology by reducing the mixing and thermal convection effects.

2.2.2 Top crust

Starting with the Advanced Containment Experiments (ACE), a program that ran at the facilities of ANL from 1988-1991 dedicated to dry-cavity MCCI, through the Melt Attack Coolability Experiments (MACE), themselves an extension of the ACE program that ran from 1989-2001 with water added from the top, to the most recent iterations of ANL experimental investigations, the Core-Concrete Interaction experimental program (CCI) and Small-Scale Water Ingression and Crust Strength (SSWICS) platforms, MCCI investigations have shown interesting results when it comes to the appearance of a crust at the interfaces with the overlaying ambient layer [149], [150].

The question of the formation of crusts along the concrete interface is still a matter of debate since it has not been observed, but it is expected from equilibrium thermodynamics. In fact, these crusts may appear temporarily and might explain the intermittent phases of ablation observed in some experiments. This point is out of the scope of the present work and will not be discussed further.

The experiments, so far, have shown that regardless of the type of concrete or the flooding conditions, a crust forms at the melt-atmosphere (air or water) interface at a particular moment in time. The presence of this crust, the result of the heat exchange mechanisms, impairs the ability of the melt pool to exchange heat with the environment. The morphology of this crust, hence its properties, consequence of the heat exchange, depends on the formation mechanism and its evolution. Dry-zones, local heterogeneous distribution of power, chemical reactions (such as the oxidation of metals), decrease in heat exchange towards the water, amongst others, may lead to a temporary and/or local increase of crust temperature causing re-melting or slight compaction of an already solidified crust.

According to Sehgal [39, p.316], for a crust to form, the melt surface temperature must be lower than or equal to solidus temperature to avoid possible re-melting. Furthermore, as expected in accidental scenarios, the crust must remain in continuous contact with the corium melt, for it to be mechanically stable. Nevertheless, during some tests with a high gas sparging rate (e.g., CCI-8 [151], [152]) it was found that the crust anchored to the lateral wall maintained structural integrity, whilst at the same time separating the crust and the melt. Evidence of the previous can be seen in figure 2.20 where the gas accumulated under the partially impermeable crust and exerted pressure from underneath further deforming the crust, leaving a large void (melt-crust separation). This crust, in the shape of a bridge, had the mechanical stability to withstand the load coming from its own weight and the overlaying water pool. On the other hand, figure 2.19 shows an MCCI experiment in which the crust seems to have anchored to the experimental test section at one point to later fail, following the descent of the corium pool level. It is worth pointing out that the phenomenon of crust anchoring is a direct consequence of the experimental test section dimensions (∼ 30x30 cm up to 1.2x1.2 m) and that during the expected accidental scenario, the anchoring is not predicted to occur thanks to the wide span of the core-catcher/reactor pit (∼ 5-6 meters in diameter depending on the reactor design [69, pp.29]).

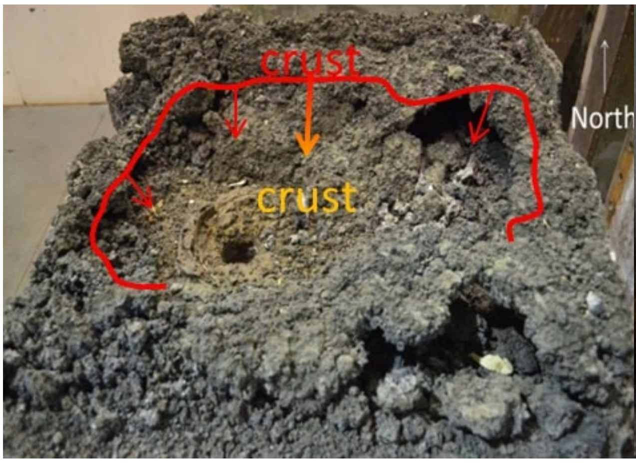

Figure 2.19 – CCI-9 apparent crust displacement with drilling hole in the center

Adapted from: [153]

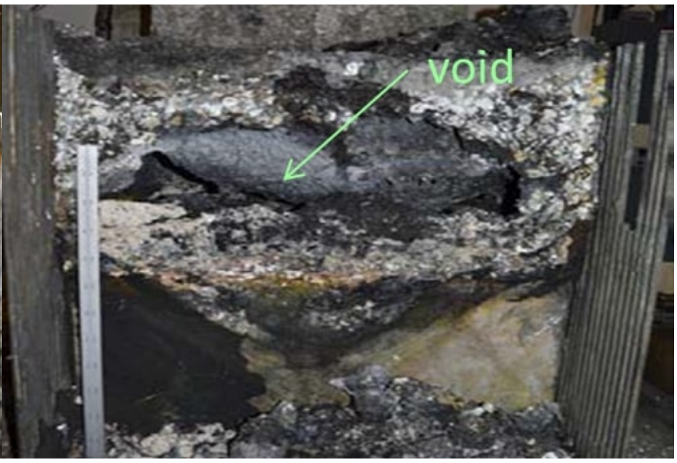

Figure 2.20 – CCI-8 large void

Taken from: [151]

2.2.3 Melt ejection and debris bed

The melt ejection phenomenon was observed for both dry conditions (on large-scale water-less corium spreading experiments) as well as in flooding condition (ECOKATS-2 [154], MACE-M3B, CCI-4,6,8 [89, pp.119-125]), recalling that the experiments took place on cavities made from a range of different concrete types, varying, in particular, in gas content. Individual experiments, such as CCI-8, show evidence of intermittent melt eruption phases [151]. These differed in intensity, as well as in conditions under which they occurred. In general terms, concretes with significantly higher gas content (such as LCS concretes) showed an increase in both the occurrence and the intensity of such eruptions. The eruptions are clearly due to the entrainment of the melt by the gas through some orifice, or crack, in the crust. Video evidence shows some of these eruptions were quite spectacular, ejecting the liquid corium across the test section, whilst others simply consisted of a fountain-like flow, which was extruded from the orifice and overflowed to the sides (such as in ECOKATS-2 [154]). Furthermore, evidence of both de-localized general eruption phases occurring through the whole extent of the crust surface, and localized eruption phases were found.

The ejected liquid forms a debris layer on top of the crust (figure 2.23) but in some cases, as observed in figures 2.21 and 2.22, a volcanic-like structure can be found instead. This may depend on the gas content and melt viscosity, which strongly depends on the amount of added concrete.

Figure 2.21 – MACE M3b test volcanic structure

Taken from: [89]

Figure 2.22 – CCI-8 volcanic structure

Taken from: Taken from: [155]

The debris found on top of the crust after some experiments are found to be of different morphology. Shapes vary from coarse (rough, edged), to drop shape debris. Drop shape debris where found in size range of few mm, and are supposed to be fragmented by hydrodynamic forces after corium jet penetration into a water pool. Unfortunately, no measure of the debris size was performed. These particles, analogous to those formed during the FCI premixing phase, transfer some of their energy to the surrounding fluid after being extruded through the crust but are generally deposited on top of the debris bed at a high temperature.

Evidence of this last effect, as shown in figure 2.23, may be inferred by looking at the shape of the debris where the particles seem to merge between them, which would indicate that solidification is partial and the final temperature upon settling is relatively high. Adding to this, as can be found in the regions closest to the volcanic structures, evidenced in figure 2.24 there are elongated drop-shaped debris which would suggest that after exiting the hole the corium dripped down and further deformed, which could not be possible if the debris were already solidified. In other words, the characteristic time for the corium to fragment and fall back is shorter than the time for it to solidify. Furthermore, the drops can be further fragmented after solidification by thermal stresses.

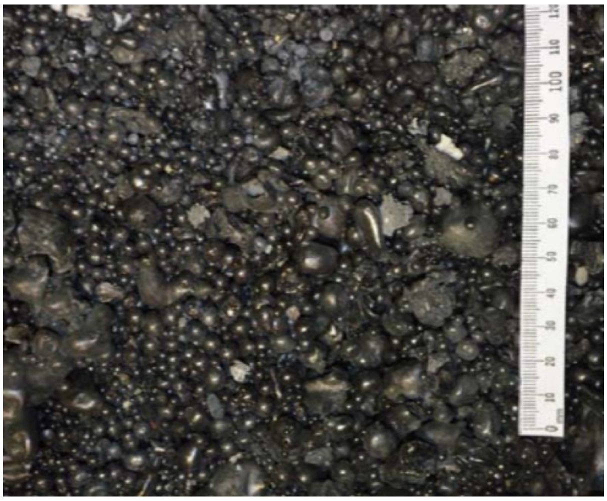

Figure 2.23 – CCI-8 Round debris bed on top of crust likely formed at one of the “violent” eruption period

Taken from: [151]

Figure 2.24 – CCI-8 volcanic structure close up showing elongated drop-like, and coalesced particles

Taken from: [156]

It is in general considered in the models (e.g. MEDICIS [157]) that these debris :

- exchange all their heat with the water; and
- are coolable.

From the previous discussion, and from the analyses performed regarding film boiling of liquid drops during an FCI [78], the first hypothesis seems very conservative and unlikely. Thus the debris should be deposited at a rather high temperature.

The second hypothesis regarding coolability also needs justification. It is based on the studies of DHF previously discussed. However, first, the debris must be cooled down before applying a DHF criterion, and this may take some time, during which the debris may re-melt. Second, the DHF criterion should take into account not only the heat generated in the bed but also the heat generated below (passing through the crust supporting the debris bed) that has to be extracted.

2.2.4 Water ingression

The crust separates the corium from the overlaying water/air, thus limiting the heat extraction from the molten pool to the coolant to conduction through the crust if it is compact. Nevertheless, the overlaying water may penetrate the crust through cracks, enhancing the cooling of the melt. This occurs when the thermal stresses induce cracking in the crust (solidified corium shrinks since the liquid corium’s density is larger than the density of solidified corium), and water percolates through them. However, proper heat exchange linked to water ingression can only occur when the water is in contact with the crust surface or in between cracks. In other words, in order for the phenomenon to result in steady-state cooling, the decay heat of the debris bed and/or the crust must be lower than the dry-out heat flux in order for it to be capable of being in contact with the surface (not having a vapor film covering it).

As shown by some MACE, SSWICS, and CCI tests, the heat exchanged with the water exceeds, for periods, the conduction-limited heat flux. Post-mortem analysis of several experiments has shown that there is a porous fracture-filled crust layer separating the final corium melt and the water layer, which serve as evidence of a certain degree of increase in the water-crust contact surface. These defects may serve as pathways for water to ingress and quench the crust. Under certain conditions, this process could undergo a positive feedback loop where the quenching of its interior would lead to further cracks hence further water ingression. Nevertheless, the phenomenon is complex, involving both the cracking of the crust by thermal and/or mechanical stresses and water penetration through these cracks. In the context of corium coolability, the SSWICS tests were designed to study the impact of this mechanism in prototypical corium pools.

Small-Scale water ingression Crust Strenght (SSWICS) experiments

The aforementioned SSWICS 1-7 experiments were carried out from 2002 to 2005 at ANL, designed to answer the following questions [158]:

1. "To what extent does water ingression into the crust increase the melt quench rate above the conduction-limited rate and how is this affected by melt composition and system pressure?
2. What is the fracture strength of the corium crust when subjected to a thermal-mechanical load and how does it depend upon the melt composition?"

A summary of the tests 1-7 characteristics is presented in table 2.2. All tests were carried out in a cylindrical test section with 30 cm of internal diameter with a corium composition of a 100% oxidized PWR corium melt with varying concrete content in a range of 4-23wt.%. The added concrete was of a different nature in different tests (LCS, Siliceous). Tests 1 through 7 were focused on measuring the boiling heat flux of the different corium melts under different sets of conditions (pressure, injection flow-rate, pre-heating of the test section, etc.), whilst subsequent test 8 through 11 (carried out from 2005 to 2009) were aimed to respond to the question of the influence of gas coming from the bottom (simulating concrete decomposition gases). Test 8-11 will not be discussed in this work.

Table 2.2 – SSWICS tests' characteristics

Parameters	**Test #** **1**	**2**	**3**	**4**	**5**	**6**	**7**
Corium mass (kg)	75	75	75	60	68	68	80
UO_2 mass (kg)	46	46	46	29	38	38	51
Initial corium temperature (K)	2573	2373	2373	2373	2373	2223	2373
Initial collapsed melt height (cm)	15	15	15	15	15	15	15
Concrete type	LCS	Siliceous	LCS	LCS	LCS	Siliceous	LCS
Concrete content in corium (%)	8	8	8	23	14	14	4
System pressure (bar)	1	1	4	4	4	1	4
Water injection period (s)	665	760	183	195	622	215	194
Water injection temperature (°C)	20	20	95	95	95	95	95
Water injection flow-rate (lpm)	4	4	12	13	6	14	13
Water injected (l)	33	39	34	40	61	47	40
Test duration (h)	2.2	1.2	1.8	2.4	2.6	3.9	1.4
Measured permeability κ ($10^{-11}m^2$)	42-53	47-51	10-11	2.8-2.9	3.6-3.8	9.2-11	N.A.

Adapted from: [159]

Figure 2.25 shows the schematic of the test section. As can be seen, the cylindrical test section is lined with MgO walls to minimize thermal losses (green parts) and has an extra ZrO_2 low density 1.3 centimeters thick layer at the bottom of the test section (orange part). A corium pool of 15 centimeters was formed via a thermitic reaction. After a small period of time, water was injected at the top of the test section, whilst the resulting vapor was extracted from the top and the heat flux measured by measuring the mass of vapor condensed, and the energy balance of the secondary loop of the condenser. Several thermocouples were installed to measure the progression of the temperature inside the melt pool, as well as the temperature of the walls at different axial positions. Nevertheless, for all tests, the thermocouples inside the melt failed at one point or another, making it hard to follow the temperature progression inside the melt region.

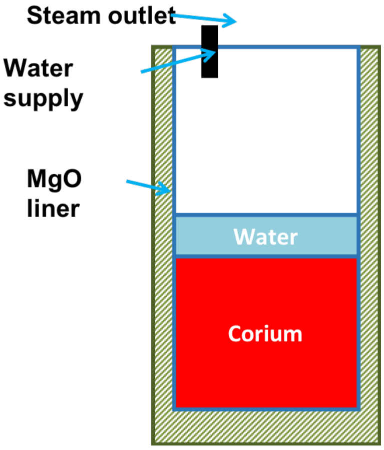

Figure 2.25 – SSWICS experimental test section scheme

Adapted from: [159]

Figure 2.26 presents the measured heat flux given for tests 1 through 7. In it, the conduction-limited curve is plotted as the black long-dashed curve, calculated using a 3D thermal heat conduction analysis code. It is crucial to note that for the critical parameter of corium thermal conductivity Lomperski et al. [159] chose to use a value of 1.5 $\frac{W}{m \cdot K}$ (although in more recent works they have used a value as low as 1.25 [160]).

Nonetheless, other authors studying the thermophysical properties of the different materials composing corium have given values dependent on the temperature, but as a global higher than 2 $\frac{W}{m \cdot K}$. To cite a few, Fink [161] shows the thermal conductivity of UO_2 as a function of temperature, where it varies from 8 down to 2-3 $\frac{W}{m \cdot K}$ from 300 K to 3200 K. Combis et al. [162] shows that the conductivity of silica varies as a function of temperature, but is more significant than 2 $\frac{W}{m \cdot K}$ for temperatures between 800 and 2400 K. Furthermore, Seibert et al. [163] show the thermal conductivity for different ratios of UO_2 to ZrO_2 between 2.5-3 $\frac{W}{m \cdot K}$ and between 2-3 $\frac{W}{m \cdot K}$ for temperatures of 500 K and 1400 K respectively. It is then difficult to foresee a situation where a full-scale corium with prototypical compositions will have a lower thermal conductivity than 2 $\frac{W}{m \cdot K}$. This last is reflected in the standard practice for authors performing calculations for full-scale corium to use values higher than 2 $\frac{W}{m \cdot K}$ (e.x. Carenini et al. [164] where the value for the thermal conductivity taken for a similar corium composition in a range of 2.45-2.8 $\frac{W}{m \cdot K}$). The corium's increased thermal conductivity would hence increase the value of the conduction-limited curve in figure 2.26. As can be seen, the heat extracted from tests 1, 2, 3 (less evident), and 7 shows some evidence of the influence of another heat exchange mechanism, supposedly water ingression, as compared to conduction. Nevertheless, after the observed plateau, there is a constant decrease in the extracted energy with a similar shape than a conduction-limited curve. The presence of this second phase in the experiments where the plateau was observed strongly suggests that if the water ingression mechanism takes effect, it does so only during a limited time. Regardless of the experiment, an intense extracted heat flux at the beginning of the water injection rapidly declines to zero before increasing again either to the observed plateau or to the conduction-limited curve. This initial extracted heat flux behavior is not conclusive since the information regarding energy absorbed by the sidewalls does not lead to decisive arguments. In either case, some part of the absorbed energy is presumably later released from the MgO wall into the test section once a penetrating front cools the inner walls.

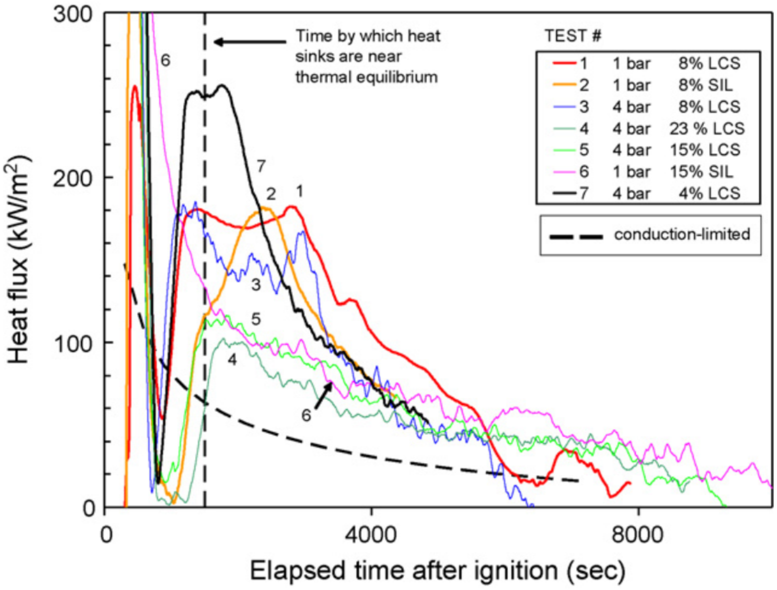

Figure 2.26 – SSWICS measured heat flux vs. conduction-limited heat flux predicted by 3D thermal heat conduction analysis code (SINDA/G)

Taken from: [160]

For all the tests, except test 7, a post-mortem permeability measurement was made, results of which are showed in figure 2.27, by extracting a section of the formed crust and using the falling head permeameter technique to measure. As can be seen, the permeability as a function of concrete content quickly decreases. Comparing the influence of pressure on permeability, it can be observed that for the same type of concrete, at higher pressures, the permeability dramatically decreases. Nevertheless, it may be possible that the permeability measured post-mortem does not represent the actual permeability linked to the extracted heat flux during the experiment.

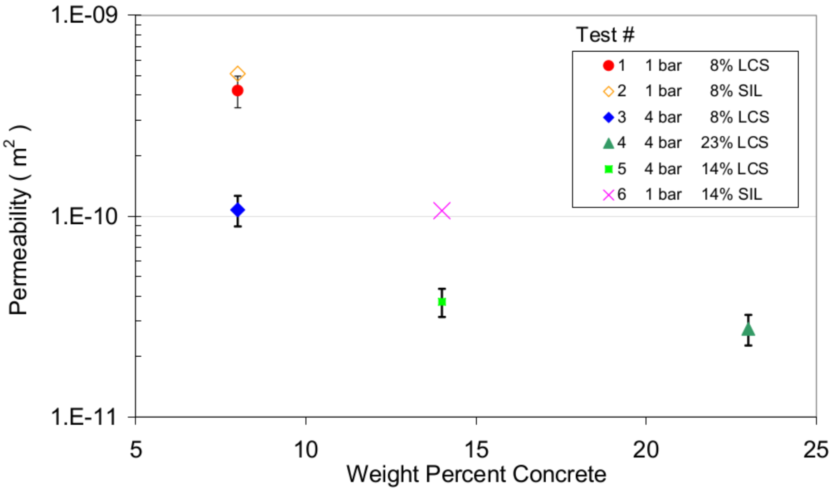

Figure 2.27 – SSWICS experimentaly measured permeability as a function of concrete content

Reproduced from: [159]

By comparing all experiments which show the plateau's presence, the most manifest tendency is the diminution of the permeability with the increasing concrete content. This is expected due to the mechanical properties of these materials, as will be explained afterward. Regarding the characterization of the impact of the two other parameters, the limited number of points does not permit unambiguous results. It may be concluded, with substantial uncertainty, that the concrete's nature has a low impact, whereas the ambient pressure has a noticeable influence, although it is probably quite hidden in the general uncertainties for reactor applications. However, this figure is misleading since only tests with concrete content smaller or equal to 8% really indicated the presence of a water ingression phase. Others are quite likely fundamentally conduction limited.

Two of the main conclusions extracted from the SSWICS experiments are [159]:

- There is a clear trend towards decreasing heat flux with increasing concrete content.
- dry-out heat flux is in the range of 300 to 50 $\frac{kW}{m^2}$ for corium containing 4-23% respectively, for siliceous or limestone/common sand concrete.

Nevertheless, the validity of the second conclusion is rather dubious and needs further clarification. Furthermore, the experiments do not give a clear insight into the mechanisms itself since no information about the progression of the solidification front, or the formation of the cracks itself can be inferred from the experiments.

Figure 2.28, which shows the top and bottom view of the SSWICS-1 test, serve as evidence of the typical post-mortem configuration of the crust layer found in most SSWICS tests. In the figure, it is possible to observe the difference between the two boundaries, where the top surface of the crust shows slight fractures mainly close to the wall (lower left part of the picture on the left) and resembles more to a porous material, whereas the bottom surface of the crust seems rather compact with large fractures. This gives rise to uncertainties regarding the fracturing process itself, and its dependability on its boundary conditions.

Figure 2.28 – SSWICS-1 post-mortem configuration. Left: Top view, Right: Bottom view

Reproduced from: [160, p.911]

Additional uncertainties come from the fact that it can be stated that the mechanism is highly heterogeneous, as inferred by figures 2.29 and 2.30 which plot the temperature of the melt region at different depths, and the temperature of the sidewall for test 7. Figure 2.30 clearly show that by t $\sim$ 1000s, all wall thermocouples at all axial positions above 50 mm were quenched. On the other hand, the thermocouples inside the melt, figure 2.29, show that for axial positions above 45 mm, a rapid quenching phase did not begin until t = 1500 s. In other words, this means that it is clear that the water penetrated forcefully through the sides of the wall, leaving a large portion of the central core melt region unquenched. Furthermore, looking at the extracted heat flux for test 7, figure 2.26, the "plateau" observed for this test begins before the beginning of the temperature drop inside the melt region. This gives rise to the question of where did the water pass through, and what part of the of the extracted heat flux actually comes from the quenching through crust formation and water penetration, and what part comes from either border effects or conduction through the crust.

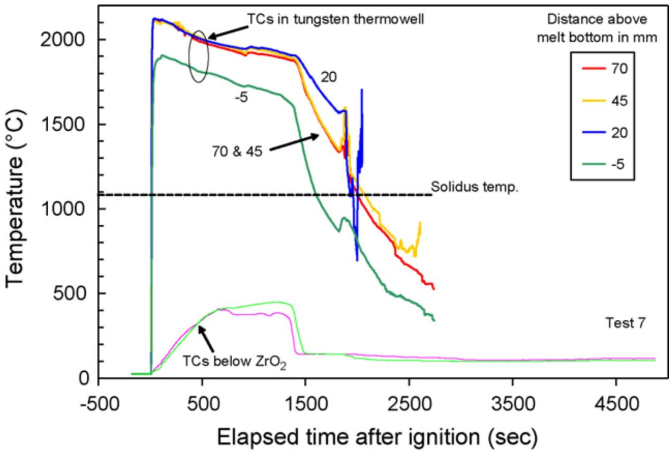

Figure 2.29 – SSWICS-7 melt temperatures

Taken from: [160]

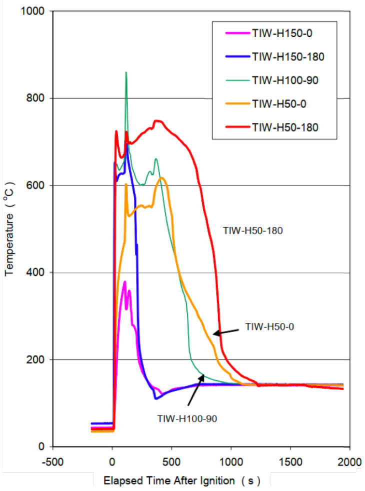

Figure 2.30 – SSIWCS-7 temperatures at the inner wall of MgO liner

Reproduced from: [159]

Core-Concrete Interaction experiments

The Core-Concrete Interaction experimental program (CCI) was carried out in ANL with the objective of extending the results from the MACE program. It aimed to achieve the following objectives [150]:

- "resolve the ex-vessel debris coolability issue through a program that focused on providing both confirmatory evidence and test data for the coolability mechanisms identified in previous integral tests, and
- address remaining uncertainties related to long-term 2-D core-concrete interaction under both wet and dry cavity conditions."

The series of 10 experiments provided information to analyze the following:

- ablation profile with different concrete types,
- dry and wet corium-concrete interaction,
- integral debris coolability data following late phase flooding, and
- data regarding the cooling transient.

Only tests 7-10 will be discussed during this work. The test CCI-10 was done recently. Tests CCI-8 and 10 were performed to study the melt ejection phenomenon, whilst CCI-7, and 9 were designed as water ingression tests. CCI-9 consisted of a 1D version of the test CCI-7. The only ablatable surface was located at the bottom of the test section; hence there was no lateral ablation replacing the ablatable later walls of CCI-7 test with MgO sidewalls. This was done in order to minimize the uncertainty effects added by the ablation in test 7, were significant eruption episodes were observed and suggestively linked to the sudden ablation period. CCI-10 test consisted of a 1D version of CCI-8 with a different concrete composition, both with high gas content. The characteristics of tests 7-10 are summarized hereafter in table 2.3. In it, the observed mechanisms are stated, as well as a summary of the test characteristics, such as the amount of total energy introduced, the amount of concrete ablated, and others.

Table 2.3 – CCI 7-10 tests' characteristics

Parameters	**CCI-7**	**CCI-8**	**CCI-9**	**CCI-10**
Corium type	PWR 6 wt.% conc.	PWR 8 wt.% conc.	PWR 6 wt.% conc.	PWR 8 wt.% conc.
Corium mass (kg)	1000	1000	1000	1000
UO_2 mass (kg)	625	606	625	606
Initial corium temperature (K)	2100	2100	2200	2100
Initial collapsed melt height (cm)	30	30	30	30
Concrete type	Siliceous	LCS (EDF)	Siliceous	Limestone-rich
Base dimensions (cm)	70x70	70x70	70x70	70x70
Ablatable dimensions	2D	2D	1D	1D
DEH time (min)	130	145	440	210
Total ablated concrete mass (kg)	380	410	185	353
Concrete ablation enthalpy $\left(\frac{MJ}{kg}\right)$	1.7	2.4	1.7	2.2
Total DEH energy input (MJ)	1506	1700	1243	1895
Losses through MgO sidewalls (MJ)	48	51	404	215
Net DEH energy input (MJ)	1458	1649	839	1680
Total concrete ablation energy (MJ)	646	984	315	777
Target heating power kW	210	210	151[a] 50[b]	151
Average net heating power kW	187	196	60[c] 25[d]	133
Average concrete ablation power (kW)	83	113	12	62
Target power input $\left(\frac{W}{kg_{UO_2}}\right)$	336	347	242[a] 81[b]	250
Average net power input $\left(\frac{W}{kg_{UO_2}}\right)$	300	323	96[c] 40[d]	220
Initial flooding time (min)	1	2	1	1
Observed debris bed	Yes	Yes	No	No
Observed eruptions	Yes	Yes	No	Yes
Volcanic structures	Yes	Yes	No	Yes
Void under crust	No	Yes	No	Yes

[a] Initial value [b] Lowered until this value, then constant [c] From t=0min to t=105 min
[d] From t=105min to t=440min

Data taken from: [153], [165], [166], [167]

Figures 2.31 and 2.32 depict the experimental platform used for the tests. The yellow parts are the refractory MgO sidewalls, the pink parts are the tungsten electrodes, the blue parts are the protective U_3O_8 layer behind the tungsten electrodes, and the grey part the ablatable concrete surfaces. The 70 x 70 cm test section was surrounded for tests CCI-7 and CCI-8 by a concrete basemat, and two ablatable concrete walls, whilst the other two sides had the tungsten electrodes used to heat-up the liquid. For tests CCI-9 and CCI-10, the two lateral ablatable concrete walls were replaced by refractory MgO sidewalls. It is essential to point out that, as for any other technique used so far, the power introduced to the melt is only, or mainly, introduced to the liquid phase, meaning that there is no heating of solidified corium, hence no residual power simulation as would be in real accidental scenario. A thermitic reaction initially formed the corium pool. All tests were carried out with completely oxidized PWR corium with different initial concrete content. The corium composition chosen for each iteration conveys a percentage of concrete added to the mix. The different iterations of the test varied in corium composition, type of concrete, decay power, and criteria for water injection, amongst others.

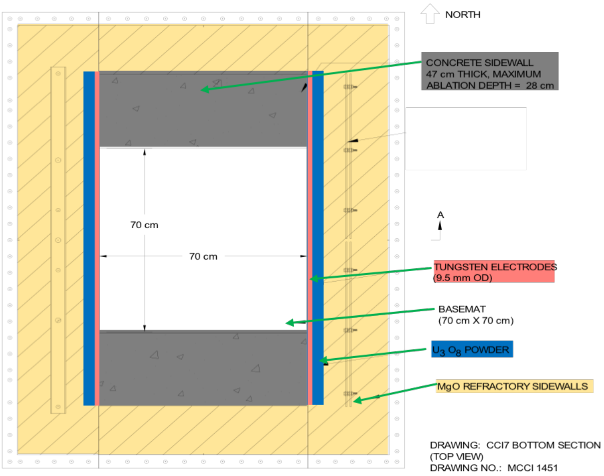

Figure 2.31 – CCI-7&8 test section top view

Adapted from: [151]

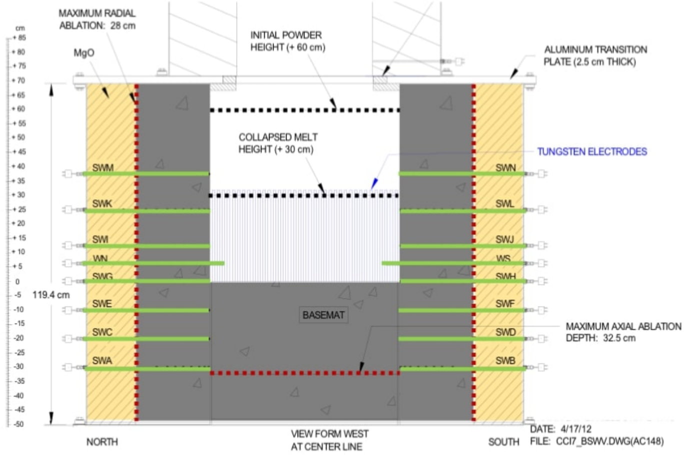

Figure 2.32 – CCI-7&8 test section lateral view, CCI-9&10 change the lateral ablatable walls by MgO sidewalls

Adapted from: [151]

Figure 2.33 shows the configuration found during the post-mortem analysis of the CCI-7 test. Recalling that this test was aimed at studying the water ingression phenomenon, hence used a low gas content concrete to suppress the melt ejection phenomenon. Nevertheless, a volcanic structure and a short period of extremely high extracted heat flux linked to a melt ejection episode were observed. As a direct result, a large particle debris bed (10 centimeters in thickness) was found at the top of a layer of the fractured crust during this test (figure 2.34). CCI-7 was found with a high content of concrete, 33%, in the crust (sample S12 from the chemical analyses performed post-test). This, amongst other results from the CCI tests, will be discussed later in section 3.2.2.2, but an important point is that, as contrary to SSWICS experiments, in the CCI-7 test, despite the high concrete content in the crust, an elevated heat flux was found in periods not affected by melt ejection. This may lead to the conclusion that the fracturing of the crust in this CCI-7 experiment was likely not linked to the same constrains. It may be that the fractures appeared as a result of a mechanical stress at a precise moment of the test (probably linked to the melt ejection periods) since the fractured crust morphology does not resemble the one found in the CCI-9 test (figure 2.19) where no evidence of melt ejection was found. Regarding the high heat flux, it may be stated that, in fact, the water ingression phenomenon was either not present or was attained during the final part of the test, where the input power was lowered. Nevertheless, the crust's final configuration was found to be quite fragile, hinting an intense fracturing. With the experimental data available, it is not possible to conclude if the numerous fractures found are formed during the course of the experiment, or are instead a result of the conditions found after the experiment had finished. Adding to that, the results do not give any insight into how the fractures were formed, or if mechanical or thermal stresses have formed them. In other words, it is not possible to conclude if the heat flux observed during the experiments can be linked to the water ingression phenomenon and if the fractures found post-mortem contributed to the quenching of the corium.

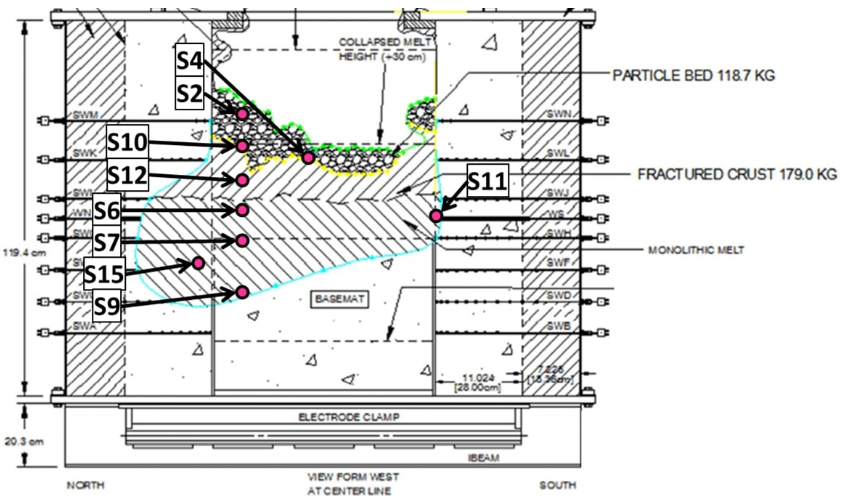

Figure 2.33 – CCI-7 post-test debris configuration and sample location (pink circles marked as S), including characterisation for different zones depending on the morphology of the debris found

Adapted from: Farmer et al. [166]

Figure 2.34 – Zoom of a part of the CCI-7 heavily fractured crust found during post-mortem analysis showing the large blocks composing it

Taken from: [155]

Another interesting result of the CCI tests is the observation of sporadic melt ejections after bulk cooling transient in almost all CCI tests, including all of the tests using LCS concrete and some with siliceous concrete. Both CCI-7 and CCI-8 tests show evidence of volcanic structures (linked to some melt ejection episodes), and a particle bed, whilst test CCI-10 showed evidence of melt ejection episodes, but no debris bed was found (or at least presented). In particular, the melt eruption episode in CCI-7 has been suggested to be caused by a sudden ablation episode, evidenced by temperature measurements, which was observed at around the same time as the heat extraction peak. Post-mortem analysis shows that at least two different melt eruption mechanisms, as shown by the presence or lack of volcanic structures, were detected at the tests where eruption periods were observed.

Adding to this, 2D ablation profile analysis has shown that there is an important radial/axial ablation disparity in siliceous concretes, were a more pronounced ablation is found in the radial direction, whilst in LCS concrete, the ablation profile is quasi-homogeneous (probably due to the gas content aiding in the mixing).

Further analysis of CCI-7-10 will be presented in section 3.2.2.

2.3 Models and constitutive laws for two-phase flows in porous media

Taking into account the major experimental difficulties of ascertaining the impact, or even the appearance, of the phenomena, modeling can prove a crucial tool to study the corium's coolability. The importance of two-phase modeling through porous media has been evidenced countless times before for a wide range of industrial/scientific applications. It is an active field of study where countless authors have developed an equally countless number of models adapted for different use. In-depth descriptions and further information can be found in [168], [169], [170], [171], [172], [173].

As presented by Macdonald et al. [172, p.199] "the complexity of the flow pattern rules out a rigorous analytic solution of the problem and suggests that an empirical or quasi-empirical correlation is the best one can hope for", also adding that the large variety of models published in the literature can be divided in: "(1) phenomenological models; (2) models based on conduit flow: (i) Geometrical models, (ii) statistical models, and (iii) models utilizing the complete Navier-Stokes equation; and (3) models based on flow around submerged objects".

The central historical equation behind current multiphase models in porous media is the single-phase Darcy's law, which has been eventually derived as a solution to the Navier-Stokes equations [174]. As stated by Hassanizadeh [175, p.49] "this is an empirical equation that was originally proposed by Henry Darcy in 1856 for describing 1D steady-state flow of incompressible water in saturated homogeneous isotropic rigid sandy soil under constant temperature". In other words, Darcy showed the linear relation between the single-phase pressure drop through the porous media and the fluid flow rate. This law assumes the dominance of viscous forces over inertial forces, neglecting the latter.

It is known that Darcy's law holds only for relatively low flow rates, and as stated by Niven [176] the deviations to Darcy's law are caused by inertial effects at the pore scale and not, initially, by the appearance of turbulence.

In general, a widespread approximation of the pressure loss in a porous medium is using the Darcy-Forchheimer law, an extension of Darcy's law for higher velocities [177]:

$$-\frac{\delta P}{\delta z} = \rho g + \frac{\mu}{\kappa} j + \frac{\rho}{\eta} |j| j \tag{2.3}$$

For 1D two-phase flow in steady-state conditions, the previous expression is extended including the formulation for relative phase-permeabilities, and potential capillary and interfacial fluid-fluid effects [177]:

$$-\frac{\delta P_i}{\delta z} = \rho_i g + \frac{\mu_i}{\kappa \kappa_{r,i}} j_i + \frac{\rho_i}{\eta \eta_{r,i}} |j_i| j_i + \frac{\delta P_c}{\delta z} + \begin{cases} \frac{F_{lv}}{\alpha} & \text{if } i = v \\ -\frac{F_{lv}}{1-\alpha} & \text{if } i = l \end{cases} \tag{2.4}$$

$$F_{lv} = 350(1-\alpha)^7 \alpha \frac{\rho_l g \kappa}{\eta \sigma_{lv}} (\rho_l - \rho_v) \left(\frac{j_v}{\alpha} - \frac{j_l}{1-\alpha} \right)^2 \tag{2.5}$$

where $\frac{\delta P_i}{\delta z} \left[\frac{kg}{m^2 s^2}\right]$ is the pressure drop of phase "i" (l for liquid and v for vapor) with respect to z, g $\left[\frac{m}{s^2}\right]$ is the gravitational acceleration, j_i $\left[\frac{m}{s}\right]$ is the superficial velocity of phase "i", $\rho_i \left[\frac{kg}{m^3}\right]$ is the density of phase "i" , $\mu_i \left[\frac{kg}{m \cdot s}\right]$ is the dynamic viscosity of phase "i", κ $\left[m^2\right]$ is the absolute permeability, η $[m]$ is the absolute passability [178], $\kappa_{r,i}$ $[-]$ and $\eta_{r,i}$ $[-]$ are the relative permeabilities and passabilities, which are often expressed as function of the sole local-averaged vapor saturation α $[-]$, σ_{lv} $\left[\frac{N}{m}\right]$ is the liquid-vapor surface tension (calculated at T_{sat}), $\frac{\delta P_c}{\delta z}$ $\left[\frac{kg}{m^2 s^2}\right]$ is the pressure drop due to capillary effects, and F_{lv} $\left[\frac{kg}{m^2 s^2}\right]$ the interfacial friction factor.

Amongst various expressions for the interfacial friction term eq. (2.5), developed by Schulenberg & Müller [179], is the one used in this work[6]. However, the interfacial friction term becomes important only at large permeabilities, mostly beyond the scope of the present work, and will be shown that it can be therefore neglected in most cases.

In these previous equations, the porous media is described by its intrinsic properties κ, η, and ε. The first accounts for κ used in Darcy's law described it as independent of the nature of the fluid, and a parameter to be determined experimentally for each different type of media used. In other words, for the flow regime where Darcy's law is valid, κ is determined by the medium's geometry. Further extensions of these relations were made to take into account the inertial effects, via the use of the Darcy-Forchheimer law.

Amongst the expressions for the porous media parameters κ and η in a bed of solid round particles, some of the most common take the following form postulated by Ergun [182] as follows:

$$\kappa = \frac{\varepsilon^3 {d_p}^2}{A(1-\varepsilon)^2} \tag{2.6}$$

$$\eta = \frac{\varepsilon^3 d_p}{B(1-\varepsilon)} = \frac{\sqrt{A}\varepsilon^{\frac{3}{2}}}{B}\sqrt{\kappa} \tag{2.7}$$

where d_p $[m]$ is the Sauter mean diameter of the debris bed constituents (spheres) [178], ε $[-]$ is the

---

[6] It has been shown in [180], [181] that this expression seems to be the most appropriate when comparing several simulations to experimental data.

porosity, and A, and B [−] are constants. The exponents of these equations may vary as proposed by, amongst others, Liu et al. [183] who replaced for κ ε^3 by $\varepsilon^{\frac{11}{3}}$. The constants A and B can also take different values. For instance, as per Ergun [182] the Blake-Kozeny equations proposed a value of A=150, whilst according to Dullien [184, p.243] Carman-Kozeny and Macdonald et al. [172, p.206] proposed a value of A=180. Furthermore for the passability, Ergun proposed B=1.75, whilst Macdonald et al. [172, p.206] proposed B=1.8-4.0 depending on the roughness of the particles.

Other authors propose formulation for debris beds with a similar form [184, p.242] here expressed as:

$$\kappa = \frac{\varepsilon^x {d_p}^2}{C} \tag{2.8}$$

where the exponent "x" varies between 1 and 6, and C is a constant fitted from their experiments. As an example, for eq. (2.8) Rumpf & Gupte proposed x=5.5 and C=5.6 in their study of uniform random particle beds of spherical particles.

Complicating matters even further, different formulations for different geometries such as fractured porous media (given in table 2.4), fibrous media ([185], [186]), amongst others, exist. For non-spherical particles, an additional parameter may be necessary to calculate the representative diameter. Indeed, a general formulation of the permeability that covers all flow regimes and geometries of porous media seems rather unlikely, hence the use of any such expression for a specific geometry must be validated.

In the present work, the porous media (debris, or crust), will be directly characterized by their permeability and passability. Hence, the simplistic formulation relating porosity and the particle diameter to both the permeability and passability, eq. (2.6), with A=150 and B=1.75 proposed by Ergun is used.

Although several relations are available to calculate the relative permeability and passability, most of them take the following form:

Table 2.4 – Relative permeabilities, relative passabilities, and coefficients

Phase	$\kappa_{r,i}$	$\eta_{r,i}$
Liquid	$(1-\alpha)^n$	$(1-\alpha)^m$
Vapor	α^n	α^m

Author	**n**	**m**
Lipinski [109]	3	3
Reed [187]	3	5
Hu & Theofanous [120]	3	6

The exponents "n" and "m", presented in table 2.4 are based on the data analyzed by the different authors. It can be noted that for the laminar case, all the authors converge to a value of n=3. For the inertial case, there is a divergence in the value of coefficient m, but the most validated case would be the one proposed by Reed [187]; hence it will be the reference value used in this work. Nevertheless, the physical validity of any of the exponents can be questioned, as it is not entirely clear the fit made on their data can be extrapolated to be used in all cases. For instance, Alemán et al. [188] argues that the validity of the standard relative permeabilities expressions, most of which are developed and validated under steady-state conditions, may not necessarily be achieved for unsteady-state conditions, e.g., "...if the interfacial tension is very small everywhere or the overall pressure gradient is very large..." steady-state formulations may not be valid.

For fractured porous media, many other formulas to calculate the relative permeability of both phases have been developed. Shown in table 2.5 are some common expressions to evaluate the relative permeabilities. It may be noted that in this context, the passabilities do not intervene since the flow is expected to be predominantly laminar.

Table 2.5 – Relative permeabilities correlations for fractured porous media

Author	$\boldsymbol{\kappa_{r,l}}$	$\boldsymbol{\kappa_{r,v}}$
Brooks et al. [189]	$\left(\frac{\alpha-S_{irg}}{1-S_{ir}-S_{irg}}\right)^4$	$\left(\frac{\alpha-S_{irg}}{1-S_{ir}-S_{irg}}\right)^2\left[1-\left(\frac{1-\alpha-S_{ir}}{1-S_{ir}-S_{irg}}\right)^2\right]$
Fourar & Lenormand [190]	$\frac{(1-\alpha)^2}{2}(2-\alpha)$	$\alpha^3+\frac{3\mu_v}{2\mu_l}\alpha\,(1-\alpha)\,(1+\alpha)$
Chima & Geiger [191]	$\frac{(1-\alpha)^2}{2}\left(\frac{2}{3}\,(1-\alpha)^2+\alpha(1-\alpha)\right)$	$\frac{\alpha^2}{2}\left(\frac{1}{3}\alpha^2+\frac{1\mu_v}{2\mu_l}\,(1-\alpha)^2+\frac{\mu_v}{\mu_l}\alpha(1-\alpha)\right)$

2.3.1 Heat transfers

The question of local boiling heat transfers in the debris bed is, in general, not addressed in dedicated literature. A lack of specific two-phase flow heat transfer models for porous media, or even sufficient data (except the recent ones by Sapin et al. [192]) were found. Thus, the models used to evaluate critical heat fluxes in debris beds or reflooding capabilities are often based on a hypothesis of local thermal equilibrium. Indeed, some dedicated models as [180] considers thermal equilibrium among all the present phases. When it is not the case, the heat transfers are rarely mentioned in the documents and papers explaining the models [193]. This is legitimate when the transients are slow and when the interfacial area is important (small beads). This assumption is however, mostly questionable when the transient is fast, in particular for reflooding problems with millimeter-size particles. The analysis performed with the models, including MC3D simulations [181], shows that, for the interpretation of the experiments and for practical applications in the field of nuclear safety, the precise knowledge of the heat transfer is not a critical point. However, for the precise evaluations of reflooding problems, this may be more problematic.

A simple criterion for the thermal equilibrium may be derived. The characteristic conduction time can be written $\delta t_{cond}=\frac{y^2}{\alpha_{th}}$ where $\alpha_{th}\left[\frac{m^2}{s}\right]$ is the thermal diffusivity coefficient and y is the characteristic distance, i.e. bead diameter. With this last it is possible then to derive a "characteristic" equilibrium velocity V_{eq}:

$$V_{eq}=\frac{y}{\delta t_{cond}}=\frac{\alpha_{th}}{y} \tag{2.9}$$

δt_{cond} corresponds indeed to a minimum time when considering an infinite heat transfer with the environment. So, regardless if the equilibrium velocity derived above is an approximation, it gives the maximum velocity estimate. For a 5-millimeter steel sphere bed, V_{eq} is about 0.1 $\frac{mm}{s}$, which is very slow, and it is likely, as will be seen, that the heat transfer does not allow thermal equilibrium. In contrast, small particles with a diameter below 1 millimeter may be cooled at conditions close to equilibrium. In short, there are a number of problems with large particles where equilibrium is not achieved, which may require a better evaluation of heat transfer to achieve more precise modeling.

IRSN and the Institute of Fluid Mechanics of Toulouse (IMFT) studied the heat transfer, from nucleate to film boiling, using an arrangement of small cylinders simulating roughly a debris bed [192], [194], although the large porosity and the 2D configuration, seen in figure 2.35, prevent any direct use for standard debris beds.

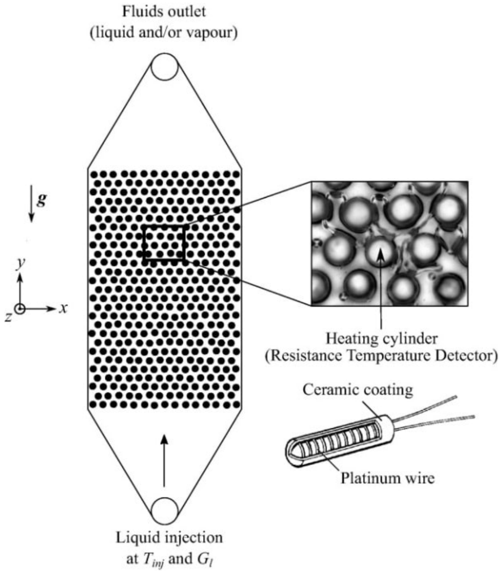

Figure 2.35 – Schematic set-up of the installation used by Sapin [194] and further improved by Gourbil [195] for the study of boiling heat transfer in porous media. Each cylinder can be used to provide controlled heat or to measure the heat transfer

Taken from [192]

Figure 2.36 provides an example of measurements of the heat flux as a function of the temperature for one single heated cylinder in a one-phase and two-phase flow configurations. In both cases, the nucleate regime and transition to film boiling are clearly observed, as well as the reciprocal transition in the cooling configuration (starting from the right side of the curves and advancing towards a lower temperature). One may then expect, in a reflooding situation, that film boiling will occur down to a quite low temperature, after which it will begin to transition to a weakly nucleate boiling flow. It is also interesting to note that following the cooling configuration, the presence of gas in the flow changes only the transition heat flux since, in the left branch, both one and two-phase flows show the same result. The film boiling heat flux itself is not modified.

Of course, the conditions depicted in this installation are quite specific. Still, it is possible to expect that heat is transferred almost under the film boiling conditions (nucleate boiling should be of weak importance) and that the existing models are relatively accurate or may need only moderate adjustment when necessary.

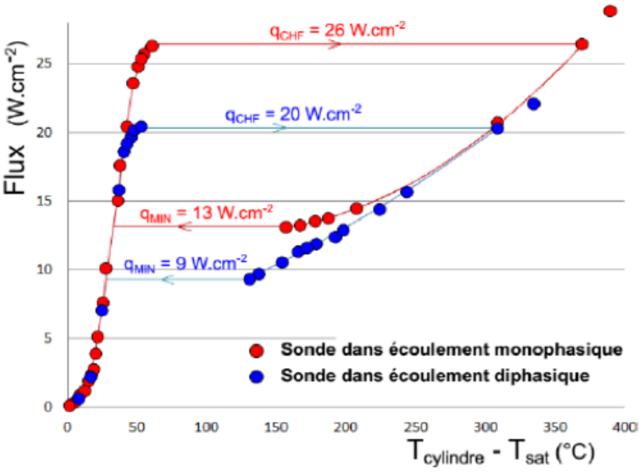

Figure 2.36 – Example of heat flux from one heated cylinder in the present of single-phase liquid flow (red dots) and in presence of two-phase flow.

Taken from [195, p.146]

2.3.2 Capillary effects

The capillary pressure, defined commonly by an expression such as "the pressure difference across the curved interface between two immiscible fluids" by Fanchi [196], may condition, or modify the way the phases flow through the porous media. Extensive efforts to study and produce analytical models or experimental correlations have taken place in the past century. Much of the early work gave light to the particular problems encountered when trying to relate mechanisms through the different scales (microscopic to macroscopic), and the common misconceptions that gave rise to misleading concepts. This last is exemplified as early as 1928-1929 when Uren (as cited in the discussions in Leverett [197]) urged to leave common misleading analogies relating capillary pressure in a particular porous media (sand) to a bundle of straight cylindrical capillary tubes by stating "an oil sand is not a 'bundle of capillary tubes' converging in a well". On the same tone, Leverett [197] suggested the "... abandonment of the 'capillary tube' concept" by substituting with two-fluid-curvature vs. water-saturation curves.

Dullien et al. [198] presented, amongst others, some experimental measurements, shown in figure 2.38, highlighting the existence of a hysteresis between cases for water imbibition ("the displacement of the non-wetting phase by the wetting phase" [199]) and drainage (non-wetting phase replacing the wetting phase). The authors explain that this hysteresis can be due to a size difference of the "voids" that control the displacement process, changing the pressure of the phase that invades the other. It is also added that another possible mechanism that could play a role in the appearance of this hysteresis is the trapping of the non-wetting phase in imbibition.

To account for the complex effects of capillarity in porous media, several correlations have been proposed, amongst which, a rather common one was formulated by Leverett [197]. The correlation, dependent on the porous media characteristics and an effective saturation function, is presented here as:

$$P_c = P_v - P_l = \sigma_{lv} \cos\theta \sqrt{\frac{\varepsilon}{K}} J\left(S^*\right) \tag{2.10}$$

with $\theta\,[°]$ the wetting angle (in general taken as 0 to maximize the function). $J\left(S\right)^*[-]$ is an non-dimensional expression called the Leverett J-function dependent of $S^*[-]$ the effective saturation, both of which may be evaluated using the equations given in table 2.6 where S_{ir} and S_{irg} are the irreducible liquid and gas saturations as shown in figure 2.38 (here both taken as 0.05). Figure 2.37 plots the correlations as a function of alpha with a secondary x-axis plotting the corresponding S^*. In it, it is possible to observe how there is a large discrepancy in the behavior of the correlations at low or high values of α, whilst between 0.4<α<0.8, the correlations developed by Lipinksi, Udell and Turland & Moore are relatively close. It can also be observed how at α values lower than 0.05 or higher than 0.95 (S^* either higher than 1 or lower than 0, linked to the minimal residual saturation), the values for most correlations are undefined.

Table 2.6 – Common expressions for Leverett J-function and the effective liquid saturation

Correlation	Equation
Effective saturation	$S^* = \frac{(1-\alpha)-S_{ir}}{1-S_{irg}-S_{ir}}$
J(S^*)-Lipinski [109]	$\frac{(S^*-1)^{0.175}}{\sqrt{5}}$
J(S^*)-Udell [200]	$1.417\left(1-S^*\right)-2.12\left(1-S^*\right)^2+1.263\left(1-S^*\right)^3$
J(S^*)-vanGenuchten [201]	$\frac{1}{5}\left(S^{*-\frac{1}{5}}-1\right)^{\left(\frac{1}{0.8}\right)}$
J(S^*)-Turland & Moore (1983)	$1.5-9.2S^*+\frac{88}{3}S^{*2}-\frac{880}{27}S^{*3} \quad if \;\; 0 \le S^* < 0.3$ $0.62-0.4S^* \quad if \;\; 0.3 \le S^* < 0.8$ $14.7-53.2S^*+66S^{*2}-\frac{55}{2}S^{*3} \quad if \;\; 0.8 \le S^* \le 1$

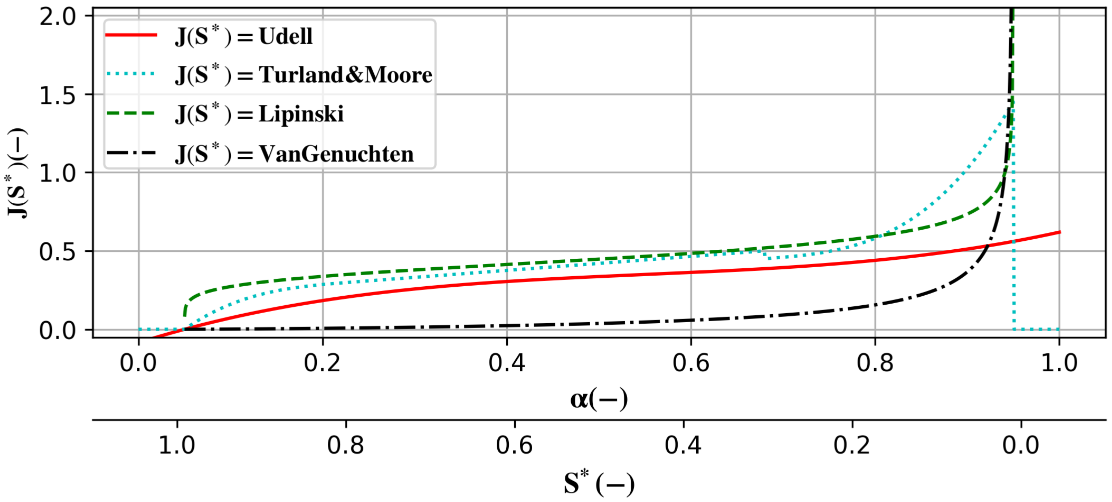

Figure 2.37 – $J\left(S^*\right)$ function as a function of α for the 4 different formulations presented in table 2.6 with $S_{ir} = S_{irg} = 0.05$

Nevertheless, numerous authors have questioned the formulations, and definition, of the capillary pressure in the complex morphology of a porous media. Hassanizadeh & Gray [202] pointed out that "...a rigorous and consistent thermodynamic theory of capillarity that provides a phenomenological correspondence among the relevant processes is still lacking". The authors explain that efforts to relate saturation with microscopic capillary pressure are often shortcoming since they are examined mainly in equilibrium conditions (and further extrapolated to dynamic conditions), and the measurement of the difference in fluid pressures are often made in the reservoirs outside the porous media (wrongfully relating bulk-reservoir pressures to local pressure differences within the porous media). Harris and Morrow point out that bulk-reservoir pressures and local pressure differences should not always be related since, at low saturation, they lose comparative significance as the conditions in the reservoir and inside the porous media become disconnected and lose direct hydraulic contact. Hassanizadeh & Gray [202] then proceeded to redefine the capillary pressure as "...an intrinsic property of the system under study expressed in terms of the change in free energy of the phases and interfaces due to a change in saturation". They continue by explaining that "...in a given porous medium containing two fluid phases, saturation and interfacial areas are independent variables", hence concluding that the common macroscopic capillary pressure-saturation relations, here presented as eq. (2.10), must be viewed as an equilibrium force and not as the definition of the capillary pressure.

The application of the formulation for the problem of debris bed reflooding is even more problematic due to the presence of the front of saturation and elevated melt temperature. This front occurs in the particular situation where the porous medium is very hot, and so the liquid cannot wet it. The formulation eq. (2.10) cannot be used, unless considering $cos\theta = 0$.

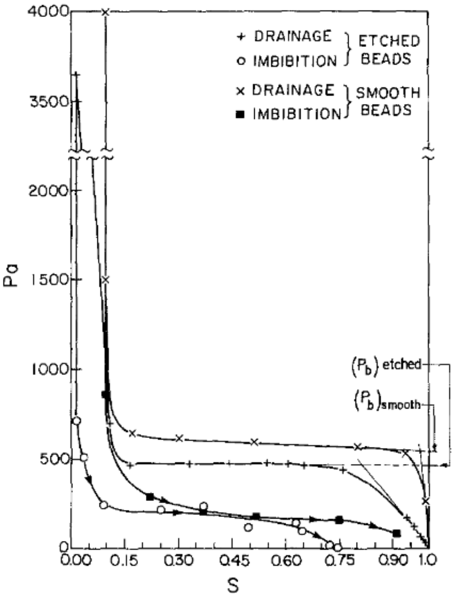

Figure 2.38 – Capillary pressure measured as a function of the liquid saturation in a debris bed made by smooth and spherical beads

Reproduced from: Dullien et al. [198]

2.3.3 Dry-out heat flux

In the debris beds, the global heat transfers from the matrix to the coolant are finally controlled by the frictions. This is due to the fact that heat is advected by the vapor, produced from the boiling of the liquid water, and the heat extracted is then limited by the possibilities for the vapor to escape the bed. From the studies of dry-out heat flux presented in section 2.1.1, several models have been developed. Most of them are built on a particular form of the Darcy law. The main difference between them is in the denominator and owes to the different assumptions taken on the form of the relative permeabilities, some of which used experimental coefficients fitted from their data. Amongst which, some widely used models are the ones formulated by Hardee & Nilson [203]:

$$\phi_{do} = \kappa g h_{lv} \frac{\rho_l}{\nu_v \left(1 + \left(\frac{\nu_l}{\nu_v}\right)^{\frac{1}{2}}\right)^2} \tag{2.11}$$

and Jones et al. [204]:

$$\phi_{do} = \kappa g h_{lv} \frac{0.015\left(\rho_l - \rho_v\right)}{\nu_v \left(1 + 0.003\left(\frac{\nu_v}{\nu_l}\right)^2\right)^{\frac{1}{4}}} \tag{2.12}$$

where $\phi_{do} \left[\frac{MW}{m^2}\right]$ is the dry-out heat flux. It is worth noting that Epstein in [205], [206] expressed both Jones and Hardee & Nilson model, for a pressure of 1 atm, as:

$$\phi_{do} = \kappa g h_{lv} \frac{\left(\rho_l - \rho_v\right)}{2\nu_v} \tag{2.13}$$

This last, nevertheless does not correspond to the models presented by Jones et al. [204], and Hardee & Nilson [203] respectively. Furthermore, the role of pressure in Epstein's formulation disappears since the liquid-viscous friction component is not present. This suggests that, while it may produce results that fall within the experimental dispersion for the laminar regime, it may not be the case at higher pressures. This is of relevance for the current work since the water ingression model developed by said author used this dry-out heat flux correlation (see eq. (2.30) in section 2.4.2).

Lipinski [207], in a paper presenting his work in [109], also proposed a model base on the more general Darcy-Forchheimer equation. Lipinski's approach is used in chapter 4 to develop a mixt model. In general, the author derived two separate expressions for both fully laminar and fully inertial regimes and combined them using an averaging function. All 3 expressions are presented here below as:

$$\phi_{do,t} = \sqrt{\eta g h_{lv}^2 \rho_l \frac{\left(\rho_l - \rho_v\right)}{\left(\rho_v^{\frac{1}{6}} + \rho_l^{\frac{1}{6}}\right)^6}} \sqrt{\left(1 + \frac{\lambda_c}{L}\right)} \tag{2.14}$$

$$\phi_{do,l} = \kappa g h_{lv} \frac{(\rho_l - \rho_v)}{\left(\nu_v^{\frac{1}{4}} + \nu_l^{\frac{1}{4}}\right)^4} \left(1 + \frac{\lambda_c}{L}\right) \tag{2.15}$$

$$\phi_{do} = \left(\frac{\phi_{do,t}^4}{4\phi_{do,l}^2} + \phi_{do,t}^2\right)^{\frac{1}{2}} - \frac{\phi_{do,t}^2}{2\phi_{do,l}} \tag{2.16}$$

where $\phi_{do,t}$, and $\phi_{do,l}$ are the dry-out heat flux correlations for the inertial and laminar regime, respectively, and L is the width of the debris bed. It is interesting to note that comparing Lipinksi's work in [109] and [207], the exponents "m" used for the inertial regime changed from 3 to 5, corresponding to the exponents presented by Reed. Figure 2.39 plots the experimental results presented in figure 2.2 as the blue circles, as well as Jones, Hardee & Nilson, Epstein, and Lipinski models as the red dotted, blue dashed, black dashed-dotted curves, and green solid respectively. As can be seen, regardless if Hardee & Nilson model falls within the experimental scatter, it is 2-3 times higher than both Jones and Lipinski models for the laminar regime. This is mainly due to the exponent used in the denominator, again which owes to the form for the evaluation of the relative permeability. The formula presented by Epstein falls as well within the experimental scatter, but it is significantly different from both the Jones and Hardee & Nilson models. Lipinski's model follows the experimental trend, and the change of slope is due to the change of regime from laminar to inertial with increasing permeability. The validity of the assumptions for using a fully laminar and a fully inertial model will be evaluated in chapter 4.

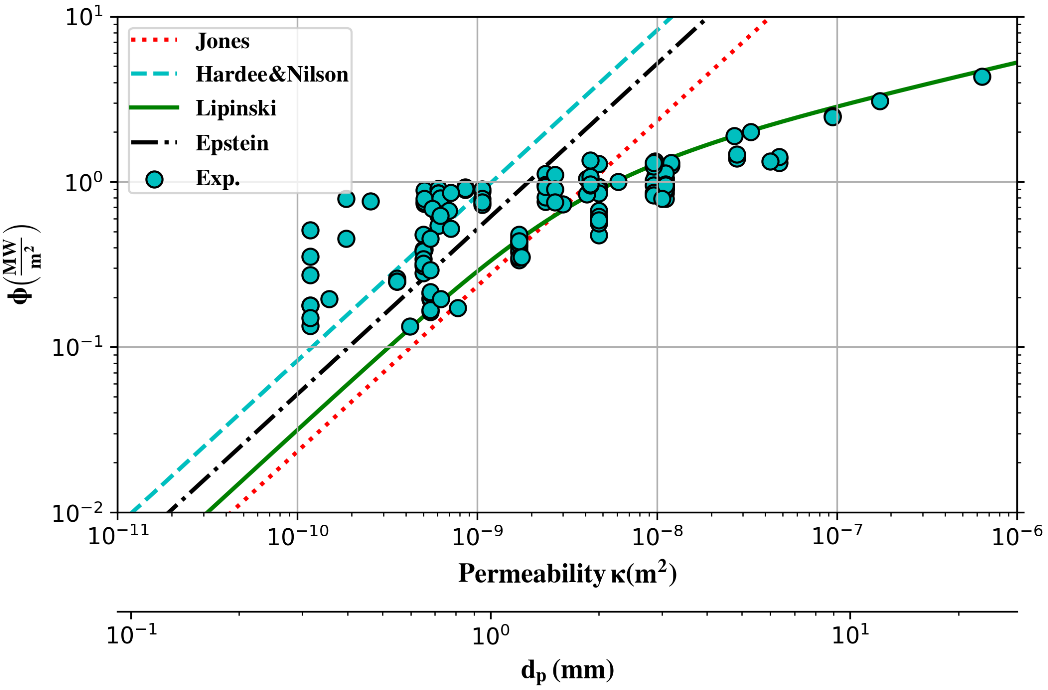

Figure 2.39 – DHF as a function of permeability from experimental data, dubbed Exp.(same as the one presented in figure 2.2), compared with Lipinski's model, eq. (2.16), Jones model, eq. (2.12), Hardee & Nilson model, eq. (2.11), and Epstein's model, eq. (2.13) with a secondary x-axis showing equivalent particle diameter using ε=0.4 and eq. (2.6)

2.4 Mechanisms and models for fractures and cracks in solidifying medium

Similar to the configuration of a debris bed, the formulations to evaluate the hydrodynamic behavior of the two-phase flow in fractures and cracks are based on Darcy's law and depend on the available surface of the flow, namely κ and the notion of relative permeability already discussed, see table 2.5. On the other hand, the formulations to evaluate this permeability are not straightforward. Although one may be very familiar with this widespread phenomenon, the mechanisms inducing fractures appearance and propagation is still an important unresolved field of research. The permeability in a fractured medium would depend on the fracture pattern, the fracture dimensions, the number of fractures per surface, amongst other parameters tightly linked to the material properties. Thus, as explained by Leguillon [208, p.538], the "different mechanisms (cooling, drying, and ageing) lead to the formation of crack patterns on the surface of some materials... are very difficult to describe in detail". In the scope of the present work, cracks will appear due to stresses induced by the change of density with tension, generally called simply thermal stresses. Examples of experiments and analyses in this context may be found in Leguillon [208], Bahr et al. [209], Bahr et al. [210], or more recently Faria Ricardo et al. [211].

2.4.1 Mechanisms of fracturing

Generally speaking, fractures will appear in a brittle material when the stresses will surpass a given value dependent on the material properties. Before establishing some elements of theories and models, it is important to stress that both oxidic corium and concrete are brittle materials. Large uncertainties exist regarding the properties of mixtures of corium oxides of type $UO_2 - ZrO_2$ and concrete oxides, but it seems that a simplified, essentially elastic, behavior might be considered. Under this assumption, somewhat classical models might be used. In contrast, it may already be highlighted that the inclusion of non-brittle materials, such as non-oxidized metal, in the corium, should lead to strongly different mechanics resulting in a need to revisit the existing models. This is out of the scope of the present work.

It is reminded that the permeability κ for a single thin planar crack is easily deduced from the laminar flow equations as $\kappa = e^2/12$. In the porous medium, one considers the superficial flow rate. The medium's permeability must then account for the "superficial" porosity ε, and so $\kappa = \varepsilon e^2/12$, where e is the thickness of the crack. For a parallel crack pattern, $\varepsilon = e/y$, where y is the crack spacing. Instead, for a squared crack patter, $\varepsilon = 2e/y$ whilst for a polygonal pattern, the closest to observations, $\varepsilon = \sqrt{2}e/y$. Clearly, the precise description of the crack pattern is out of reach, but it may generally be approached here as:

$$\varepsilon = C\frac{e}{y} \tag{2.17}$$

where C is a constant depending on the pattern, between 1 and 2.

The superficial porosity is also related to the shrinkage of the material after solidification and cooling, as a function of its thermal expansion coefficient β $\left[\frac{1}{K}\right]$ and temperature drop $\delta T\,[K]$:

$$\varepsilon = \beta\delta T \tag{2.18}$$

Generally speaking, the permeability may be then written under the form:

$$\kappa = \frac{1}{C^2}\frac{\varepsilon^3 y^2}{12} = \frac{1}{C^2}\frac{y^2(\beta\delta T)^3}{12} \tag{2.19}$$

The point of the modeling is then to determine the crack spacing.

A first approach for the crack evaluation in a brittle material was provided by Griffith & Taylor [212]. They stated that the cracks would appear when the elastic energy contained in a constrained material is sufficient to create new surfaces, a process that needs a specific energy per unit surface (surface tension). This is equivalent to a nucleation process. The elastic energy is due to the stress induced by the change in density while the material temperature decreases. This may be called the thermal stress. It is crucial here to emphasize the fact that only the elastic deformation is a reversible process, and thus the related accumulated energy can be released. This energy is the product of the strain by the stress. It is also clear that the boundary conditions, i.e., the constraint of the problem are essential to determine both the stress and the strain precisely.

To fix ideas, the case of slow uniform cooling of a slab laterally constraint can be examined. Further simplifying, a null Poisson coefficient will be considered so that the elastic stress due to thermal shrinking is simply $E\beta\delta T_c$, with E $\left[\frac{kg}{ms^2}\right]$ being the Young modulus and $\delta T_c\,[K]$ the variation of temperature from which a solid-elastic behavior appears to the one where cracks will appear. The strain itself is $\beta\delta T_c$ and thus the elastic energy may be written:

$$E_e = E(\beta\delta T_c)^2 \tag{2.20}$$

This embedded elastic energy must at least balance the surface energy of the new cracks, G_{cr} $\left[\frac{J}{m^2}\right]$, where S $\left[m^2\right]$ is the surface of the created cracks per unit volume, and G_{cr} the necessary energy per unit surface (also called the toughness of the material or the fracture energy surface density). S depends on the crack pattern but is roughly about twice the inverse of the crack spacing y, which is then determined as:

$$y = 2\frac{G_{cr}}{E(\beta\delta T_c)^2} \tag{2.21}$$

A second condition allows to determine δT_c: the stress due to thermal shrinking must be greater or equal than the tensile strength σ_{cr} $\left[\frac{kg}{ms^2}\right]$:

$$E\beta\delta T_c \geq \sigma_{cr} \tag{2.22}$$

Thus, the approximate solution is:

$$y = 2\frac{G_{cr}E}{{\sigma_{cr}}^2} \tag{2.23}$$

hence the permeability:

$$\kappa = \left(\frac{G_{cr}E}{{\sigma_{cr}}^2}\right)^2 \frac{(\beta\delta T)^3}{3C^2} \tag{2.24}$$

For non-uniform cooling processes due to, e.g., a thermal shock, the method is similar for the determination of the initial crack spacing and length, except that the strength is computed as an integral along the crack. Thus, the initial crack formation can, in principle, be derived from the evaluation of the surface heat transfer and heat conduction inside the material. Formally, with l being the crack length, the crack spacing can be expressed as:

$$y = 2\frac{\int_0^l G_{cr}\,dz}{\int_0^l E(\beta\delta T_c)^2\,dz} \tag{2.25}$$

similarly, the critical stress becomes:

$$\sigma_{cr} = \int_0^l E\beta\delta T_c\,dz \tag{2.26}$$

and thus, an equivalent expression to eq. (2.23) can be derived only if the Young modulus is constant. In any case, eq. (2.23) may be used as a first approximation, provided proper averages of E, G_{cr} and β are used.

According to Faria Ricardo et al. [211], for a sudden thermal shock, once a set of cracks has appeared, these cracks are constrained to propagate with the same spacing until an instability takes place leading to a selection of propagating cracks and arrest of the others. This selection leads to a reduction in the number of cracks, which in turn grow in thickness. This might be due to the fact that in a pure conduction problem, the temperature gradient thickness tends to increase. Indeed, Bahr et al. [210] proposed a simple scaling law between the spacing y, the crack length l, and the cooling penetration depth δ :

$$\frac{y}{l} = C\left(\frac{y}{\delta}\right)^2 \tag{2.27}$$

the constant C being of the order of 0.5. Roughly, by scaling the crack length with δ, it is possible to obtain that the crack spacing scales simply with the length. As the permeability is a growing function of the crack spacing, this should lead to a positive gradient of permeability with depth.

In a situation with water ingress in the solidifying material, the cooling regime will change once the penetration occurs, leading to a constant heat flux, that is a constant thermal gradient thickness δ. The crack geometry should not drastically change from that moment on. In any case, there should be a concentration of cracks at the top surface, and a subsequent decrease of crack number (increase crack spacing) with depth up to an equilibrium.

In both situations, the limitation of heat flux should come from the smallest permeability region, that is at the top surface, in the zone of initial cracks.

A further complication comes from the possible heterogeneity of the material, temperature gradient, and particularly heat losses in the experiments.

Last but not least, the crack spacing is then a function of physical properties E, G_{cr} and β that are far from being well determined for a representative corium-concrete mixture. Large variations of values of the related properties for the main components (UO_2, ZrO_2, SiO_2, $CaCO_3$, Al_2O_3, etc.) are found in the literature. The tensile strength of the corium used in the SSWICS tests was tentatively measured by Lomperski & Farmer [213], but the crust specimens were quite damaged, which led to values much smaller than those they used for their own evaluations of the Lister-Epstein model (see section 2.4.2). Even more problematic, the surface energy is hardly found. Only data for limestone and glasses could be found. Adding to this, the Young modulus shows drastic changes with temperatures. For example, for limestone, it may change from 70 GPa to about 0 from 0°C to 1000 °C [214].

2.4.2 The Lister-Epstein water ingression model

In the context of MCCI, the SSWICS experimental results were compared by Lomperski and Farmer to a model initially proposed by Lister [215], in the context of vulcanology for the penetration of water into hot rocks, and further extended by Epstein [206] for water ingression.

According to the "Lister-Epstein" model, the crack pattern and associated permeability are continuously driven by the thermal stress, itself driven by the heat transfer. In turn, the heat transfer is related to the permeability, using porous media CHF heat flux. As already discussed in section section 2.3.3 Epstein uses a somehow flawed simplification, eq. (2.13), of the Jones correlation eq. (2.12). This implies that the validity of the model at higher pressures is questionable since the part depending on the formulation of the dry-out heat flux of porous media lacks the liquid viscous term. This results in a dry-out formulation linked to the continuous permeability creation by the fracturing process, itself driven by the flux inside the crust and the one coming from underneath the crust. The configuration and boundary conditions considered for Epstein's extension of the Lister model are shown in figure 2.40.

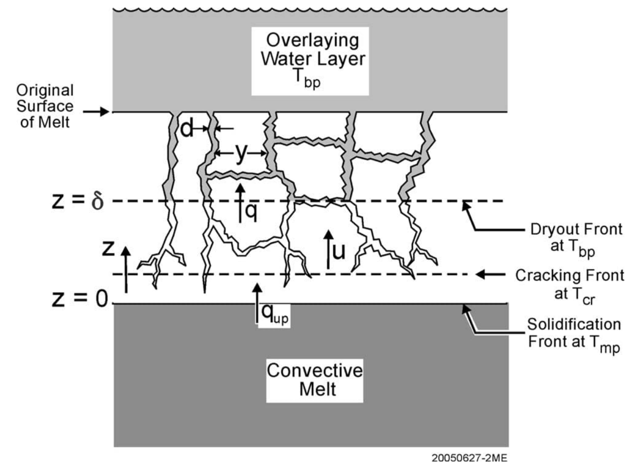

Figure 2.40 – Epstein model schematic showing the configuration taken into account for developing eq. (2.33)

Taken from: Epstein [206]

The model proposes a simplified evaluation of the crack spacing in the permeability formulation eq. (2.19) (with the factor C being taken at $\sqrt{2}$) by considering that it is related to the temperature drop thickness δT_{crack} necessary to cause a crack by an excess of tensile strength. This hypothesis is not justified by the authors. In other words, the hypothesis states that the crack length scales directly with the crack spacing, which, in view of the previews discussions and the scaling law eq. (2.27), might be considered as an acceptable approximation. Epstein presents the process as a continuous one, but without loss of generality, it might as well be considered a discrete progression where the cracks are generated step by step. Then, roughly:

$$y = \lambda_{cr} \frac{\delta T_{crack}}{\phi_{do}}$$

where λ_{cr} $\left[\frac{w}{mK}\right]$ is the thermal conductivity of the crust. This implies that the permeability is of the form:

$$\kappa = \frac{\sqrt{2}}{12} \varepsilon^3 \left(\lambda_{cr} \frac{\delta T_{crack}}{\phi_{do}} \right)^2 \tag{2.28}$$

Then, eq. (2.13) takes the general form:

$$\phi_{do} = \frac{\sqrt{2}}{12} \varepsilon^3 \left(\lambda_{cr} \frac{\delta T_{crack}}{\phi_{do}} \right)^2 g h_{lv} \frac{(\rho_l - \rho_v)}{2\nu_v} \tag{2.29}$$

The exact final derivation is a bit lengthy. More precisely, the Lister-Epstein model reads (taking also account of the upward heat flux at the melt-crust interface ϕ_{up}):

$$\phi_{do} = gh_{lv}\frac{(\rho_l - \rho_v)}{2\nu_v}\left[\beta_{cr}\left(T_{crack} - T_{sat}\right)\right]^3 \varUpsilon \tag{2.30}$$

with $\varUpsilon$:

$$\varUpsilon = \left(\frac{16\sqrt{2}N\alpha_{th}\rho_{cr}^2\left[h_{fs} + c_{p,cr}\left(T_{sol} - T_{sat}\right)\right]^2}{3\left(\phi_{do} - \phi_{up}\right)^2\left[T_{sol} - T_{crack} + \frac{h_{fs}}{c_{p,cr}}\frac{\phi_{do}}{\phi_{do} - \phi_{up}} + \frac{\phi_{up}}{\phi_{do} - \phi_{up}}\left(T_{sol} - T_{sat}\right)\right]}\right)^{\frac{4}{5}}$$

where N is a numerical constant = 0.1 $\left[K \cdot m^{\frac{1}{2}}\right]$, α_{th} $\left[\frac{m^2}{s}\right]$ is the thermal diffusivity of the crust material (calculated with eq. (2.31)), β_{cr} $\left[\frac{1}{K}\right]$ is the linear thermal expansion coefficient of the crust material, T_{sol} [K] is the solidification temperature of the crust material, T_{crack} [K] is the cracking temperature of the crust material (calculated with eq. (2.32)), ϕ_{up} $\left[\frac{MW}{m^2}\right]$ is the heat flux coming from underneath the solidification front (convective from the melt layer, conductive, etc), h_{fs} $\left[\frac{J}{kg}\right]$ is the latent heat of fusion of the crust material,

$$\alpha_{th} = \frac{\lambda_{cr}}{\rho_{cr}c_{p,cr}} \tag{2.31}$$

$$T_{crack} = T_{sol} - \frac{\sigma_{cr}}{E\alpha_{th}} \tag{2.32}$$

where ρ_{cr}, and $c_{p,cr}$ are the density and heat capacity of the crust material.

In the case there is no heat transfer from the bottom part of the crust to the crust itself, as in the case of SSWICS tests, ϕ_{up} would be null, hence eq. (2.30) would reduce to:

$$\phi_{do} = \left(gh_{lv}\frac{(\rho_l - \rho_v)}{2\nu_v}\right)^{\frac{5}{13}}\left[\beta_{cr}\left(T_{crack} - T_{sat}\right)\right]^{\frac{15}{13}}\left(\frac{16\sqrt{2}N\alpha_{th}\rho_{cr}^2\left[h_{fs} + c_{p,cr}\left(T_{sol} - T_{sat}\right)\right]^2}{3\left(T_{sol} - T_{sat} + \frac{h_{fs}}{c_{p,cr}}\right)}\right)^{\frac{4}{13}} \tag{2.33}$$

From his preliminary applications to MCCI situations, Epstein [205, p.4-4] clearly stated that by directly extrapolating "Lister's creep theory...to relatively high-temperature solidified corium, we must conclude that cracking and water ingression due to crust-cooling shrinkage is not possible under the strong convection conditions that prevail within MCCI corium pools". However, Lomperski & Farmer [160] have used the model to compare to the experimental results of the SSWICS tests.

As previously discussed, critical parameters in this model are the mechanical properties of the material, namely here the Young's modulus, and the critical tensile strength. Note that the surface energy, G_{cr}, is not present in this "Lister-Epstein" model, meaning that the energy criterion may not be satisfied. Furthermore, it is recalled that the conductivity of corium-concrete mixtures is also subjected to significant uncertainties.

Figure 2.41 shows the extracted heat flux of the SSWICS tests as a function of the concrete content, compared to the results of the Lister-Epstein model. For the experimental points plotted in the figure 2.41, it is vital to precise their measurement method. For the tests 1,2,3 and 7, the ones showing a plateau, a 200 seconds average of the measured heat flux at a seemingly random time, t=1500 s, was retained. For the other tests, those without plateau, here without clear evidence of water ingression, the reported value is the heat flux taken at the same time. Thus note that all of the presented values are not coming from the same mechanism. More precisely, the heat flux for the plateau-less tests can be entirely linked to conduction limited heat flux. This should explain why the data is very close. This might lead to an erroneous interpretation of the graph as it may be understood that water ingression heat flux presents a plateau for concrete fractions larger than 10-14%.

Nevertheless, the model seems to fit qualitatively well the experimental result. As seen, there is an inflection point around 14% that fits remarkably well the reported experimental results. In fact, the shape of the curves, including the inflection point, comes from the drastic change of the evaluation of the corium thermodynamical properties, in particular, the corium solidification temperature (see figure 2.18). Thus the model leads then to conclude that for these types of material composition, the efficiency is mainly a function of the solidification temperature, the variations of other material properties have a minor impact. Nevertheless, Lompersky and Farmer did not explain why no heat flux plateau could be (clearly) observed at a concrete fraction larger than 8 %. Low extracted heat fluxes should lead to long plateaus, which should, in principle, be more easily observable.

Moreover, the self-propagation mechanism proposed in the Lister-Epstein model leads to an additional critical remark when considering the permeability measurements of 6 of the 7 SSWICS tests, figure 2.27. Considering tests SSWICS 1-3, all with 8 % of concrete, where an almost constant WI heat transfer of around 150-180 $\frac{kW}{m^2}$ could be observed (more or less clearly), the permeability measured should be the same for all tests (κ is a function of the compressibility and local heat transfer). The permeability of test 3 (shown in table 2.2), performed at 4 bar, however, is four times smaller compared to the first two. Thus, as per these tests and measurements, the permeability may not be a direct function of the WI heat transfer, hence directly contradicting even the simplified formulation (without ϕ_{up}) of eq. (2.33). Nonetheless, keeping the hypothesis that the heat flux somehow drives the permeability, it comes to conclude that it is the initial heat transfer, through film boiling at the upper surface in the first phase of contact of water with the melt, that drives the permeability.

Finally, the Lister-Epstein model only gives an estimation of the plateau as a result and does not introduce any notion of the time this plateau might be active, hence giving no explanation of why the heat flux is reduced to a conduction limited one after some time.

It may then be argued that the SSWICS experiments and the Lompersky-Farmer model show some unclear arguments that render the conclusions on the role of water ingression on corium with low concrete content, and its presence in corium with higher concrete content, quite uncertain.

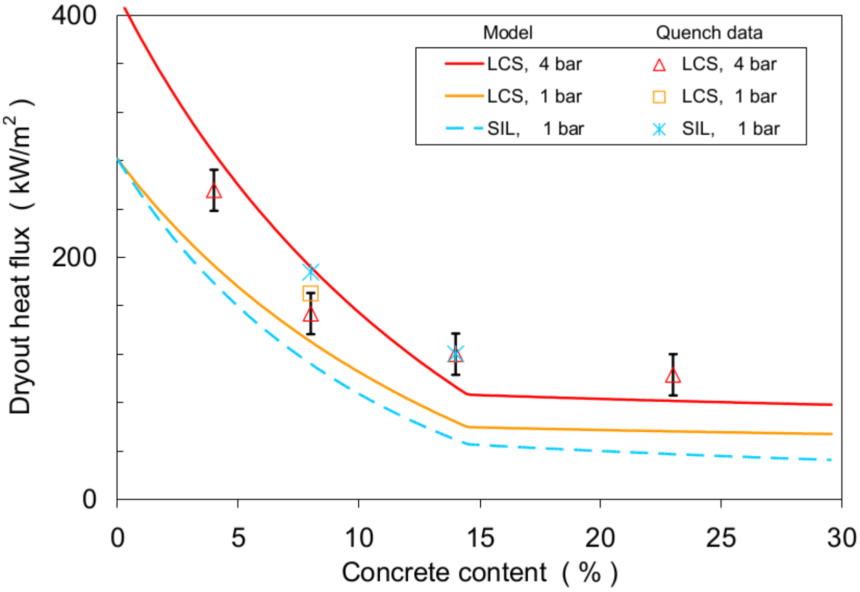

Figure 2.41 – SSWICS test extracted heat flux as a function of concrete content

Taken from: [159]

2.4.3 The Yeo et al. water ingression model

Very recently, Yeo & No [216] proposed a detailed analytical modeling to describe the SSWICS tests. However, the resulting model is intricate, and the solution method is quite elusive. Numerous unclear and crucial assumptions are referred to Yeo's thesis manuscript, which is not readily available [7].

The model proposes a description with 4 stages:

- dry corium melt cooling (by radiation essentially): start of the formation of a crust;
- further cooling of the crust by film boiling;
- fracture of the crust; and finally
- water penetration.

The crust is meshed, with moving boundary at the melt interface, whereas the liquid melt and the environment (air or water on top) are considered as boundary conditions. The essential points here are related to fracture formation and water penetration heat transfer.

The modeling of fracture formation follows partly the description summarized in section 2.4.1. At first, the criterion of maximal tensile strength is used to express the crack length l. However, after some unclear explanation, this depth is set as a constant value taken at 1 mm [216, p.223] , all along the process. The fracture then proceeds step by step per 1 mm. Then the crack spacing is evaluated in order to get the permeability. To do so, an equation similar to eq. (2.25) is derived, except that the integral is

---

[7] The research led to a Korean web site.

computed only for temperature profile. So only constant (averaged) mechanical properties are considered. The formulation also incorporates a fitting constant ξ given at the end to fit the experimental results (figure 2.27). Using the same material properties as those given by Lomperski and Farmer, ξ is set to 60 [216, p.227], which seems quite high for a simple fitting parameter. Note that the value of the used surface energy is not given in the paper. However, the permeability is not used in the following to describe the water ingression heat flux. In fact, the crack spacing is used to evaluate a characteristic size of the "cell" after fracturing ($d_{32} = 1/(4y^{-1} + l^{-1})$). As l is much smaller than y it results that the characteristic size is close to l and so the impact of the complicated procedure for computing the fracture pattern has likely a minimal influence on the overall results of the model.

Indeed, the water ingression heat flux is computed by considering a mixed representation of porous medium and flow in separated cracks. The heat flux from the cracks is computed as $\frac{h_{nb}}{d_{32}}$, leading to an ambiguous interpretation. Furthermore, after some unclear explanation, h_{nb} is taken, again, at the fixed value of 100 $\frac{W}{m^2K}$. All in all, the authors are finally able to retrieve quasi-perfectly the extracted heat flux for the SSWICS tests, including those where a water ingression phenomenon could not be observed. Again, the period of decreasing heat flux after the plateau is not explained.

2.5 Short description of MC3D

Multi-Component 3D (MC3D) is a framework for developing models, called "applications", related to multiphase flows. Developed initially by CEA (the code was then called TRIO-MC, as part of the TRIO set CFD models), then by IRSN, applications were developed, for the most, for describing phenomena related to nuclear safety. Note, for example, an application devoted propane jet flashing [217]. About 10 applications have been developed, but only two are now available in the standard version, both devoted to the description of Fuel-Coolant interaction. The first one, PREMIX, is devoted to the premixing phase of FCI, thus describing the fragmentation and dispersion of a hot liquid corium jet into water. The second, EXPLO, is devoted to the explosion phase, i.e., fitted to describe high shock waves escalating and propagating in a multiphase flow, due to very fine fragmentation and specific heat transfers.

The PREMIX application is quite generalist and can be used, possibly slightly modified (or with some specific options), for various other problems, such as two-phase flow in porous media [181], or the melt dispersion in a DCH event [77]. Thus, the application used in this work is the PREMIX application. PREMIX makes use of a specific field, called JET, to describe continuous (unfragmented) configurations of melt, such as the compact jet or corium pool. In the present case, this field is not used, and the corium, whatever its state, as debris or as compact pool/crust, will be described by the so-called DROPS field, initially fitted to describe fragmented drops of melt or solid balls. Also, in the calculations presented hereafter, the matrix, composed of "drops", is fixed on the mesh, thus avoiding the momentum calculations for this field (and for the jet).

As indicated in its name, MC3D is a 3D Computational Multi-Phase Fluid Dynamics (CMFD) code. As the code investigates in general flow with fast transients and fast boiling, it is based on a semi-implicit model. The eulerian description is used for all phases. In PREMIX, the following fields are available:

- liquid water,
- steam,
- non-condensable gases, considered as perfect gases,
- fuel drops, with possibly a MUSIG like description with several fields having different diameters,
- the continuous corium field, not used during this work.

More details on the numerics can be found in [181].

2.5.1 Heat transfers

As indicated at the beginning of this chapter, two-phase heat transfers in debris beds and fractures have not been investigated experimentally, except with the recent work by Sapin [194] and Gourbil [195]. One of the only indications currently at disposal comes from this last work, which tends to hint that heat transfer should occur, for the most part, under the film boiling regime, and that the heat transfer itself is not much affected by the presence of bubbles.

Thus, the standard models of the PREMIX applications should be preserved, possibly with some slight adjustments. In the bubbly configuration, the heat transfer models also make the hypothesis of cooling of the melt particles, and so the film boiling is the primary heat transfer, down to the minimum film boiling temperature (T_{sat} + 100 in PREMIX for saturated flow), where a simple transition to 1-phase convection is imposed. Thus nucleate boiling is not taken into account. A previous attempt to incorporate such a regime did not show any decisive impact from the comparison of calculations with reflooding experiments.

Film boiling is a crucial point for the FCI, and lots of work has been done in order to provide state-of-the-art modeling. In particular, the pool boiling situation (low Reynolds flows) is modeled with attention and verified on dedicated experiments.

PREMIX considers the configuration map depicted in figure 2.42, where according to the local gas saturation, the flow is considered as "bubbly", below a threshold denoted α_B, and as "droplet-flow", beyond a second threshold α_D. In between, a composition of the two configurations is computed. In the bubbly flow, the drops (porous medium) are entirely in contact with the water, via a vapor film. In the droplet-flow, the drops are all in contact with the gas. Nevertheless, a drop-drop heat transfer is considered.

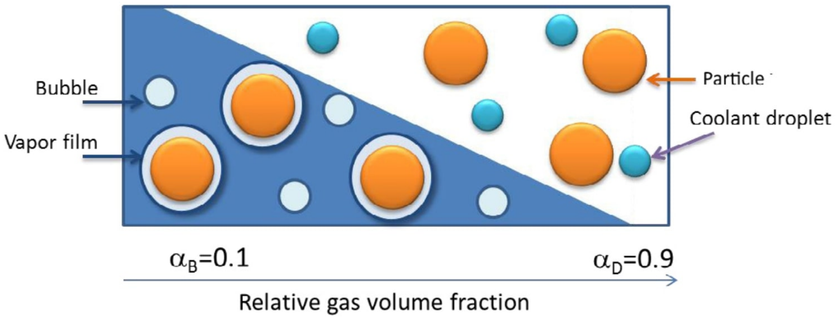

Figure 2.42 – MC3D flow configuration map as a function of the relative void fraction, i.e. gas saturation

The model also offers a quite complex calculation for the internal heat transfer around bubbles and drops. As the flow is mostly at saturation temperature, the bubbles have a weak impact, thus making it possible to be neglected. In contrast, the liquid droplet may evolve in a rather hot vapor (uncooled region). The fragmentation model is likely unable to account for the impact of this last with the porous medium, but no specific attention was paid. Instead, the droplets are set to a small parametric value (100 μm) to ensure they can rapidly exchange their heat.

2.5.2 Friction laws

As previously stated, MC3D is similar to a platform for the development of a multiphase flow models. Hence, the momentum equation is much more complete than necessary in general for flow in porous media. The generic equation for the component "i" are written at the faces delimiting the cells as:

$$\bar{\alpha}_i\bar{\rho}_i\frac{\partial\overrightarrow{V_i}}{\partial t}+\tilde{\alpha}_i\tilde{\rho}_i\left(\overrightarrow{V_i}\cdot\nabla\overrightarrow{V_i}\right)=-\bar{\alpha}_i\overrightarrow{\nabla}P+\bar{\alpha}_i\bar{\rho}_i\overrightarrow{g}-K_{i,j}\left(\overrightarrow{V_i}-\overrightarrow{V_j}\right)+M_{add} \tag{2.34}$$

where α_i is the volume fraction of component i, the subscript j stands for the other present components, $\bar{.}$ is the averaged quantity of the two adjacent cells, $\tilde{.}$ stand for the convected quantity (e.g., upstream value), $K_{i,j}$ is the friction coefficient between components i and j, and M_{add} is for various additional effects such as drift or added mass, not relevant in the present case.

MC3D contains several available friction laws in the compact melt configuration (porous medium), see [181] for details. The code also includes dedicated formulations for interfacial liquid-gas frictions. But, as will be seen, they generally have a moderate impact on the problems in the scope of the present work. For the relative permeabilities and passabilities used to calculate the two-phase fluid-drop frictions, most of the calculations have been made with the Ergun formulation using Reed coefficients (presented in table 2.4). Nevertheless, the preliminary calculations were performed with the Schulenberg formulation [179], presented here as:

Later, it appeared that using Reed's formulation is more satisfactory, and the evaluations made in the second part of the work were done with it.

Table 2.7 – Schulenberg's formulation for relative permeabilities and passabilities

Phase	$\boldsymbol{\kappa_{r,i}}$	$\boldsymbol{\eta_{r,i}}$
Liquid	$(1-\alpha)^3$	$(1-\alpha)^5$
Vapor	α^3	$0.1(1-\alpha)^4$ if $0 < 1-\alpha < \sqrt{0.1}$ $(1-\alpha)^6$ if $\sqrt{0.1} < 1-\alpha < 1$

It must be highlighted that the code does not take into account the capillary effects. The choice was made not to incorporate them as long as the verification of the accuracy of the available models is not demonstrated, for the problems that have to be investigated, with reflooding fronts, and flow configurations as film boiling. Regardless, the analysis performed in the present work indicates that the effect should be rather minor in general.

The specific challenge that is imposed by the friction formulations regarding, at least, the numerics for the computation of the frictions close to sharp changes of saturation or medium characteristics. Details can be found in appendix A. Nevertheless, in general, the difficulty comes due to the highly nonlinear form of the friction laws with respect to the void fraction.

Raverdy et al. [181] provided a synthesis of verification of the models and their capabilities. More recently, the use of MC3D's DEBRIS model was also verified against the bottom reflooding situation with heterogeneous debris bed, from comparison to the PEARL experiments [128], [218]. The model can adequately evaluate the deviation of the flow, as seen in figure 2.43, that may occur in case of important difference of temperatures or debris diameter, as a function of the ambient pressure. In fact, the problem of bottom reflooding appears quite simpler than the opposite case. This is due to the fact that bottom reflooding, in general, occurs with a forcing of liquid flux. The top reflooding is driven by gravity and is then much more sensible to the local phenomena and pressure fluctuations. This is likely the reason why no communication could be found in the literature on this issue.

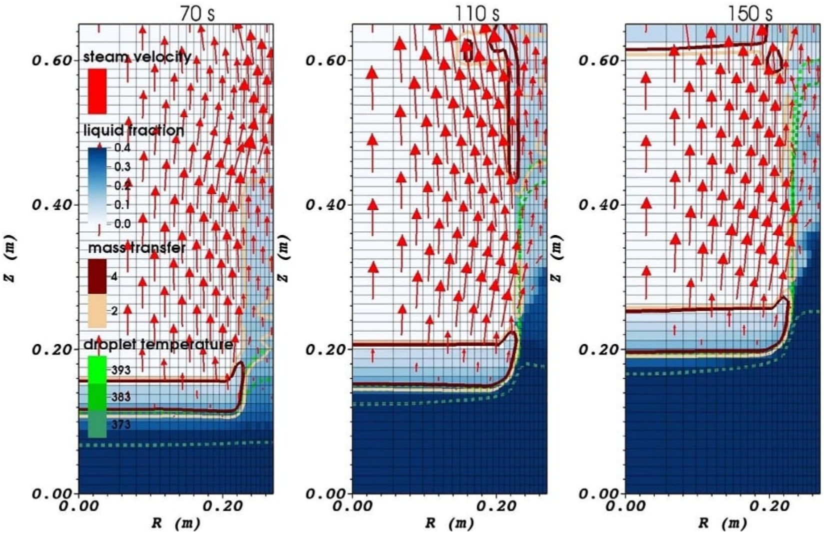

Figure 2.43 – MC3D simulation showing the capability of the code to correctly evaluate the deviation of the flow found in the PEARL PA_2 test. Three distinct time snapshots showing steam velocity (vectors), liquid fraction (field), mass transfer between liquid water and vapour (solid curves; values in $\frac{ks}{m^3 s}$) and droplet temperature (dashed curves; values in K).

Takes from: [218]

2.6 Conclusions

The complex nature of MCCI phenomenology represents an essential challenge for the proper evaluation of the stability of the expected configurations. Vis-a-vis the limited conditions in which existing models have been validated, and experimental research has investigated, the need to establish the governing mechanics to extrapolate to accidental scenarios correctly has been highlighted.

For debris beds, extensive experimental and theoretical investigations have explored the stationary initially-flooded ability of the layer to extract heat. Naturally, the first question that arises is if the penetrating front is stable. It is not evident if the specific flow patterns (instabilities) found in the basic configuration of one fluid overlaying another, likewise observed experimentally in a porous medium in the context of hydro-geology, will prevail when evaporation and residual power inside the medium are taken into account. Furthermore, the effects of the flow configuration on the ability of the initially-dry heated debris bed layer to extract heat have not been solved. In general, the expected initial conditions in the debris bed (high initial temperature, varying permeability, etc.) leads us to question the validity of the models found in the literature when applied to the MCCI context.

For water ingression, the governing dynamics are even more elusive. Elemental questions can be posed from the start when analyzing the experimental results. It has been presented that the underlying mechanism of fracturing that governs the permeability in a fractured porous media is far from conclusive. The validity of the available formulations, in particular the Lister-Epstein model, has to be analyzed with respect to the considerable uncertainty of material properties, which are themselves scarce or non-existent. Moreover, the current methodologies to calculate the properties of the composite materials (species mass or volume-weighted average) involved in the MCCI context are also highly dubious regarding the heterogeneity of the properties as a function of the temperature and the vast difference between the individual materials in the mixtures. Adding to this, the presence, or lack thereof, a plateau where the phenomenon "has been identified" leads to questions of temporal scale where there could be an increment in heat extraction via this mechanism. The lack of plateau with increasing concrete-content corium (as expected in an accidental scenario) also conveys further incertitude in the existence of the phenomenology itself. What can be expected, or what should be used if the residual power is also included in these high concrete corium mixtures? Furthermore, acknowledging that extensive experimental investigations are not likely to be pursued, from the modeling point of view, can water ingression be correctly approximated using a dry-out heat flux debris bed formulation by adjusting the permeability?

Chapter 3

Preliminary Analysis of Top-Reflooding

Contents

As previously stated, the particular situation of interest expected in an ex-vessel scenario is a layer of corium in a range of different configurations overlaying a concrete content. The two specific configurations that will be studied, namely a super-heated initially dry debris bed and a fractured porous media, are both expected to be subjected to a residual power.

In view of the lack of further experimental data to study the top-reflooding configuration of a dry-superheated heat-generating debris bed, the purpose of this chapter is to first present in section 3.1 exploratory numerical simulations are presented with the help of the MC3D code. Afterwhich, an in-depth analysis of the MCCI SWWICS and CCI test dedicated to the water ingression phenomenon in the fractured corium crust configuration is presented in section 3.2.

3.1 Penetration in debris beds: preliminary simulation of the Ginsberg experiments

On the basis of the geometrical configuration and initial conditions of the tests performed by Ginsberg, a first input file used to perform MC3D calculations was constructed, here schematized in figure 3.1. The input file consisted of a cylindrical simulation with 12 radial meshes covering the extent of the radius of the experimental test section (54mm) and 60 total axial meshes (40 10mm meshes and 20 meshes with progressively increasing height at the top). The 300mm height debris bed, red zone in figure 3.1, was simulated using MC3D's DEBRIS model, and further fixing the zone (not calculating the momentum equations for the steel spheres) not allowing the "steel spheres" to move. The diameter of the steel spheres, d_p=3.18 mm, the porosity of the debris bed ε=0.401, the initial temperature, T_0=900 K, and the pressure in the domain P=1 atm were taken from experimental initial conditions. Two boundary conditions, orange and dark blue zones at the top of figure 3.1, were used to simulate the water input and the vapor outlet, and maintain the pressure conditions inside the domain at 1 atm. As in the experimental test section, the bottom of the domain was closed to allow water accumulation. Furthermore, an initial quantity of water at saturation temperature was allowed to fall on top of the debris bed to initiate the water penetration, light blue zone in figure 3.1.

In order to better study the water penetration, two small modifications were made from the standard default MC3D version available at the time of simulations (MC3D V.3.9.1). The limits for the flow chart shown in figure 2.42 were changed. α_B was changed from 0.1 to 0.01, whilst α_D was changed from 0.9 to 0.99. This was done with the purpose of eliminating the effect of the transition that would occur at relatively low values of α that could impact the results. Nevertheless, in contrast, more recent evaluations discussed in the next chapter were made with $\alpha_B = 0.5$, thus enhancing the debris-water contact and so the debris-water heat transfer. In any case, these changes are inducing in general second-order impacts on the simulations.

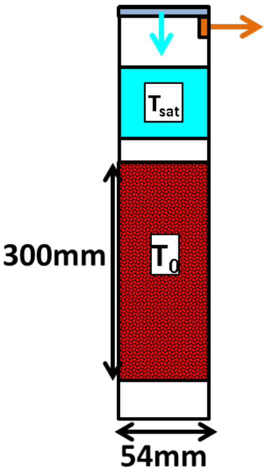

Figure 3.1 – Ginsberg MC3D input file scheme. Debris bed using MC3D's DEBRIS model as the red zone, with the location of the initial boundary conditions at the top and the water at saturation temperature as the light blue zone

Also, the numerical limit for the friction factors in the DEBRIS zone was decreased from 2E+8 to 2E+7 $\left[\frac{kg}{m^3 s}\right]$ (factor $K_{i,j}$ in eq. (2.34)). The formulation of the relative permeabilities and passabilities used to calculate the friction, presented in table 2.4, are highly non-linear, and as can be seen in eq. (2.4) divide the term hence tend to lead to artificially high friction values when the saturation of a phase is low. This posed a problem since, in the cell further down from where the front was located, the values of the liquid saturation were low. Hence the friction was numerically high, in turn restricting the advancement of the front. The reduction of the maximum friction value tends to facilitate the progression of the water in dried cells. Again, in the calculations performed in the next chapters, this modification was improved for a better understanding. This was done by imposing a minimum saturation for the calculation of the relative permeabilities and passabilities instead of directly limiting the friction factor.

Figures 3.2 to 3.7 show the results of a characteristic simulation with $d_p = 3.18mm$, at different times. Each figure plots the liquid relative volume fraction (water saturation [-], or TXLIQREL in the figures) contained in the cell in the left part, the temperature of the debris bed (T_0 [K]) in the middle part and the superficial vapor velocity (j_v in $\left[\frac{m}{s}\right]$) in the rightmost part. As can be seen, preferential water channels develop after an initial penetration of the overlying water. Most importantly, the water penetration through the new-formed preferential channels is found to flow in a two-phase configuration. This last can be inferred by looking at the water saturation in the fingers, and non-negligible vapor superficial velocity (positive means flowing upwards) inside the same channels. In other words, counter-current flow within the fingers and single-phase vapor flowing in the dry zones. This is in disagreement with Ginsberg's interpretation, figure 2.8, where the fingers are composed of pure water and the generated steam escape through the gas channels between the water fingers.

Similarly to the Ginsberg's and Cho et al. observations, two quenching phases can be clearly distinguished. A first penetrating phase and a second upward phase governed by the accumulation of the water flowing through the fingers.

Nevertheless, the finger evolution can also be seen to be limited in these preliminary calculations by the meshing. Once a finger has formed, it follows the mesh. This leads to question if the flow configuration found in the results of these simulations represents physical phenomena or is a direct numerical result by the lack of sufficiently refined meshing.

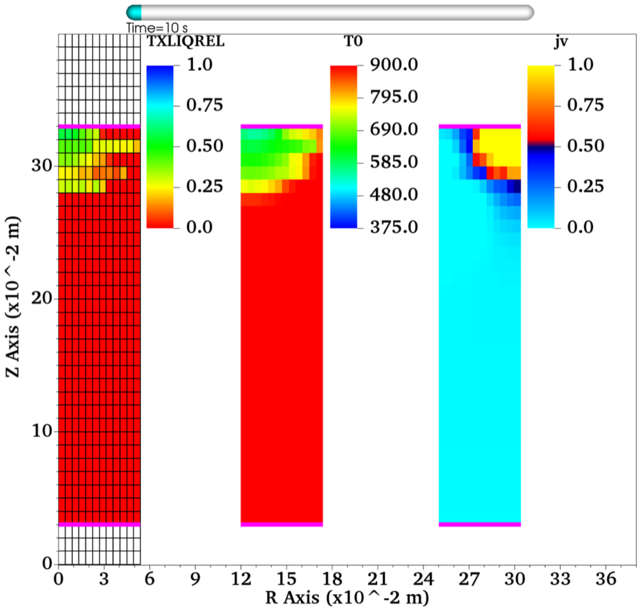

Figure 3.2 – Ginsberg calculation with $T_0 = 900K$ and $d_p = 3.18mm$ at t=10s

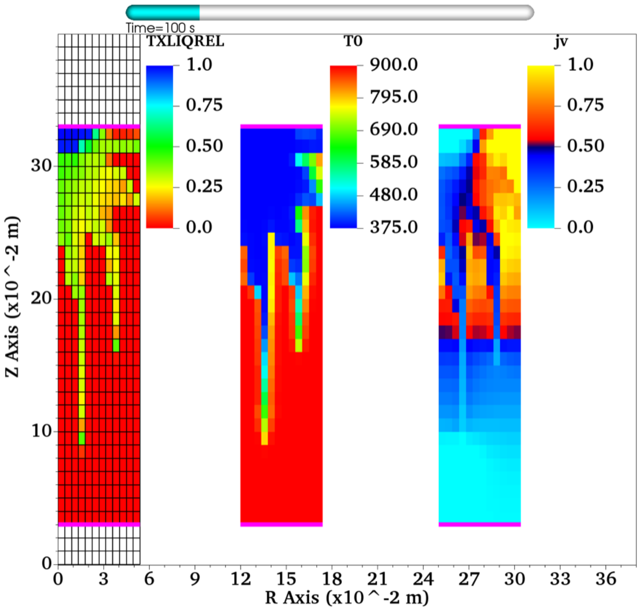

Figure 3.3 – Ginsberg calculation with $T_0 = 900K$ and $d_p = 3.18mm$ at t=100s

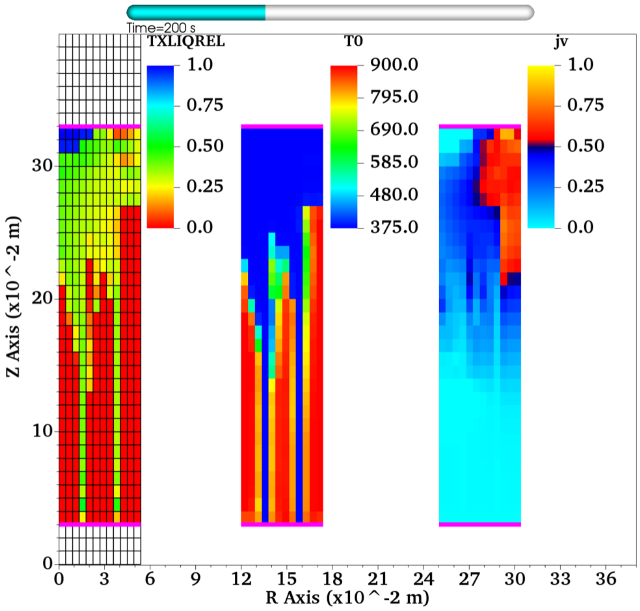

Figure 3.4 – Ginsberg calculation with $T_0 = 900K$ and $d_p = 3.18mm$ at t=200s

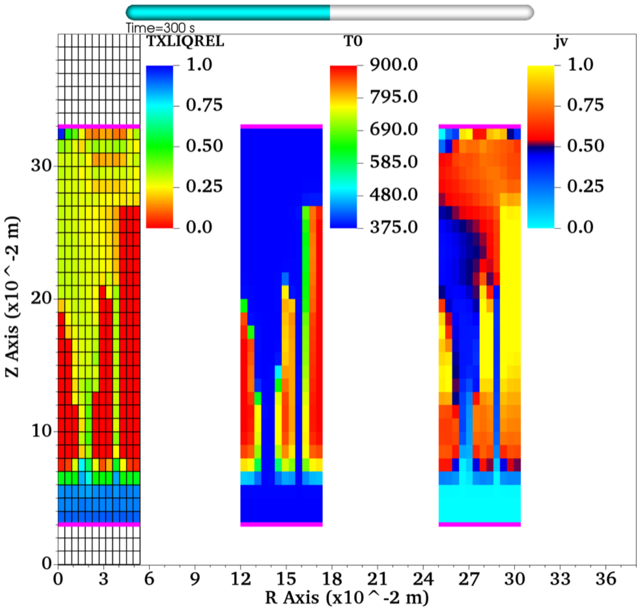

Figure 3.5 – Ginsberg calculation with $T_0 = 900K$ and $d_p = 3.18mm$ at t=300s

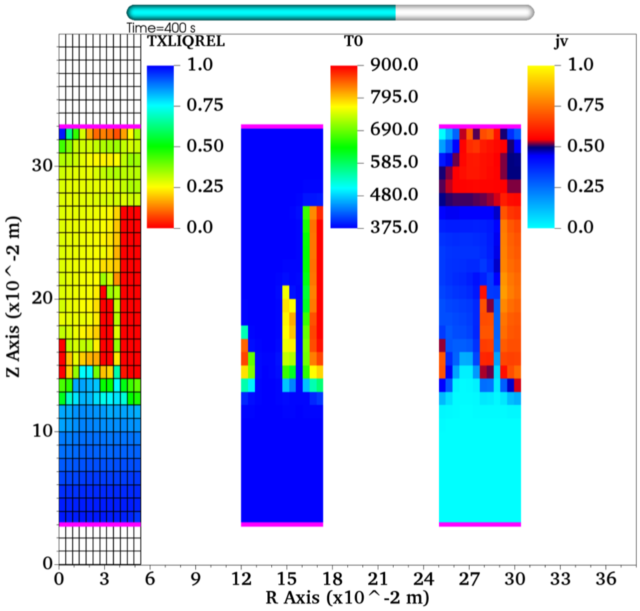

Figure 3.6 – Ginsberg calculation with $T_0 = 900K$ and $d_p = 3.18mm$ at t=400s

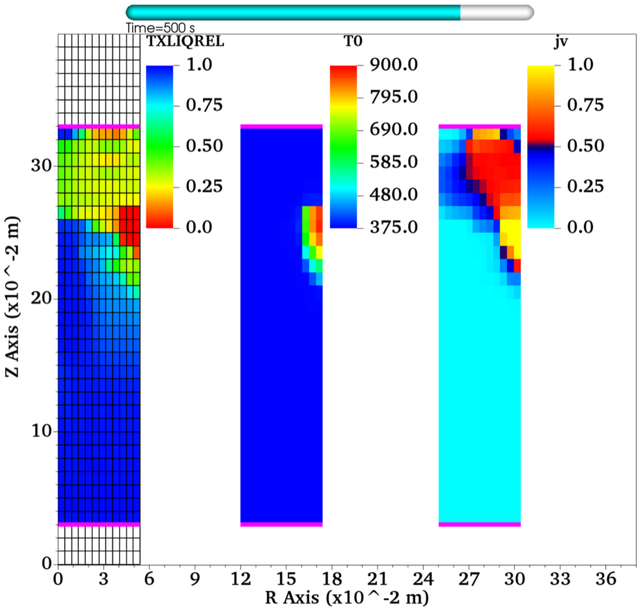

Figure 3.7 – Ginsberg calculation with $T_0 = 900K$ and $d_p = 3.18mm$ at t=500s

Further preliminary meshing tests were made by refining the radial meshing in order to try and obtain a dimension of the characteristic width of the water channels without success. This study was reattempted later with improved code modifications and is discussed in the chapter dedicated to 2-dimensional effects.

Although no convergence could be obtained regarding the precise flow structure, it is remarkable that the global behavior regarding heat extraction rapidly converges. Figure 3.8, plots the extracted heat flux with five different meshing as a function of time. As can be seen, the overall behavior of the different meshing does not significantly affect the extracted heat flux. It is important to note that for the calculation using one radial mesh, the beginning is different since, due to numerical problems, the water did not penetrate until later (at around 100 seconds), but converges to the values found with other meshing. The oscillations in the curves are due to the repetitive cycles of the water going in, evaporating, and restricting water to come in (by pushing the overlying water pool with the generated vapor).

The overall quenching time is slightly affected since the end of the first downward penetrating phase and the second upward phase are slightly modified. This is due to the fact that with the larger numbers of meshes, more radial meshes were already quenched during the first phase with respect to the original meshing. In other words, once the second phase began, a more substantial proportion of the debris bed had already been quenched, leading to a faster accumulation. For the calculation with one mesh, the second phase is nonexistent since the bed is completely quenched by the time the water penetrated the entire length of the bed (not shown in the figure).

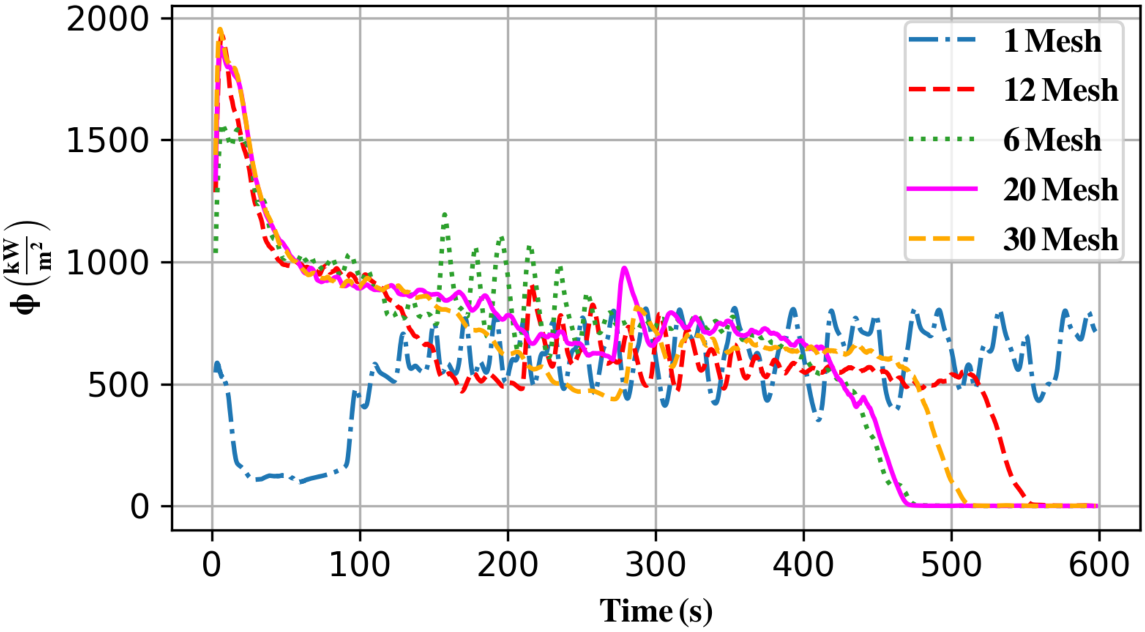

Figure 3.8 – Extracted heat flux in Ginsberg calculations with $T_0 = 900K$ and $d_p = 3mm$ at t=150s with different number of radial meshes

Using the original meshing (12 radial meshes), preliminary calculations of the influence of the temperature were also made. Figure 3.9 plots results of these calculations at the same time, t=100 s, for five different initial temperatures: T_0 =523, 623, 773, 923, and 1600 K. As can be seen, the front advancement is, as expected, slower with increasing temperature. In the figure 3.9, the calculation with $T_0 = 523K$ (leftmost) the quenching is in the second upward accumulating phase. Furthermore, at low temperatures, the water finger seems to be wider. Nevertheless, the appearance of the fingers at lower temperatures may be suppressed by the velocity of the advancing front. In other words, the characteristic time of appearance, and the width, of the water fingers might be offset by the size of the domain here calculated.

This last might be appreciated in figure 3.10, which plots the state of the penetrating fingers at the moment when the front reaches the bottom of the domain. At low temperatures, the appearance of advancing water fingers seems to be at the lowermost meshes, whereas with increasing temperature, the fingers appear and dominate the penetration, starting from higher meshes.

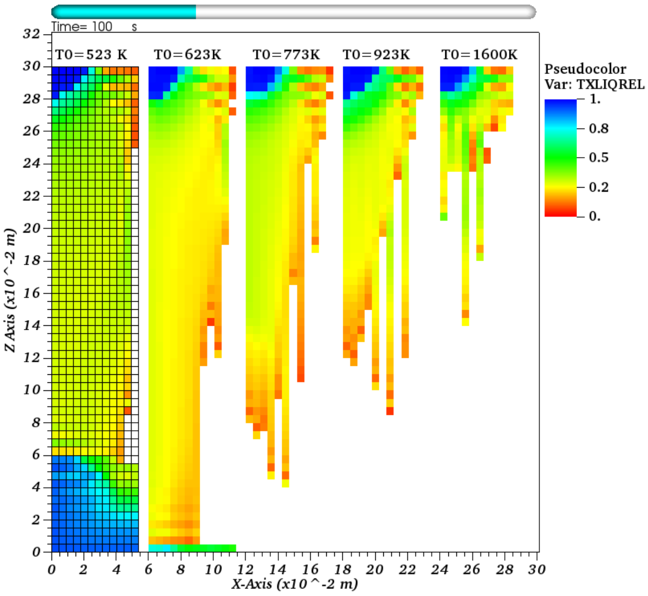

Figure 3.9 – Ginsberg calculations with different T_0 and $d_p = 3mm$ at t=100s showing the front location and the liquid saturation

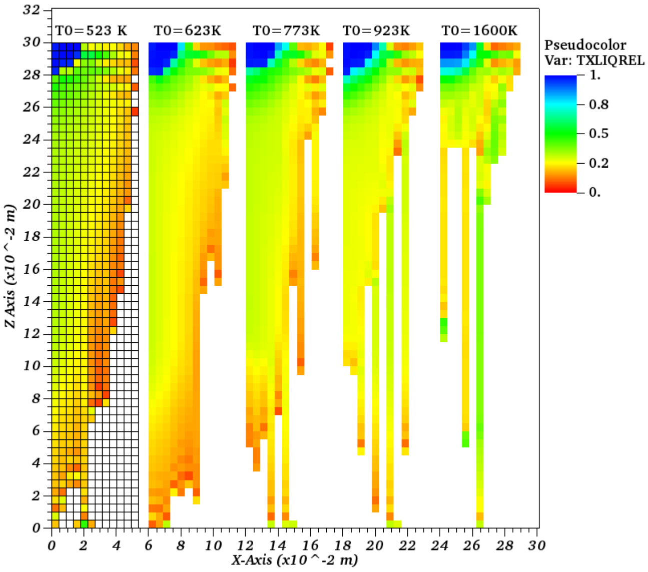

Figure 3.10 – Ginsberg calculation with $d_p = 3mm$, and T_0 =523, 623, 773, 923, and 1600 K showing the liquid saturation at t= 50, 80, 120, 145, and 250 s respectively

Figure 3.11 plots the extracted heat flux as a function of time for the calculations with different initial temperatures. For the lower temperatures, the extracted heat flux is slightly lower than for the rest of the calculations. This might be due to the low energy contained in the debris bed as compared with the higher initial temperature calculations. Furthermore, the lack of manifest presence of water fingers in the low-temperature calculations might restrict the extraction of energy.

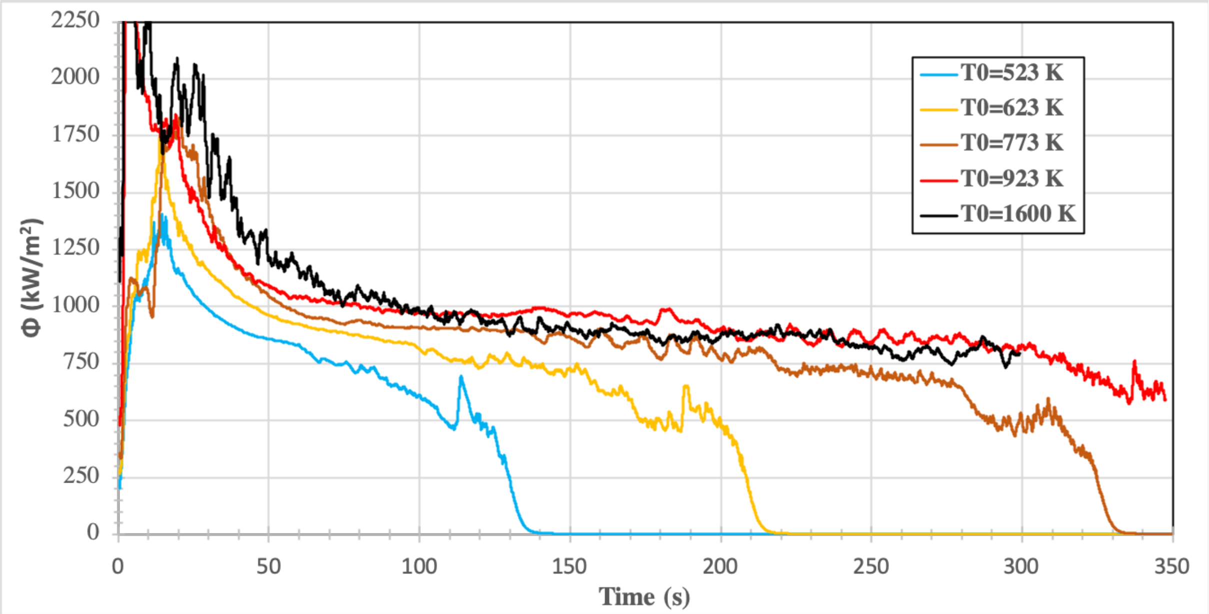

Figure 3.11 – Extracted heat flux in Ginsberg 1D calculation with different T_0, $d_p = 3mm$

From the preliminary calculations, in general, the appearance and configuration of the water fingers, and the extracted heat flux, were found to be affected by the initial temperature of the debris bed. Moreover, regardless of the meshing, the water penetrating the debris bed was found to flow in a two-phase configuration with a relative water saturation of 20 -30%.

Acknowledging that the configuration of the water fingers is impacted the meshing, the extracted heat flux remains relatively the same. In other words, for the cases without residual power in the debris, one-dimensional calculations could be used for first-order approximations regarding the extracted heat flux. For this reason, 1D calculations and analysis will be performed in Chapter 4 to study the limits and the governing dynamics of the penetrating water. Nevertheless, the configuration proves vital to study the stability of the configurations of interest. Hence more in-detail 2D calculations and analysis will be presented in Chapter 5.

3.2 Penetration in fractured crust

The particular configuration observed during several experiments of a distinguishable fractured crust is of significant interest for evaluating the cooling capabilities of corium pools. Figure 3.12 schematizes the expected configuration, where due to thermal stresses, and quite possibly others, a solidified, but hot, layer would continue to cool down and hence shrink. During this process, fractures in the material would form, allowing the partial water percolation. Nevertheless, the temperature of the material, far from the water temperature, would, in principle, impede or at least restrain the percolation of the water. Furthermore, depending on the nature of the formation, the layer is expected to be a more or less porous material. The continuous presence of a thermal gradient between the quenched part of the crust and the bottom interface with the corium pool signifies that the material also conducts a certain amount of energy towards the quenched part. In other words, as seen in the figure, there is a competition between the fracturing of the crust material, hence the hydrodynamics of the counter-current flow through the pores and newly-formed fractures, and the conductive heat flux that traverses the crust. As presented before, this configuration is the object of recent, and current, analytical, and experimental studies.

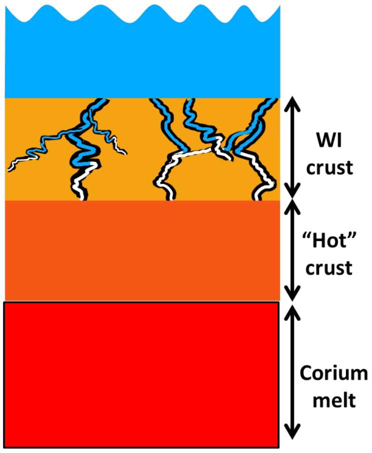

Figure 3.12 – Water ingression configuration scheme

3.2.1 Analysis of SSWICS experiments

It is reminded that the significant available specific experimental results using prototypical corium were obtained by Lomperski, Farmer, and co-workers in the frame of the OECD MCCI program [160], [219]. They investigated the cooling of mixtures of corium and concrete slag by water injected from the top in a cylindrical test section. To reduce the phenomenological complexity, the cavity receiving the corium was protected by a MgO layer, so that no degradation of the test section occurred. However, the system was subject to important heat losses on the bottom and on the side since MgO conductivity is rather high. Also, no sustained power was introduced in the corium to simulate residual power, so the experiment results should not be directly extrapolated for safety evaluations, and the applicability of the models for a real situation should be justified with care. The corium was a mixture of UO_2/ZrO_2 formulated to have a core-to-cladding oxide mass ratio of 2.44 with added concrete of two types: LCS, i.e., limestone with a high content of calcite ($CaCO_3$), and SIL, i.e., siliceous, with a high content of silicon oxide. Four different concrete mass fractions in the corium mixtures were considered: 4, 8, 15, and 25 %. Finally, two ambient pressures were used: 1 and 4 bars. The heat flux through the crust is obtained by an indirect measure of the vapor flux produced by water boiling.

The figure 2.26 is reproduced from [219] and reports the measured heat flux for the first 7 SSWICS tests. The legend directly indicates the nature of the concrete, mass fraction, and ambient pressure. For all the tests, but the n°6, there is an unclear first period with a peak, then a sharp decrease towards a nearly null flux, and a second increase. The 0-flux period is, in fact, attributed to the period of water injection in the test section. The released heat flux is then partially consumed during this period by the heat up of water up to saturation.

In 3 of the 7 tests (n°1, 3, and 7), a more or less clear heat flux plateau can be observed, which is interpreted as the result of water ingression in the crust. In contrast, the tests n°4, 5, and 6 show a heat transfer very similar to pure conduction. The figure also shows the results of a simulation by the authors assuming purely conductive heat extraction, taking into account the heat losses in the experiments. This result was supposed to demonstrate the effectiveness of water ingression in any situation, as the conduction-limited heat flux is, from the simulation, largely below the experimental heat fluxes. However, as discussed in section 2.2.4, Lomperski and Famer used a conduction coefficient of 1.25 $\frac{W}{mK}$, which seems rather small as the corium conductivity is more often considered to be in the range from 2 to 3 $\frac{W}{mK}$. Clearly, doubling the conductivity coefficient results in comparable heat fluxes for the conduction-limited case and for tests 4, 5, and 6. In fact, the conclusions from Lomperski and Farmer are not so clear as they stated that "these three heat flux curves all resemble the conduction-limited solution, which would be expected if water ingression played a minor role in cooling. Still, the corium crack structure for these tests was found to be similar to that of the other, higher heat flux tests, suggesting that even for these low heat flux tests, water accounts for a significant portion of the difference between the measured heat flux and the conduction solution" [160, p.911]. However, the mechanism of how a limited water ingression would increase the extracted heat flux as compared with conduction was not clarified. Nevertheless, they considered that water ingression occurred in any case and reported the WI flux as being the one measured in the period following the water injection period (vertical dashed line). Then, from their interpretation, the tests with the highest amount of concrete showed similar WI heat flux, around 100 $\frac{kW}{m^2}$. In this work, the results are considered to be not sufficiently clear and decisive to draw such conclusions. In the case of test n°2, no real plateau was observed, but the high level of extracted heat flux leads to consider that water ingression occurred to some extent, and the measured peak heat flux should provide a reasonable approximation.

Recalling the preliminary and conservative conclusions, water ingression was observed only for the mixtures with 4 and 8 % of concrete, whereas a conductive transfer occurred for tests with 15 and 23 %. Regarding the measured heat flux, it may be noted that tests 1, 2 and 3, with 8 % of concrete led to comparable levels between 150 and 180 $\frac{kW}{m^2}$, whereas test 7, with 4 %, led to a noticeably higher flux of about 250 $\frac{kW}{m^2}$, so, again, an important impact of the concrete mass fraction. Last, it is essential to highlight that the slow decrease following the WI plateau in tests 1, 2, 3, and 7 was not be explained by Lompersky and Farmer. Following the Lister-Epstein model, the water ingression process should continue up to the complete cooling since the heat flux produces the permeability, which permits, in turn, a given level of heat extraction. A clarification is then needed on this point for the consideration of the validity of the interpretations and models.

For 6 of the SSWICS tests, the permeability was determined by the measure, after the test, of water flow through the ingot, with the assumption of Darcy flow. The two graphs of figure 3.13 show these measurements as a function of the concrete nature (limestone and siliceous) and the ambient pressure (1 or 4 bars). The most unambiguous tendency is the diminution of the permeability with increasing concrete content. The primary reason is not so apparent and will be re-discussed. Regarding the characterization of the impact of the two other parameters (concrete nature and pressure), the limited number of points does not permit unambiguous conclusions. It may be stressed, with intense uncertainty, that the nature of the concrete has a low impact, whereas the ambient pressure has a noticeable influence. The origin of the role of pressure is also not so clear and may be related to the two-phase flow characteristics and hence be explained by its impact on heat transfer, on which the crack spacing depends. This is indeed the hypothesis of the Lister-Epstein model. However, considering the three first tests, all with 8 % of concrete, an almost constant WI heat transfer of around 150-180 $\frac{kW}{m^2}$ could be observed (more or less clearly) whereas permeability varies by a factor of about 5. Thus, it may be concluded, on the contrary, that the permeability is not a direct function of the WI heat transfer (the WI heat flux is in contrast expected to be a linear function of the permeability). Nevertheless, the dependence with pressure necessitates the hypothesis that the permeability is driven by the heat flux. A possible solution for this contradictory statements is that it is the initial heat transfer in the first phase of contact of water with the melt, through film boiling at the upper surface, before ingress of the water in the crust, that drives the permeability.

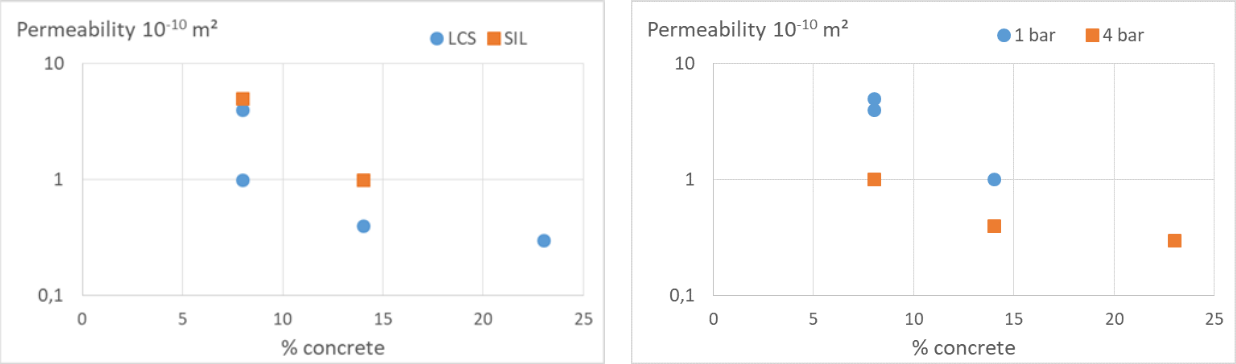

Figure 3.13 – Measured permeability of the SSWICS ingots after tests. Left: impact of concrete nature; right, impact of ambient pressure. Data from [219]

As already discussed in the chapter 2, Lompersky & Farmer applied a model initially developed by Lister [215] and extended by Epstein [205], [206] to describe the SSWICS results. A first remark is that the model is used to describe both the cases with identified WI period, as well as those, quite doubtful, without direct WI observation. The model shows a decreasing heat flux with the amount of concrete, up to a plateau, or a slowly decreasing region for concrete fractions larger than about 15 %. This change in regime of the model is attributed to the change of solidification temperature in the corium-concrete mixtures, the solidus reaching a plateau at about 2000 K for the same concrete fraction (see figure 2.18). A second source of uncertainty in the application of the model was already commented while discussing the measured permeability. Again, the Lister-Epstein model postulates that the permeability is a direct function of the water ingression heat flux, which seems to contradict the experimental results.

Furthermore, recalling that the permeability in the Lister-Epstein model, eq. (2.30), depends on the material properties, the slight variation in the properties for SSWICS-3 and 4 presented by Lomperski & Farmer [160] (specially β=8.1, and 7.3 $\times 10^{-6}$ $\left[\frac{1}{K}\right]$ for SSWICS 3 and 4 respectively), is not sufficient to account for the variation in the measured permeability (factor 3.5-4 comparing SSWICS 3 to SSWICS-4). Indeed, the permeability calculated using the fracturing mechanism explained in section 2.4.1, on which the Lister-Epstein model is based upon, does depend on β, but so should it depend on G_{cr} and E. Even more so, the dependency of the material properties to temperature is not accounted for in the evaluation of the SSWICS tests. The importance of the temperature dependency is particularly evident in the value of E since for some of the constituents of prototypical MCCI corium (i.e., the limestone in the concrete), the property changes by a factor of 30 in the range of temperatures of interest [214]. Nevertheless, neither G_{cr} nor β nor E are properly characterized for prototypical corium. Figure 3.14, plots the post-mortem configuration of SSWICS tests 3 & 4 (same type of concrete and pressure but different concrete content) as viewed from the bottom. In it, it can be seen that the overall morphology of the fractures remains relatively the same. The space between the fractures seems to be the same; on the other hand, the "thickness" of the fractures is not since for the SSWICS-4 test, the test with higher concrete content (23% vs. 8%), the fractures appear to be thinner. This last can serve as an indication of the influence of β in both tests, which should have a substantial impact on the permeability, not reflected in the properties presented in [160].

Figure 3.14 – SSWICS-3 & 4 post-mortem configuration viewed from the bottom. Left: SSWICS-3 with 8% LCS concrete, Right: SSWICS-4 with 23% LCS concrete

Adapted from: [160, p.916]

To conclude, the situation is quite conflicting, with experimental evidence of the phenomenon's existence, but apparent difficulties characterize it precisely. Summarising:

- the phenomenon is well-identified only for limited amounts of concrete in the corium;
- the absence of direct observation for large contents is not explained;
- the slow heat flux decrease following the WI plateau has not received any explanation either;
- permeability measurements indicate an impact of the ambient pressure which should come from the surface heat flux, not the water ingression heat flux itself;
- the Lister-Epstein model yields result contrasting the experimental observations.

For these reasons, a clarification for the interpretation of the SSWICS experiments, the modeling, and the extrapolation to the real situation is needed.

3.2.2 Analysis of the CCI experiments

As mentioned in section 2.2.4, some of the Core-Concrete Interaction experimental program (CCI) tests were designed to study the water ingression phenomenon in prototypical conditions. Compared to SSWICS tests, CCI tests get closer to the expected real case scenario. Firstly, and probably most importantly, CCI tests include concrete ablation. This not only changes the corium pool material properties but also makes it challenging to pinpoint the governing mechanism throughout the course of the test. Secondly, CCI tests include the simulation of residual power via direct electrical heating of the corium. It is important to recall that this last is only introduced in the liquid parts of the corium, whereas in a real case, the residual power would also be present in the already solidified parts, here the crust or the debris bed. Furthermore, SSWICS and CCI differ in the test section dimensions, hence entailing possible scale effects difficult to characterize due to the limited available data. Finally, extrapolation of the SSWICS results in CCI tests is questionable since as contrary to CCI tests, in SSWICS, the crust, once formed, only evolves in a particular way through the propagation of the cracks via the effects of its thermal constraints as explained in section 2.4.1. In CCI, both the addition of material into the crust and the heat transferred to its bottom part would greatly modify its evolution. Additionally, in the CCI tests, it is not possible to evaluate the crust conditions throughout the course of the tests; hence the post-mortem results would probably show the crust in a different state as to the one that would eventually be involved during the WI phenomenon.

3.2.2.1 Previous tests: CCI-7 & 8

CCI-7 and 8 tests conducted between 2012 and 2015 consisted of 2D tests designed for studying water ingression and melt ejection phenomena, respectively. A summary of their characteristics was given in table 2.3. Figure 3.15 plots the extracted heat flux as the discontinuous red curves and the input power as the blue curve for CCI-7. As can be seen, during the late part of the test, beyond the period labeled as "apparent melt eruption", a high heat flux of $\sim 300\frac{kW}{m^2}$ can be observed, anyhow lower than the input power. Post-mortem chemical analysis found that the concrete content in the crust was close to 33%. Thus, as per the results of the SSWICS tests, the high heat flux found here is rather uncharacteristic for a test with a high concrete content in the crust in the context of WI. This last would lead to indicate that, in fact, the water ingression phenomenon for CCI-7 test was either not present, or was attained only during the final part of the test, when the input power was lowered. The extracted heat flux could instead be linked to conduction through a relatively thin crust, the debris quenching for the period after the melt ejection, or through fracturing linked to another mechanism, i.e., not from thermal stresses, but maybe mechanical stresses (coming from melt ejection episode, or rapid ablation).

On the other hand, for test CCI-8 Meignen & Garrier [155] have estimated that for the phases where no melt ejection was present, an averaged heat flux of $\sim 180\frac{kW}{m^2}$ was extracted through the crust, lower than the $\sim 400\frac{kW}{m^2}$ introduced. The results indicate that during these phases, water ingression might have limited the heat exchange between the corium pool and the overlying water. Nevertheless, for this test, it is essential to note that a large amount of energy is extracted during the melt ejection episodes.

The results of these two CCI tests seem to show that if no melt ejection episodes are to be expected, the water ingression phenomenon would limit the heat extracted, and would be helpful only during the late phase in the accidental progression.

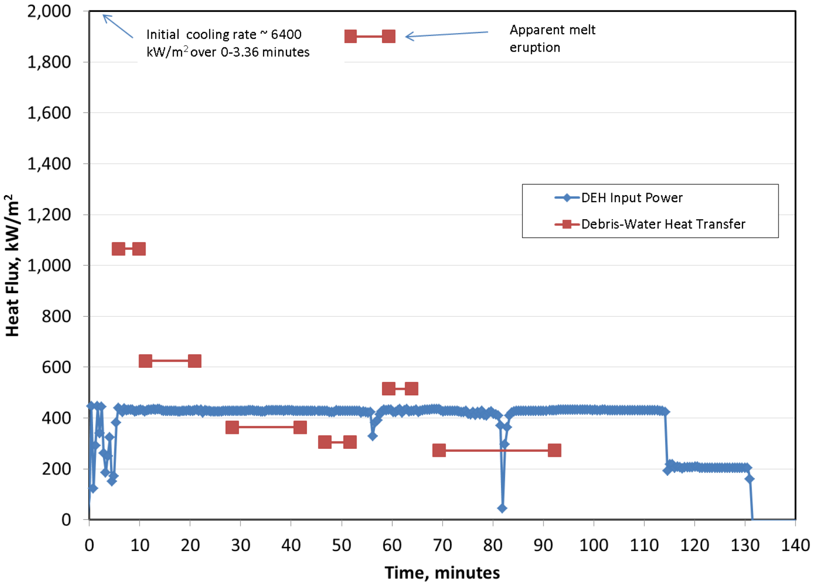

Figure 3.15 – CCI-7 experimental corium-water heat flux, and net input power

Taken from: [166, p.48]

3.2.2.2 CCI-9

As presented in section 2.2.4, this CCI test had the specific aim to study the water ingression phenomenon in siliceous concrete in a simplified 1D geometry. The heat exchanged, presented as the discontinuous red curves in figure 3.16, between the debris and the water, was calculated following the water level inside the test section, between water addition periods, measured by a differential pressure sensor. In the figure, the input power is also plotted as the solid green curve. The test had a dedicated steam collecting pipe that should have led the produced vapor to a condenser. Unfortunately, the steam pipe suffered a breach, probably during the initial melt generation via the thermitic reaction, that impeded another accurate measurement of the extracted heat flux. In previous CCI tests, sudden sharp peaks were associated with melt eruptions. The lack of peaks in CCI-9 alongside the lack of volcano-like structures found in the post-mortem analysis suggests that in this test, there was no melt eruption per se. Furthermore, the small amount (56 kg) of loose debris found at the top of the crust (probably linked to the initial melt splatter towards the lateral walls which could have fallen during the post-mortem test section disassembly) in test 9 also serves as proof of no violent melt ejections.

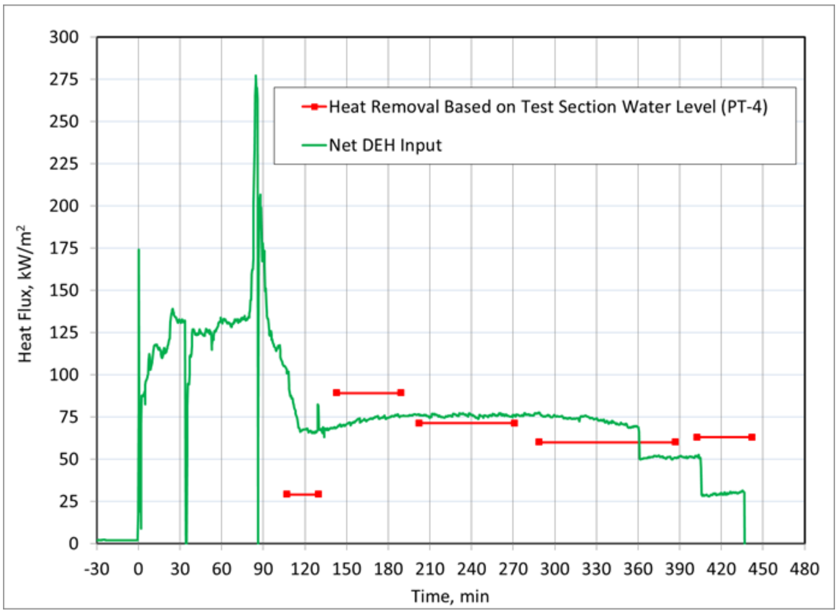

Figure 3.16 – CCI-9 experimental corium-water heat flux, and net input power

Taken from: [153]

Taking into account the melt eruption observed in test 7, with the same type of concrete but in a 2D test section and with a different input power profile, the lack of melt ejection episodes in this test 9 may reinforce the hypothesis the eruption observed in the test 7 test was due to a sudden concrete ablation. This last may have caused a massive injection of gas into the melt that, in turn, led to the melt ejection.

Figure 3.16 also points out the lack of abrupt reduction in the heat extracted in CCI-9, suggesting that there was always a melt-crust contact (backed by the lack of large void zones in the center of the test section during the post-mortem analysis). During the late stage of the experiment, time $>$ 150 min, it can be observed that the heat extracted by the water roughly approximates the power imposed on the liquid melt. In other words, the heat extracted is rather linear and decreasing over time, meaning stable cooling condition was probably achieved. Nevertheless, as can be seen in figure 3.17, which presents the ablation profile for the different quadrants as a function of time, concrete ablation does not stop even when stable cooling conditions are attained. A first "linear" phase of ablation up until 75 minutes can be observed, followed by a sudden, and important, ablation in the center and west side of the test section. The origin of the rise in ablation speed observed at t $\sim$85 min can be roughly matched (with a slight shift in time) with the power rise at around t=80min, observed in figure 3.16, whilst the subsequent "stabilization" coincides with the plateau of constant power level for the rest of the experiment. The curves also show that the ablation was not homogeneous. In the center and west quadrant, the ablation was faster than in the rest of the test section, whilst the ablation almost doubled in depth in the center comparing to the eastern quadrants.

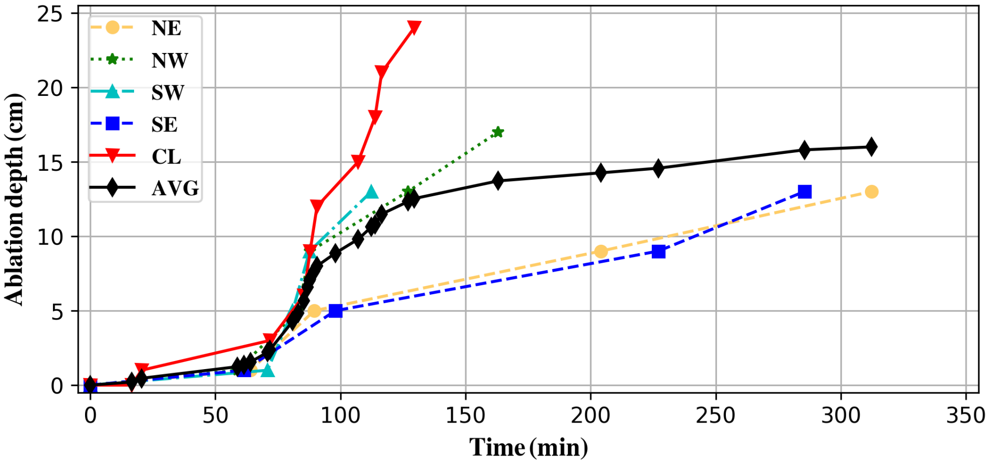

Figure 3.17 – CCI-9 axial ablation depth as a function of time by quadrant.N for north, S for south, E for east, W for west and CL for center line

Adapted from: [153]

Figure 3.18 shows the ablation depth measured by the thermocouples on each quadrant and the centerline. In the figure, each different colored line plots the profile at a different time. The solid line plots the final ablation measurement, corresponding to the final state of the ablation profile. As can be seen, during the input power peak (t=80 to ∼ 120 min), the ablation's heterogeneity becomes evident. It seems plausible that the power introduced into the test section during this period was concentrated in the melt in the central-west region of the test section leading to this heterogeneity in the ablation profile. Shortly after the peak (at around 140-160 min), the ablation stops on the west side, but it continues for another 150 minutes on the east side, which was less ablated than both the center and the west side. In other words, once the ablation stops at the west and center, the east side continues to ablate and reduces the disparity between the two sides to a 5 cm difference at the end. This might suggest that even when "steady-state" cooling was reached, there was still a certain amount of corium melt that led to 5 centimeters of ablation in the least ablated side.

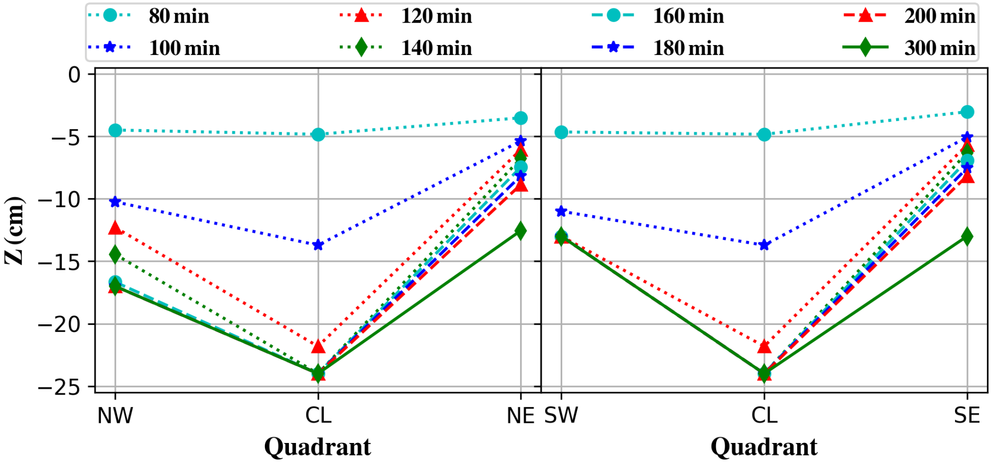

Figure 3.18 – CCI-9 axial ablation profile at different times by quadrant. N for north, S for south, E for east, W for west, CL for center line, and AVG for average

Figure 3.19 plots the input heat flux (dashed-dotted green curve) compared to both the measured extracted heat flux (dashed blue curve), and the concrete ablation profile converted to a heat flux (dotted red curve) estimated by using the ablation profile and the concrete's properties, presented in table 2.3, to calculate the ablated mass as a function of time, hence the heat flux. As can be seen, the sum of both the extracted heat flux by water evaporation and the energy needed to ablate the concrete, plotted as the solid black curve, is almost equal to the input energy in the late phase of the experiment. Nevertheless, as per the heating technique used, the constant power introduction is delivered mostly to the liquid parts of the corium. This would mean that with parts of the corium already solidified, the energy introduced by unit volume of the remaining corium would increase. This might explain the constant, slow, ablation profile on the east side. In other words, with a decreasing volume of liquid corium, the power would be concentrated to the reduced corium pool; hence the heat exchanged at the corium-concrete interface would increase, allowing the ablation of the concrete even by small amounts of liquid corium.

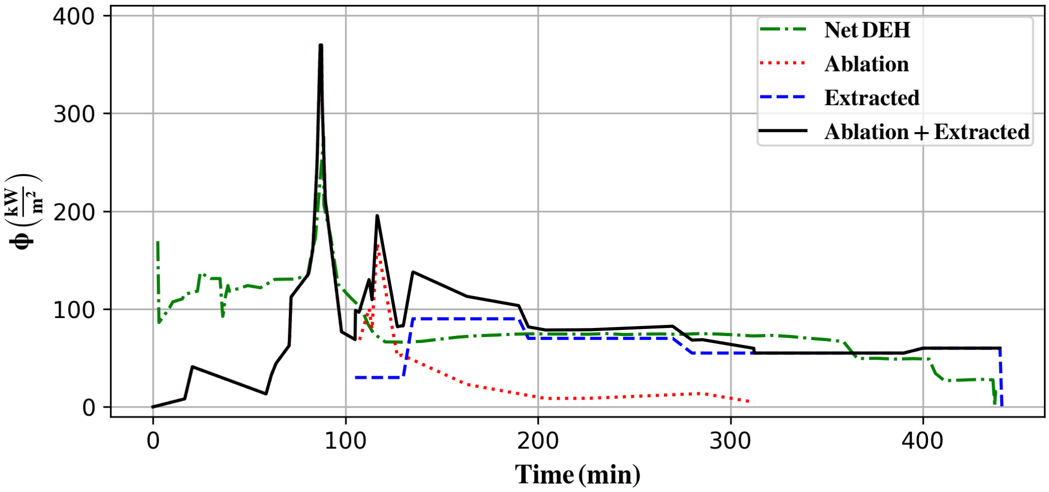

Figure 3.19 – CCI-9 Input flux compared to measured extracted heat flux and concrete ablation flux

The post-mortem samples devoted to the chemical analysis were taken from different sections of the test, some of which are illustrated as yellow and blue dots in figure 3.20. The blue dots correspond to the samples taken at the center of the section in increasing depths. The lower dashed black line represents the initial concrete profile. The results of the chemical analysis are presented in table 3.1 for samples 2 through 5 and 7 along the centerline. These results are not completely conclusive as for determining the experimental transient evolution, although they provide certain clues. Looking at samples 2 to 5, the increase in slag content (concrete + other minor elements) with depth suggests that the solidification of the lower parts occurred later. Sample 7 contradicts this previous statement since it's found around the same height as sample 2 but contains a high slag content which seems to indicate this sample solidified late during the experiment, but is still found at the top of the crust. The increase of slag content in the corium pool lowers the density of the corium; hence, the difference in density should lead to the accumulation of high concrete content corium at the top of the pool. Finding high concrete-content material at the top of the crust suggests that some slight crust renewal throughout the experiment occurred.

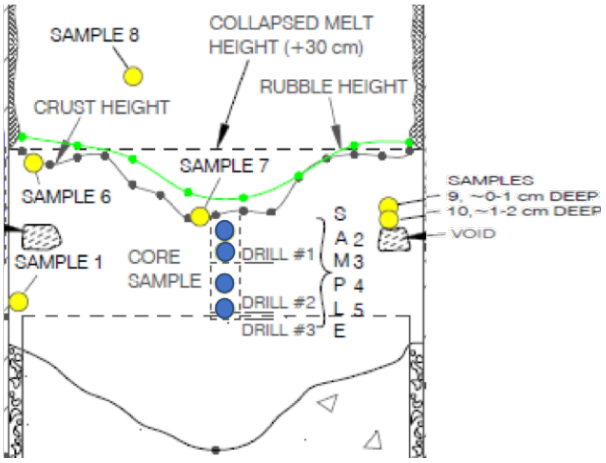

Figure 3.20 – CCI-9 Post-mortem configuration showing the ablation profile and the chemical sample location as the yellow and blue circles

Adapted from: [153]

Table 3.1 – CCI-9 post-mortem chemical analysis results,where height 0 corresponds to the original concrete surface (dashed line in figure 3.20), whilst height 18 cm would correspond to the top surface of the crust

Characteristic	Corium sample				
	2	3	4	5	7
UO_2 content (%)	64.55	50.47	43.06	41.84	57.54
ZrO_2 content (%)	27.39	21.75	19.44	19.64	24.73
Slag content (%)	8.06	27.78	37.51	38.52	17.73
Height from original concrete surface (cm)	13.5-18	9-13.5	1.5-9	0-1.5	17-18

As mentioned before, a priory, the permeability of a crust would be generated during the initial heat transfer in the first phase of contact of water with the melt, through film boiling at the upper surface. Nevertheless, the permeability in this test quite likely evolved throughout the course of the test. Successive events of crust partial remelting and resolidification would have occurred and would have strongly affected the morphology. There are no elements to confirm neither the initial crust generated nor the evolution of the crust. For this reason, the analysis here below should only be taken as an attempt to perform a first-order estimate of the ability of the crust found post-mortem to extract the heat based on the experimental results of the SSWICS tests.

From the chemical samples made in the middle of the test section (samples 2 to 5), a concrete content profile as a function of depth can be estimated. The samples give an average value of the slag content over the entire length of the sample. Considering the given values as the value at the middle of the sample (midpoint of sample's thickness), the concrete content as a function of the height was calculated by interpolating between the samples, taking height 0 as the dashed line in figure 3.20, which corresponds to the initial concrete surface. Using the results from the SSWICS experimental program [220], presented in figure 2.27, and extrapolating to higher concrete contents (since SSWICS highest concrete content experiment was 24%), the corresponding permeability profile was also estimated. Both curves are plotted in figure 3.21, where the black curve is the concrete content as a function of the height, starting at the initial 6% at the top of the crust (18 cm with respect to the initial concrete surface), whilst the dashed red curve is the corresponding permeability as a function of the height in a secondary y-axis. In the concrete content curve, it is possible to observe that there is a rapid concrete incorporation after the first few centimeters in depth. The slope of this curve then abruptly changes between samples 3 and 4, and then remains relatively constant for the last two samples (the two deep-most). By extrapolating the slope between samples 3 and 4, and the slope between samples 4 and 5, and assuming samples 4 and 5 solidified after the end of the experiment, an estimation of the crust/melt interface was made at the intersection of the slopes (as can be seen in the dotted grey curves and grey dot in figure 3.21). A permeability measurement of a 5±1 cm thick section of the "top crust" (whose location is not precisely mentioned) was made. The reported value ranges between 5.5E-11 to 1.5E-10 m^2, and the concrete content is taken as the initial one, 6%. Nevertheless, the concrete content should increase with increasing depth as per the concrete content reported for the samples used in the chemical analysis. At the depth corresponding to the thickness of the top crust slab, the concrete content would undoubtedly be higher. Using the permeability curve as a function of depth in figure 3.21, the permeability at the corresponding depths would be 2.5-8.5E-11 m^2. Likewise, the concrete content would then be 16-25%. The measured permeability for CCI-9 would be slightly higher for the appropriate corresponding concrete content, but as a first-order approximation, the permeability would be comparable to that reported in SSWICS at the appropriate concrete content level.

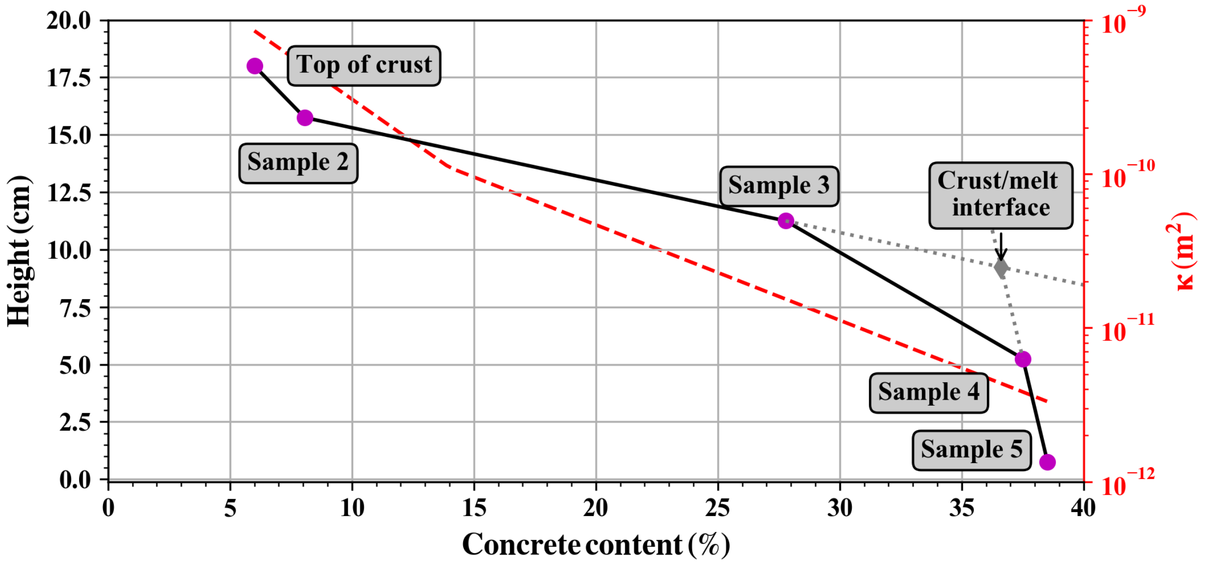

Figure 3.21 – CCI-9 post-mortem sample height and corresponding permeability profile, in a secondary y axis estimated using SSWICS permeability-concrete content measurements, both as a function of concrete content

From the permeability profile, it is possible to estimate the corresponding DHF as a function of the height using the Jones, eq. (2.12), Lister, eq. (2.13), and Lister-Epstein, eq. (2.33), models. The results are plotted as the blue lines in figure 3.22. From the intersection between the DHF curves, and the experimentally measured extracted heat flux during the late phase of the experiment (~80 $\frac{kW}{m^2}$), it is possible to estimate the limit of the effective water ingression thickness in the crust. At this low heat flux, the corresponding DHF calculated by the Jones or the Lister-Epstein model is almost the same;

hence the corresponding effective water ingression thickness is almost the same (black dotted lines in the figure). Using this effective WI thickness and the interface between the crust/melt pool, it is possible to distinguish three different zones: the melt pool, a hot crust, and a quenched crust (WI), represented by the colored zones in figure 3.22.

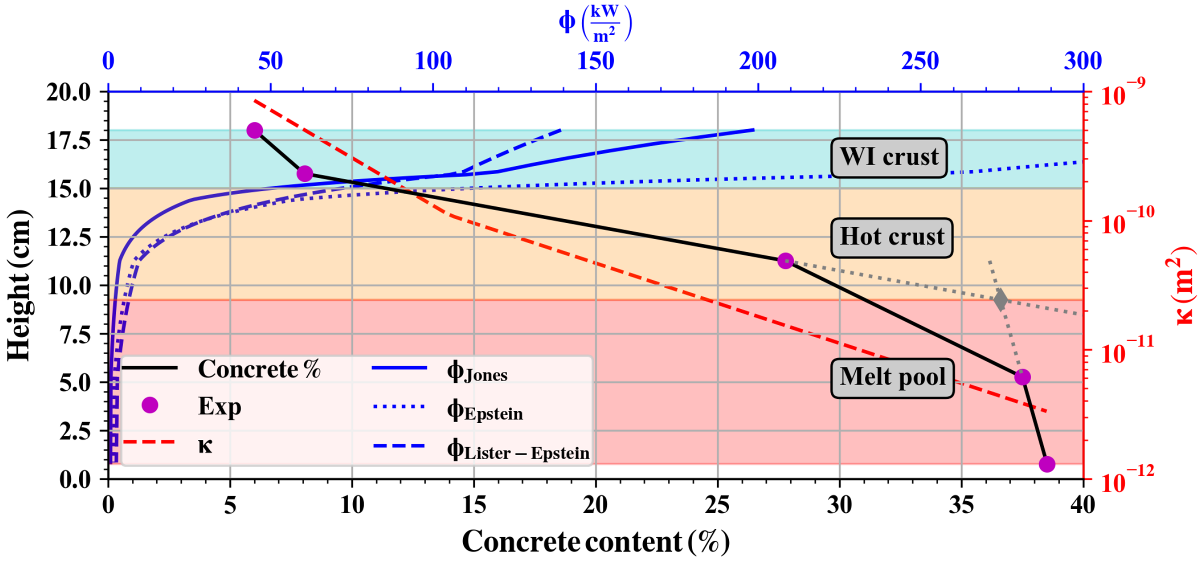

Figure 3.22 – CCI-9 post-mortem sample height, corresponding permeability and heat flux profile estimated using SSWICS permeability-concrete content measurements and Jones, eq. (2.12), Lister, eq. (2.13), and Lister/Epstein, eq. (2.33), models

To corroborate the previous estimation, conduction limited heat flux curves were calculated using the following approximation:

$$\phi_{cond} = \lambda_{cr} \frac{\Delta T}{e_{cr}} \tag{3.1}$$

where λ_{cr} $[\frac{W}{mK}]$ is the crust thermal heat conduction coefficient, ΔT [K] is the difference in temperature between the top and bottom surface of the crust, and e$_{cr}$ [m] is the crust thickness. The conduction limited heat flux curves were constructed by assuming a ΔT of 1500 K between the melt pool and the top of the crust, using different values of thermal conductivity for corium λ_{cr} =3.0, 2.5 [164], and 1.25 [160] $\frac{W}{mK}$, and by varying the crust thickness from the crust-melt interface to the top of the crust. These last are plotted as the green curves in figure 3.23. As can be seen, at the intersection between the conduction curves and the calculated DHF curves, the results remain coherent to the limits of the average late phase heat extraction of ~60-80 $\frac{kW}{m^2}$. The interface between the "WI crust" and the "Hot crust" calculated with λ_{cr}=3.0 $\frac{W}{m \cdot K}$ coincides with the WI models. Using λ_{cr}=2.5 $\frac{W}{m \cdot K}$, there is a slight discrepancy in the interface between the two methods, hence in the proportion of the hot crust/total crust ratio. Nevertheless, the heat flux calculated either with the conduction or the WI models falls within the experimental uncertainty using the corresponding hot crust thickness. The intersection of the conduction curve with a thermal conductivity of 1.25 $\frac{W}{m \cdot K}$ is out of the experimental uncertainty range, hence this value of conductivity does not seem plausible. The impact of the water ingression mechanism can be estimated by comparing the thickness of the dry crust ~5.5-6 cm, and the total crust ~9 cm. For CCI-9, the impact of the water ingression phenomenon is limited, since it represents an increment of around 50-60% from the conduction limited heat flux, in terms of increased thickness of solidified crust.

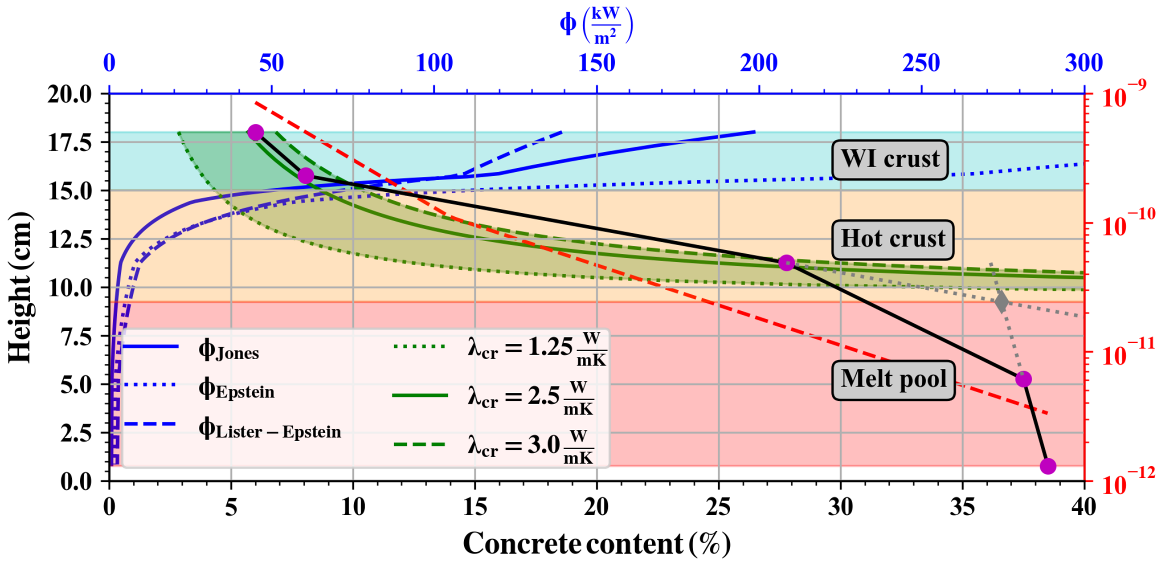

Figure 3.23 – CCI-9 post-mortem sample height, corresponding permeability and heat flux profile estimated using SSWICS permeability-concrete content measurements and Jones, eq. (2.12), Lister, eq. (2.13), and Lister/Epstein, eq. (2.33), models, compared with conduction curves

Taking into account the mass of the added concrete (185 kg of ablated concrete, from which 170 were incorporated to the melt), and the initial melt mass (1000 kg), it is possible to estimate the average concrete content at the end of the experiment as 20% (170 + 60 kg of initial concrete in the melt). From the chemical samples, it is easy to see that the crust gains mainly concrete, as the concentration found in the samples reached this value, or above, quite quickly. Assuming two limits for the average concrete content within the final melt as 15% and 25% figure 3.24 plots the corresponding concrete content for the final melt pool as the vertical dashed black lines going from the depth of the final κ measurement (sample 5), to the maximal ablation depth registered by the thermocouples (-24 cm). As can be seen, the concrete content in the remaining corium pool is lower than the one found in the lowermost chemical sample. This supports the hypothesis that there was some form of corium pool stratification (or concrete "chunks" accumulation), where the lower density high concrete content corium rises through the pool and comes in contact with the crust. It may be so that this is a direct result of some partially degraded slabs of concrete that quickly rise, due to the large density difference, and accumulate on the bottom of the crust before completely being incorporated into the corium melt. In other words, it may be that pieces of degraded partially molten concrete rise and "stick" to the bottom of the crust.

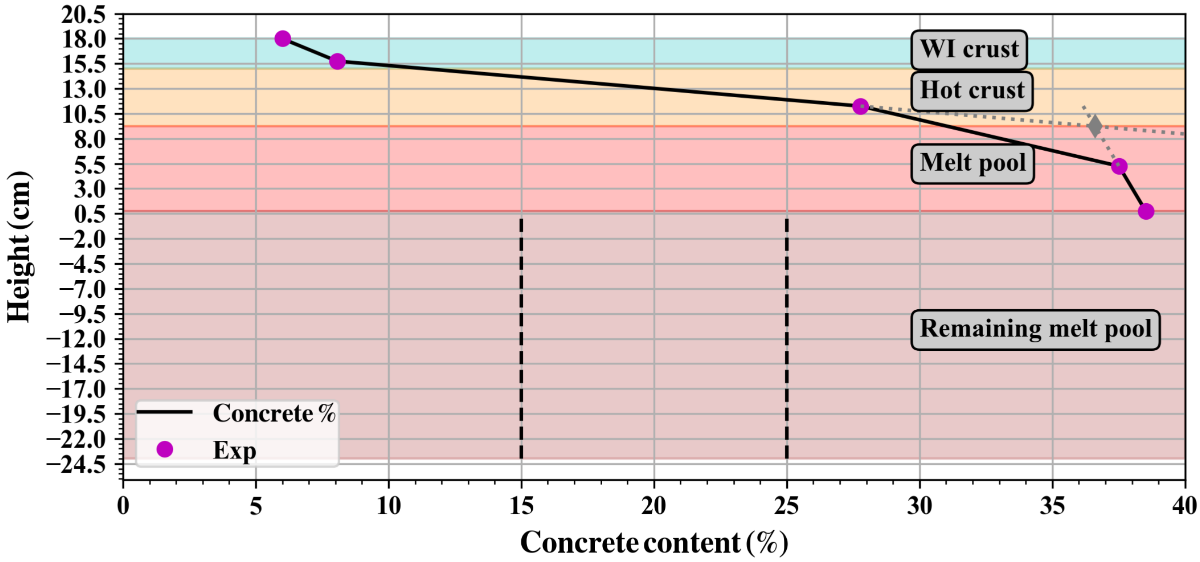

Figure 3.24 – CCI-9 final configuration

3.2.2.3 CCI-10

Recalling that the CCI-10 test was designed to study the melt ejection phenomenon in a particular concrete with high gas content, preliminary results confirm with video evidence at least three melt ejection periods. Other melt ejection episodes, suggested by the authors, inferred from thermocouple data (not confirmed with video evidence) are not present in the extracted heat flux curves (seen in figure 3.25 plotting the extracted heat flux and the input flux) [8]. As can be seen, the extracted heat flux is lower than the input by a relatively large margin (100-150 $\frac{kW}{m^2}$ extracted in average to ∼300 $\frac{kW}{m^2}$ introduced) meaning that concrete ablation would have probably progressed if the test would have continued. The experiment was terminated when all the thermocouples in the centerline inside the concrete failed or presented evidence of concrete ablation. In other words, the experiment was terminated for security reasons in the installation since in the centerline, where the concrete ablation was fastest, all the remaining thermocouples failed at 210 min, meaning the ablation could no longer be monitored. The final concrete ablation depth in the centerline reached 31 cm and could have possibly continued if the test had carried on.

Despite the observed and suggested melt ejection episodes, interestingly, no debris bed layer was found, as depicted in figure 3.26. This last might suggest that regardless of the efficient heat exchange that would occur during melt ejection periods, the stability of the produced layer is not guaranteed. A volcano-like formation was found in one of the corners of the test section. As in the CCI-8 test, a large void was found, resulting from the experimental test section's geometrical limitations, potentially impeding the continuous contact between the melt and the crust for periods of time. Furthermore, it was found, through chemical analysis from post-mortem chemical samples, that the primary central crust on top of the void section formed quite quickly. This last can be inferred since the concrete content went from 8.79 to 15.8 wt.%

---

[8] The difference between the red and the black curves is the method of measurement. The red curve is an estimation of the heat flux based on the condensation of the out-flowing steam in the condensation tank, whilst the black curve is an energy balance of the secondary side of the quench system

with increasing crust depth (the samples marked by the blue dots) compared to the initial 8 wt.% at the beginning of the test. The nature of the formation of the crust is not explained, and the influence of the renewal of the crust through melt ejection episodes, if any, remains elusive.

The low content in the crust, in addition to the observed heat flux, might indicate that outside the melt ejection episodes, the extracted heat flux could correspond to the water ingression phenomenon through the quickly formed crust. By performing the same type of analysis as for CCI-9, comparing the ~100-150$\frac{kW}{m^2}$ extracted during the late phase of the test, it can be estimated that the thickness of the "Hot crust" would fall between 2.5-4.5 cm considering λ_{cr}=2.5-3.0$\frac{W}{mK}$ respectively. Compared to the total crust thickness of 17 cm, this thickness can be interpreted as an increment of around 320-580% from the conduction limited, in terms of increased solidified crust thickness. Nevertheless, the crust in this experiment was separated from the melt, as suggested by the void found underneath. This would imply that the evolution of the crust would be different than the one in CCI-9, which would impede a direct comparison of the efficiency of the WI mechanism. Permeability measurements allowing to perform a more in-depth water ingression analysis are not given as of this date.

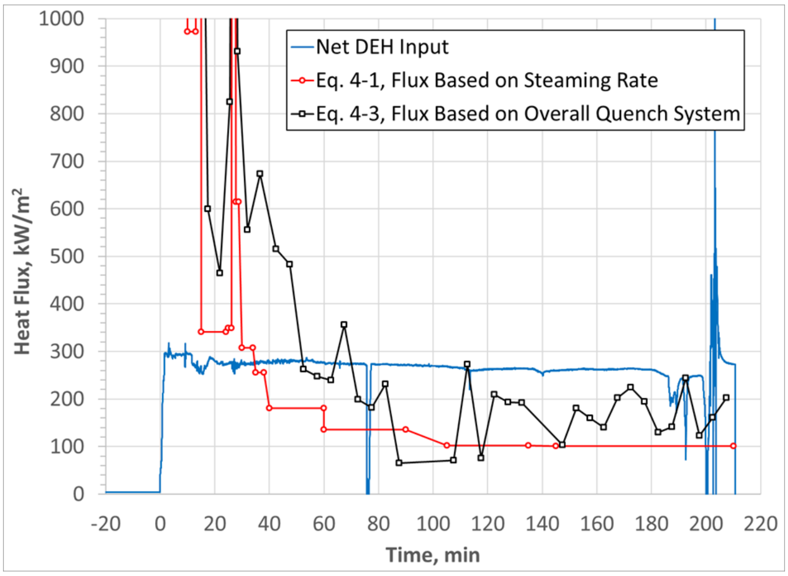

Figure 3.25 – CCI-10 experimental corium-water heat flux, and net input power

Taken from: [167]

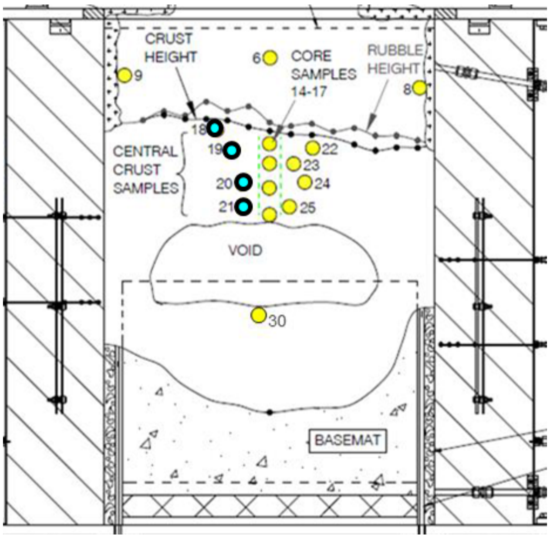

Figure 3.26 – CCI-10 Post-mortem configuration showing the ablation profile and the chemical sample location as the yellow and blue circles

Adapted from: [167]

3.2.2.4 Conclusions of CCI tests

Summarizing:

- CCI-7 shows an extracted heat flux too large to be comparable with the WI flux observed during the SSWICS tests;
- there is evidence that for the periods with no melt ejection in CCI-8 the extracted heat flux through the crust on top of the void is in the upper limit of the WI;
- results from CCI-9 suggest that for the particular power injected the effects of WI were low and compared to conduction limited heat flux;
- and CCI-10 indicate that for the period after melt ejection, the extracted heat flux through the crust on top of the void is coherent with the WI flux observed during the SSWICS test, nevertheless is half as the one injected, not preventing the concrete ablation.

These results tend to indicate that for high power experiments, the extracted heat flux is higher than what would be expected if the WI phenomenon was present. If the crust remained in contact with the melt, it would have been possible to remelt a part of the crust, hence extract more heat through other mechanisms, i.e., conduction. This last would seem to have occurred in the CCI-7 experiment.

On the other hand, for the experiment with low power (CCI-9), the heat flux extracted matches the injected power, hence the effects of the phenomenon would also be limited, as the heat could easily be transferred through the crust.

3.3 Conclusions

The two-dimensional patterns found in the preliminary calculations presented during this chapter show an interesting mechanism of water penetration through a super-heated initially dry debris bed. These calculations also show that the heat flux extracted remains relatively constant for the case of no residual power input. Nevertheless, the question remains on the mechanisms governing the heat extraction and the effects the residual power would have in both a case with and a case without the fingering observed. In the case of a fractured porous media, the experiments shed only some light in the constrains of the WI phenomenon, and not on the mechanism itself. Regardless if it is clear that the mechanism has an apparent maximum concrete fraction upon which it remains valid, this effectiveness in the case of the presence of residual power, or a more realistic configuration with both an overlaying debris bed and a corium pool underneath, is still not assured. In the subsequent chapters, an analytical model will be used to explore the mechanism, and the governing dynamics of the phenomena, as well as some numerical simulations extrapolating to a more realistic scenario, will be presented.

Chapter 4

One-dimensional Analysis

Contents

The previous chapter quickly presented the analysis of the configurations of interest parting from preliminary MC3D simulations for the debris bed and the reinterpretation of experimental results of MCCI platforms for the water ingression phenomena. The analysis showed certain frailty in the current understanding of the mechanisms and stability of these configurations. For this reason, the purpose of this chapter is to construct an analytical model for steady 1D two-phase flow in porous heated media, in section 4.1, to further extend it to an unsteady situation, section 4.2, and finally analyze different configurations in sections 4.3 and 4.4. The interest of this is to attempt to analytically determine the dominant parameters of two-phase water penetration into porous media in different permeability regimes, with the purpose of evaluating the maximal heat flux that can be extracted from a volumetrically heated, initially dry-hot debris bed whilst remaining stable (no re-melting). In addition, the model results can be compared to those obtained with MC3D, which provides cross-validation.

4.1 Dry-out heat flux in flooded debris bed

To recall, as explained in section 2.3 for 1D two-phase flow in steady-state conditions, the 1D two-phase steady-state pressure loss in a porous medium is given by:

$$-\frac{\delta P_i}{\delta z} = \rho_i g + \frac{\mu_i}{\kappa \kappa_{r,i}} j_i + \frac{\rho_i}{\eta \eta_{r,i}} |j_i| j_i + \frac{\delta P_c}{\delta z} + \begin{cases} \frac{F_{lv}}{\alpha} & \text{if } i = v \\ -\frac{F_{lv}}{1-\alpha} & \text{if } i = l \end{cases} \tag{2.4}$$

$$F_{lv} = 350(1-\alpha)^7 \alpha \frac{\rho_l g K}{\eta \sigma_{lv}} (\rho_l - \rho_v) \left(\frac{j_v}{\alpha} - \frac{j_l}{1-\alpha} \right)^2 \tag{2.5}$$

As proposed by Ergun [182] the porous media parameters κ and η in a bed of solid round particles, which are intrinsic properties of the bed (function of the constituents of the beds, i.e. the particles), can be evaluated with:

$$\kappa = \frac{\varepsilon^3 {d_p}^2}{A(1-\varepsilon)^2} \tag{2.6}$$

$$\eta = \frac{\varepsilon^3 d_p}{B(1-\varepsilon)} = \frac{\sqrt{A}\varepsilon^{\frac{3}{2}}}{B} \sqrt{\kappa} \tag{2.7}$$

4.1.1 Laminar case

For simplicity, following the approach taken by Lipinski [109] in order to establish a method, only laminar effects are considered, without taking into account:

- the capillary effects, which will be investigated in section 4.1.3, nor
- the interfacial friction term.

In the vapor phase, gravitational pressure drop effects are deemed negligible, hence the pressure drop can be written as:

$$-\frac{\delta P_v}{\delta z} = \frac{\mu_v}{\kappa \kappa_{r,v}} j_v \tag{4.1}$$

whilst for the liquid phase the momentum balance equation can be expressed as:

$$-\frac{\delta P_l}{\delta z} = \frac{\mu_l}{\kappa \kappa_{r,l}} j_l + \rho_l g \tag{4.2}$$

with $j_i\left[\frac{m}{s}\right]$ being the superficial velocity of phase "i" (v for vapor and l for liquid).

Momentum balance

At each height z, the pressure gradient is presumed common to all phases, and can thus be expressed as follows:

$$-\frac{\delta P_i}{\delta z}=\frac{\mu_v}{\kappa\kappa_{r,v}}j_v=\frac{\mu_l}{\kappa\kappa_{r,l}}j_l+\rho_l g \tag{4.3}$$

Mass balance

In steady-state conditions, there is no mass accumulation and thus the upward vapor mass flux is equal to the downward liquid mass flux, and is formulated as:

$$\rho_v j_v=-\rho_l j_l \tag{4.4}$$

Substituting eq. (4.4) into eq. (4.3) (i.e. balancing mass fluxes, viscous shear and gravity) yields the following relationship between the vapor flux and local void saturation, α, at each elevation z (included in the terms $\kappa_{r,v}$ and $\kappa_{r,l}$):

$$j_v\equiv j_{v,\lambda}=\frac{\frac{\rho_l}{\rho_v}\kappa g}{\frac{\mu_l}{\rho_l\kappa_{r,l}}+\frac{\mu_v}{\rho_v\kappa_{r,v}}}=\frac{\frac{\rho_l}{\rho_v}\kappa g}{\frac{\nu_l}{\kappa_{r,l}}+\frac{\nu_v}{\kappa_{r,v}}} \tag{4.5}$$

were $j_{v,\lambda}\left[\frac{m}{s}\right]$ is the superficial vapor velocity in the purely laminar regime (denoted with the subscript λ).

Using the formulations of the relative permeabilities in table 2.4, the gas flux can be linked to local void saturation. The result is shown in figure 4.1, which plots the superficial vapor and liquid velocities, given by eq. (4.5) and eq. (4.4) respectively, for a representative debris bed with κ=1.2E$\times10^{-9}m^2$ (which corresponds to d_p= 1mm, ε = 0.4), and evaluating the fluids properties at 100°C and 1 atm. As can be seen, for any given $j_{i,\lambda}$, there are two possible values for α, i.e., two possible physical configurations, and a maximum located at a void saturation around 0.75. The maximum represents then a critical max flux beyond which the 2-phase flow is unstable (and, likely, not possible). In other words, the maximal amount of vapor that can flow out of the bed in stable conditions is located at $j_{v,\lambda}^{crit}$ and if the imposed $j_{v,\lambda}$ exceeds this value, it would then lead to dry-out conditions.

The existence of this $j_{v,\lambda}^{crit}$, given by the hydrodynamics of the system, would occur at a critical value of α here called α_{λ}^{crit}. This last can be analytically found by inserting both $\kappa_{r,l}$ and $\kappa_{r,v}$ presented in table 2.4 in eq. (4.5) and maximizing the partial derivative of the denominator with respect to α:

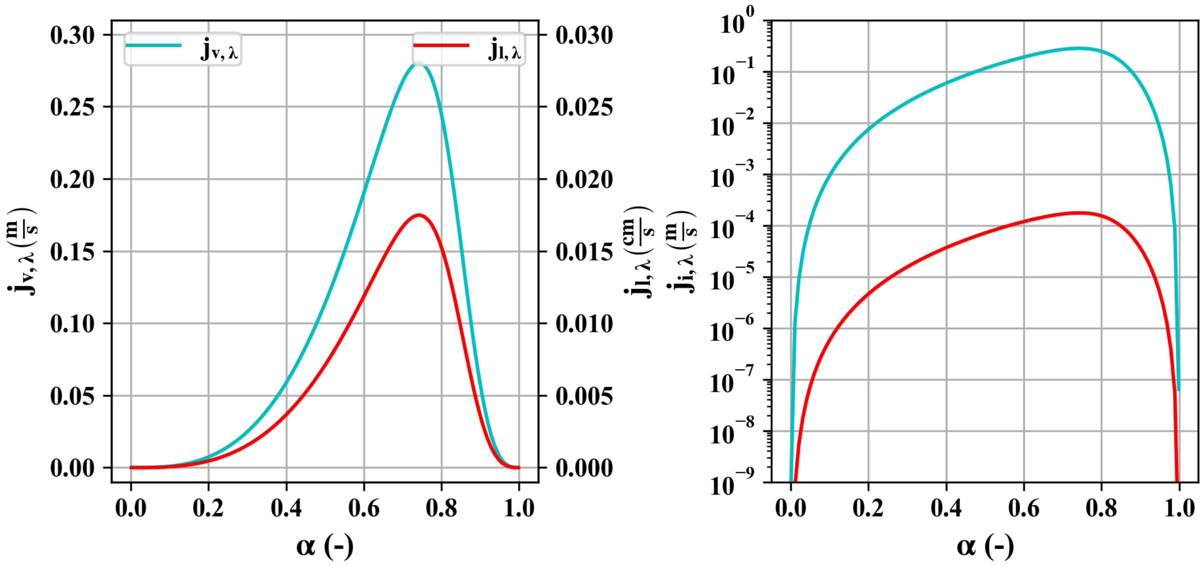

Figure 4.1 – Laminar liquid and vapor superficial velocities as a function of α at 1 atm for κ=1.2E$\times10^{-9}m^2$ ($d_p = 1mm$), and $\varepsilon = 0.4$

Left: $j_{l,\lambda}$ in left axis $\left(\frac{m}{s}\right)$, $j_{l,\lambda}$ in right axis $\left(\frac{m}{s}\right)$; Right:Logarithmic scale $\left(\frac{m}{s}\right)$

$$\frac{\delta\left(\frac{\nu_l}{\kappa_{r,l}}+\frac{\nu_v}{\kappa_{r,v}}\right)}{\delta\alpha} = \frac{\delta\left(\frac{\nu_l}{(1-\alpha)^n}+\frac{\nu_v}{\alpha^n}\right)}{\delta\alpha}$$

$$n\frac{\nu_l}{(1-\alpha)^{(n+1)}} - n\frac{\nu_v}{\alpha^{(n+1)}} = 0$$

$$\alpha_\lambda^{crit} = \left[1+\left(\frac{\nu_l}{\nu_v}\right)^{\frac{1}{n+1}}\right]^{-1} \tag{4.6}$$

At this critical value, recalling that for debris bed in most cases n=3, $j_{v,\lambda}$ and $j_{l,\lambda}$ become:

$$j_{v,\lambda}^{crit} = \frac{\frac{\rho_l}{\rho_v}\kappa g}{\frac{\nu_v}{\left[1+\left(\frac{\nu_l}{\nu_v}\right)^{\frac{1}{4}}\right]^{-3}} + \frac{\nu_l}{\left[\frac{\left(\frac{\nu_l}{\nu_v}\right)^{\frac{1}{4}}}{1+\left(\frac{\nu_l}{\nu_v}\right)^{\frac{1}{4}}}\right]^{3}}} \tag{4.7}$$

$$j_{l,\lambda}^{crit} = \frac{\kappa g}{\dfrac{\nu_v}{\left[1+\left(\dfrac{\nu_l}{\nu_v}\right)^{\frac{1}{4}}\right]^{-3}} + \dfrac{\nu_l}{\left[\dfrac{\left(\dfrac{\nu_l}{\nu_v}\right)^{\frac{1}{4}}}{1+\left(\dfrac{\nu_l}{\nu_v}\right)^{\frac{1}{4}}}\right]^{-3}}} \tag{4.8}$$

To estimate in which range of permeabilities the initial assumptions of neglecting inertial terms remains valid figure 4.2 plots each term in the R.H.S of eq. (2.4) for both liquid and vapor phases evaluated at the critical point $j_{v,\lambda}^{crit}$, eq. (4.7), and $j_{l,\lambda}^{crit}$, eq. (4.8), as a function of κ. In the left side, it is possible to observe that for the vapor phase, when $\kappa{<}10^{-9}m^2$ the inertial, and interfacial terms quickly become negligible. The gravitational pressure loss term remains constant, but is again negligible compared to the viscous term. On the right side, for the liquid phase with $\kappa{<}10^{-8}m^2$ the same is true for the inertial and interfacial pressure loss terms. In other words, the formulation for $j_{i,\lambda}$, eq. (4.7) and eq. (4.8), are valid for κ below $10^{-9}m^2$. It can be noted that the viscous pressure loss terms are constant since the term $\frac{\mu_i}{\kappa\kappa_{r,i}}j_{i,\lambda}$ depends on $j_{i,\lambda}$ which in turn depends linearly on κ, canceling out in the end.

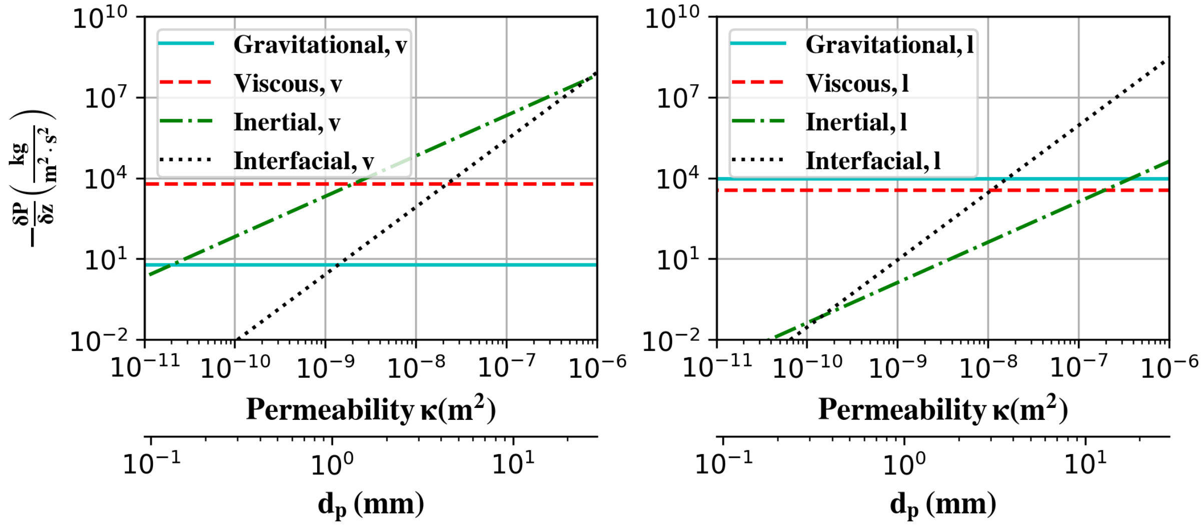

Figure 4.2 – Pressure drop terms of eq. (2.3) evaluated with $j_{v,\lambda}^{crit}$, eq. (4.7), and $j_{l,\lambda}^{crit}$, eq. (4.8), as a function of κ and n=3

Left: Pressure loss terms for vapor phase; Right:Pressure loss terms for liquid phase

Figure 4.3 plots $j_{v,\lambda}$, eq. (4.5), as a function of α at different pressures. As can be seen, the value of the maximum superficial velocity strongly decreases when the pressure increases. On the other hand, the location of α_{λ}^{crit} decreases slowly towards 0.5 as the pressure increases. This is logical since when the pressure approaches the critical point (P~227 atm), both the density and the viscosity of water and vapor tend towards the same value, or in other words, water and vapor become the same fluid.

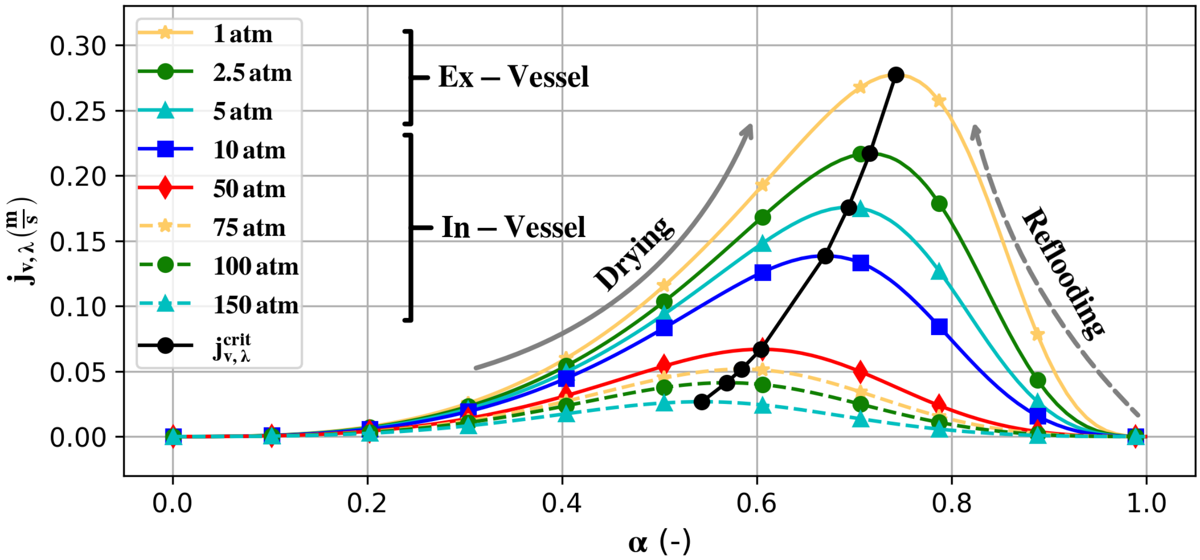

Figure 4.3 – Laminar vapor superficial velocity, $j_{v,\lambda}$, as a function of the vapor saturation for different pressures, $\kappa{\sim}1.20{\times}10^{-9}m^2$ ($d_p = 1mm$)

The left part of the curves has been observed both experimentally [221] and numerically [181]. This is likely due to the fact that the vapor flux is imposed in the experiments, and that they all start from already flooded configuration ($\alpha = 0$). It may be possible to expect that the right part of the curves is encountered in reflooding configuration (in particular), which may be experimentally challenging to observe in steady situations.

Energy balance

In the heated debris bed, at each elevation, the vapor flux comes from the water vaporization below Z due to volumetric power. In MCCI conditions, part of the vapor flux, $j_{v,0} and \rho_{v,0}$, may also come from the concrete ablation. In the case of saturated water, as expected in accidental scenarios, this vaporization exactly balances the input energy below Z:

$$\rho_v j_v(z) - \rho_{v,0} j_{v,0} = \frac{1}{h_{lv}} \int_0^z P_v dz = \frac{P_v Z}{h_{lv}} = \frac{\phi}{h_{lv}}$$

$$\phi = (\rho_v j_v - \rho_{v,0} j_{v,0})\, h_{lv} \tag{4.9}$$

with $\phi \left[\frac{W}{m^2}\right]$ being the extracted heat flux per (horizontal) surface of porous media, which in this case comes from the deposited volumetric power (P_v) up to the height Z, and h_{lv} $\left[\frac{J}{kg}\right]$ the latent heat of vaporization. Incorporating eq. (4.7) into eq. (4.9) yields a relationship between the input power, which equals to ϕ in steady state, and the local vapor saturation α in the terms of relative permeabilities $\kappa_{r,l}$ and $\kappa_{r,v}$ defined in table 2.4:

$$\phi = \left[\frac{\kappa \rho_l g}{\dfrac{\nu_l}{\kappa_{r,l}} + \dfrac{\nu_v}{\kappa_{r,v}}} - \rho_{v,0} j_{v,0} \right] h_{lv} \tag{4.10}$$

As mentioned before, the critical heat flux per horizontal surface of debris bed in two-phase flow is obtained by evaluating eq. (4.10) at $j_{v,\lambda}^{crit}$, hence at $\alpha = \alpha_{\lambda}^{crit}$, which would result in:

$$\phi_{\lambda}^{crit} = \left[\frac{\kappa \rho_l g}{\nu_l \left[1 + \left(\frac{\nu_v}{\nu_l}\right)^{\frac{1}{4}}\right]^3 + \nu_v \left[1 + \left(\frac{\nu_l}{\nu_v}\right)^{\frac{1}{4}}\right]^3} - \rho_{v,0} j_{v,0} \right] h_{lv} \tag{4.11}$$

In the case where there is no vapor flux coming from below the debris bed, eq. (4.11) simplifies to:

$$\phi_{\lambda}^{crit} = \kappa g h_{lv} \frac{\rho_l}{\nu_l \left[1 + \left(\dfrac{\nu_v}{\nu_l}\right)^{\frac{1}{4}}\right]^3 + \nu_v \left[1 + \left(\dfrac{\nu_l}{\nu_v}\right)^{\frac{1}{4}}\right]^3} \tag{4.12}$$

Figure 4.4 plots the value of ϕ as a function of α at different pressures. It is possible to observe, than on the contrary to $j_{v,\lambda}^{crit}$, ϕ_{λ}^{crit} increases significantly with pressure (recalling that the value of α_{λ}^{crit} decreases with pressure). This last can be understood as the effect of the increase of the density of the vapor at saturation temperature at each pressure since the vapor occupies less space in between the pores. On the other hand, the flux is also proportional to the latent heat, which in turn tends to 0 when the pressure approaches the critical point. Both effects compete with increasing pressure, resulting in a pressure where the power extracted is maximized. Nevertheless, the validity of the equations becomes questionable at very high pressures since other effects may not be taken into account. It is also noticed that the maximum (critical) heat flux does not occur at void saturation tending to 1, but quite far below. This is due to the fact that the superficial velocity is maximal when the sum of the liquid and vapor viscous friction terms are minimal. Adding to this, it is noticed that below critical conditions, two 2-phase configurations are possible. This may induce some instability of the flow when approaching α_{λ}^{crit}.

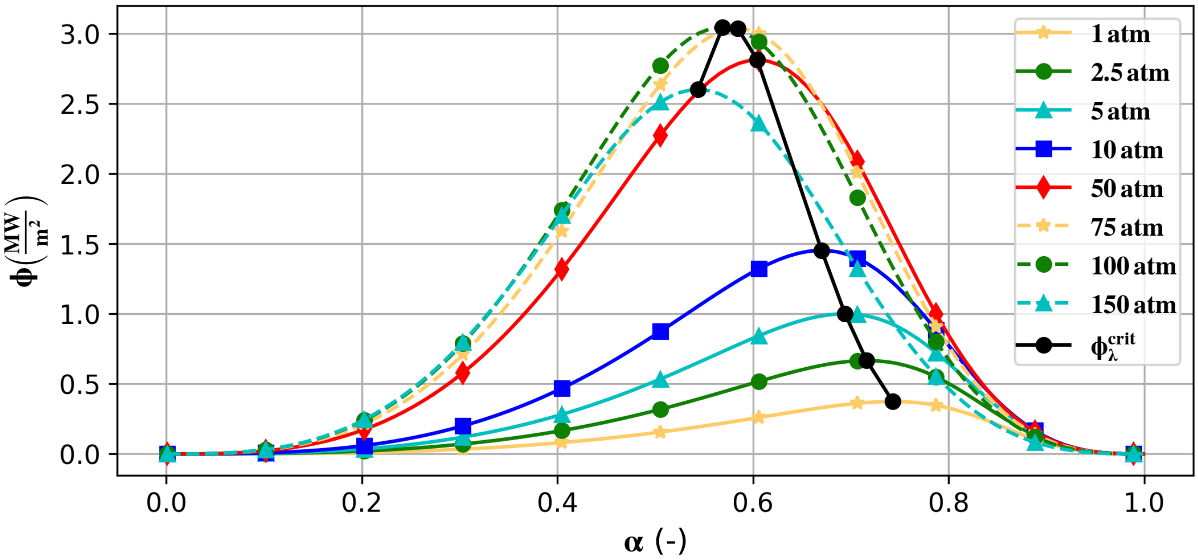

Figure 4.4 – ϕ, eq. (4.10), as a function of the vapor saturation for different pressures, $\kappa \sim 1.20 \times 10^{-9} m^2$ $(d_p = 1mm)$

Comparing eq. (4.12) Jones' model, eq. (2.12), and Epstein's model, eq. (2.13), which is inscribed in the model Lister-Lomperski eq. (2.30) for the water ingression, recalled here below:

$$\phi_{do} = \kappa g h_{lv} \frac{0.015\,(\rho_l - \rho_v)}{\nu_v \left(1 + 0.003\left(\frac{\nu_v}{\nu_l}\right)^2\right)^{\frac{1}{4}}} \tag{2.12}$$

$$\phi_{do} = \kappa g h_{lv} \frac{(\rho_l - \rho_v)}{2\nu_v} \tag{2.13}$$

It is clear that the main difference comes from the denominator. The liquid term in the denominator provides a correction regarding the impact of the pressure by including the viscous term for the liquid phase, which is not present in the Epstein model. Figure 4.5 shows how Epstein's model departs further and further from eq. (4.12) with increasing pressure, where Epstein's model would overestimate the extracted heat flux. The contrary can be said for the Jones model, where the extracted heat flux would be underestimated. Regardless, the importance of the liquid viscous terms can be highlighted here.

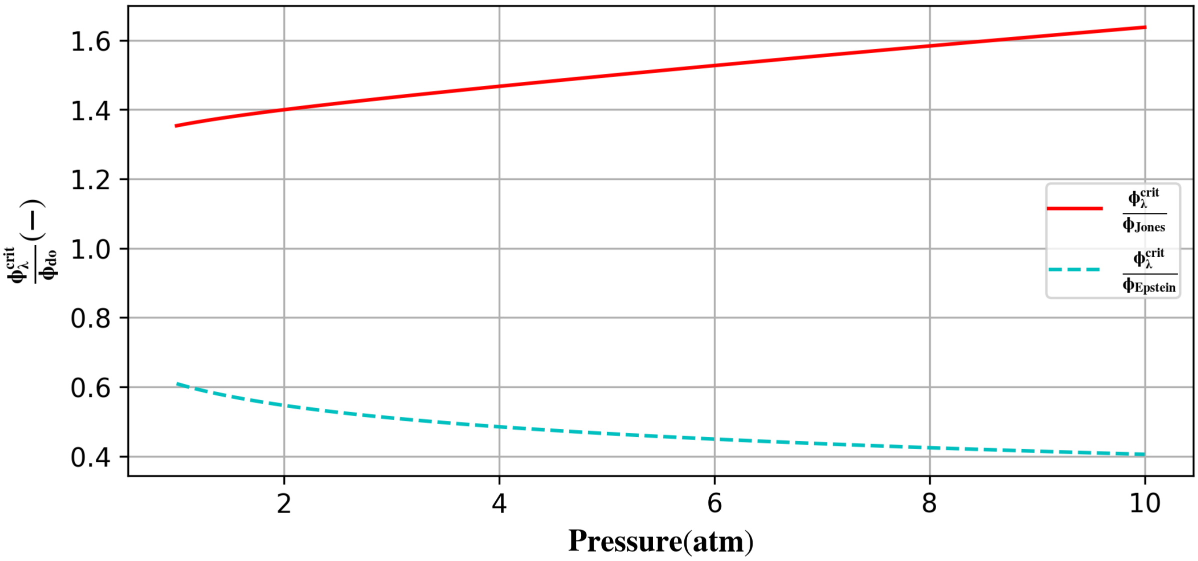

Figure 4.5 – Ratio between ϕ_λ^{crit}, eq. (4.12), and both ϕ_{Jones} (dashed blue curve), eq. (2.12), and $\phi_{Epstein}$ (solid red curve), eq. (2.13), as a function of pressure, with $\kappa \sim 1.0 \times 10^{-10} m^2$ ($d_p = 0.3mm$)

4.1.2 Inertial case

Although figure 4.2 tends to indicate that a purely inertial regime would be unlikely, an expression for it will be hereafter derived, following the same procedure as for the laminar case. Again neglecting the capillarity, considering only the inertial effects for both the liquid and vapor phase, the pressure drop equations can be written for the vapor phase as:

$$-\frac{\delta P_v}{\delta z} = \frac{\rho_v}{\eta \eta_{r,v}} |j_v| j_v \tag{4.13}$$

For the liquid:

$$-\frac{\delta P_l}{\delta z} = \frac{\rho_l}{\eta \eta_{r,l}} |j_l| j_l + \rho_l g \tag{4.14}$$

At each location Z, the pressure gradient is common to all phases, and is expressed as follows:

$$-\frac{\delta P_i}{\delta z} = \frac{\rho_v}{\eta \eta_{r,v}} |j_v| j_v = \frac{\rho_l}{\eta \eta_{r,l}} |j_l| j_l + \rho_l g \tag{4.15}$$

Substituting eq. (4.4) into eq. (4.15) yields the following relationship between the vapor flux and local saturation at each elevation Z :

$$j_{v,\tau} = \sqrt{\frac{\frac{\rho_l}{\rho_v^2}\eta g}{\frac{1}{\rho_l \eta_{r,l}} + \frac{1}{\rho_v \eta_{r,v}}}} = \sqrt{\frac{\frac{\rho_l}{\rho_v^2}\frac{\sqrt{150}}{1.75}\varepsilon^{\frac{3}{2}}\sqrt{\kappa g}}{\frac{1}{\rho_l \eta_{r,l}} + \frac{1}{\rho_v \eta_{r,v}}}} \tag{4.16}$$

with $j_{v,\tau}$ $\left[\frac{m}{s}\right]$ being the vapor superficial velocity of phase in the inertial regime (denoted with the subscript τ).

Figure 4.6 plots the superficial vapor and liquid velocities, given by eq. (4.16) and eq. (4.4) respectively, for a representative debris bed consisting of particles with $d_p = 8.5mm$, m=5, $\varepsilon = 0.4$, and evaluating the vapor properties at 100°C and 1 atm. As can be seen for this regime the maximum is around α =0.77, here called α_τ^{crit}.

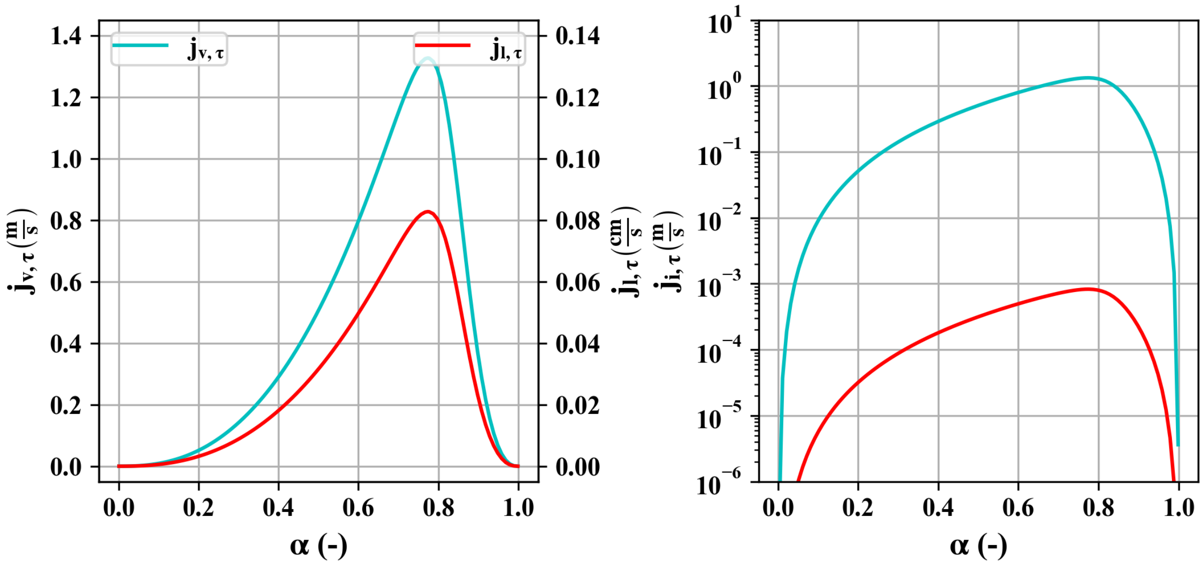

Figure 4.6 – Inertial liquid and vapor superficial velocities as a function of α at 1 atm for κ=8.6×$10^{-8}m^2$ ($d_p = 8.5mm$), and $\varepsilon = 0.4$

Left: $j_{l,\tau}$ in left axis, $j_{v,\tau}$ in right axis (different units); Right:Logarithmic scale $\left(\frac{m}{s}\right)$

α_τ^{crit} can be analytically found by inserting both $\eta_{r,l}$ and $\eta_{r,l}$, presented in table 2.4, in eq. (4.16) and maximizing the partial derivative of the denominator with respect to α:

$$\alpha_\tau^{crit} = \left[1 + \left(\frac{\rho_v}{\rho_l}\right)^{\frac{1}{m+1}}\right]^{-1} \tag{4.17}$$

α_τ^{crit} is equal to 0.836, 0.774, and 0.742 for the m values given in table 2.4 by Lipinski [109], Reed [187], and Hu & Theofanous [120] respectively. It is recalled that in the laminar regime, α_λ^{crit}, is in the order of 0.745. It is essential to highlight that the values of α here found may provide an explanation of the saturation in the two-phase fingers observed in the calculations presented in chapter 3.

At this critical value $j_{v,\tau}^{crit}$ and $j_{l,\tau}^{crit}$ become:

$$j_{v,\tau}^{crit} = \sqrt{\frac{\frac{\rho_l}{\rho_v}\eta g}{\left[1+\frac{\rho_v}{\rho_l}^{\frac{1}{m+1}}\right]^{m+1}}} = \sqrt{\frac{\frac{\rho_l}{\rho_v}\frac{\sqrt{150}}{1.75}\varepsilon^{\frac{3}{2}}\sqrt{\kappa g}}{\left[1+\frac{\rho_v}{\rho_l}^{\frac{1}{m+1}}\right]^{m+1}}} \tag{4.18}$$

$$j_{l,\tau}^{crit} = \sqrt{\frac{\frac{\rho_v}{\rho_l}\eta g}{\left[1+\frac{\rho_v}{\rho_l}^{\frac{1}{m+1}}\right]^{m+1}}} = \sqrt{\frac{\frac{\rho_v}{\rho_l}\frac{\sqrt{150}}{1.75}\varepsilon^{\frac{3}{2}}\sqrt{\kappa g}}{\left[1+\frac{\rho_v}{\rho_l}^{\frac{1}{m+1}}\right]^{m+1}}} \tag{4.19}$$

Figure 4.7 plots each term in the R.H.S of eq. (2.4) for both liquid and vapor phases evaluated at the critical point $j_{v,\tau}^{crit}$, eq. (4.18), and $j_{v,\lambda}^{crit}$, eq. (4.19). For the vapor phase, the inertial pressure drop terms become dominant after κ=1×10$^{-8}m^2$, whilst for the liquid phase both inertial and viscous terms are negligible with respect to the gravitational term. Nevertheless, interfacial friction begins to take an important role at large permeability values (κ>4×10$^{-7}m^2$).

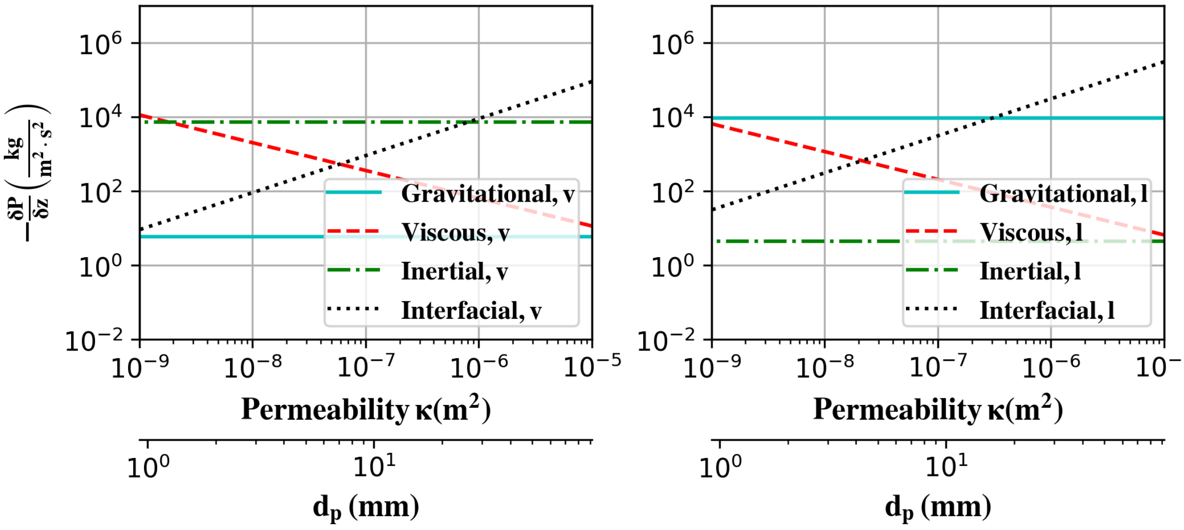

Figure 4.7 – Pressure drop terms of eq. (2.3) evaluated with $j_{v,\tau}^{crit}$ (eq. (4.18)) and $j_{l,\tau}^{crit}$(eq. (4.19)) as a function of κ and m=5

Left: Pressure loss terms for vapor phase; Right:Pressure loss terms for liquid phase

Energy balance

Inserting eq. (4.5) into eq. (4.9):

$$\phi = \left[\sqrt{\frac{\rho_l \eta g}{\frac{1}{\rho_l \eta_{r,l}} + \frac{1}{\rho_v \eta_{r,v}}}} - \rho_{v,0} j_{v,0}\right] h_{lv} = \left[\sqrt{\frac{\rho_l \eta g}{\frac{1}{\rho_l (1-\alpha)^m} + \frac{1}{\rho_v \alpha^m}}} - \rho_{v,0} j_{v,0}\right] h_{lv} \tag{4.20}$$

Once again, the critical heat flux in two-phase flow is obtained by evaluating eq. (4.20) at $j_{v,\tau}^{crit}$, hence at $\alpha = \alpha_\tau^{crit}$, which would result in:

$$\phi_\tau^{crit} = \left[\sqrt{\frac{\rho_l \rho_v \eta g}{\left[1 + \frac{\rho_v}{\rho_l}^{\frac{1}{m+1}}\right]^{m+1}}} - \rho_{v,0} j_{v,0}\right] h_{lv} = \left[\sqrt{\frac{\rho_l \rho_v \frac{\sqrt{150}}{1.75} \varepsilon^{\frac{3}{2}} \sqrt{\kappa g}}{\left[1 + \frac{\rho_v}{\rho_l}^{\frac{1}{m+1}}\right]^{m+1}}} - \rho_{v,0} j_{v,0}\right] h_{lv} \tag{4.21}$$

As before, in the case of no vapor coming from the concrete decomposition, eq. (4.21), simplifies to:

$$\phi_\tau^{crit} = \sqrt{\frac{\rho_l \rho_v \eta g h_{lv}^2}{\left[1 + \frac{\rho_v}{\rho_l}^{\frac{1}{m+1}}\right]^{m+1}}} = \sqrt{\frac{\rho_l \rho_v \frac{\sqrt{150}}{1.75} \varepsilon^{\frac{3}{2}} \sqrt{\kappa} g h_{lv}^2}{\left[1 + \frac{\rho_v}{\rho_l}^{\frac{1}{m+1}}\right]^{m+1}}} \tag{4.22}$$

Equation (4.20) corresponds directly to Lipinski's 0D model in the inertial regime (eq.(6-9) in Lipinski [207]).

It is possible to build an analytical solution for the full problem at all ranges of permeability κ, still neglecting capillary effects, by merging ϕ_λ^{crit} and ϕ_τ^{crit} as follows:

$$\phi_{\lambda-\tau} = min(\phi_\lambda^{crit}, \phi_\tau^{crit}) \tag{4.23}$$

4.1.3 Capillary effects

Including the capillary effects can be done by adding eq. (2.10) into the momentum balance equations and linearizing the term $\frac{\delta P_c}{\delta z}$ over the entire length of the debris bed Z [m] by $\frac{\delta J\left(S^*\right)}{\delta z} = \frac{\varDelta J\left(S^*\right)}{\varDelta Z}$. To do this, one must evaluate the difference in the Leverett function between the bottom and the top of the debris be. Firstly, assuming that at the bottom of the bed, Z=0, there is no vapor flux coming from underneath the debris bed, the void fraction would be 0; hence the effective saturation is null, and so is the Leverett J-function. On the other hand, if the void fraction over the entire length of the debris bed is constant (coming from the evaporation of the water due to the residual power in the debris bed components), the term $\frac{J\left(S^*\right)}{z}$

can be evaluated at α_{crit}. In this case, $\dfrac{\Delta J\left(S^{*}\right)}{\Delta Z}=\dfrac{J\left(S^{*}@\alpha_{crit}\right)-J\left(S^{*}@\alpha=0\right)}{\Delta Z}=\dfrac{J\left(S^{*}@\alpha_{crit}\right)-0}{\Delta Z}$ Hence $\Delta J\left(S^{*}\right)$ can be approximated as $J\left(S^{*}@\alpha_{crit}\right)$. More reliable formulations may be established, but the one here used may be sufficient at first contrasting the uncertainty arising from it with the various significant uncertainties from other parameters.

Introducing a capillary length[9] as Λ_c as:

$$\Lambda_c=\frac{\sigma_{lv}\cos\left(\theta\right)}{\rho_l g}\sqrt{\frac{\varepsilon}{\kappa}} \tag{4.24}$$

In fact, this leads to a corrective term to be multiplied for the previous laminar and inertial critical fluxes (eq. (4.12) and eq. (4.22) respectively), and eq. (4.23) would then become:

$$\phi_{\lambda-\tau,c}=min\left(\phi_{\lambda}^{crit}\left(1+\frac{\Delta J\left(S^{*}\right)}{\Delta Z}\Lambda_c\right),\phi_{\tau}^{crit}\sqrt{1+\frac{\Delta J\left(S^{*}\right)}{\Delta Z}\Lambda_c}\right) \tag{4.25}$$

Figure 4.8 plots the capillary length as a function of the permeability in the ranges of interest. As can be seen, the capillary length increases as the permeability decreases, whilst the same can be said when the porosity, ε, increases. On the right part of the figure, the evaluation of the Leverett J-function with the 4 different formulations presented in table 2.6 shows completely different values depending on the formulation. Nevertheless, for a value close to α_{λ}^{crit}, most are between 0.4-0.6; hence the value of capillary length shown in the left part would be halved.

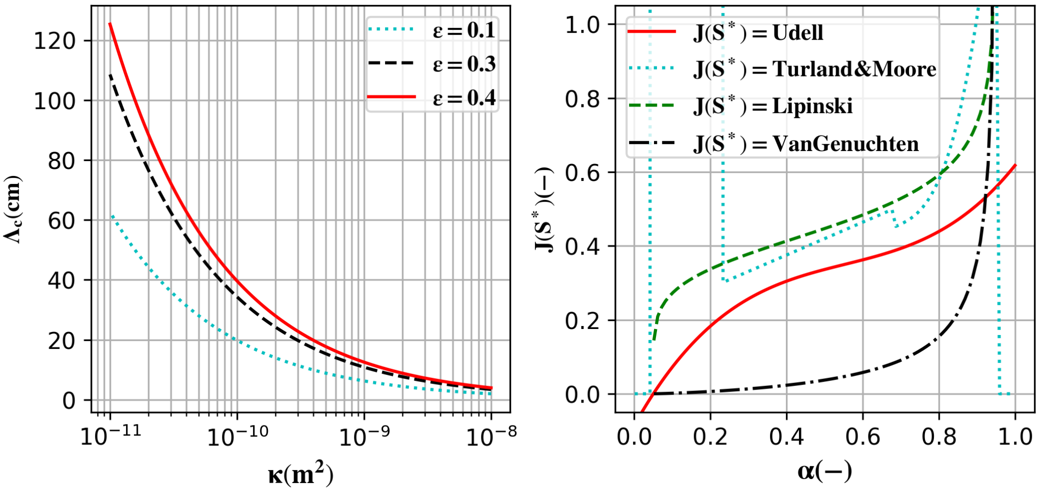

Figure 4.8 – Capillary length and the Leverett J-function. Left:Capillary length as a function of the κ for 3 different values of ε; Right:$J\left(S^{*}\right)$ function as a function of α for the 4 different formulations presented in table 2.6 with $S_{ir}=S_{irg}=0.05$

---

[9] Noting that Lipinski [109] suggests a formula presented in table 2.6 to evaluate the Leverett J-function. Nevertheless, the final formula for Λ_c given in eq.(4-1) in [109] the function $J\left(S^{*}\right)$ disappears and a 6 is placed coming from the division of a $\sqrt{150}$ by the $\sqrt{5}$ in his $J\left(S^{*}\right)$. Nevertheless, the term linked to the effective saturation disappears. Evaluating his proposed formula for $J\left(S^{*}\right)$ for a range of values of S^{*}does not equal to 6 in any case, hence deviating from the original formulation of Leverett.

The subscript c is added to indicate the capillary term has been added to the corresponding equation. For the case of $\phi_{i,c}^{crit}$ (with the subscript "i" either λ for the laminar regime and τ for the inertial regime), it is noticed that with the approximation $\frac{\delta J\left(S^{*}\right)}{\delta z}=\frac{\Delta J\left(S^{*}\right)}{\Delta Z}$, the critical flux depends on the height of the flooded bed Z (or height between the beginning of the flooded area and the location of the critical point). Figure 4.9 plots the derived critical heat flux, eq. (4.23), and eq. (4.25) as a function of permeability (with the approximate corresponding d_p in the secondary x-axis underneath) against experimental data. The dots plot a series of different dry-out experiments with a similar configuration (cylindrical test section, atmospheric pressure, water injection from the top, initially flooded debris bed, injected water temperature at, or close to, saturation temperature, steel particles, similar debris bed height, etc.) from Hofmann [118], Miyazaki et al. [117], Barleon et al. [116], Atkhen & Berthoud [122], Squarer et al. [123], amongst other taken from the review paper of Lipinski [207] (from the unpublished works of Barleon & Werle, Gabor & Cassulo, Dhir & Catton, Keowin, Gabor et al., Somerton et al., Trenberth & Stevens, Squarer & Peoples, Sowa). The debris bed heights ranged from 0.02 m to 0.64 m with a mean of 0.15 m. The solid black curve plots eq. (4.23) without taking into account capillary effects, whilst both the dotted and the dashed black lines plot eq. (4.25) using the Udell formulation [200] for two different debris bed height. Despite simplifications, the formulation seems sufficiently accurate for the inertial regime, noting a slight underestimation that may be adjusted by changing the coefficient "m" used for the relative passability correlations. In the laminar regime, the situation is much more complex as the proposed formulation seems to give a minimum. The large scatter of experimental result is in general attributed to the fact that, in such conditions, the actual characteristics of the debris bed, notably the permeability, are often uncertain, as they may be modified by the flow forces themselves (small particles may move at the top section of the bed and modify the configuration, hence the dry-out heat flux [117]). At low values of bed height, this last may drastically modify the initial conditions, giving rise to a larger experimental scatter. Nevertheless, the capillary effects are perceptible, although they are still largely within the scatter.

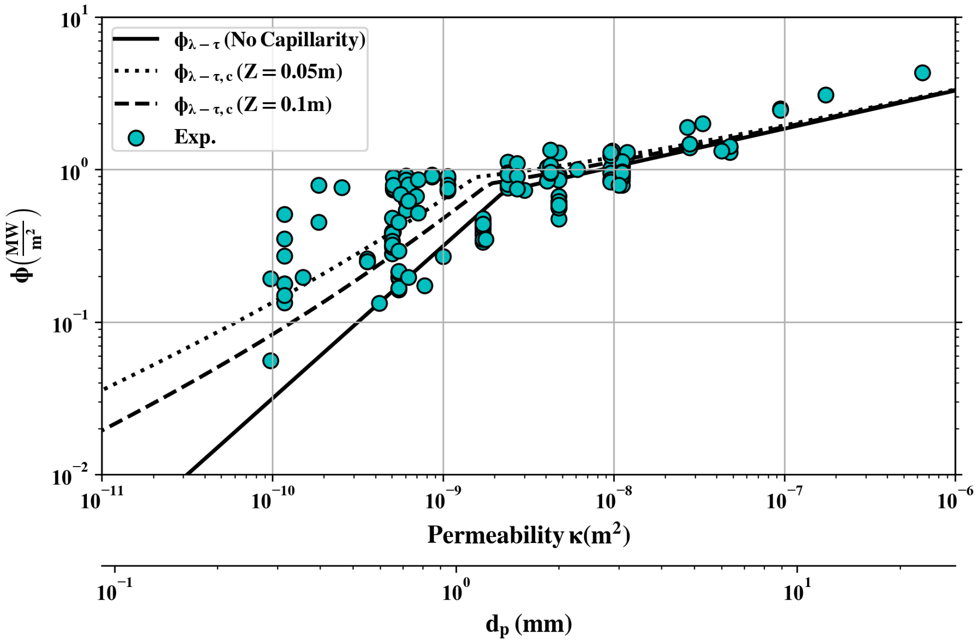

Figure 4.9 – $\phi_{\lambda-\tau}$, eq. (4.23), and $\phi_{\lambda-\tau,c}$ using the Udell formulation presented in table 2.6 as a function of permeability compared to the experimental data

The use of the different correlations presented in table 2.6 leads to changes that are moderate and still within the uncertainties as can be seen in figure 4.10, which plots eq. (4.23) evaluated with the different correlations for relative permeabilities. As can be seen, both Udell and Turland & Moore correlations give a similar behavior, whilst vanGenuchten correlation follows the same trend but results in a lower ϕ. For all further capillary applications, Udell's formulation will be used for $J(S^*)$ for simplicity.

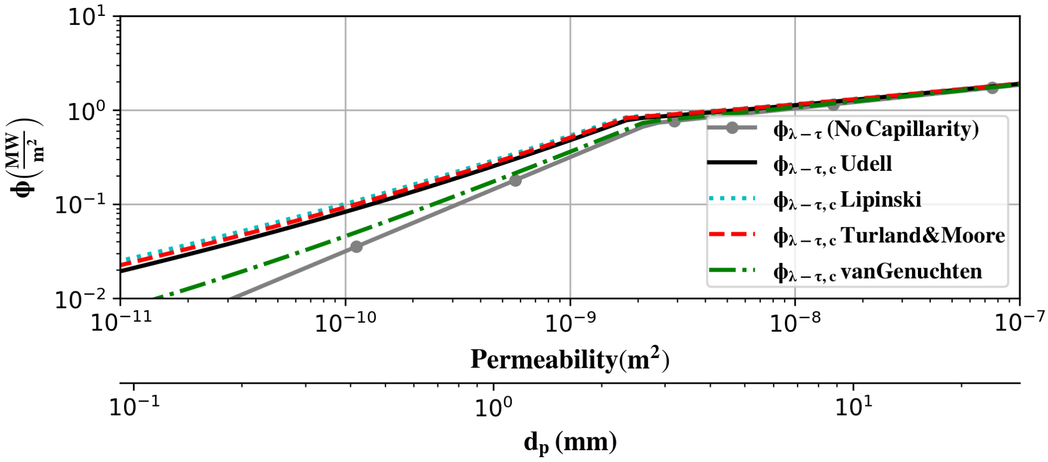

Figure 4.10 – $\phi_{\lambda-\tau}$, eq. (4.23), and $\phi_{\lambda-\tau,c}$, eq. (4.25), evaluated with different capillarity functions presented in table 2.6 and Z=0.1m as a function of κ

4.1.4 Mixed case

By observing both figure 4.2 and figure 4.7 it is easily concluded that a purely inertial model is not completely representative. More precisely, it is observed that for the vapor phase the more predominant friction terms are the laminar and inertial terms. For the liquid phase, the gravitational and the laminar terms dominate the pressure drop over the ranges of κ of interest (up to debris bed with particles of $d_p \leq 10mm$). The interfacial friction term may begin to be of interest for the liquid phase starting from $\kappa = 10^{-8}m^2$. Furthermore, it can be seen that whatever the case, the total pressure drop is dominated by the vapor phase until around $\kappa = 10^{-7}m^2$. This means that to obtain one equation that is valid throughout the range of permeability of interest, up to $\kappa = 10^{-7}m^2$, the momentum balance equation between both phases can be written as [10]:

$$-\frac{\delta P}{\delta z} = \frac{\rho_v}{\eta\eta_{r,v}}|j_v|j_v + \frac{\mu_v}{\kappa\kappa_{r,v}}j_v = \frac{\mu_l}{\kappa\kappa_{r,l}}j_l + \rho_l g \tag{4.26}$$

Solving from eq. (4.4) and eq. (4.26), $j_{v,mix}$ can be expressed as:

$$j_{v,mix} = \left(\frac{\nu_v}{\kappa_{r,v}} + \frac{\nu_l}{\kappa_{r,l}}\right)\frac{\eta}{\kappa}\frac{\eta_{r,v}}{2}\left[\left(1 + \frac{4\dfrac{\kappa^2}{\eta}\dfrac{1}{\eta_{r,v}}\dfrac{\rho_l}{\rho_v}g}{\left(\dfrac{\nu_v}{\kappa_{r,v}} + \dfrac{\nu_l}{\kappa_{r,l}}\right)^2}\right)^{\frac{1}{2}} - 1\right]$$

$$j_{v,mix} = \left(\frac{\nu_v}{\kappa_{r,v}} + \frac{\nu_l}{\kappa_{r,l}}\right)\frac{\sqrt{150}}{1.75}\sqrt{\frac{\varepsilon^3}{\kappa}}\frac{\eta_{r,v}}{2}\left[\left(1 + \frac{4\dfrac{\sqrt{150}}{1.75}\sqrt{\dfrac{\varepsilon^3}{\kappa^3}}\dfrac{1}{\eta_{r,v}}\dfrac{\rho_l}{\rho_v}g}{\left(\dfrac{\nu_v}{\kappa_{r,v}} + \dfrac{\nu_l}{\kappa_{r,l}}\right)^2}\right)^{\frac{1}{2}} - 1\right] \tag{4.27}$$

were $j_{v,mix}$ $\left[\frac{m}{s}\right]$ is the superficial vapor velocity for the mixed regime (denoted with the subscript mix. Figure 4.11, figure 4.12, and figure 4.13 plot the vapor superficial velocity j_v using the three different models for three different values of κ (with d_p =0.89, 3.18, and 8.5 mm) as a function of alpha. In all three figures $j_{v,\lambda}$ (eq. (4.5)), $j_{v,\tau}$ (eq. (4.16)), and $j_{v,mix}$ (eq. (4.27)) are plotted by the dashed blue curves, the red dotted curves and the solid green curves respectively. As can be seen, $j_{v,mix}$ resembles both $j_{v,\lambda}$ and $j_{v,\tau}$ in their respective domain. In the laminar regime, the lower the κ the closer both values get to one another (i.e. at really low values of κ $j_{v,mix} = j_{v,\lambda}$), whilst approaching to the limit of the laminar regime, $j_{v,mix}$ is lower than $j_{v,\lambda}$. On the other hand, for the inertial regime, the larger the value of κ, the larger the value of the maximal $j_{v,mix}$. This increment of the maximal j_v in the laminar regime for the mixed model comparing to the symmetrical inertial model (using the same coefficient for the relative passabilities "m "=5) comes from the fact that the liquid laminar friction term in eq. (4.26) is less restrictive than the liquid inertial friction term in eq. (4.15), both of which govern the second part of the curve (at large

---

[10] The interfacial friction terms can be included, but this leads to a formulation that is not easily traceable.

values of α).

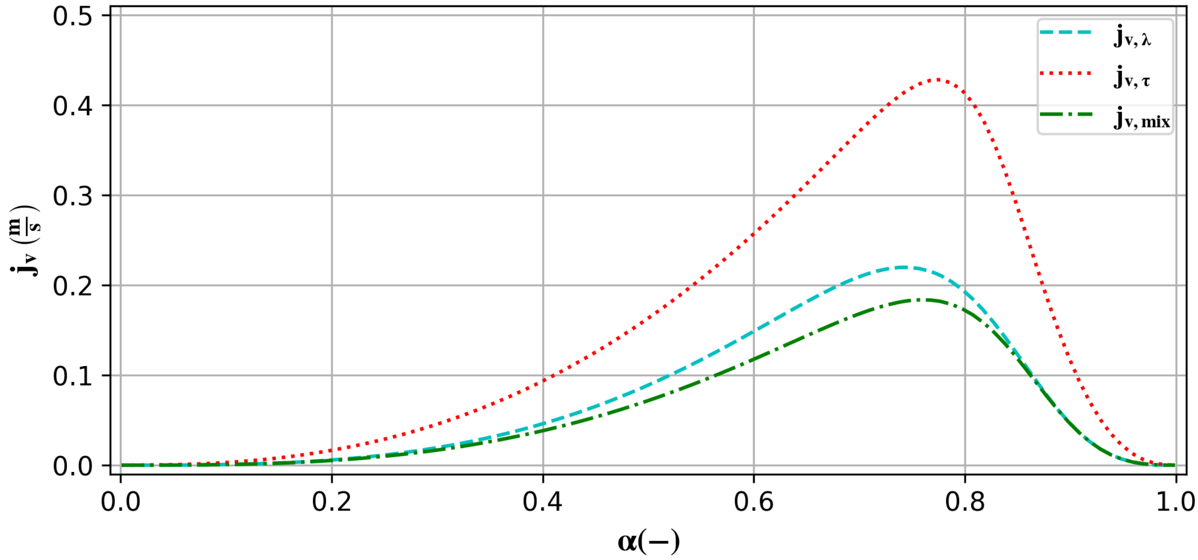

Figure 4.11 – j_v evaluated with eq. (4.5), eq. (4.16), and eq. (4.27) as a function of α with κ=$1.2\times10^{-9}m^2$ ($d_p = 0.89mm$)

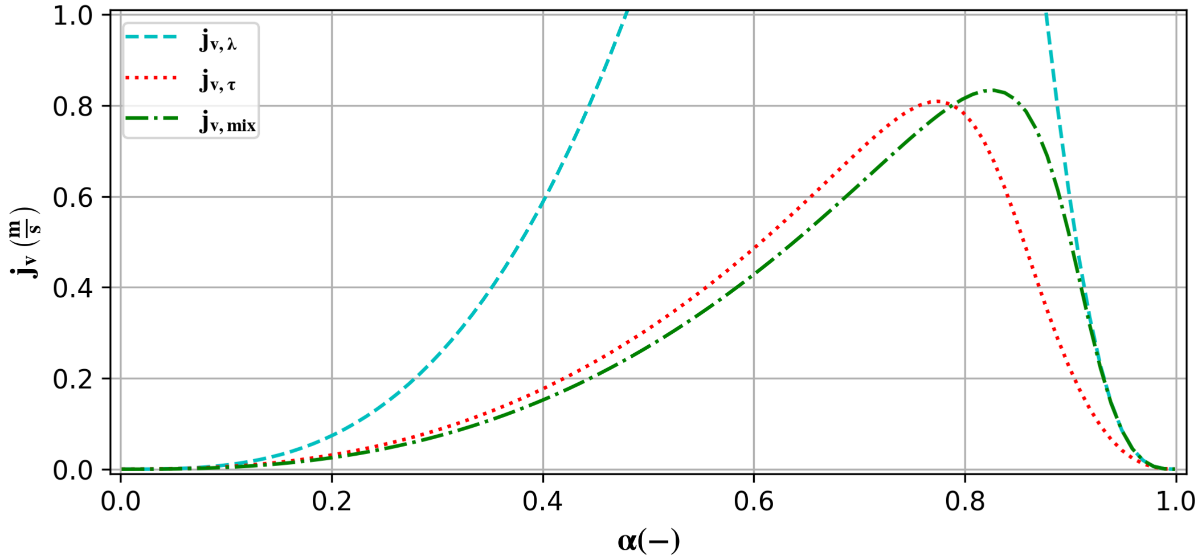

Figure 4.12 – j_v evaluated with eq. (4.5), eq. (4.16), and eq. (4.27) as a function of α with κ=$1.2\times10^{-8}m^2$ ($d_p = 3.18mm$)

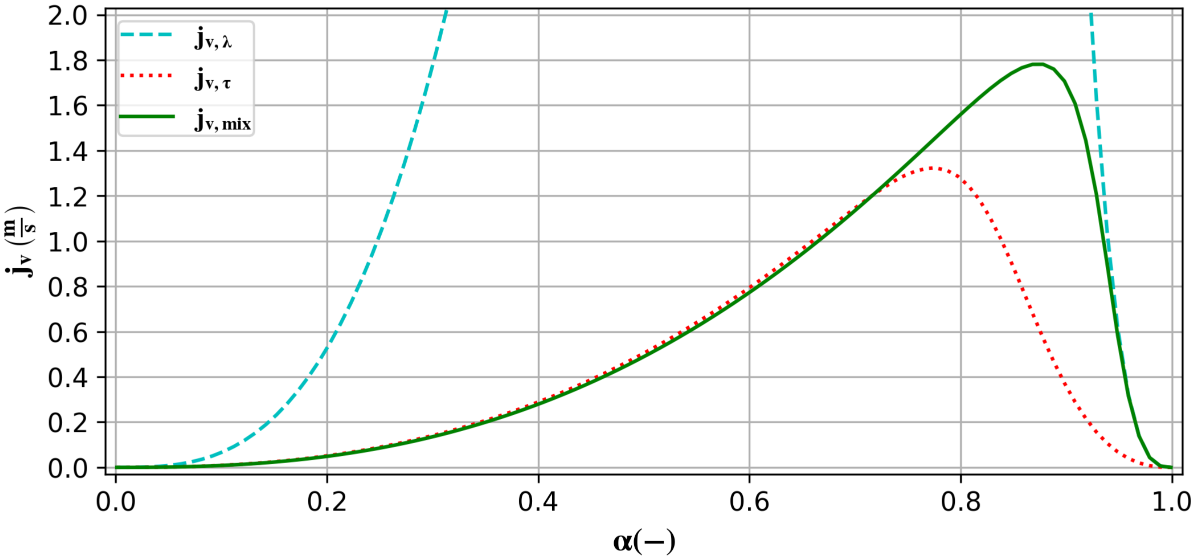

Figure 4.13 – j_v evaluated with eq. (4.5), eq. (4.16), and eq. (4.27) as a function of α with κ=8.6×10$^{-8}m^2$ ($d_p = 8.5mm$)

Nevertheless the location of the maximal α is neither α_λ^{crit} nor α_τ^{crit}, but a value between α_λ^{crit} and 1. This last value cannot be easily obtained analytically by following the same method as in section 4.1.1 and section 4.1.2, but can be numerically obtained without major difficulties.

Adding the capillary term results in:

$$j_{v,mix,c} = \left(\frac{\nu_v}{\kappa_{r,v}} + \frac{\nu_l}{\kappa_{r,l}}\right)\frac{\eta}{\kappa}\frac{\eta_{r,v}}{2}\left[\left(1 + \frac{4\frac{\kappa^2}{\eta}\frac{1}{\eta_{r,v}}\frac{\rho_l}{\rho_v}g}{\left(\frac{\nu_v}{\kappa_{r,v}} + \frac{\nu_l}{\kappa_{r,l}}\right)^2}\left(1 + \frac{\Delta J\left(S^*\right)}{\Delta Z}\Lambda_c\right)\right)^{\frac{1}{2}} - 1\right] \tag{4.28}$$

Re-evaluating eq. (4.9), with eq. (4.28) results in:

$$\phi_{mix,c} = \left(\frac{\nu_v}{\kappa_{r,v}} + \frac{\nu_l}{\kappa_{r,l}}\right)\frac{\eta}{\kappa}\frac{\eta_{r,v}}{2}\rho_v h_{lv}\left[\left(1 + \frac{4\frac{\kappa^2}{\eta}\frac{1}{\eta_{r,v}}\frac{\rho_l}{\rho_v}g}{\left(\frac{\nu_v}{\kappa_{r,v}} + \frac{\nu_l}{\kappa_{r,l}}\right)^2}\left(1 + \frac{\Delta J\left(S^*\right)}{\Delta Z}\Lambda_c\right)\right)^{\frac{1}{2}} - 1\right] \tag{4.29}$$

The value at which $\phi_{mix,c}$ is maximal, $\phi_{mix,c}^{crit}$, is obtained by numerically searching for the value of α that maximizes it. Figure 4.14 compares $\phi_{mix,c}^{crit}$, eq. (4.29), with $\phi_{\lambda-\tau}$, eq. (4.23), as a function of κ. The black curve plots $\phi_{\lambda-\tau}$, whilst the red curves plot $\phi_{mix,c}^{crit}$. The dashed and dashed-dotted plot both equations taking into account the capillary terms using two different values for Z. As can be seen, $\phi_{mix,c}^{crit}$ can accurately capture the trends for both regimes without the need of minimizing between the purely laminar and purely inertial formulations. Comparing with eq. (4.23), it can be seen that for large values

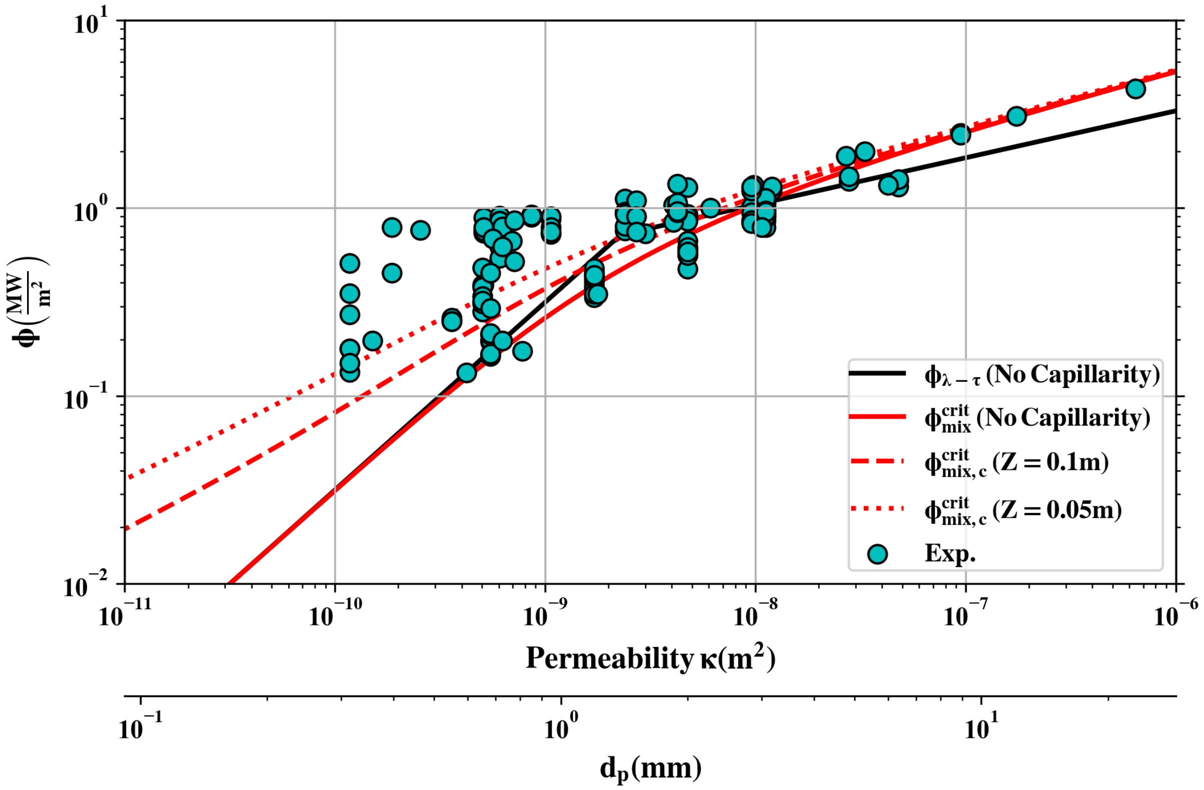

Figure 4.14 – $\phi_{\lambda-\tau}$, eq. (4.23), $\phi_{mix,c}^{crit}$, eq. (4.29), as a function of permeability compared to the experimental data

of κ, i.e., in the inertial regime, the value is higher and fits better the experimental data without the need of modifying the coefficients "m" used. The validity of choice for the coefficient "m" to be used is questionable, nevertheless as stated by Clavier [221], a larger coefficient "m" translates to an increased pressure loss hence a lower water percolation and a lower CHF. Here the coefficient m=5, as proposed by Reed [187], is deemed the most accurate for the current purpose. Overall, $\phi_{mix,c}^{crit}$ can be used as to obtain the steady-state value of CHF for a debris bed as a continuous function regardless of the value of κ. However, for this case, the value of α at which the maximum is located, α_{mix}^{crit}, cannot be easily found analytically. For this reason, and observing that in the respective domains, the mixt model and the fully laminar or inertial models are equivalent. In the subsequent sections, either the fully laminar or the fully inertial formulation will be used to extend to an unsteady 1D water penetration configuration.

Figure 4.15 shows the results of the COOLOCE experiments [102], [124], [222] which were conducted at varying pressures. The debris bed was formed of a mixture of particles varying from 0.815 - 1.126 millimeters in diameter, with a mean of 0.97. Plotted in black dots are the experimental data, the red dashed-dotted line, the blue dashed line, and the green dotted line plot $\phi_{\lambda-\tau}$, eq. (4.23), ϕ_{mix}^{crit}, eq. (4.29) without the capillary term, and Epstein's model, eq. (2.13), respectively with d_p=0.97 mm. The colored shaded regions plot the same equations evaluated with the experimental minimum and maximum d_p of 0.815 and 1.126 mm. As can be seen, eq. (4.29) follows best the experimental trend, whilst eq. (4.23) overestimates the extracted heat flux at higher pressures. Epstein's model quickly overestimates the

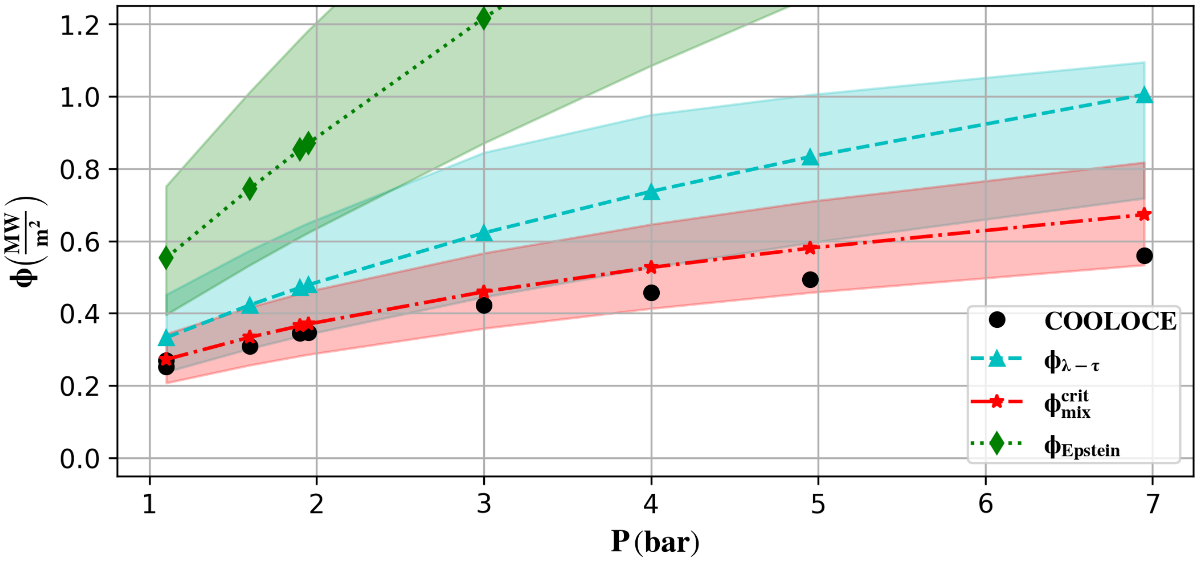

Figure 4.15 – $\phi_{\lambda-\tau}$, eq. (4.23), ϕ_{mix}^{crit}, eq. (4.29) without the capillary term, and Epstein's model, eq. (2.13), as a function of pressure compared to COOLOCE experimental data using $\varepsilon = 0.39$, d_p=0.97 mm for the curves, and d_p=0.815 and 1.126 mm for the shaded regions.

extracted value and does not function well at high pressures. This is to no surprise, as it does not include any liquid viscosity terms, which become essential at higher pressures.

4.2 One-dimensional top-reflooding model

At a certain moment after its creation, the debris bed is to be first reflooded with water traversing through the entire length of the debris bed. In this section, the unsteady 1D water penetration, depicted in figure 4.16, will be studied. The debris bed is once again characterized by its permeability, κ, which could be constant or a function of z (κ=κ(z)). The green zone represents the already quenched portion of the debris bed ($T = T_0$, whilst the black zone is the remaining unquenched zone.

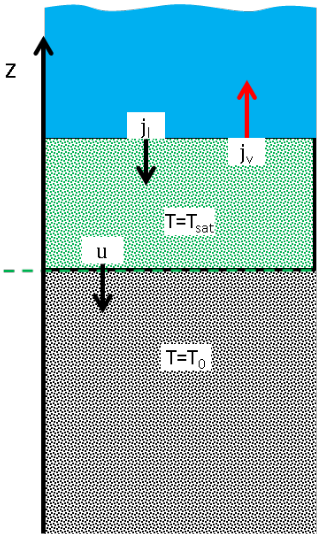

Figure 4.16 – 1D water penetration scheme

As compared to the steady-state case, there will be an additional vapor flux coming from underneath the front.

Assuming that the flow below the front is steady, that the front has no thickness (sharp front), and that along z the energy is entirely converted into latent heat of vaporization (total equilibrium of liquid and water vapor), the effective mass flux (and heat flux), eq. (4.9), can be expressed as:

$$j_v \rho_v = \frac{1}{h_{lv}} \left[\phi_z + u\left(1-\varepsilon_0\right)\rho_d c_{p,d} \mathit{\Delta} T\right] + \rho_{v,0} j_{v,0} \tag{4.30}$$

with $\phi_z = P_v Z \left[\frac{MW}{m^2}\right]$ being the volumetric residual power over the entire length Z per unit surface, $c_{p,d}$ $\left[\frac{J}{kgK}\right]$ the heat capacity of the material that constitutes the debris bed , $\mathit{\Delta} T$ $[K]$ being the temperature difference between the initial temperature of the debris bed, T_0, and T_{sat}, ε_0 $[-]$ the porosity at the lower boundary (here equal to ε), and u $\left[\frac{m}{s}\right]$ the velocity of the cooling front.

It is important to note that if the front progresses, there would be a disequilibrium in the mass balance since a mass fraction, here called, X_{H_2O} $[-]$ would be used to fill (partially) the empty pores at the front. As before, for simplicity the vapor flux coming from below will be neglected, hence eq. (4.4) can be rewritten as:

$$j_v \rho_v + \rho_l \left(j_l + X_{H_2O} u \varepsilon_0\right) = 0 \tag{4.31}$$

4.2.1 Laminar regime

In the laminar regime, solving for the unsteady superficial velocity j_v (here called $j^P_{v,\lambda}$) using eq. (4.31), and eq. (4.3) (laminar term for the vapor phase; laminar, and gravitational for the liquid phase, and including capillary term), and with $u = u_\lambda$ results in:

$$j^P_{v,\lambda} = \frac{\frac{\rho_l}{\rho_v} Kg}{\frac{\nu_l}{\kappa_{r,l}} + \frac{\nu_v}{\kappa_{r,v}}} \left(1 - \frac{\nu_l}{\kappa_{r,l}} \frac{\varepsilon_0 X_{H_2O} u_\lambda}{\kappa g} + \frac{\varLambda_c}{Z} \varDelta J\left(S^*\right)\right) \tag{4.32}$$

From eq. (4.30) and eq. (4.32), u_λ, the front penetration velocity, can be expressed as:

$$u_{\lambda,c} = \frac{\rho_l g \kappa \kappa_{r,l} h_{lv} \left(1 + \frac{\varLambda_c}{Z} \varDelta J\left(S^*\right)\right) - \phi_z \kappa_{r,l} \left(\frac{\nu_l}{\kappa_{r,l}} + \frac{\nu_v}{\kappa_{r,v}}\right)}{\mu_l X_{H_2O} \varepsilon_0 h_{lv} + \left(1 - \varepsilon_0\right) \rho_d c_{p,d} \varDelta T \kappa_{r,l} \left(\frac{\nu_l}{\kappa_{r,l}} + \frac{\nu_v}{\kappa_{r,v}}\right)} \tag{4.33}$$

Since the experiments consider the top-reflooding configuration of a debris bed without volumetric power, the term ϕ_z is 0. Adding to this, assuming that on top of the flooding front, the configuration does not evolve with height (boiling occurs at the front only) hence the term $\varDelta J\left(S^*\right)$ is null, and thus so is the capillary effect.

In this work, this last term is also presumed to be negligible at the front itself, particularly regarding to the strong boiling effects. Furthermore, if one is to take the formulation of the Leverett J-function, evaluating $\frac{\varDelta J\left(S^*\right)}{\varDelta Z}$, in this case, is more problematic. Just below the front $\alpha = 1$ since there is no liquid water present, only a fraction of the vapor produced during the evaporation. In this case $\frac{\varDelta J\left(S^*\right)}{\varDelta Z} = \frac{J\left(S^* @ \alpha_{crit}\right) - J\left(S^* @ \alpha = 1\right)}{\varDelta Z}$ is negative since $J\left(S^* @ \alpha = 1\right) > J\left(S^* @ \alpha_{crit}\right)$. This would suggest that the capillary pressure, in this case, would impede the front to advance since the liquid water would instead be "pulled inside" the finger and not in the direction of the advancing front. Although saturation overshoot has been observed in porous media experiments (as seen in section 2.1.4), it is highly dubious that the formulation for the capillary pressure here presented remains valid with high temperatures and residual power both contributing to evaporation of the liquid water, with an advancing front and in transient conditions. The capillary pressure formulations in this situation surely need revisiting in order to conclude its role in the coolability of the porous media, but it remains an important research effort surpassing the purpose of this work.

For these reasons, for the laminar regime without volumetric power and neglecting the capillary effects, the formulation reduces to:

$$u_\lambda = \frac{\rho_l g \kappa \kappa_{r,l} h_{lv}}{\mu_l X_{H_2O} \varepsilon_0 h_{lv} - \left(1 - \varepsilon_0\right) \rho_d c_{p,d} \varDelta T \kappa_{r,l} \left(\frac{\nu_l}{\kappa_{r,l}} + \frac{\nu_v}{\kappa_{r,v}}\right)} \tag{4.34}$$

Equation (4.34) may be further simplified if the term $\mu_l X_{H_2O} \varepsilon_0 h_{lv}$ can be neglected. In such case, u_λ can be written as:

$$u_\lambda = \frac{\phi_\lambda^{crit}}{(1-\varepsilon_0)\,\rho_d c_{p,d} \Delta T} \tag{4.35}$$

where ϕ_λ^{crit} is the critical heat flux for a homogenous debris bed, described by eq. (4.11) and eq. (4.12). Then,

$$\phi_\lambda^P = u_\lambda\,(1-\varepsilon_0)\,\rho_d c_{p,d} \Delta T = \phi_\lambda^{crit} \tag{4.36}$$

the penetration heat flux ϕ_λ^P becomes the critical heat flux in the same homogeneous debris bed, without consideration of the capillary effects. This result is then subject to the hypothesis that $\mu_l X_{H_2O} \varepsilon_0 h_{lv}$ is negligible compared to the evaporation effects. This hypothesis can be evaluated, and the result can be seen in figure 4.17, where both terms in the denominator of eq. (4.34) are compared for two different temperatures, considering that the upstream flow behaves similarly to a critical cooling flow in a heated debris bed. Both terms $\kappa_{r,l}$ and $\kappa_{r,v}$ are evaluated at $\alpha = \alpha_\lambda^{crit}$ using the equation presented in table 2.4 using the Reed coefficients. As the water saturation X_{H_2O} after the front should be quite close to the "critical" water saturation ($\sim 0.2-0.3$, it is seen that the impact is small and often negligible. Furthermore, with increasing temperature, the effects become more negligible.

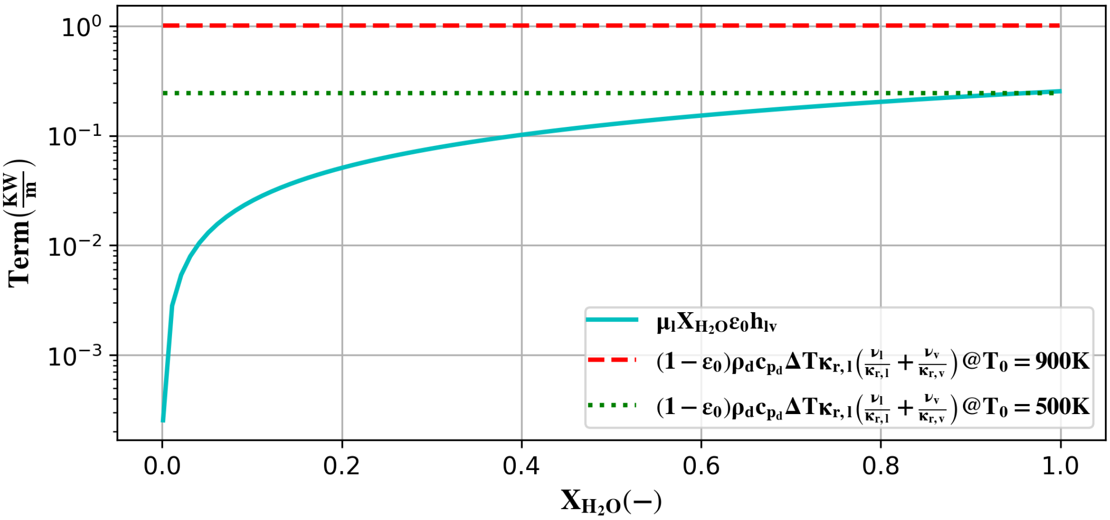

Figure 4.17 – Denominator terms in eq. (4.34) as a function of X_{H_2O} evaluated at $\alpha = \alpha_\lambda^{crit}$ at different temperatures T_0

To conclude this point, the rather common hypothesis eq. (4.36) is legitimate in the following conditions:

- negligible effect of the additional water necessary for the progressing front (high temperature, small porosity);
- no account of the capillary effects (no internal power); and

- the flow structure is upstream, dictated by the critical flow that can allow the necessary transport of heat by the vapor.

The second condition is somewhat subject to the uncertainty of the hypotheses here used. This may however, mean that the heat flux in a penetrating unheated medium (as it is the case for the experiments) is larger than the critical one in a heated medium.

The third condition means that ϕ_λ^{crit} in eq. (4.36) should not be considered at the local conditions around the cooling front but at the upstream smallest permeability.

For the case of water penetrating a heated material, as expected in a real accidental situation, the scenario is a bit more complex:

- local capillary effects should be added;
- the flow structure (local saturation) changes along the cooled region.

4.2.2 Inertial and mixed regimes

For the fully inertial regime, as discussed previously, the capillary pressure effects can be neglected. Following the same approach as before, the front velocity u_τ is given by the following 2 equations that can be solved numerically:

$$j_{v,\tau}^P = \frac{1}{\rho_v \eta_{r,l}} \frac{X_{H_2O}\varepsilon_0 u_\tau}{\left(\frac{1}{\rho_l \eta_{r,l}} + \frac{1}{\rho_v \eta_{r,v}}\right)} \left(1 \pm \sqrt{1 - \rho_v \eta_{r,l} \left(\frac{1}{\rho_l \eta_{r,l}} + \frac{1}{\rho_v \eta_{r,v}}\right) \left(1 - \frac{g \eta \eta_{r,l}}{X_{H_2O}^2 \varepsilon_0^2 u_\tau^2}\right)}\right) \tag{4.37}$$

$$u_\tau = \frac{j_{v,\tau}^P \rho_v h_{lv} - \phi_z}{(1 - \varepsilon_0)\, \rho_d c_{p,d} \Delta T} \tag{4.38}$$

Finally for the mixed case, the front velocity u_{mix} is given by the following 2 equations (that can be solved numerically without major difficulties):

$$j_{v,mix}^P = \left(\frac{\nu_l}{\kappa_{r,l}} + \frac{\nu_v}{\kappa_{r,v}}\right) \frac{\eta}{\kappa} \frac{\eta_{r,v}}{2} \left[\sqrt{1 + 4\frac{\kappa^2}{\eta} \frac{1}{\eta_{r,v}} \left(\frac{\nu_l}{\kappa_{r,l}} + \frac{\nu_v}{\kappa_{r,v}}\right)^{-2} \left(1 - \frac{\varepsilon_0 X_{H_2O} u_{mix}}{\kappa g} \frac{\nu_l}{\kappa_{r,l}}\right)} - 1\right] \tag{4.39}$$

$$u_{mix} = \frac{j_{v,mix}^P \rho_v h_{lv} - \phi_z}{(1 - \varepsilon_0)\, \rho_d c_{p,d} \Delta T} \tag{4.40}$$

To evaluate the representativity of the model, one-dimensional MC3D calculations were performed. Some slight modifications to the code were introduced and are discussed in appendix A. For these calculations, the simulation domain was constructed to resemble the Ginsberg experiments, with a water injection boundary condition that matched the top of the debris bed. A series of simulations with varying T_0, and particle diameter d_p were made. Figure 4.18 shows as an example a MC3D calculation at one particular instant in time (t=370 s.). In it, it is possible to see that for this 1D calculation, the distance between the advancement of the water, and the totally quenched region is rather small. In other words, the advancing front is rather thin. Furthermore, the liquid saturation (shown in the left part of the figure) can be seen to be in the order of 25-30 %, which is in coherence with what is expected from the model.

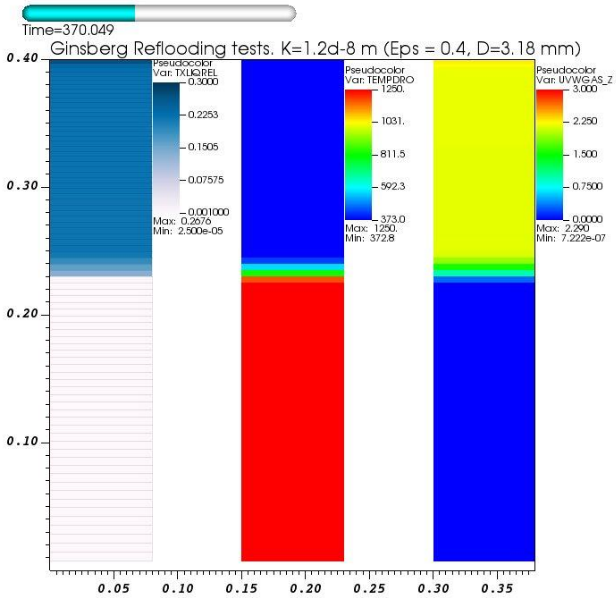

Figure 4.18 – 1D Ginsberg like MC3D calculation showing the penetrating front in the left, the temperature of the debris in the middle, and the vapor velocity in the right at t=370 seconds with d_p= 3mm, P=1atm, and T_0= 1250 K

Figure 4.19 shows the comparison of the 1D unsteady model (solid red curve) in both regimes (left: laminar, right: inertial) compared with the 1D unsteady mix model (dashed orange curve) for the corresponding debris bed with 1D MC3D simulations (green triangles) and the experimental results coming from Ginsberg et al. [130] (blue circles) at different temperatures T_0. It must be reminded that, in these experiments, the flooding occurred in two steps, first with the development of water channels that penetrate the bed. This last signifies, in essence, that the flooding occurs in a two dimensional way. However, it was estimated that these channels occupied a surface fraction of about 0.3-0.4. Thus, in the 1D model, the front velocity is expected to be lower by an inverse factor of the surface fraction (to extract the same amount of energy). As can be seen, the 1D model shows the same trend as the experimental data and the MC3D calculation results, where the downward front velocity u decreases as the temperature increases. Considering the previous comments regarding the 2D nature of the flow in the experiments, one may conclude that the front velocity is slightly overestimated, except at low temperatures where the velocity is underestimated (low ΔT with respect to T_{sat}). The MC3D calculations reproduce the experiments qualitatively, except for the case at low permeability and high temperatures.

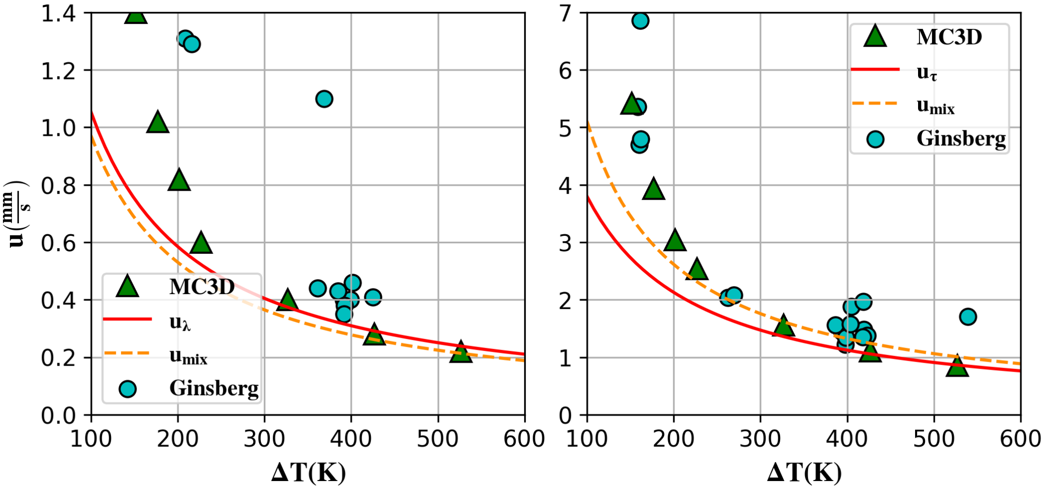

Figure 4.19 – Penetrating front velocity comparison, Ginsberg et al. [130] vs. MC3D 1D simulations and 1D unsteady model with $\rho_d = 7800\left(\frac{kg}{m^3}\right)$, $c_{p,d} = 500\left(\frac{J}{kgK}\right)$

Left:$d_p = 0.89mm\left(\kappa = 9.4E \times 10^{-10}m^2\right)$, $Z = 0.4m$, $\varepsilon = \varepsilon_0 = 0.403$, eq. (4.35) as the solid red curve, and the solution of eqs. (4.39) and (4.40) as the dashed orange curve
Right: $d_p = 3.18mm\left(\kappa = 1.2E \times 10^{-8}m^2\right)$, $Z = 0.3m$, $\varepsilon = \varepsilon_0 = 0.401$, the solution of eqs. (4.37) and (4.38) as the solid red curve, and the solution of eqs. (4.39) and (4.40) as the dashed orange curve

Figure 4.20 plots the extracted heat flux from MC3D 1D simulations (green triangles), the experimental results coming from Ginsberg et al. [130] (blue circles) and the 1D unsteady model (solid red curve) at different temperatures T_0. In this case, it can be seen that the experimental extracted heat flux for both sets of debris bed does not show a large impact of the temperature, but rather has an uncertainty probably linked to the measurements. Contrary to the experiments, MC3D simulations clearly show an important effect of the temperature. As explained before, at a lower temperature, the effects of the additional water necessary for the progressing front cannot be neglected anymore, hence the respective models at low temperatures where evaluated with $X_{H_2O} = 1 - \alpha$. Taking into account that during the penetration part of the liquid served to advance the front, there is less liquid available to be evaporated. This, in addition to the relatively large front penetration velocity at low temperatures, the extracted heat flux decreases with decreasing temperature.

Regardless of the model used, in the laminar case, the heat flux is slightly overestimated for both size of particles. As before, this is explained by the 2D nature of the experiments compared to the 1D model and simulations.

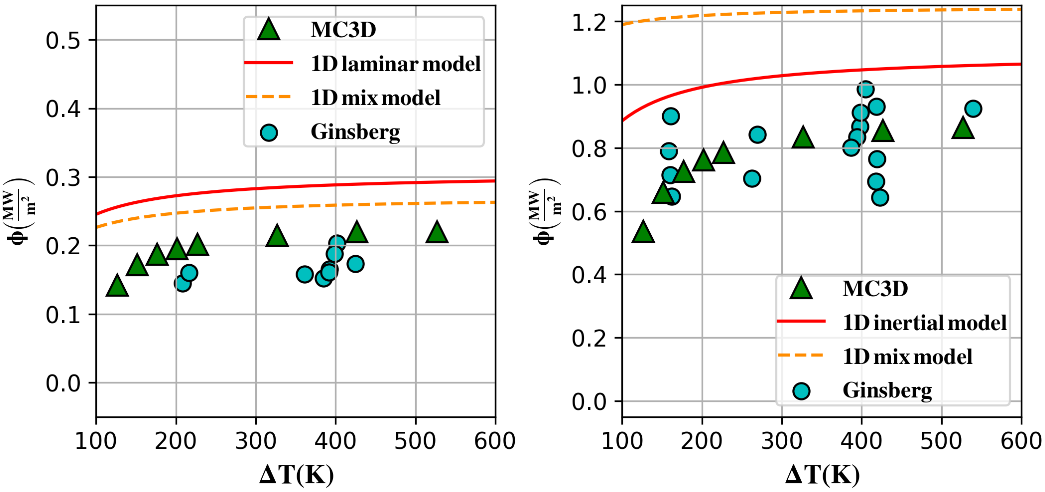

Figure 4.20 – Extracted heat flux comparison, Ginsberg et al. [130] vs. MC3D 1D simulations and 1D unsteady model with $\rho_d = 7800 \left(\frac{kg}{m^3}\right)$, $c_{p,d} = 500 \left(\frac{J}{kgK}\right)$

Left: $d_p = 0.89mm \left(\kappa = 9.4E \times 10^{-10} m^2\right)$, $Z = 0.4m$, $\varepsilon = \varepsilon_0 = 0.403$, eq. (4.36) as the solid red curve, and the solution of eqs. (4.39) and (4.40) as the dashed orange curve
Right: $d_p = 3.18mm \left(\kappa = 1.2E \times 10^{-8} m^2\right)$, $Z = 0.3m$, $\varepsilon = \varepsilon_0 = 0.401$, the solution of eqs. (4.36) to (4.38) as the solid red curve, and the solution of eqs. (4.36), (4.39) and (4.40) as the dashed orange curve

4.3 Fractured porous media - application to SSWICS tests

4.3.1 Application of the one-dimensional analytical model

A particular expected configuration of porous media is the so-called fractured corium crust. In this case, the average permeability of such media (as found in the SSWICS experiments) tends to be lower than $\kappa = 1 \times 10^{-9} m^2$. The crust is assumed to be relatively hot, but colder than the solidification temperature of the specific material. For such configuration, the water of the overlaying pool must first penetrate this hot material and later continue the solidification of the melt pool found underneath. In the absence of residual power in the crust, the heat extracted from this crust would come from the cooling of such material via the vaporization of the infiltrated water.

The front velocity is not known in these experiments. However, in application of eq. (4.36), the extracted heat flux is close to the critical heat flux that may be obtained in a porous media with the same permeability. So, eq. (4.29) can be directly used to estimate the heat flux extracted during the penetration. Figure 4.21 shows the results of two SSWICS tests and eq. (4.23). The dashed lines plot eq. (4.29) using the relative permeabilities in table 2.5. As can be seen, all formulations of the relative permeabilities, except Chima & Geiger, lead to similar results compared to the formulation presented in table 2.4. The different correlations don't change the shape of the curve, but rather slightly increase or decrease the ϕ_{mix}^{crit} without converging to a particular zone within the experimental uncertainty. Henceforth, in this work, for the fractured porous media configuration ϕ_λ, eq. (4.10), with the Fourar & Lenormad formulation will be used.

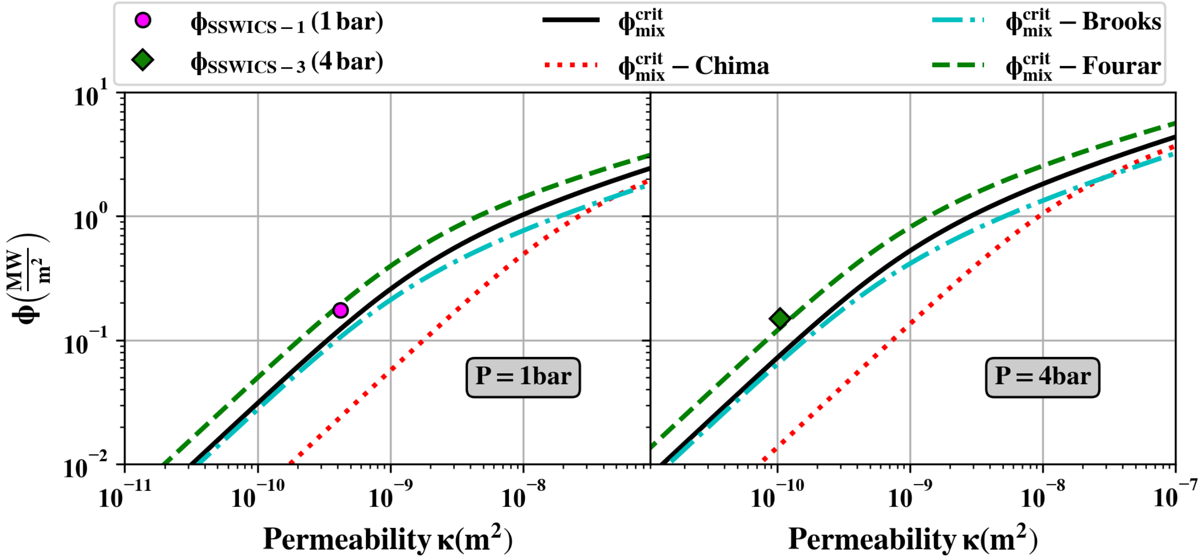

Figure 4.21 – ϕ_{mix}^{crit} given by eq. (4.29) compared to SSWICS W-I using the different fractured porous media formulations, given in table 2.5, for the relative permeability

Left: SSWICS-1 (P=1bar);Left: SSWICS-1 (P=4bar)

From the measured permeabilities in the SSWICS tests, it is possible to evaluate the heat flux by using the mixt model in conjunction with the Fourar & Lenormand relative permeability formulation. Figure 4.22 plots the experimental values of SSWICS-1,2,3, and 7 as the green markers in both the left and right part of the figure. The left plots ϕ_λ (see eq. (4.10)) using the Reed formulation for the relative permeabilities as the red markers, whilst the right using the Fourar&Lenormand formulation for the relative permeabilities (see table 2.5). For easier recognition, the big markers plot experimental results, and the small dashed-line markers plot the results of the model. As can be seen, using the Fourar & Lenormand results in larger values and seems to give a better agreement since they reproduce the experimental values at both pressures. Regardless of the model and formulation of the relative permeability used, it is noted that a steady decrease in the heat flux is observed with increasing concrete content. This comes from the fact that with increasing concrete content, there is a quasi-linear decreasing permeability since the inertial effects are negligible. Nevertheless, for the cases with concrete fraction larger than 8%, the order of magnitude of the heat fluxes, some tenths of $\frac{kW}{m^2}$, should have been observable in the SSWICS tests, figure 2.26. One remaining question is then the reason for the absence of the heat flux plateau.

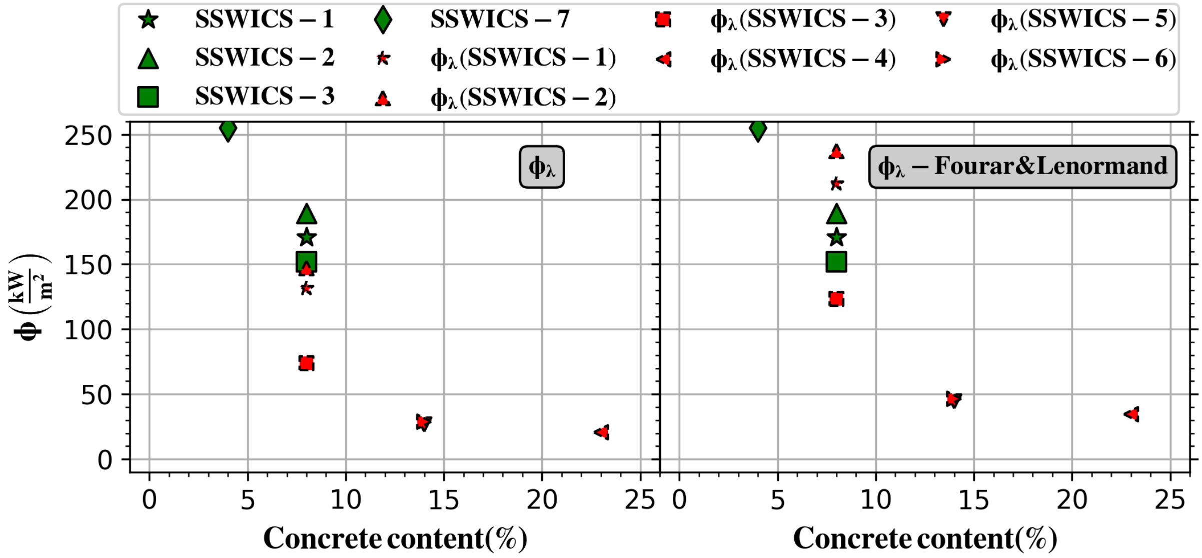

Figure 4.22 – SSWICS 1,2,3 and 7 results compared ϕ_λ, eq. (4.10) neglecting the capillary term, and with/without the use of the Fourar & Lenormand formulation for the relative permeability as a function of the concrete content. For easier recognition big markers plot experimental results and small dashed-line markers plot the results of the model.

Left: Reed formulation for the relative permeabilities (see table 2.4)
Right: Fourar&Lenormand formulation for the relative permeabilities, see table 2.5)

4.3.2 Application of the MC3D-PREMIX model

The same evaluations can also be made with the MC3D-PREMIX model. Appendix A presents rapidly the modifications made to the model for the present work. Regarding the application to water ingression, in principle, the water traverses the crust through more or less parallel, and probably not communicating, cracks, so some modification of MC3D was needed to compute the SSWICS tests:

- introduction of a dedicated correlation for the relative permeabilities: the Fourard & Lenormand model was chosen;
- no account of the inertial friction term, and
- strong increase of the lateral frictions (not necessary for these 1D calculations).

However, as MC3D is not fitted to compute two-phase flows with porosities as small as 1-2 %, the calculations were made with an imposed porosity of 10 %, to avoid possible numerical nuisances that would blur the analysis and further add obstacles. Fitting the particle diameters with the low porosity, it was possible to obtain the desired permeability. Evidently, the range of permeabilities tested was kept in agreement with the experimental measures. The expected impact on the calculation results falls mostly within the uncertainty margin of the problem. In these 1D calculations, the permeability is fixed for the entire domain. The permeability could be made to vary roughly as a function of the temperature through a variable density. Still, the calculations show that the water cannot penetrate deeply into the hot crust, hence resulting in comparable outcomes with the initial fixing of the permeability. An essential difference with the previous debris bed calculations is the account of the conductivity, as the presence of the melt under the crust is continuous. It is hypothesized that the fractures do not perturb the conduction significantly. It is finally necessary to highlight that the horizontal upper surface heat flux cannot be easily computed with the current modeling. The upper surface is very roughly modeled with a large permeability and porosity conditions. Hence, the initial period of film boiling on the flat surface is not precisely computed. However, the heat transfer is rapidly limited by conduction, before reaching a water ingression period, if any.

Obviously, due to the various uncertainties and in particular, the experimental permeabilities, which are post-mortem mean values, a precise validation is not sought for, but rather the calculations are used as a qualitative interpretation of the experimental results.

The meshing used for the 1D calculation is shown in figure 4.23. It is a slowly progressive mesh with increasing mesh sizes with increasing depth. A better precision is needed at the top to capture the beginning of penetration. The figure also shows the volume fraction of the DROPS field, $1-\varepsilon$, i.e., the corium medium. As can be seen, the water region above the melt pool is not represented. Instead, a pressure boundary condition is imposed, with an imposed volume fraction of water of 1 [11]. It is also noted that the 3 uppermost meshes (blue zone) have an imposed DROPS volume fraction of 0.8, to facilitate the penetration at the beginning. These three cells with a larger permeability do not impact the water ingress flow characteristics in the core of the melt, with a chosen porosity of 10 % i.e., a volume fraction of 0.9 (green zone). The lowest-most zone represents the MgO basemat supposed to thermally isolate the corium and minimize the heat losses. In fact, the contrary is true. MgO has rather high conductivity Slifka et al. [223], so noticeable heat losses are expected. Numerically, this initially "cold" (T_{sat}) MgO layer is, in fact, simulated with the same field as the corium with two key differences. First, the conductivity coefficient of this MgO zone is set to that of MgO, which strongly depends on the temperature. This is legitimate since the density of corium is about twice that of MgO ($\sim 3700\frac{kg}{m^3}$), whereas the opposite is true for heat capacity ($\sim 1000\frac{J}{kgK}$ for MgO vs. $\sim 500-600\frac{J}{kgK}$ for corium), so that the product $\rho \cdot Cp$ is close to that of the corium. Furthermore, the porosity of this field is minimized, and no water is allowed to traverse this layer.

Nevertheless, heat losses at the lowest boundary (between what would be the bottom of the MgO layer and the atmosphere) are not considered. The intermediate zirconia thin layer between the melt and the MgO layer is not taken into account as its conductivity is similar to the corium.

Table 4.1 provides information related to the MC3D initial conditions and the results of the water ingression heat flux plateau. The melt properties are those reported by Farmer and Lompersky, see [160], slightly rounded as the precision given by the authors probably surpasses the actual uncertainties[12], although, regarding the physical properties needed for theses thermo-dynamical calculations (density, latent heat, specific heat) these uncertainties are considered as reasonable, due the relatively high accuracy of the databases (e.g., NUCLEA) on this point. Nevertheless, as already discussed, regarding the melt conductivity, the values taken as either 1.5 either 1.25 $\frac{W}{mK}$ in Farmer and Lompersky works are here considered to be too low, hence a value of 2.5 $\frac{W}{mK}$ is used in these calculations.

---

[11] Only water can enter the domain is the pressure is smaller than the imposed one.

[12] The properties are not constant but vary notably with temperatures.

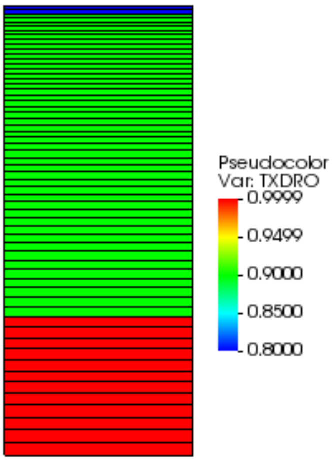

Figure 4.23 – 1D mesh for MC3D calculations of the SSWICS tests

Table 4.1 – SSWICS initial conditions for MC3D calculations and results.

Test	**% conc.**	κ $(\mathbf{m^2})$	$\mathbf{T_{sol}}$ **K**	$\mathbf{T_{liq}}$ **K**	$\mathbf{c_p}$ $\mathbf{\frac{J}{kgK}}$	$\mathbf{h_{fs}}$ $\mathbf{\frac{MJ}{kg}}$	ρ $\mathbf{\frac{kg}{m^3}}$	$\mathbf{T_{corium}}$ **K**	**P** **bar**	$\phi_{\mathbf{calc}}$ $\mathbf{\frac{kW}{m^2}}$	$\phi_{\mathbf{exp}}$ $\mathbf{\frac{kW}{m^2}}$
1	8	$4{,}0\times10^{-10}$	2000	2600	500	0,4	7300	2600	1	194	175
2	8	$5{,}0\times10^{-10}$	2000	2400	500	0,4	7300	2400	1	242	180
3	8	$1{,}0\times10^{-10}$	2000	2400	500	0,4	7300	2400	4	120	150
4	23	$2{,}5\times10^{-11}$	1400	2400	600	0,65	5600	2400	4	30	-
5	14	$3{,}8\times10^{-11}$	1400	2400	550	0,6	6500	2400	4	45	-
6	14	$1{,}0\times10^{-10}$	1400	2400	550	0,6	6200	2250	1	60	-

ε is the porosity, κ: permeability, c_p: heat capacity, h_{fs}: fusion heat, T_{sol}: solidus temperature, T_{liq}: liquidus, ρ: density, T_{corium}: initial temperature, P: pressure, P_{res}: residual power, ϕ_{calc}: calculated WI heat flux, ϕ_{exp}: experimental WI heat flux

Figure 4.24 shows the heat flux extracted at the top boundary for each calculation. For all cases, it is possible to observe three distinct "phases". An initial period of high heat flux and subsequent sharp decrease. This period seems rather uncertain, but as stated previously, the initial period of film boiling is not adequately modeled. After a specific time (better appreciated in the SSWICS-3 calculation, dubbed SS3 in the figure), the water penetrates promptly up to a certain length resulting in a heat flux spike. This is to be considered as a numerical effect accompanying the beginning of the water penetration. After which the heat flux reaches a plateau, i.e., the water ingression plateau. One should observe that the duration of the plateau is much longer than in the experiments. However, for tests 4, 5, and 6, with low permeabilities, the plateau is low and reached lately. During this water ingression, the water penetrates the length of the domain. An important finding from these calculations is that once the water reaches the bottom of the domain, the plateau suddenly stops and the presence of quite slow decreasing heat flux after the plateau [13] can be observed. During this third phase, the heat flux can be linked to the released of the energy coming from the MgO basemat, which is transferred back to the solidified cooled corium. This decrease is much later and sharper than in the experiments.

---

[13] This is not observed in the calculations 3 to 6 because they were stopped before the complete cooling.

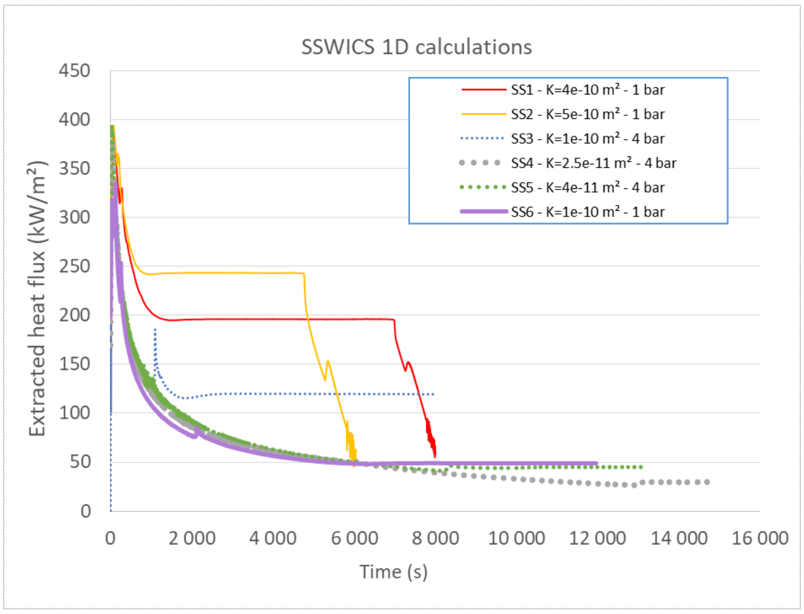

Figure 4.24 – SSWICS 1D MC3D calculation extracted heat flux

Figure 4.25 illustrates the SSWICS-1 calculation behavior for three different times. The left part plots the liquid volume fraction and the level at which the temperature of the corium is lower than $T_{sol} = 2000K$ as the red lines. The middle part plots the corium temperature, whilst the right part plots the vapor velocity. Due to the conduction, the temperature gradient is rather smooth. This is not obvious from the pictures, but time 1500 seconds marks approximately the moment when the heat is extracted solely through the transport of vapor in the crust. Before that moment, water slightly penetrated the hot crust; hence the heat is probably extracted both by conduction and by water ingression. A significant amount of heat is transferred to the MgO layer before the water reaches it. From that moment, the heat is transferred back to the solidified corium, which leads to the slow heat flux decrease seen in figure 4.24.

Figure 4.26 illustrates the SSWISC-6 calculation behavior at 3 different times. Contrary to the SSWICS-1 calculation, the melt is entirely solid by t=3000 seconds, whereas water ingresses the crust by t=7000 seconds when a large part of the heat has already been extracted. At the end of the calculation, t=12000 seconds, the water has penetrated about half of the melt. Thus the expected end of the water ingress period should be by t=17000 seconds, far beyond the test duration. SSWICS-4 and 5 are even more problematic since water ingress occurs very late and has a rather minor effect since most of the heat has already been extracted by that moment.

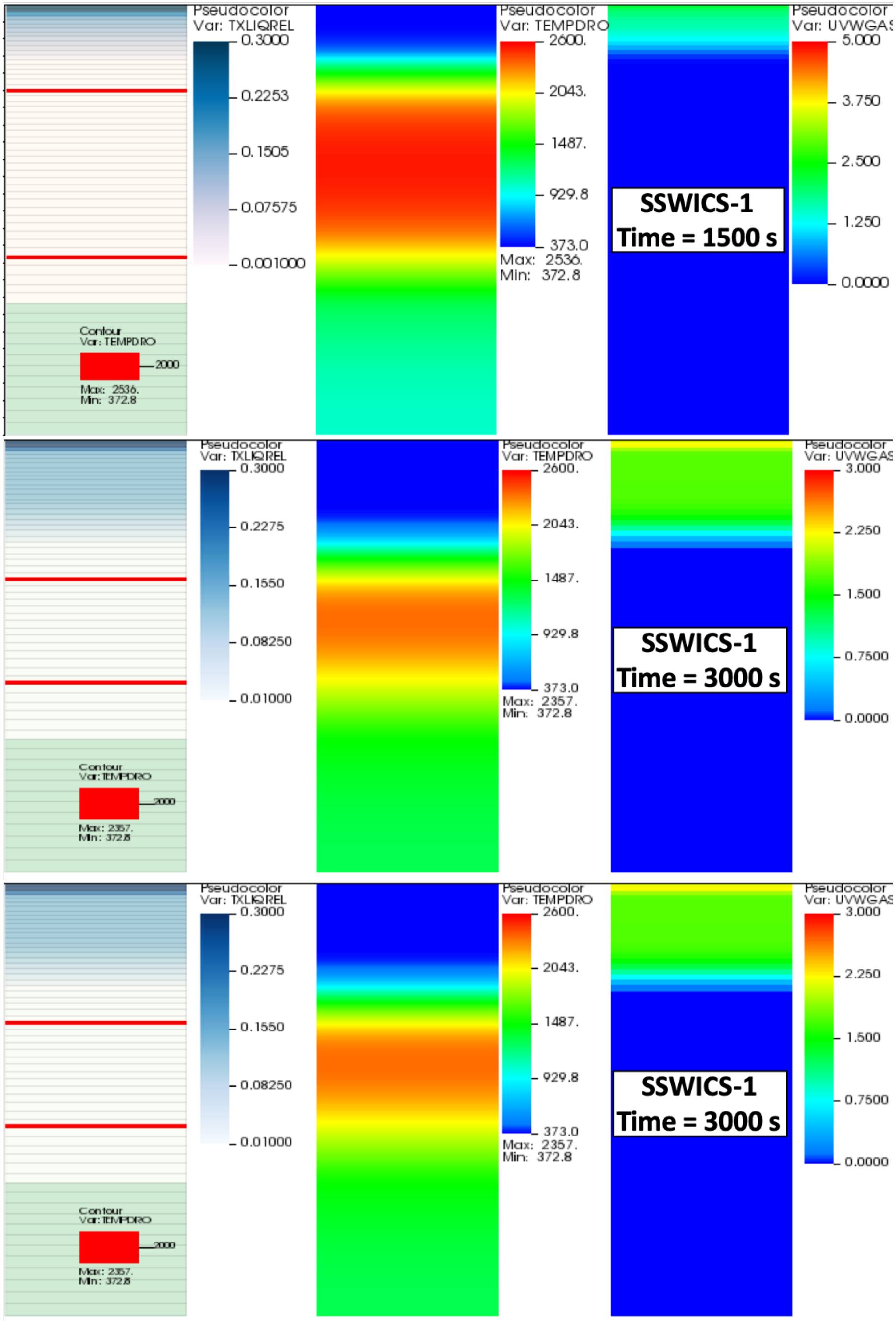

Figure 4.25 – SSWICS-1 1D MC3D calculation at t=1500s., 3000 s. and 6500 s

Left: liquid volume fraction and level where T=$T_{sol} = 2000K$ (red lines); middle: corium temperature; right: gas velocity

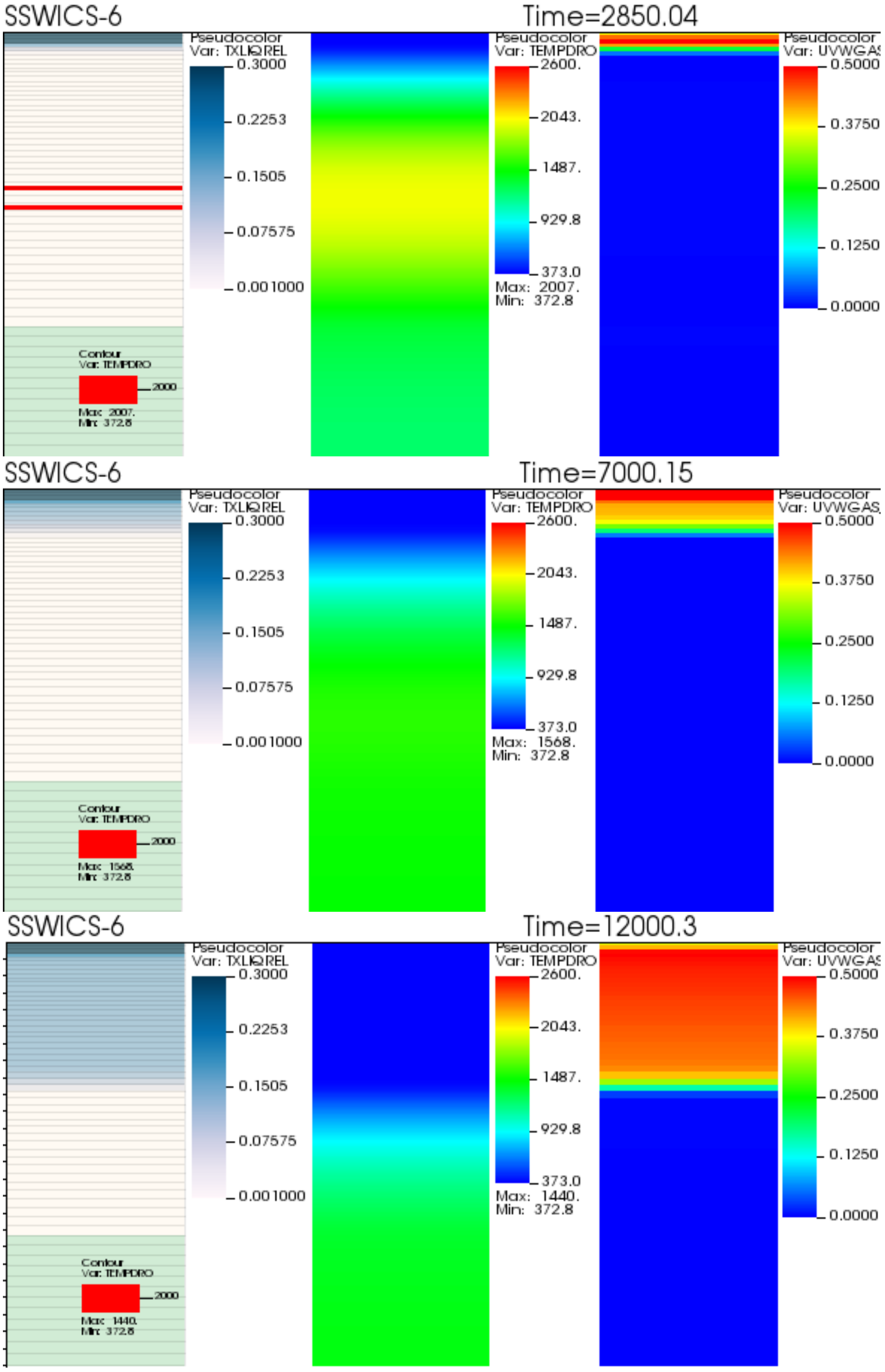

Figure 4.26 – SSWICS-6 1D MC3D calculation at t=3000s., 7000 s. and 12000 s

Left: liquid volume fraction and level where T=$T_{sol} = 2000K$ (red lines); middle: corium temperature; right: gas velocity

Figure 4.27 gives the computed WI heat flux as a function of the permeability, compared with the experimental values (tests 1, 2 and 3), and ϕ_{mix}^{crit} at 1 (solid red curve) and 4 bars (dashed green curve). For a given ambient pressure, it is verified that the behavior is quasi-linear with the permeability, in accordance with the Darcy law. The results of MC3D calculations are plotted as the green and red square markers. The big squares plot the simulations made at 1 bar, whilst the small squares plot the simulations at 4 bars. Note that the tests at 1 bar are somewhat over-predicted, whereas the one at 4 bars is a bit under-predicted. With the small number of data, it is not possible to give a definitive conclusion. Nevertheless, it may be argued that the measured permeabilities are in quite good agreement with the measured heat flux.

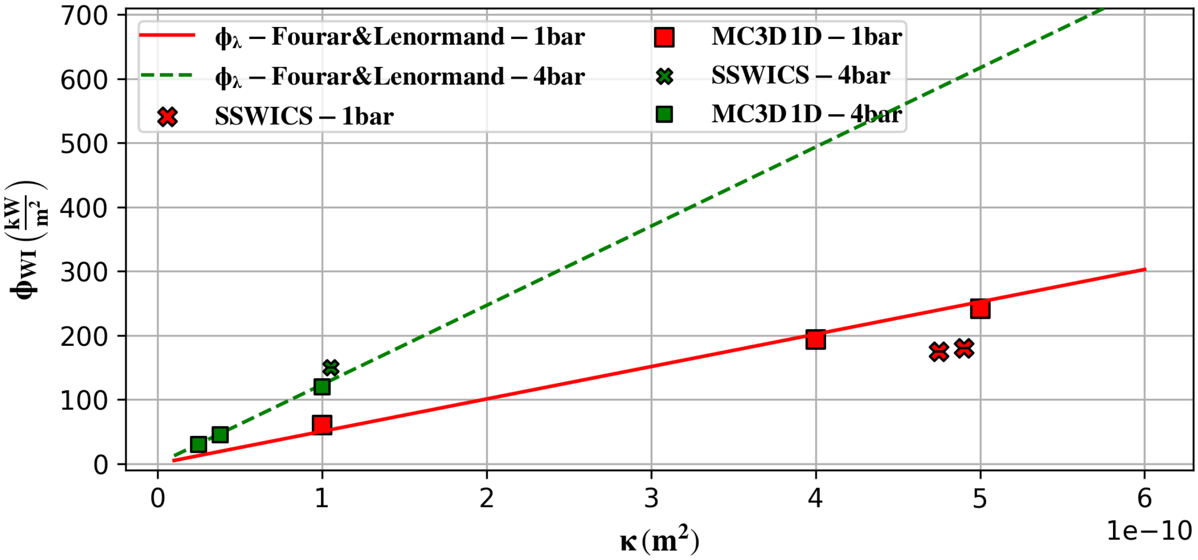

Figure 4.27 – Extracted water ingression heat flux in the SSWICS 1D calculations with MC3D compared to experimental values and ϕ_λ using the Fourar&Lenormand formulation for the relative permeabilities. Large symbols are the cases at 1 bar, whereas the smaller ones are the cases at 4 bars. MC3D calculations were made with two slightly different values of the permeability for the 1 bar case.

4.4 Application

For a reactor case, considering one-dimensional situations where the debris lay on a corium solidified pool, or on a crust, or for a fractured crust on top of a liquid pool with:

- internal power inside the debris bed; and
- heat input from below, as for the MCCI situation,

it is possible to evaluate the stability of the configuration. Using the density of the corium, the available surface below the RPV, and assuming the quantity of corium extruded from it (here assumed to be ~110 tonnes of corium with a $UO_2 - ZrO_2$ mass ration of 2.44), the corium can be expected to be found either in compact configuration of around 30 centimeters or as a debris bed of around 45 centimeters in thickness.

Figure 4.28 plots the expected residual power as a function of time in $\frac{MW}{m^3}$ of corium for different corium-concrete mixtures. The solid green curve plots the values presented in figure 1.20 converting them into $\frac{MW}{m^3}$ by using a corium composition with a $UO_2 - ZrO_2$ mass ration of 2.44, and with $\rho_{UO_2} = 9000\frac{kg}{m^3}$ and $\rho_{ZrO_2} = 6000\frac{kg}{m^3}$. The dashed red, dotted blue, dashed-dotted grey, and solid black curves plot the values when adding 5,15,25, and 65wt% of concrete into the mixture, with $\rho_{concrete} = 2500\frac{kg}{m^3}$. As can be seen, the residual power by m^3 of corium is reduced by a factor ~1.75 when 25wt% of concrete has been added into the mixture. It is important to note that the density of the concrete cannot be defined straightforwardly since the density of its components varies drastically with the temperature. Nevertheless, the value here used can be seen as an order of magnitude approximation that shows the important density difference with the concrete-less corium and its direct effect in the residual power by volume.

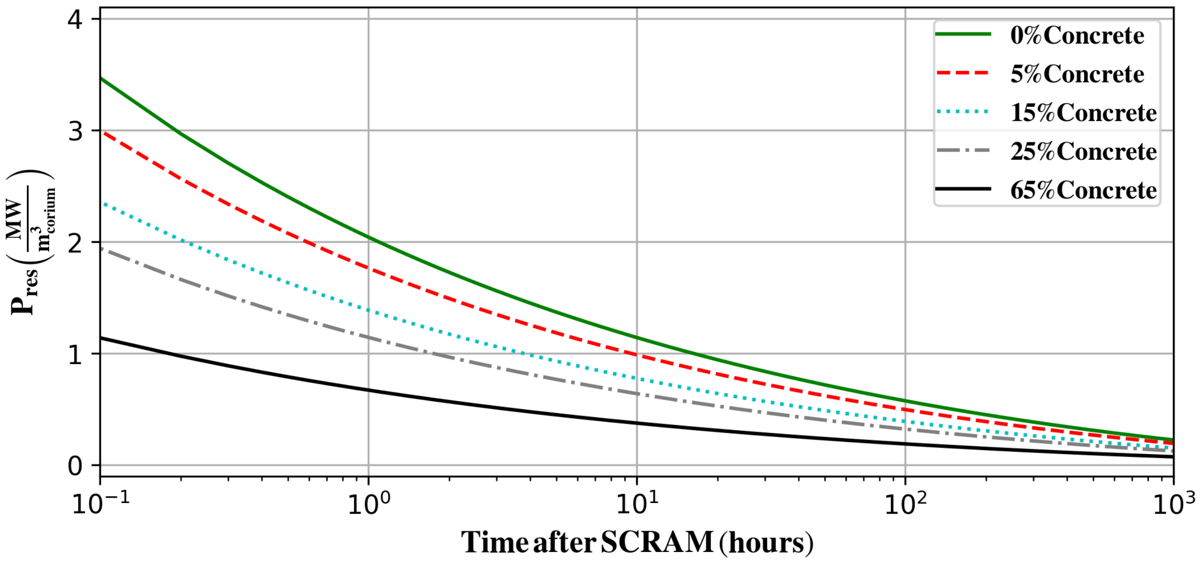

Figure 4.28 – 900 MWe PWR residual power as a function of time for different corium-concrete compositions with a $UO_2 - ZrO_2$ mass ratio of 2.44 and where the SCRAM one year after reactor start-up

In general, in such cases, the penetration velocity is given by eq. (4.40), $j^P_{v,mix}$.Furthermore, the effects of additional water at the front may be neglected. To do so, the conditions at the most unfavorable elevation have to be considered, likely at the top of the debris bed. In eq. (4.40), ϕ_z should account for the effective residual power going into the debris bed, i.e., subtracting the part going to ablation and conduction through the concrete, or adding the energy coming from underneath the debris bed through the crust. Hence eq. (4.40) can be expressed as:

$$u_{mix} = \frac{j^P_{v,mix}\rho_v h_{lv} - \phi_z + \phi_s}{(1-\varepsilon_0)\,\rho_d c_{p,d} \Delta T} \tag{4.41}$$

where $\phi_s\left(\frac{MW}{m^2}\right)$ is either negative in the case energy is arriving from the bottom of the debris bed, or positive if it is leaving the debris bed through conduction to the concrete.

4.4.1 Debris bed over concrete

For this particular situation, the question posed is to verify that the penetration occurs sufficiently rapidly before the heat up causes remelting the unquenched part. First, considering, quite conservatively, that the conduction in the concrete is strictly null so that no heat loss occurs, a simple competition of u_{mix}, eq. (4.40), and the residual power transferred to the unquenched region can be made. It is recalled that a debris bed can be formed throughout an MCCI due to the melt ejection coming from the concrete ablation gases. Acknowledging the lack of precise experimental confirmation of the characteristic size of the particles created during these ejections, close visual observations show that they range in the order of few millimeters. By evaluating the penetration velocity, including the volumetric power term, and iterating to take into account the heat up o the material from the initial temperature, it is possible to estimate a maximal quenchable debris bed thickness. To obtain such results, it is necessary to first settle an initial debris bed temperature T_0, a fusion temperature for the material T_{melt}, here 2500 K, the residual power ϕ_v, time step, and the material properties, here $\rho = 7000\frac{kg}{m^3}$, and $c_p = 400\frac{J}{kgK}$ After which, each iteration of u_{mix}, will give a distance quenched and the rise of temperature in the material before the next iteration. The value ϕ_v is multiplied each iteration by the cumulative distance quenched, in order to obtain ϕ_z to be used in eq. (4.40). The maximal thickness of the debris bed quenchable before remelting of the material starts is plotted in figure 4.29. The figure is divided into four quadrants where the abscissa is ϕ_v, and the ordinate the d_p used for calculating u_{mix}. The color code plots the maximal bed height that was quenched at each different power, whilst the black dashed lines separate the color values by increasing steps of 0.025m. The different quadrant plots the results of this iterative process with an initial T_0 of 1000, 1500, 2000, and 2400 K for the top left, top right, bottom left, and bottom right quadrant respectively. As can be seen with increasing temperature, the maximal thickness of the quenchable debris bed quickly reduces. As an example, by comparing the upper right and lower left quadrants, it is possible to see that with the same $\phi_v = 1.0\frac{MW}{m^3}$ and $d_p = 1mm$ passing from an initial temperature T_0 of 1500K to 2000K reduces the maximal quenchable thickness from ∼24 to ∼15cm.

Nevertheless, the high melt temperature, T_{melt}, valid for corium mixtures of $UO_2 - ZrO_2$, is no longer valid with the addition of the concrete constituents. A more representative T_{melt} might be the solidification temperature of the corium mixture, shown in figure 2.18, recalling that this temperature is difficult to define, hence it is hard to characterize it for a general case. Nevertheless, as shown in figure 2.18, the solidification temperature hardly evolves after a concrete concentration of 30%, and it is in the order of 1600 K. Figure 4.30 plots the results using T_{melt} of 1600 K. It is possible to observe how, for an initial debris bed temperature T_0 of 1500 K, even with large particles, the maximum thickness of a coolable initially hot debris bed quickly decreases with increasing ϕ_v. This last would signify that if the high temperature ejected particles would quickly accumulate following MCCI melt ejections, they would tend to remelt and agglomerate.

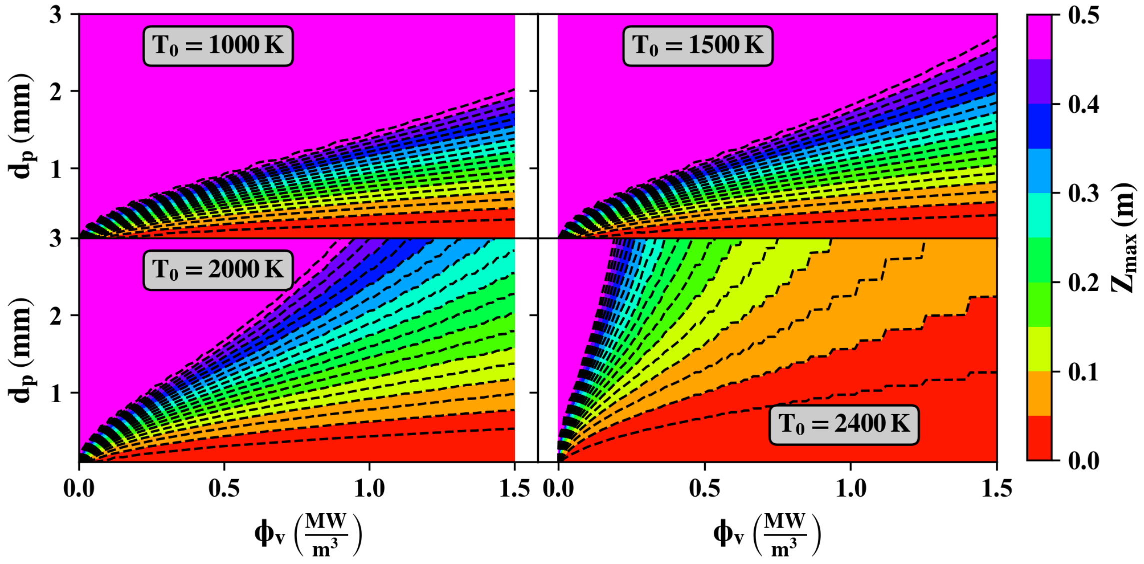

Figure 4.29 – Maximum debris bed height as a function of d_p and residual power ϕ_v considering 4 different initial temperatures and $T_{melt} = 2500K$

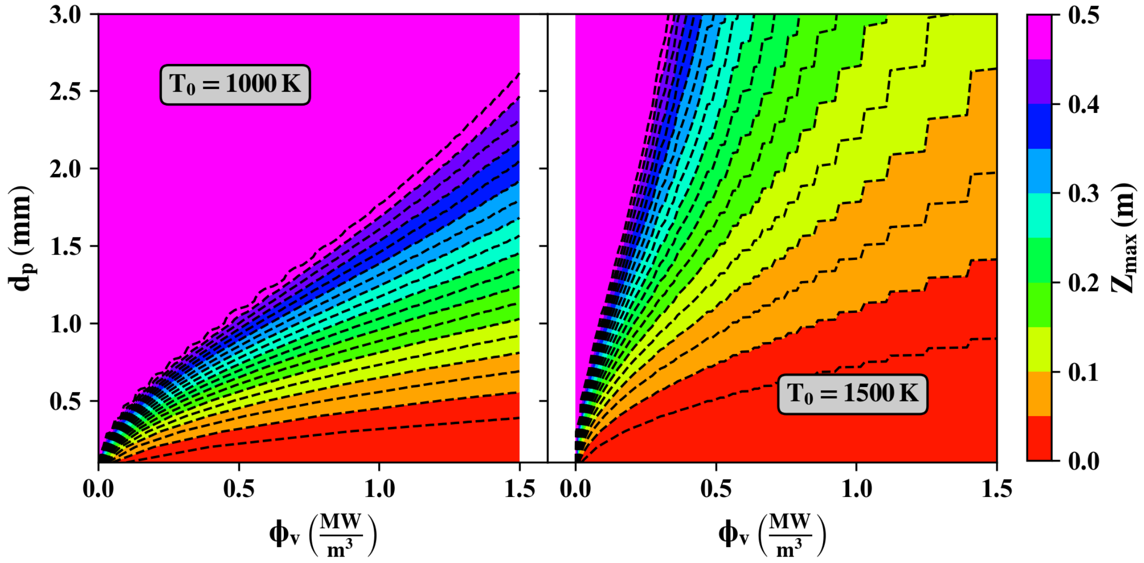

Figure 4.30 – Maximum debris bed height as a function of d_p and residual power ϕ_v considering 2 different initial temperatures and $T_{melt} = 1600K$

However, the most likely situation is that the debris bed also heats the concrete. In such a situation, the actual cooling limit may be given by the upper concrete melting, which occurs for a much lower temperature. Note that much before the melting, the concrete should start degradation and release vapor and gases that should, in principle, be taken into account. This would impose an unsteady model of concrete degradation, which is out of the scope of the present work. It will be here consider that due to the rather long time scale, and to the rather low conductivity of the concrete, the concrete top surface reaches the temperature of the overlying debris bed rapidly. Figure 4.31 plots the same kind of analysis as before with $T_{melt} = 1200K$. In this case, only the initial temperature of $T_0 = 1000K$ was tested since if the initial temperature is larger than the limit, it would immediately lead us to an unquenchable situation. As can be seen, the maximum quenchable debris bed before reaching the concrete ablation temperature quickly becomes small with increasing power and decreasing particle diameter.

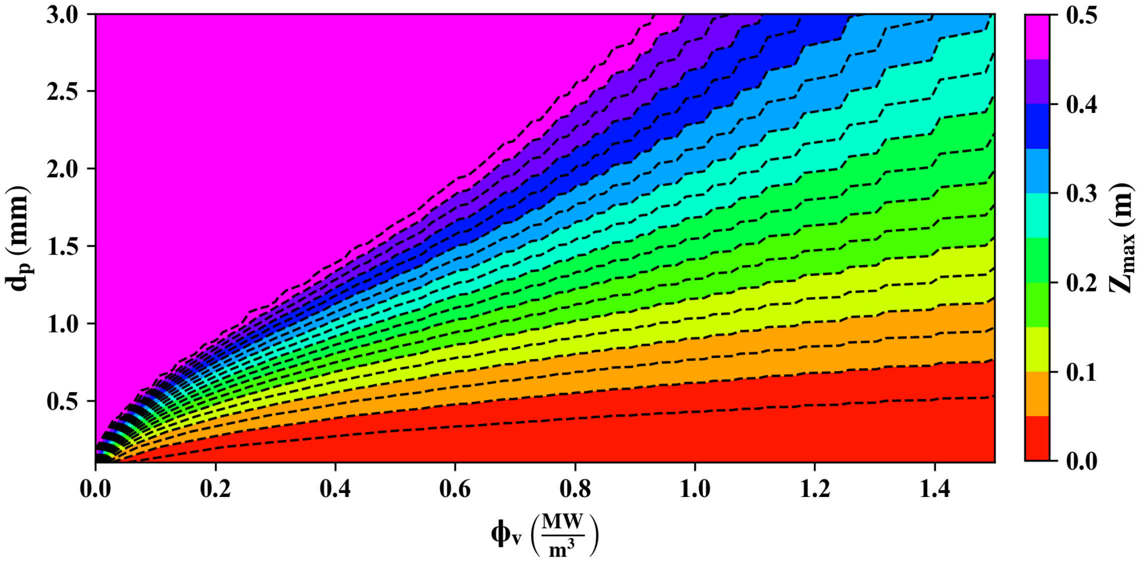

Figure 4.31 – Maximum debris bed height as a function of d_p and residual power ϕ_v with $T_{melt} = 1200K$, and $T_0 = 1000K$

4.4.2 Debris bed over corium crust

The case of a the debris bed on top of the corium crust will now be discussed. To achieve stability of the compound debris-bed/corium-crust layer, the hot partially solidified particles would first need to be quenched. Subsequently, the final debris bed configuration should be able to accommodate the heat coming from the corium crust, as well as the residual power contained in the corium particles. Nevertheless, the entire sequence, schematized in figure 4.32, should occur before either the corium crust or the debris bed remelt.

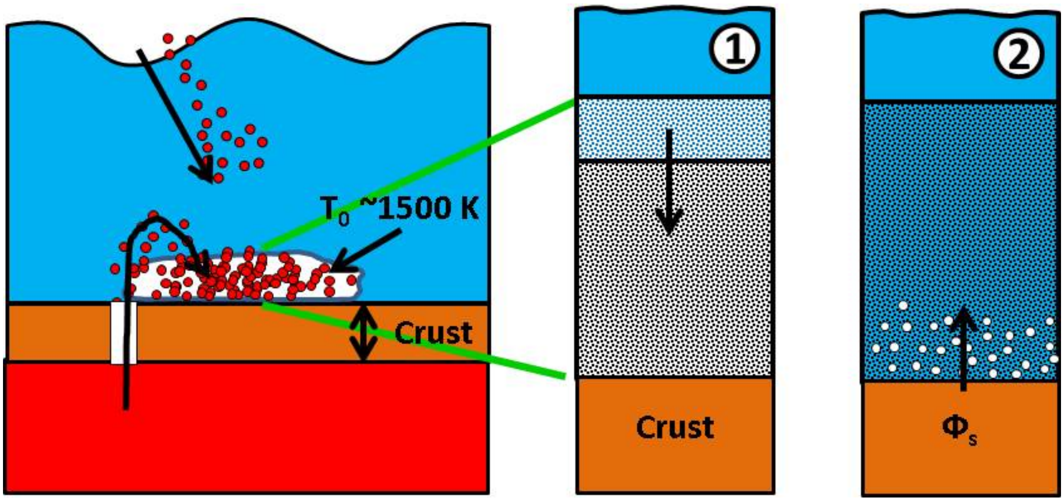

Figure 4.32 – Cooling scheme of debris bed over corium crust

In other words, the debris bed-corium crust layer is subject to two limiting criteria. The first one presented in section 4.4.1, gives the upper quenchable debris bed thickness limit for a corresponding volumetric power, particle diameter, and initial temperature.

For the second limiting criteria, the now quenched debris bed has to accommodate the power coming from the crust, ϕ_s without becoming unstable. Recalling that the maximum power a debris bed can evacuate can be evaluated with ϕ_{mix}, eq. (4.29), the maximum debris bed thermohydraulically stable thickness would then be $\frac{\phi_{mix}}{\phi_v}$, where ϕ_v would be $\int_{z_{cr}}^{z_{bed}} P_v \varepsilon \delta z$, plus ϕ_s, which itself would be $\int_0^{z_{cr}} P_v \delta z$. Different combinations of crust-debris beds could potentially give the same value of ϕ_v; hence figure 4.33 plots an equivalent maximal corium layer thickness as a function of the particle diameter for 3 different values of ϕ_v.

Comparing the maximal thickness presented in figures 4.30 and 4.33 it can be clearly seen that for the expected temperatures ($T_0 > 1000K$, and $T_{melt} \sim 1600K$) the temperature criterion becomes the limiting one. For all the diameters in the range of interest at powers larger than $\phi_v \sim 0.3\frac{MW}{m^3}$, the maximal debris bed thickness is less than 30 cm, which is lower than the maximal thickness at those diameters and values of ϕ_v in figure 4.33. On the other hand, for small temperatures, and large ϕ_v, the hydrodynamic criterion becomes the limiting one.

Regardless of the limiting criterion, given an initial temperature, a residual power, and the characteristic diameter of the debris bed particles, it is possible to estimate the stability of the layer using these two criteria.

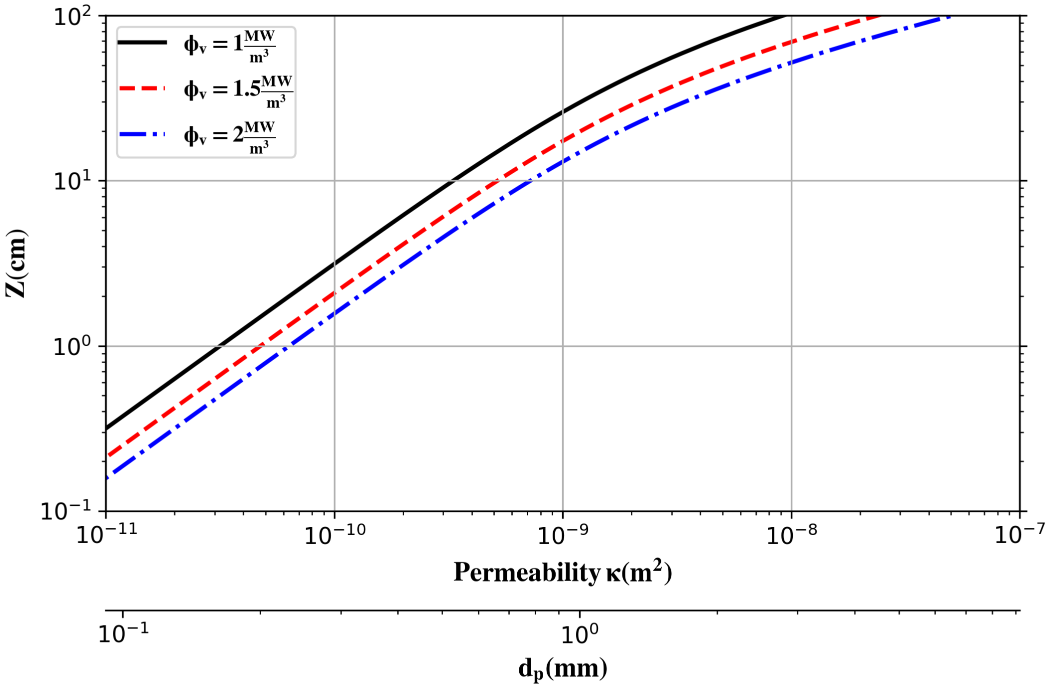

Figure 4.33 – Maximum quenchable corium thickness (including corium debris bed and corium crust) as a function of ϕ_v and the debris particle diameter

4.4.3 Water ingression

Now for the other corium configuration of interest, the contribution of water ingression for some typical situations may be approximately evaluated, still with a one-dimensional approach, with MC3D calculations. Compared to the previous SSWICS calculations, presented in section 4.3.2, the following modifications were done:

- the corium part is subjected to a volumetric power;
- the MgO layer is replaced by a concrete material with a large depth;
- the conductivity of the melt, when it is liquid, is multiplied by a large factor (100) in order to simulate roughly a good mixing due to bubbling during the ablation;

Note that, in contrast with the experiments, the corium is fully heated, whatever its solidification state. In fact, as the problem is nearly semi-infinite, no stable solution can be reached. The aim is to seek both, for a given volumetric power, if the situation can be stabilized regarding the concrete ablation and the thickness of the solidified layer. In the calculations, the ratio of downward energy flux (into the concrete) to the total input power is about 25 %, in the range of the experimental values so that the approximate modeling might be used for a first-order estimate.

For the present application, the situation investigated is the one for corium mixture similar to the SSWICS-1 test, i.e., with about 8 % of concrete, or, more appropriately with a permeability of $\kappa = 4 \times 10^{-10} m^2$.

This experiment was chosen since it was found as the most favorable case (most considerable impact of W-I) in the experiments (excluding SSWICS-7 where a permeability measurement was not made). For this application, a volumetric power of $\phi_v = 1\frac{MW}{m^3}$ corresponds to a surface heat flux $\phi = \phi_v \cdot z \cdot (1-\varepsilon)$ of about $180\frac{kW}{m^2}$, which is slightly less than the potential extraction by water ingression, which should then be quite efficient. The initial temperature conditions were set to a homogeneous T_0 in the corium part equal to the experimental temperature, and the concrete material layer set at saturation temperature.

The impact on the extracted top heat flux is given in figure 4.34 for three different volumetric powers: 0.5, 1 and 2 $\frac{MW}{m^3}$, which may cover the range of residual power to be expected at least 10 hours after reactor SCRAM[14](see figure 4.28). Up to $1\frac{MW}{m^3}$ the system succeeds to extract the expected heat flux of about $200\frac{kW}{m^2}$.

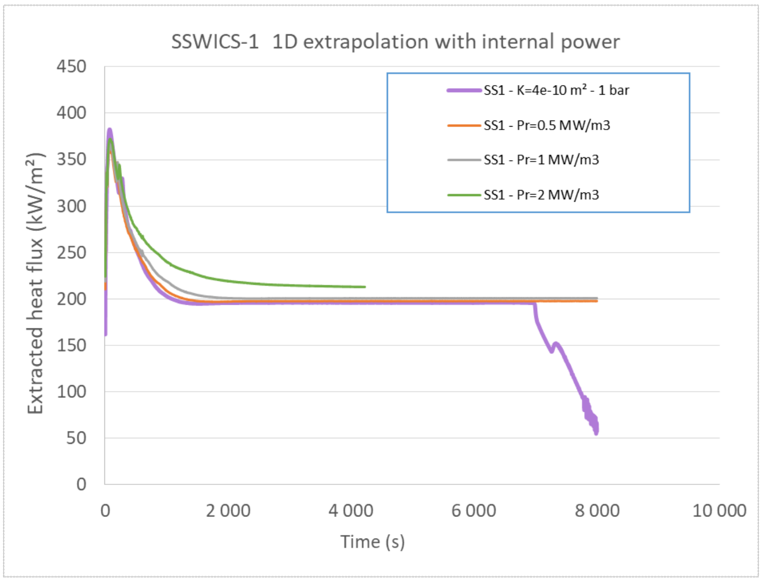

Figure 4.34 – Impact of residual power on the extracted heat flux in a SSCWICS-1 configuration for 3 values of the internal power for $\kappa = 4 \times 10^{-10} m^2$

The case of $1\frac{MW}{m^3}$ is depicted in figure 4.35 for a time of 8000 seconds after the contact with water. In this figure, the blue line indicates roughly the cooled part of the melt (with a temperature lower than 400 K). The red line indicates the limits of solidification of the melt (T $<$ solidus temperature), whereas the green line roughly indicates the limits where concrete has reached ablation temperature. Despite the roughness of the modeling, it seems quite clear that the system is not stable regarding ablation. It is noticed that, due to the local thermal disequilibrium, the corium and the coolant are not necessarily at the same temperature in a mesh where the water is present. This would depend on the exact interfacial area and heat transfer mechanism. It is seen that, for this case, a significant ablation should have occurred, so the situation is not stable from this point of view. It is also noted that the temperature in the molten part has reached a quite high value, more than 2800 K. Nevertheless, water ingression allows the crust to grow in thickness to about 10 cm.

---

[14] emergency shutdown of the nuclear reactor

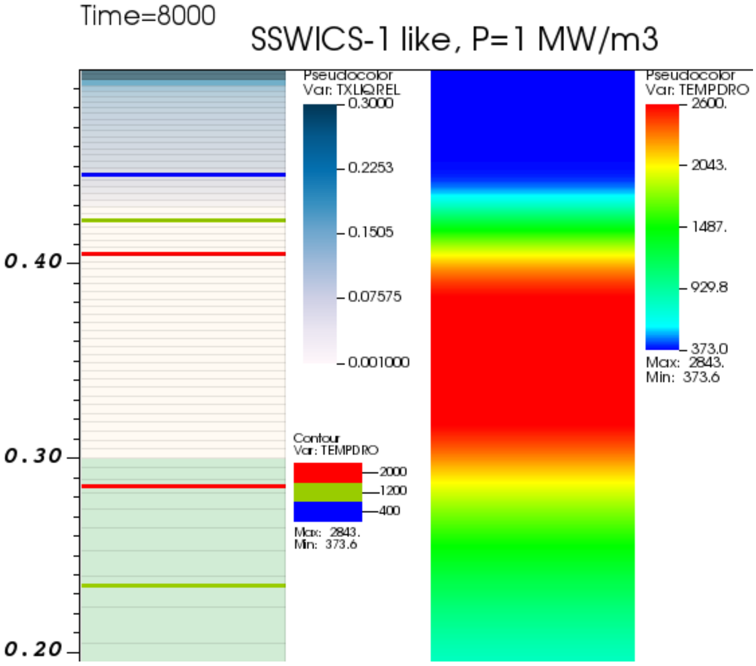

Figure 4.35 – Impact of residual power in a SSCWICS-1 configuration with an internal power of $1\frac{MW}{m^3}$

Left: water ingress in the melt and temperature levels related to cooled situation (blue line) and solidified melt (red). Right: temperature of the melt and concrete. The concrete occupies the 30 lower cm.

The case with lower power of $0.5\frac{MW}{m^3}$ $(90\frac{kW}{m^2})$ is shown in figure 4.36 for the same time. Ablation again is noticeable. In reality, the conditions for the melt, hence its properties, may change slightly, but the progression of the water ingression zone is much more critical. Indeed, a full solidification is reached in this calculation after about 9500 seconds, a complete water ingression obtained after about 12000 seconds. A total ingression is reached because of the low level of internal power, about half of the possible extraction.

In contrast, in the case with higher internal power of $2\frac{MW}{m^3}$ $(360\frac{kW}{m^2})$, as seen in figure 4.37, the calculation tends to indicate that the heat extraction surpasses the pure water ingression value, meaning that the heat is extracted for a large part through thermal conduction via a thin crust. The calculation was stopped due to the corium reaching a temperature of 3500 K, due to an insufficient heat extraction (and absence of ablation[15]). Also shown in figure 4.37, the water ingression region is very limited in depth; hence its impact is constrained.

---

[15] Note that the time shown here is $\frac{1}{4}$ compared to the other calculations.

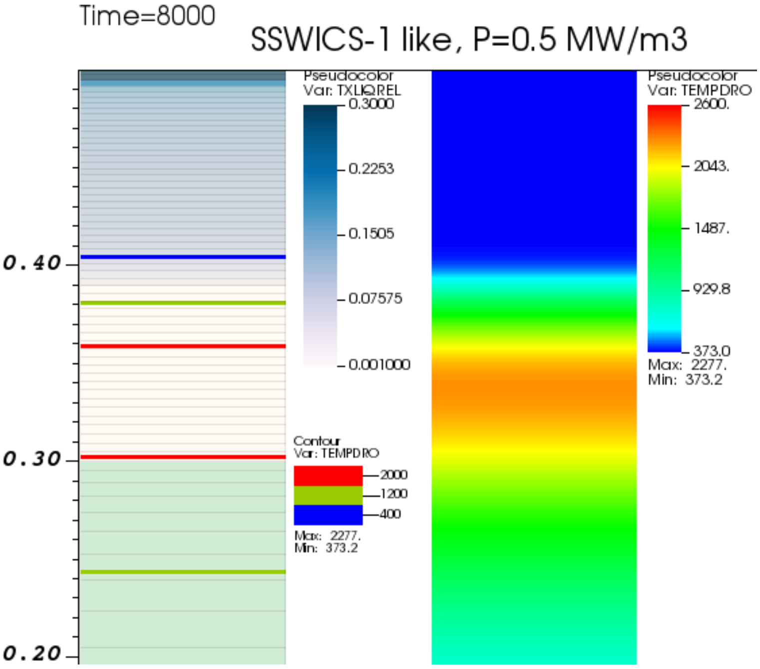

Figure 4.36 – Impact of residual power in a SSCWICS-1 configuration with an internal power of $0.5 \frac{MW}{m^3}$. Legend as figure 4.35.

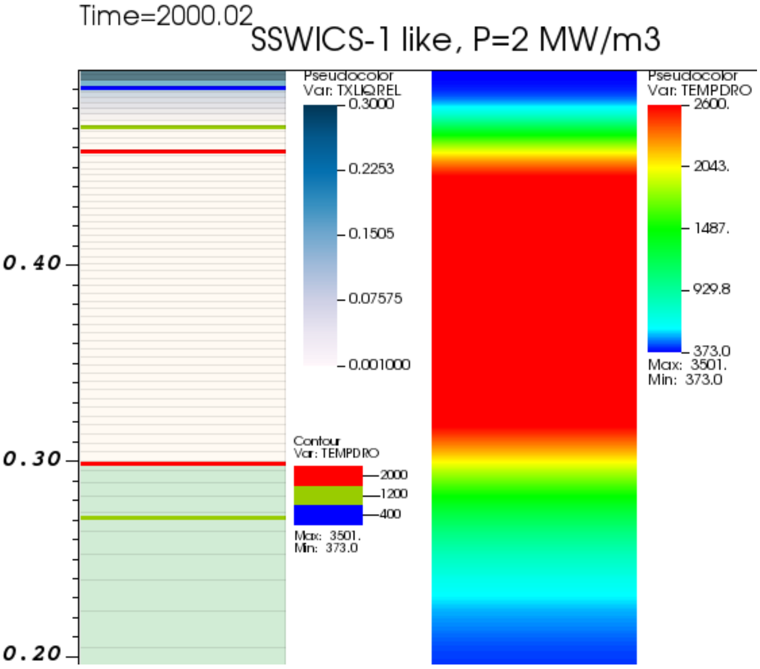

Figure 4.37 – Impact of residual power in a SSCWICS-1 configuration with an internal power of $2 \frac{MW}{m^3}$. Legend as figure 4.35.

4.4.4 CCI-9

Finally, in the interest of studying MCCI in more prototypical conditions, further MC3D calculations in conditions similar to CCI-9 test were made to give a consistency to the preliminary analysis performed in section 3.2.2.2. In particular, the interest here is to look for crust conditions and water ingression characteristics that may be coherent with the findings from the second stage of the experiment, with low input power.

In this case, the lower boundary is an imposed flux of gas coming from the ablation. The gas flux imposed was estimated from the experimental data, assuming a boundary temperature of 1500 K (meaning that the gas exits at around the concrete ablation temperature presented in section 1.1.2.7), with an imposed gas velocity of 0.01 $\frac{m}{s}$. The purpose of adding the gas from ablation was to verify that the potential pressurization below the crust is low and that it does not affect the water ingression. The heat transfer towards the concrete (and thus ablation) is not evaluated.

In these preliminary calculations, the corium is defined here with two zones: a lower zone with a gas volume fraction of 0.2, and an upper zone that simulates the crust. The first zone may be quite representative of a liquid corium bubbly flow. This point is however, not critical in the present simulation. The second zone simulates the crust quite approximately since, of course, the cooling of corium typically defines the crust. Thus, a verification of the consistency of this representation is made a posteriori.

The lower zone is, in fact, mainly dedicated to simulating the heated part of the corium in the experiment. It is reminded that, according to experimenters and specialists, the input heat goes mainly to the liquid part with the used techniques. A residual power of 0.4 $\frac{MW}{m^3}$ was chosen. With such a residual power, the heat flux to be extracted on the top surface is about 0.4x0.8x0.2=64 $\frac{kW}{m^2}$, which, taking into the losses and the ablation is in the range of the effective experimental value (see figure 3.16).

As for the permeability of the crust zone, it is reminded that the analysis in section 3.2.2.2 used the correspondence between permeability and concrete content made by Lompersky and Farmer, although it was shown that this extrapolation is questionable.Following this analysis, it has been chosen to test the cases:

- $\kappa = 4 \times 10^{-10} m^2$ (upper limit)
- $\kappa = 1 \times 10^{-10} m^2$ (lower limit)
- mixed case with $\kappa = 4 \times 10^{-10} m^2$ in the upper part of the crust and $\kappa = 1 \times 10^{-10} m^2$ in the lower part.

Note finally that the MC3D model was slightly modified in order approximately simulate the mixing related gas flow from ablation, by multiplying the conductivity by a factor 10 when the melt is liquid, whereas the standard value is used when it is solid. Note that the distinction solid/liquid is made from the knowledge of the actual computed temperature, disregarding the zone (crust or bubbly). The transition temperature is 1900 K, the average value of the solidus (1400 K), and the liquidus (2400 K) for the chosen composition, representative of a corium with 15 % of concrete.

Figure 4.38 provides visualizations of the water saturation in the leftmost image, the temperature of the corium in the second, the pressure of the domain in the third and the initial configuration in the rightmost image (to remind the extent of the zones) for the first case with $\kappa = 4 \times 10^{-10} m^2$. Two instants are represented, showing the progression of the water and the complete cooling of the crust. This is clearly not in agreement with the analysis in section 3.2.2.2, showing that the permeability cannot be taken homogeneously from the correspondence with the concrete content on the top of the crust.

Similarly, figure 4.39 provides visualizations after 10,000 s. (167 mn), at the end of the calculation. In contrast, no water penetration is observed, and the heat is extracted solely by conduction. In fact, the situation is not fully stabilized since the temperature in the lower heated part is very slowly decreasing (not shown). Nevertheless, penetration of water is not expected since the WI heat flux evaluated by MC3D with this permeability is about 60 $\frac{kW}{m^2}$ (figure 4.27). The extent of the solidified zone (in between the red and orange lines on the left) seems quite small compared to its hypothetical extent following the preliminary analysis.

Finally, the stratified case, as hypothesized from the previous analysis, is visualized in figure 4.40. As expected, the water penetrates the zone with the highest permeability only. Again, the situation is slowly evolving, but the second picture at t=8500 s. indicates a reasonable extent to the solid layer (in between the red and orange lines on the left image) compared to the choice for the crust zone in the data set.

In all the calculations, the melt temperature is probably a bit high compared to the experimental data. However, the calculations do not take into account the beginning of the test with higher input heat. The difference should not have a substantial impact.

Furthermore, the pressurization is also very weak for the configurations tested here, meaning that the gas is able to traverse the crust. However, the pressure might rapidly increase with decreasing the permeability, so that, based on mechanical arguments to be elaborated, a minimum permeability may be evaluated [16].

---

[16] However, the experiments tend to indicate that the systems evolve preferentially towards the formation of a volcano

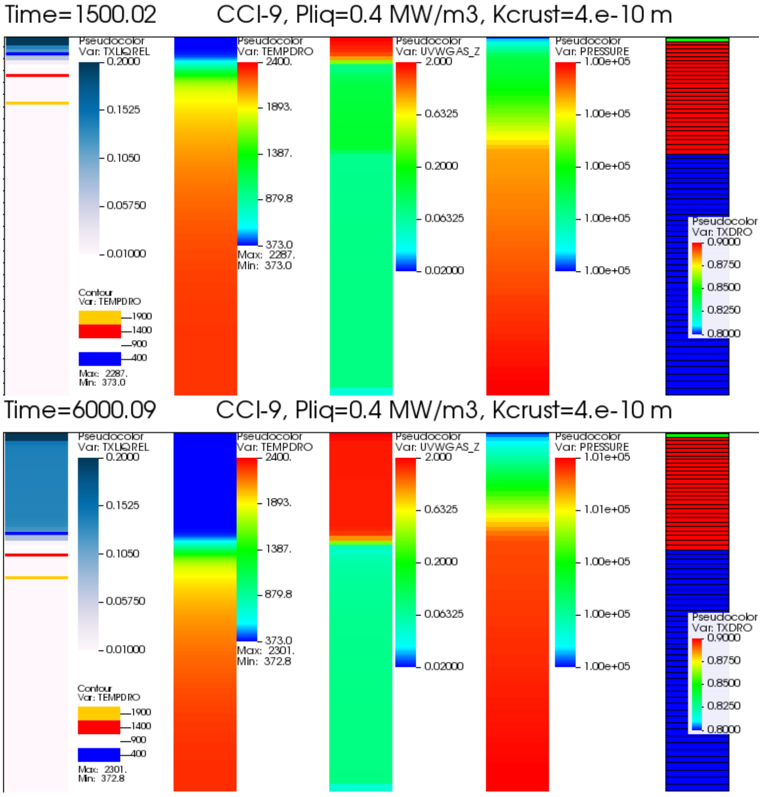

Figure 4.38 – Configuration of a CCI-9 like MC3D 1D calculation with permeability $\kappa = 4 \times 10^{-10} m^2$

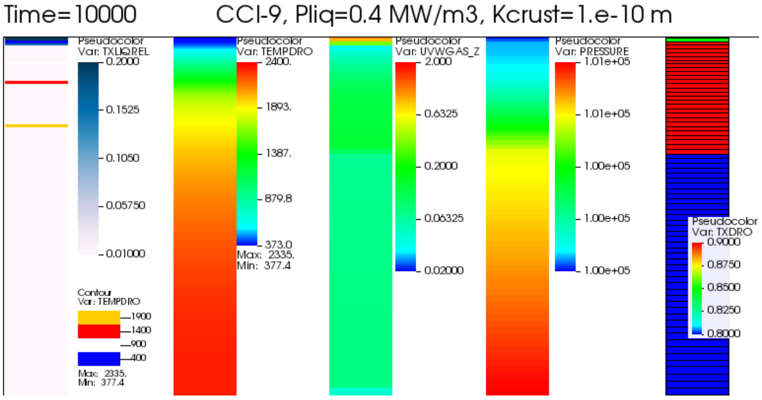

Figure 4.39 – Final configuration of a CCI-9 like MC3D 1D calculation with permeability $\kappa = 1 \times 10^{-10} m^2$

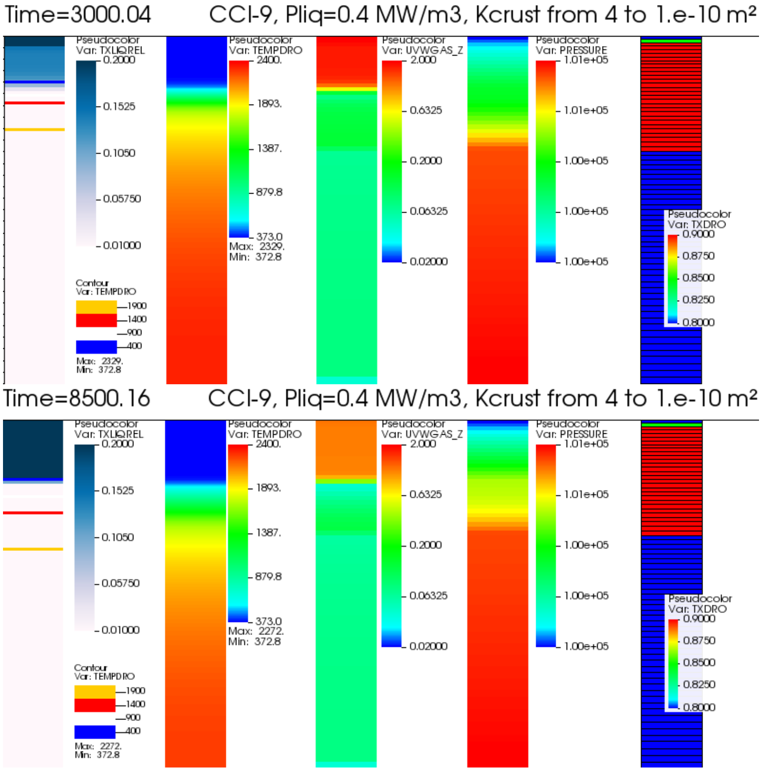

Figure 4.40 – Configurations of a CCI-9 like MC3D 1D calculation with stratified permeability

The extracted heat flux as a function of time is shown in figure 4.41. As can be seen, the extracted heat flux tends towards the expected value, with a quasi-steady situation, at the end of calculation for the first case with $\kappa = 4 \times 10^{-10} m^2$. In contrast, the case $\kappa = 1 \times 10^{-10} m^2$ shows a slow decrease representative of conduction. Finally, the stratified case with 2 permeabilities shows a heat flux representative of the first case in the beginning, during the water penetration, and then a slow decrease due to the limitation by conduction.

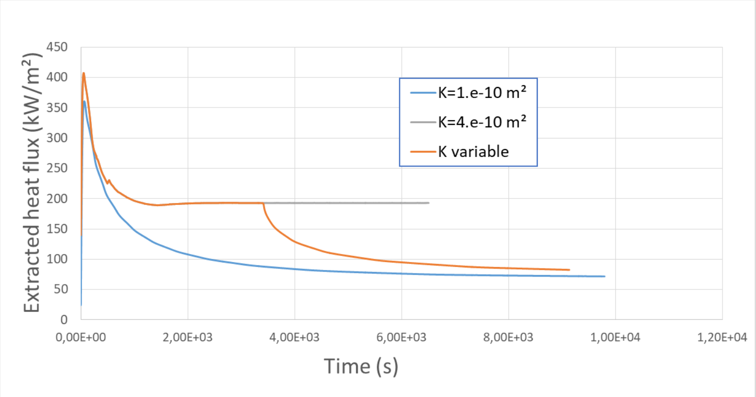

Figure 4.41 – Extracted heat flux in the 3 MC3D 1D simulations CCI-9

Despite the approximate nature of the calculations, these results are consistent with the preliminary analysis, with the presence of an upper fractured "wet crust" subjected to water ingression, and a lower part impermeable to water, due to a stratification of the permeability, itself due to a stratification of the concrete content. The heat flux with this stratified approximation tends rapidly towards the pure conduction case so that the impact of water ingression is difficult to conclude on this basis. However, the calculation confirms the hypothetical size of the crust with the stratified hypothesis.

Despite the incertitude of the SSWICS experimental results, the results of the CCI-9 analysis presented in section 3.2.2.2 and the MC3D simulations tend to indicate that indeed, there could be an absolute permeability that would inhibit the water ingression mechanism. It is also noted that, at least numerically, the difference between the permeability that allows water ingression and the one where it is inhibited is not significant ($\kappa = 4 \times 10^{-10} m^2$, and $\kappa = 1 \times 10^{-10} m^2$ respectively). This, in addition with both the visual observations of a rather constant distance between fractures (see figure 3.14) and the non-linearity (high dependence) of the material property coefficients in the fracture mechanics formulas, could lead to the hypothesis that the dominant parameter is the change of β with the addition of concrete. Therefore, it would then be reasonable to assume that there is a limiting concrete content above which the phenomena are no longer present.

Nevertheless, a direct relation between the concrete content and the permeability should not be expected to be found from a direct extrapolation of the SSWICS results. The border effects and heat losses in the experiments may have greatly affected the local permeability, hence the overall water ingression phenomena. For this reason, it is of great importance to evaluate the two-dimensional effects.

4.5 Conclusions

The evaluation of the stability of the configurations of interest through the model here proposed has proved useful in understanding the limitations of the coolability of corium. The minutia of the flow characteristics when the water penetrates and cools down an initially hot corium layer subjected to residual power have been reviewed. The sensibility of the configuration to the intrinsic characteristics of the medium has been highlighted. The application of the models has resulted in the proposal of two simple criteria needed for the stability of the corium layer on top of a concrete layer.

For the mechanism of water ingression, a particular binary state of the crust was observed. Either its characteristics allow the water to percolate through it and end up fully flooded, or the water only begins to percolate once the crust is sufficiently cooled down through conduction; hence it is completely dry through the process. This change of state is particularly sensitive to the permeability of the medium, and local heterogeneity might onset any change. Regardless, knowing the permeability a priory, coupled with the use of a relative permeability formulation for these types of fracture porous media in the proposed model, the results are deemed coherent with the few experimental results.

Nevertheless, the observed two-dimensional effects in the experiments (SSWICS, Ginsberg, Cho.), as well as the preliminary calculations, may have a substantial effect in the stability, and coolability, of the corium layer, since they affect the flow structure. For this reason, the two-dimensional effect will be studied in the next chapter.

Chapter 5

Two-dimensional Effects

Contents

In the previous chapter an analysis of the reflooding problem with the limiting assumption of one-dimensional flow has been presented. However, various experiments (e.g. [130]) and the preliminary MC3D calculations in chapter 3 suggest a possible unstable behavior for reflooding with the development of liquid "fingers". The characteristics and the impact of this instability need to be addressed. Furthermore, in a real case (e.g., in experiments), the debris bed may be heterogeneous both in configuration (for example, different permeabilities) and in temperature (for example, through heat losses). In particular, the SSWICS experiments could be approximately evaluated, provided the knowledge of the mean permeability, but the short duration of the heat flux plateau, when they are observed, indicates the possibility 2D effects linked to radial heat losses.

In this chapter, two-dimensional effects will be investigated through an extension of the previous model to a simplified pseudo-2D situation in section 5.1. More precisely, the 1D model will be extended to a two-zone or two-channel configuration. Furthermore, evaluations of more accurate two-dimensional unsteady penetration simulations using MC3D will be presented in section 5.2.

5.1 Two-channel steady analytical model

In order to evaluate a two-phase flow through an initially hot and dry debris bed, the 1D analytical model is here extended into a pseudo-2D model (two 1D zones) with the aim of analyzing the stability conditions of the flow in such configuration and its impact in the ability of the porous media to release energy to an overlying water pool. In other words, the aim is to search for steady-state (or quasi-steady) two-phase flow conditions beyond a CHF to analyze if and under which circumstances a partial dry-out with stability (no re-melting) of the debris bed can be assured. To recall, the flow configuration in a steady-state two-phase flow below or at critical heat flux was analyzed in section 4.1. It was observed that the CHF occurs due to dynamical effects maximizing the liquid and vapor flow. As a reminder, the CHF occurs for a specific vapor saturation, governed by the friction terms, tending to 0.5 close to critical pressure, and of the order of 0.75 at 1 bar, depending mainly on the actual bed characteristics (permeability).

In reality, the stability of a two-zone configuration, where a volumetric source term would heat up the debris bed whilst a competing penetrating front would quench a section of the bed, is not likely by nature. Hence, as a first approach, an approximate situation where the debris bed in the dry zone is not further heated by the volumetric power will be developed. The initial temperature conditions of the dried zone do not change, or if they do, they do so slowly. In such a situation, it will be assumed that the flow is separated horizontally into two distinct zones: a two-phase countercurrent flow penetrating the debris bed and an upward single-phase super-heated vapor flow, as is shown in figure 5.1. The green zone represents the quenched portion of the debris bed (T$\sim T_{sat}$), where its lateral (radial) extent occupies a fraction $f_{2\phi}$ of the total horizontal surface. The grey zone represents the dry zone, which in turn occupies the rest of the horizontal surface fraction: $1 - f_{2\phi}$. The 2 zones may have different bed characteristics, i.e., different permeability. In this case, the temperature of the two-phase zone is to be considered at T_{sat}, whilst the temperature of the dry zone is T_0. Likewise, the vapor exiting from both zones is at the temperature of the zone.

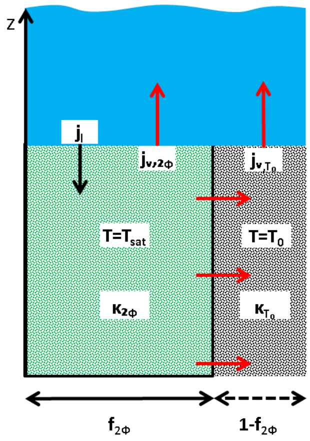

Figure 5.1 – Steady 2-Zone two-phase flow scheme

5.1.1 Laminar case

For the sake of simplicity in this first approach, the modeling will be limited to a purely laminar situation. As before, at each height z, the pressure is presumed common between both phases in the two-phase zone and between each zone. This means, of course, that the flow is essentially one-dimensional, with only minor 2D perturbations.

In the two-phase zone, dubbed $f_{2\phi}$, the relation between the pressure drops for the two phases at any given elevation, eq. (4.3), is maintained, rewritten with modified subscripts as:

$$-\frac{\delta P}{\delta z} = \frac{\mu_{v,T_{sat}}}{\kappa_{2\phi}\kappa_{r,v}} j_{v,2\phi} = \frac{\mu_l}{\kappa_{2\phi}\kappa_{r,l}} j_l + \rho_l g \tag{5.1}$$

where the permeability can be denoted with the subscripts 2ϕ, or T_0 for the two-phase zone and the dry zone, respectively. For the dry zone $(1 - f_{2\phi})$, it is necessary to introduce a new single-phase momentum balance:

$$-\frac{\delta P}{\delta z} = \frac{\mu_{v,T_0}}{\kappa_{T_0}} j_{v,T_0} \tag{5.2}$$

where x_{v,T_i} represents property x (either ρ, μ, or ν) for the vapor phase evaluated at temperature T_{sat} for the two-phase zone or T_0 for the dry zone. Assuming that the pressure gradient between the two zones remains equal amongst each phase, it is possible to equate a relation between the superficial vapor velocities in each zone as:

$$\frac{\delta P}{\delta z} = \frac{\mu_{v,T_{sat}}}{\kappa_{2\phi}\kappa_{r,v}} j_{v,2\phi} = \frac{\mu_{v,T_0}}{\kappa_{T_0}} j_{v,T_0} \tag{5.3}$$

which can be rewritten as:

$$j_{v,T_0} = \frac{\mu_{v,T_{sat}}}{\mu_{v,T_0}} \frac{\kappa_{T_0}}{\kappa_{2\phi}} \frac{1}{\kappa_{r,v}} j_{v,2\phi} \tag{5.4}$$

that, assuming homogeneous permeability $(\kappa_{T_0} = \kappa_{2\phi})$, results in:

$$j_{v,T_0} = \frac{\mu_{v,T_{sat}}}{\mu_{v,T_0}} \frac{1}{\kappa_{r,v}} j_{v,2\phi} \tag{5.5}$$

Also, a new continuity equation that equates the relationship between the partitioning of the descending liquid mass flux into an upward flow of vapor in the single-phase region, $1 - f_{2\phi}$, and another in the two-phase region, $f_{2\phi}$, can be expressed as:

$$\rho_{v,T_{sat}} j_{v,2\phi} f_{2\phi} + \rho_{v,T_0} j_{v,T_0} \left(1 - f_{2\phi}\right) = -\rho_l j_l f_{2\phi} \tag{5.6}$$

where $f_{2\phi}$ is the surface fraction of the bed subjected to a two-phase flow configuration. Combining eq. (5.4) with eq. (5.6), the liquid mass flux as a function of the vapor flux in the two-phase region $(j_{v,2\phi})$ and the surface fraction $(f_{2\phi})$ would be written as:

$$j_l = -\frac{\rho_{v,T_{sat}}}{\rho_l} \left(1 + \frac{\nu_{v,T_{sat}}}{\nu_{v,T_0}} \frac{\kappa_v}{\kappa_{2\phi}} \frac{1}{\kappa_{r,v}} \frac{1 - f_{2\phi}}{f_{2\phi}}\right) j_{v,2\phi} \tag{5.7}$$

Substituting eq. (5.7) into eq. (5.1) as:

$$\frac{\mu_{v,T_{sat}}}{\kappa_{2\phi}\kappa_{r,v}} j_{v,2\phi} = \frac{\mu_l}{\kappa_{2\phi}\kappa_{r,l}} \left(\frac{\rho_{v,T_{sat}}}{\rho_l} \left(1 + \frac{\nu_{v,T_{sat}}}{\nu_{v,T_0}} \frac{\kappa_{T_0}}{\kappa_{2\phi}} \frac{1}{\kappa_{r,v}} \frac{1-f_{2\phi}}{f_{2\phi}} \right) \right) + \rho_l g \tag{5.8}$$

yields the following expression for $j_{v,2\phi}$, as a function of the local saturation and $f_{2\phi}$:

$$j_{v,2\phi} = \frac{\dfrac{\rho_l}{\rho_{v,T_{sat}}} \kappa_{2\phi} g}{\dfrac{\nu_{v,T_{sat}}}{\kappa_{r,v}} + \dfrac{\nu_l}{\kappa_{r,l}} \left(1 + \dfrac{\nu_{v,T_{sat}}}{\nu_{v,T_0}} \dfrac{\kappa_{T_0}}{\kappa_{2\phi}} \dfrac{1}{\kappa_{r,v}} \dfrac{1-f_{2\phi}}{f_{2\phi}} \right)} \tag{5.9}$$

It is easily verified that for eq. (5.9) at the limits $f_{2\phi} = 1$ and $\kappa_{T_0} = \kappa_{2\phi}$, eq. (4.5) is found.

5.1.1.1 Homogeneous permeability

Figure 5.2 plots eq. (5.9) on the left side, and eq. (5.5) on the right side for the limiting case (with ratio of permeabilities = 1, in other words $\kappa_{T_0} = \kappa_{2\phi}$), as a function of the vapor saturation in the two-phase zone α with 3 different values of $f_{2\phi}$ (0.8,0.5, and 0.25), T_0=500 K, and P=1 atm. For $j_{v,2\phi}$ on the left side, the solid green curve plots $j_{v,2\phi}$ with $f_{2\phi}$=1, which is equivalent to eq. (4.5). On the right part of the figure eq. (5.5) It can be noted that the value of α where $j_{v,2\phi}$ is maximal, here called $\alpha_{j_{2\phi,crit}}$, decreases as $f_{2\phi}$ decreases, whilst for j_{v,T_0} it is always at $\alpha = 0$. This last limit, where $\alpha = 0$, can be interpreted as having all the vapor in the two-phase zone migrate to the dry zone, hence leaving 2 fully single-phase flow zones (a penetrating liquid zone, and an upward escaping super-heated vapor zone).

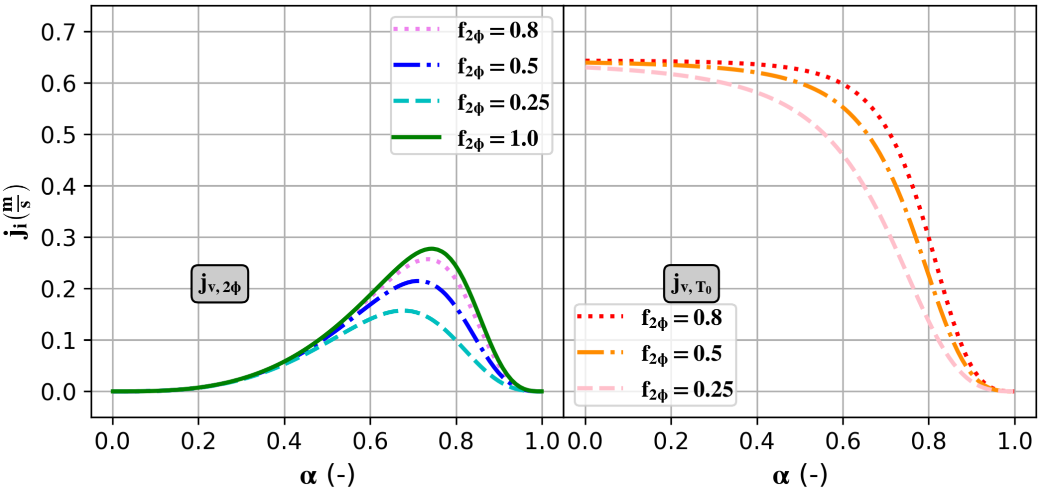

Figure 5.2 – Superficial vapor velocity for the two-phase zone $j_{v,2\phi}$ and the dry zone j_{v,T_0} for $\kappa \sim 1.2 \times 10^{-9} m^2$ ($d_p = 1mm$), P=1atm, and T_0= 500 K at different $f_{2\phi}$ with $\kappa_{2\phi} = \kappa_{T_0}$

Left: $j_{v,2\phi}$, eq. (5.9); right: j_{v,T_0} eq. (5.5)

As in the previous chapter, to maximize the heat flux, it is necessary to maximize the total vapor mass flux escaping the debris bed. Figure 5.3 plots the mass flux of both the saturated vapor and the super-heated vapor as a function of α for different values of $f_{2\phi}$ with T_0= 500 K. At first, it is observed that there might be a transition of the flow nature at $f_{2\phi}$=0.337. Above this value, the maximum value is found for a vapor saturation in the two-phase zone larger than 0.432. When $f_{2\phi}$<0.337, the maximum is instead found for a vapor saturation equal to 0, that is, for a purely single-phase liquid flow in the "two-phase" zone. The value for the lowest $f_{2\phi}$ ($\sim$0.337) plotted in figure 5.3 was numerically obtained and is the value at which there is still a maximal total mass flux at a value of α above $\alpha = 0$. In other words, this minimal $f_{2\phi}$, hereinafter referred to as $f_{2\phi,min}$, would represent the flow configuration where any further reduction in $f_{2\phi}$ would result in the two-phase zone becoming a single-phase liquid zone. It is also noted with attention that, for the given conditions in the figure, the total mass fraction increases when the two-phase region decreases, meaning that the higher energy may be extracted in that situation.

Comparing figure 5.2 and figure 5.3 it is evident that the value of α at which there is a maximum total mass flux for each value of $f_{2\phi}$ is not at $\alpha = \alpha_{j_{2\phi,crit}}$. This can be understood as a result of the pressure and mass balances between the phases and the zones. With decreasing vapor saturation in the two-phase zone, the vapor is then forced to exit through the dry zone (to maintain the mass balance with the penetrating liquid), and since with higher temperatures the vapor density is lower, it occupies more space and therefore its flux ($\dot{m_{v,T_0}}$) is highest where all the vapor is forced to exit in through the dry zone ($\alpha = 0$ in the two-phase zone). Counteracting this effect, the lower the value of α, the lower the saturated-vapor mass flux ($\dot{m_{v,T_{sat}}}$) in the two-phase zone. That is, the more vapor escapes through the dry zone, the less it escapes through the two-phase zone and vice-versa. Hence, the maximal overall mass flux of vapor is at a value of α between 0 and $\alpha_{j_{v,2\phi,crit}}$.

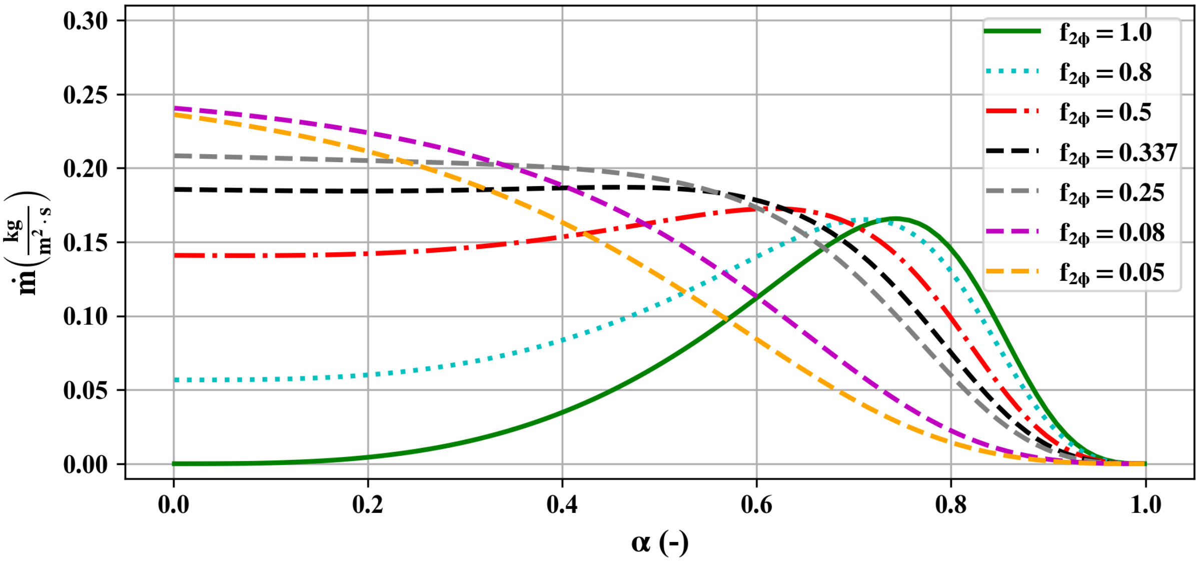

Figure 5.3 – Total mass flux $\dot{m}$, left hand side of eq. (5.6), for $\kappa \sim 1.2 \times 10^{-9} m^2$ ($d_p = 1mm$), P=1atm, and T_0= 500 K at different $f_{2\phi}$

The total power that can be extracted through the debris bed, here called ϕ_{2z}, can be estimated as:

$$\phi_{2z} = \underbrace{j_{v,2\phi}\rho_{v,T_{sat}}h_{lv}f_{2\phi}}_{\text{vapor traversing } f_{2\phi} \text{ zone}} + \underbrace{j_{v,T_0}\rho_{v,T_0}h_{lv}\left(1-f_{2\phi}\right)}_{\text{vapor traversing 1-}f_{2\phi}\text{ zone}} + \underbrace{\phi_{\Delta T}}_{\text{vapor heat up in 1-}f_{2\phi}\text{ zone}} \tag{5.10}$$

where the sum of the first two terms, which is the energy extracted from the two-phase zone, can be expressed as:

$$\phi_{2\phi} = j_{v,2\phi}\rho_{v,T_{sat}}h_{lv}f_{2\phi}\left(1+\frac{\nu_{v,T_{sat}}}{\nu_{v,T_0}}\frac{1}{\kappa_{r,v}}\frac{1-f_{2\phi}}{f_{2\phi}}\right) \tag{5.11}$$

In order for the vapor that flows through the dry zone to exit at T_0 it must, in fact, absorb some energy given by the debris bed. The energy absorbed by the vapor to heat from T_{sat} to T_0 is here approximated as:

$$\phi_{\Delta T} \approx \overline{\rho_d c_{p,d}} j_{v,T_0}\Delta T\left(1-f_{2\phi}\right) \tag{5.12}$$

with both $\overline{\rho_d}$ and $\overline{c_{p,d}}$ being the density and specific heat capacity of the vapor at a mean temperature between T_{sat} and T_0.

The upper part of figures 5.4 and 5.5 plot the overall extracted heat flux ϕ_{2z}, eq. (5.10), for different values of $f_{2\phi}$ at 1 atm with 1 mm particles and T_0= 500, and 700 K respectively. The solid green curves plot the values at $f_{2\phi} = 1$, which is equivalent to eq. (4.10), for comparison. As can be seen, the overall extracted heat flux (per m^2 of total surface) increases with decreasing $f_{2\phi}$ up until $f_{2\phi} = 0.08$ (for T_0= 500 K) which in turn results as an absolute maximum, meaning that any further decrease of $f_{2\phi}$ would instead result in a decrease of extracted ϕ. As pointed out before, at low values of $f_{2\phi}$, the maximal occurs at $\alpha = 0$. In other words, the heat extraction would be maximized in a two-zone configuration with a purely single-phase liquid flow in the "two-phase" zone and a pure super-heated vapor zone. This is due to the fact that the liquid superficial velocity would be larger whilst flowing in a purely single-phase configuration in the $f_{2\phi}$ zone. Nevertheless, this would mean that all the vapor produced in the "two-phase" zone would immediately be transferred laterally to the dry zone, which is not entirely logical. In reality, the radially flowing vapor would be subjected to friction; hence, depending on the size of the fingers, it would not be immediately transferred to the dry zone. Furthermore, only at low temperature, an increase of the extracted heat flux is observed compared with the case with $f_{2\phi} = 1$. Case in point, with T_0= 700 K (see figure 5.5), even with the low value of $f_{2\phi} = 0.08$ the overall extracted heat flux is only slightly larger than with $f_{2\phi} = 1.0$, and comparing it with the case of T_0= 500 K (see figure 5.4) it is evident that this "global maximum" decreases with temperature. This would tend to indicate that with completely homogeneous debris bed, both in temperature and permeability, at high temperatures, the configuration that maximizes heat extraction is one with $f_{2\phi} = 1.0$. On the other hand, at low temperatures (<700 K), there are values of $f_{2\phi} < 1.0$ where the maximum is larger than with $f_{2\phi} = 1.0$ at values of $\alpha > 0$. In other words, for temperatures close to the saturation temperature, there are two-zone configurations with an overall increase in heat extraction. Furthermore, comparing the cases of T_0=500 and 700 K, it can be observed that $f_{2\phi,min}$ (the value of $f_{2\phi}$ where there is still a maximum at a value of $\alpha > 0$) decreases with the temperature. Nevertheless, at $f_{2\phi,min}$ the maximum is placed at a value of α here called $\alpha_{f_{2\phi,min}} \sim 0.432$.

The lower parts of figures 5.4 and 5.5 plot $\frac{\phi_{2\phi}}{f_{2\phi}}$ (eq. (5.11)) on the left, and $\left(\frac{\phi_{\Delta T}}{1-f_{2\phi}}\right)$ (eq. (5.12)) on the right both normalized over their respective surface fractions. In other words, the lower left part plots the total energy absorbed through the evaporation of liquid into vapor per m^2 of the two-phase surface. As expected, with lower values of $f_{2\phi}$, the extracted heat flux greatly increases. This again comes from the fact that for these configurations, the maximum occurs with a single-phase liquid flow in the "two-phase" zone and the vapor flowing out through the dry zone. In these theoretical cases, the liquid velocity is increased since it is only limited to single-phase friction terms with the debris bed particles. Finally, the lower right parts show the energy absorbed by the outgoing vapor that flows through the dry zone (per m^2 of dry zone surface). In it, it is evident that the energy absorbed increases with increasing temperature, but is remarkably lower than the energy extracted from the two-phase zone.

Essentially, what this means is that considering the case with residual power, it is evident that the configuration, even in the case of moderate initial temperatures, is unstable. This last can be deduced since with increasing temperature, the amount of energy extracted by the vapor flowing in the dry zone increases, but would be substantially lower than the residual power. This would mean that the energy extracted from the debris bed by heating up the vapor would not suffice to counterbalance the effects of the residual power. Furthermore, even if for a small range of low temperatures, the configuration could extract more overall heat, the increasing temperature in the dry zone would, in turn, lead to a decrease of overall heat extraction with increasing temperature, regardless of the value of $f_{2\phi}$. In other words, a "steady" condition would quickly deteriorate and become unstable with a dry zone, which heats up with time.

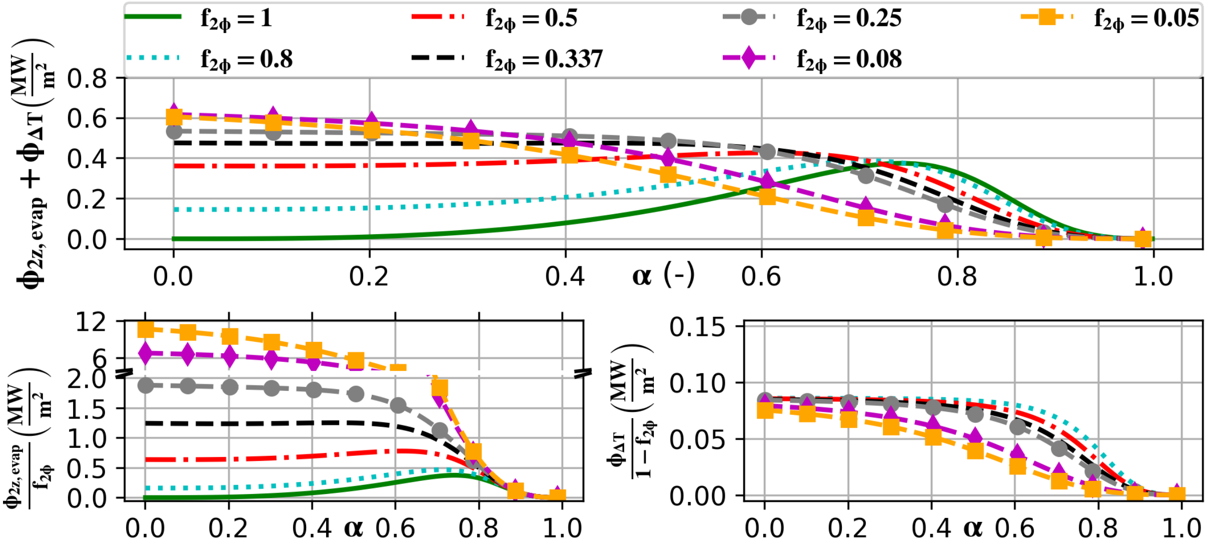

Figure 5.4 – $\phi_{2\phi}$, eq. (5.11), and $\phi_{\Delta T}$, eq. (5.12), $\kappa \sim 1.2 \times 10^{-9} m^2$ ($d_p = 1mm$), P=1atm, and T_0= 500 K at different $f_{2\phi}$

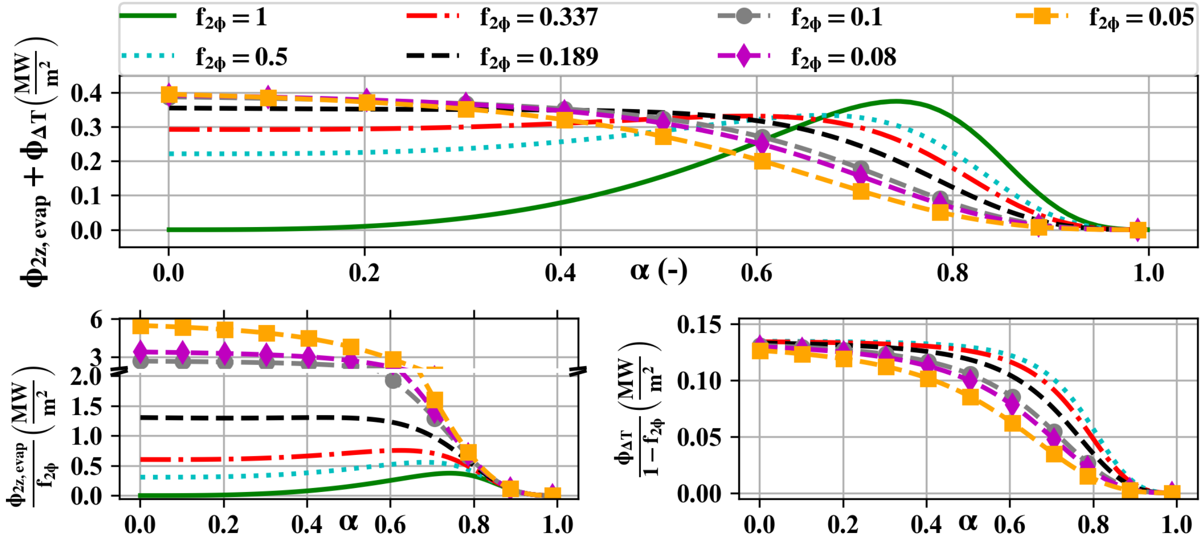

Figure 5.5 – $\phi_{2\phi}$, eq. (5.11), and $\phi_{\Delta T}$, eq. (5.12), $\kappa \sim 1.2 \times 10^{-9} m^2$ ($d_p = 1mm$), P=1atm, and T_0= 700 K at different $f_{2\phi}$

5.1.2 Mixed case

For larger particles, the same type of approach can be used to construct a model that includes the inertial effects. The momentum balance for the two zones can be expressed as:

$$-\frac{\delta P}{\delta z} = \frac{\mu_{v,T_{sat}}}{\kappa_{2\phi}\kappa_{r,v}} j_{v,2\phi} + \frac{\rho_{v,T_{sat}}}{\eta_{2\phi}\eta_{r,v}} j_{v,2\phi}^2 = \frac{\mu_l}{\kappa_{2\phi}\kappa_{r,l}} j_l + \rho_l g \tag{5.13}$$

$$\frac{\delta P}{\delta z} = \frac{\mu_{v,T_{sat}}}{\kappa_{2\phi}\kappa_{r,v}} j_{v,2\phi} + \frac{\rho_{v,T_{sat}}}{\eta_{2\phi}\eta_{r,v}} j_{v,2\phi}^2 = \frac{\mu_{v,T_0}}{\kappa_{T_0}} j_{v,T_0} + \frac{\rho_{v,T_0}}{\eta_{T_0}} j_{v,T_0}^2 \tag{5.14}$$

Solving numerically eqs. (5.6), (5.13) and (5.14), with homogeneous permeability κ and passability η, leads to obtain $j_{v,2\phi}$, and j_{v,T_0} plotted in figures 5.6 and 5.7 for T_0= 500 and 1000 K with d_p= 3 mm. As can be seen, the temperature range where a possible equilibrium is larger. Figure 5.7 shows how even at T_0= 1000 K some solutions seem plausible from the heat extraction point of view. Nevertheless, as before, the extracted heat flux in the dry zone is remarkably lower than the imposed residual power equivalent to classical CHF.

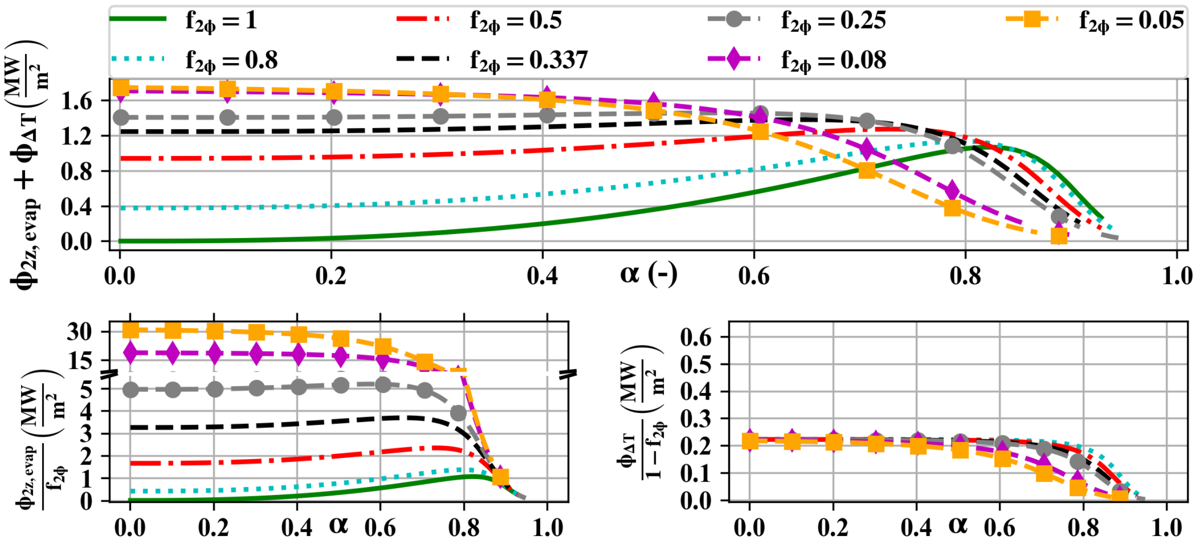

Figure 5.6 – $\phi_{2\phi}$ and $\phi_{\Delta T}$ calculated with $j_{v,2\phi}$ and j_{v,T_0} solving from eqs. (5.13) and (5.14), $\kappa \sim 1.2 \times 10^{-8} m^2$ ($d_p = 3mm$), P=1atm, and T_0= 500 K at different $f_{2\phi}$

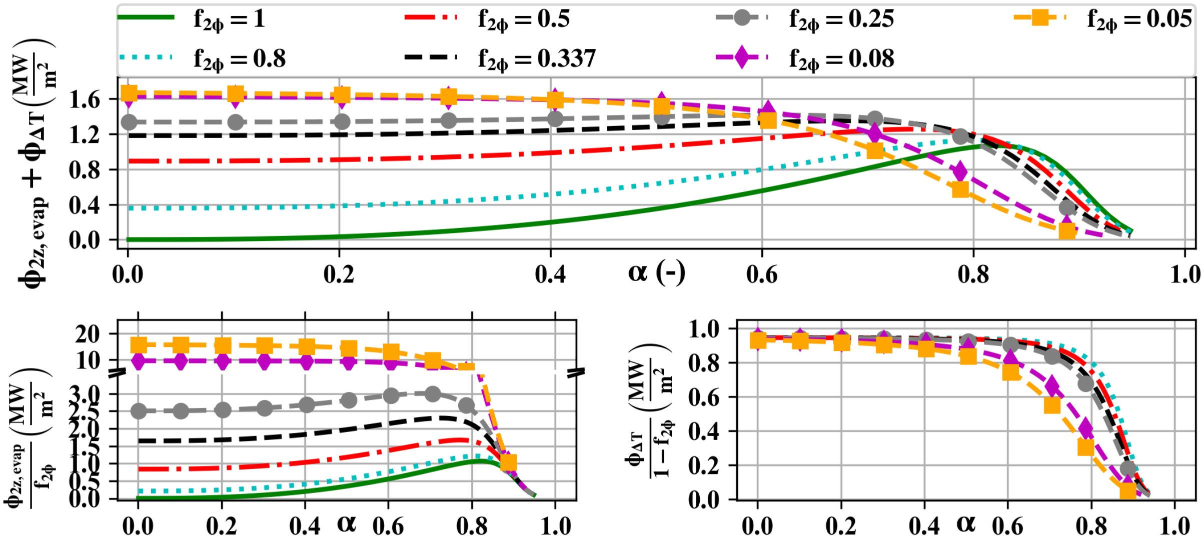

Figure 5.7 – $\phi_{2\phi}$ and $\phi_{\Delta T}$ calculated with $j_{v,2\phi}$ and j_{v,T_0} solving from eqs. (5.13) and (5.14), $\kappa \sim 1.2 \times 10^{-8} m^2$ ($d_p = 3mm$), P=1atm, and T_0= 1000 K at different $f_{2\phi}$

5.2 Unsteady reflooding 2D

As the steady reflooded situation cannot be stable beyond the CHF, the question is posed regarding the stability of the water reflooding front. It is reminded that Ginsberg et al. [129] indicated that in their reflooding experiments, the water was penetrating as channels. In contrast, Cho et al. [132] observed an unstable front with one single large central channel. The interest in the section is to provide a first analysis of the instability occurrence and mechanisms. First, the two-zone analytical model is applied to analyze the possibility of front penetration velocity from the energetic point of view by estimating it using an expression similar to eq. (4.35). Afterward, analysis related to the front stability in debris bed and in the fractured crust will be approached with the help of MC3D simulations.

5.2.1 Unsteady 2-zone analytical model

Having seen that the configuration is mostly unstable by nature, in the real case, the stability of the overall debris bed would be a competition between the penetrating front and the heating of the dry zone. Following the analysis presented in section 4.2, where it was seen that the penetrating front velocity can be linked to the extracted heat flux, an expression similar to eq. (4.35) can be used to estimate the penetrating front velocity by replacing ϕ_{λ}^{crit} by $\frac{\phi_{2\phi}}{f_{2\phi}}$ at the maximal α for each $f_{2\phi}$.

$$u_{2z} = \frac{\dfrac{\phi_{2\phi}}{f_{2\phi}}}{(1-\varepsilon_0)\,\rho_d c_{p,d} \Delta T} \tag{5.15}$$

Figure 5.8 plots the results of eq. (5.15) as a function of $f_{2\phi}$ for T_0 =700 and 1000 K with d_p= 3mm. In reality, this last result in an overestimation of the velocity since eq. (4.35) is developed for the laminar regime, but it serves as a first-order approximate that would capture the tendency with respect to the temperature. The figure also plots the numerical values found in 2D MC3D calculations that will be presented in section 5.2.3. As can be seen, with increasing $f_{2\phi}$ decreases until reaching values comparable to the ones presented in section 4.2. Furthermore, it is evident that the penetrating front velocity is larger than the 1D one (equivalent to the one using $f_{2\phi}$=1).

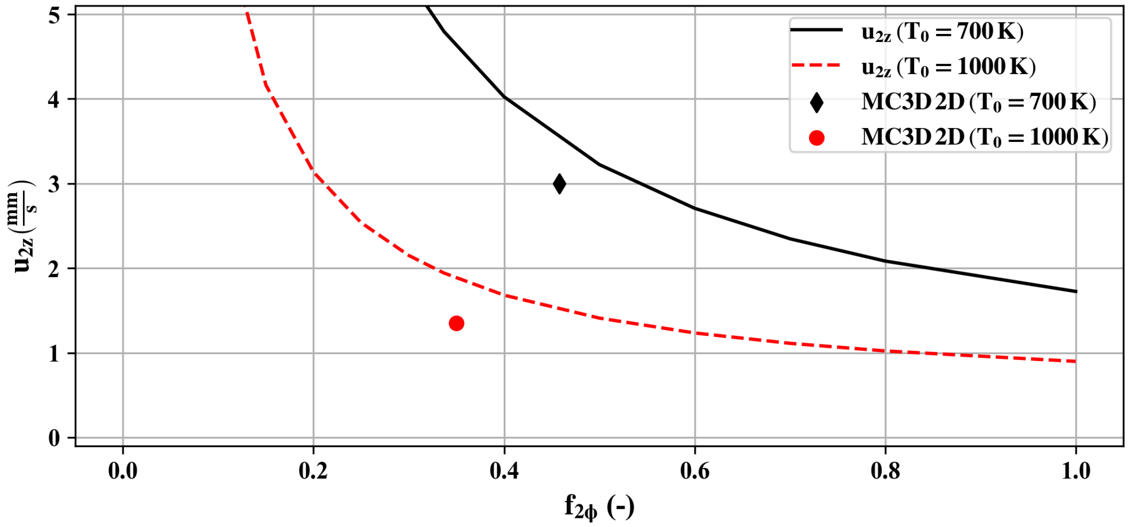

Figure 5.8 – Unsteady 2D penetration velocity u_{2z} as a function of $f_{2\phi}$ for T_0= 700, and 1000 K with d_p=3 mm compared with 2D MC3D results presented in section 5.2.3.

Although figure 5.8 serves as an indication of the possible 2D penetrating front velocities, further analysis will be performed with the help of MC3D code in the following sections.

5.2.2 Instability analysis in debris bed with MC3D-PREMIX

The preliminary MC3D calculations of the Ginsberg experiments presented in section 3.1, indicated, in coherence with the findings of Ginsberg, that the water penetration front was unstable with descending two-phase flow fingers. However, these simulations also showed the dependency of the flow configuration in the meshing, although the overall heat extraction was found independent of it. The previous analytical modeling indicated the possibility to have such kind of configuration with one-phase or two-phase fingers separated by upward gas flows, although the situation should be less favorable on the energetic point of view.

The origin of the instability found in the simulation is not so clear. Instabilities in porous media in general allude to the Saffman-Taylor instability [135], [137]. These instabilities arise from the difference of viscosity or, more properly, viscous frictions across the waterfront. However, the instability was also observed in the Ginsberg tests, taking place for the most part in a mixed laminar-inertial regime, so that viscous frictions are not dominant. The second obvious mechanism that comes in mind is the Rayleigh-Taylor instability, due to acceleration effects (with gravity as a special case) [224]. However, the front propagation is clearly a function of the permeability and passability, as well as temperature, so a direct application will not provide satisfactory results [17]. Furthermore, the front is evaporating, and the liquid phase seems, in fact, to be subjected to a two-phase flow. Due to the large number of interacting processes, particularly the two-phase aspect at one side of the front, a stability analysis could not be attempted during this work.Rather, in this section, the aim is to provide a preliminary instability study based on 2D numerical simulations with MC3D. This numerical study might then be used as support to properly establish a theory describing the process.

The initial conditions are similar to those of the one-dimensional simulations, with a subdivision of the mesh in the lateral direction. The analysis is restricted to a 2D Cartesian geometry, with a domain of 40 cm height. After successive trials, a reliable lateral meshing was found with 64 lateral cells for 16 cm, i.e., mesh size of about 2.5 mm for the mixed inertial-laminar situation (d=3 mm), or, equivalently 128 cells for 20 cm, hence mesh size of 1.5 mm. However, for laminar cases (d=1 mm), simulations have also been performed with finer grids and smaller domains. Two types of top boundary conditions have been used as these ones are suspected of having a strong impact. In any case, this first approach aims to analyze the specific instability of the penetration front, so that potential perturbations in the overlying water pool (large convection rolls) should not participate.

The boundary conditions BC-1 are those used in the 1D calculations: the top mesh corresponds to the top of the debris bed, and the topmost meshes are already quenched and full of water. Also, a random porosity ε of 0.4 ± 0.05 was set in the top meshes. The boundary condition at the top of the domain imposes the pressure, and only allows liquid to enter into the domain. The initial conditions are depicted in figure 5.9. The boundary conditions BC-2 are similar, but the top mesh is without any debris, and the

---

[17] The Rayleigh-Taylor model is a function of the acceleration and densities of the fluids.

debris bed is with homogeneous temperature (no topmost quenched meshes). These conditions are less restrictive than BC-1, which, somehow, forces the flow to be quasi 1D at the top of the domain. For the sake of analyzing flow instabilities, the BC-2 conditions seem more reliable.

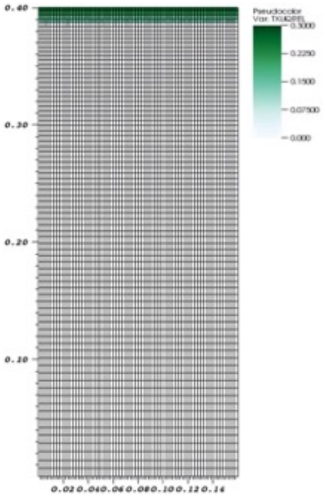

Figure 5.9 – 2D refined meshing with BC-1 boundary for top reflooding instability simulations plotting in green the water saturation

5.2.3 Simulations in the inertial regime

Figure 5.10 plots the results of a simulation with BC-1 conditions for $d_p = 3mm$ with $T_0 = 1000K$ at three different times (100, 275, and 400 seconds) showing in green shades the liquid saturation (topped at a maximum of 0.3 for better visualization), with the background color (red to light blue) being the temperature of the drops, and the small vectors are plotting the velocity of the vapor.

In the leftmost image, the initial instabilities' observed wavelength seems to be in the order of magnitude of the mesh size. Although quite chaotic and with different sizes, it is possible to visualize certain wavelengths, which may indicate that, since the mesh size is in the order of magnitude of the debris size, the flow is unconditionally stable under all wavelengths (looking at wavelengths smaller than the debris size makes no sense). Afterward, as observed in the image in the middle, the smallest wavelengths merge, and larger ones appear and begin to dominate the penetration. These predominant fingers are of a typical length-scale in the order of the centimeter. The merging process of the two-phase water fingers appears to be linked to the cooling of the space between successive fingers by the water vapor that traverses it. Finally, in the image on the right, it is seen that the merging process continues, although it is limited here by the domain dimensions. Interestingly, the "root of the fingers", i.e., the mean height (or mean interface) at which the entire (or almost entire) width of the domain is quenched and with the presence of water, advances in a quasi 1D manner. This last can be linked to the boundary conditions BC-1 since the "initial water penetration" was imposed from the initialization of the simulation in the topmost meshes.

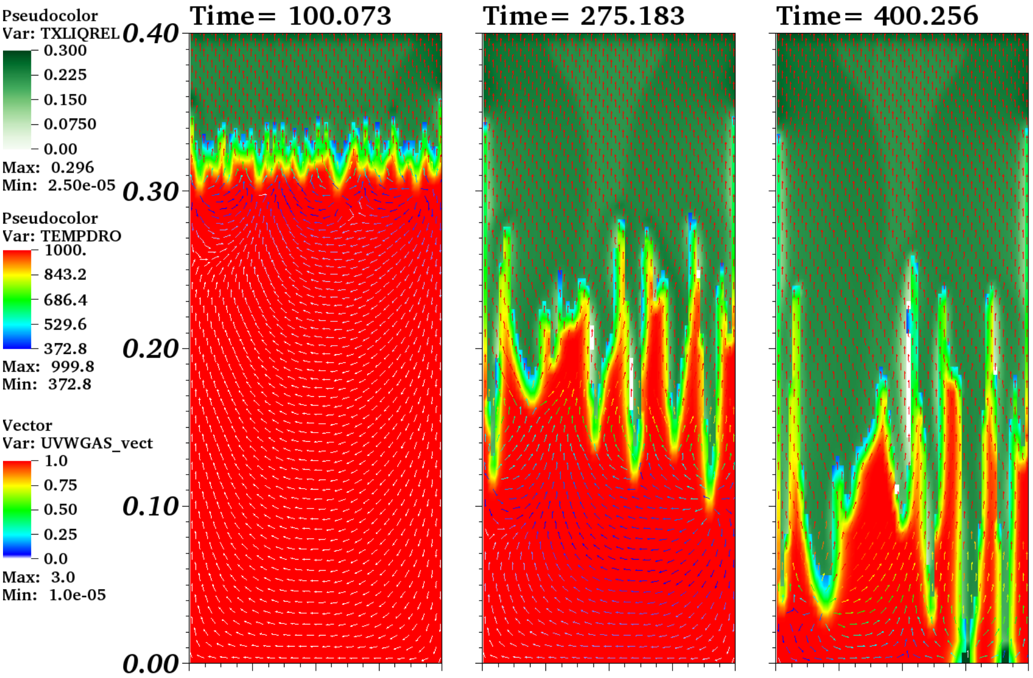

Figure 5.10 – 2D instability progression for $\kappa \sim 1 \times 10^{-8} m^2$ ($d_p = 3mm$), P=1atm, BC-1, and $T_0 = 1000K$ showing the configuration at three different times

A simulation with the same characteristics with the boundary conditions BC-2 was performed for both the 64 and 128 lateral mesh domains, with very similar results regardless of the mesh number. Results for the extended domain are shown in figures 5.11 and 5.12 using a different presentations. The first one plots the temperature of the debris at three distinct times, whilst the second figure plots the water saturation contoured by two temperature levels also for two different times. Clearly, the configuration is very different compared to BC-1, although the mechanisms of instability are likely the same. With these boundary conditions, it is observed that the instabilities are developing from an initial small wavelength and then growing in width by aggregation (pairing) of the smaller wavelength. An important difference is that an instability with an approximately sinusoidal shape, in the beginning, is not observed, but rather the instability is manifested through the appearance of fingers. After 40 seconds, as can be seen in the topmost image in figure 5.11, 13 penetrating fronts are emerging, with thus a typical wavelength of about 2.5 cm (so about 8 times the diameter of the particles). However, once again, a selection seems to occur so that approximately one finger develops over two. After 160 seconds, only 4 fingers are predominantly developed, leaving behind 3 or 4 smaller ones. At the end of the simulation (230 seconds), shown in the left part of figure 5.12, the leftmost finger has again developed predominantly over all the others. This last situation may however, be impacted by the domain size.

Another important difference with simulations BC-1 and with 1D simulations is the fact that the water penetrates in the cyclic pulsating way. This can be observed in figure 5.12. Comparing the right and the left part of the figure, it is clear that the water is not present in the fingers at all times. This means that the liquid saturation is not homogeneous in the quenched region. The fingers have a liquid saturation that varies in pulses from nearly 0 to around 40-50%. In contrast, the fingers that stop advancing are progressively drying (the debris remains cold; however, for these simulations, the residual power was not introduced).

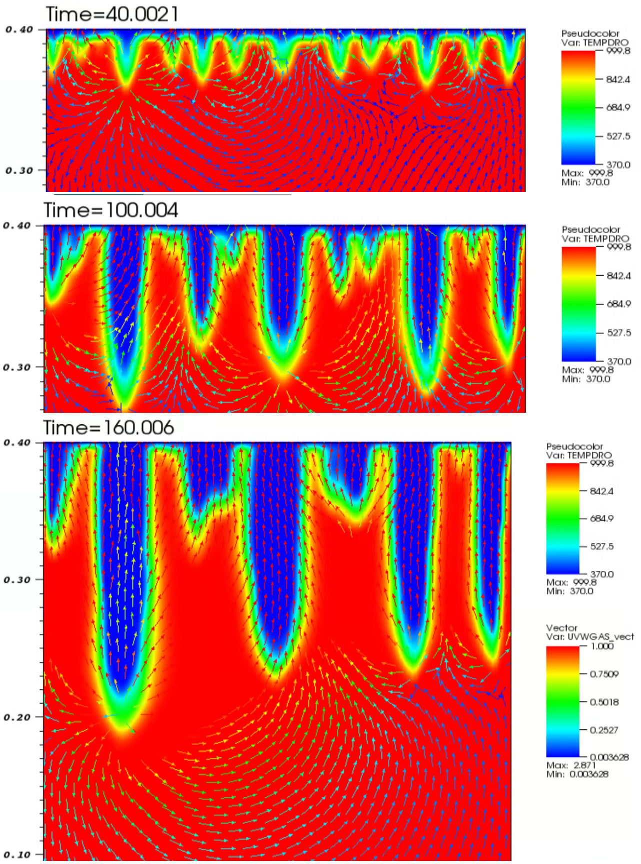

Figure 5.11 – 2D instability progression for $\kappa \sim 1 \times 10^{-8} m^2$ ($d_p = 3mm$), P=1atm, and $T_0 = 1000K$ with BC-2 conditions, and extended mesh (128 lateral cells, 32 cm), showing the configuration at three different times. Background color is the debris temperature, and the small vectors plot the vapor velocity.

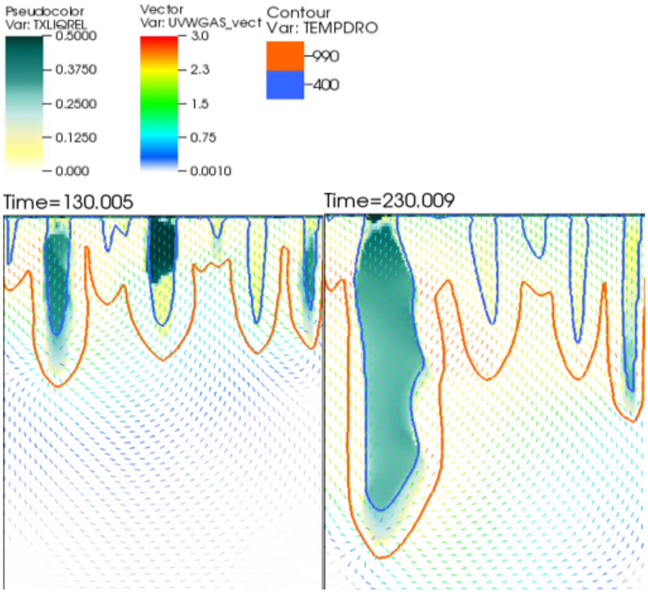

Figure 5.12 – Same simulation as in figure 5.11 with a different view highlighting the water penetration, at t=130 and 230 s. Background color is the liquid saturation, and the blue and orange contour show two temperature levels

Figure 5.13 plots the extracted heat flux of both a 1D and the 2D simulations as a function of time. As can be observed, the green 1D and the yellow 2D BC-1 curves are almost directly over posed. This is due to the quasi 1D behavior of the advancing "mean interface" in the BC-1 2D simulation. This limits the extraction of the heat flux consistently with the analytical modeling results: as the heat flux is limited by the flow conditions above the interface where the flux is extracted, the final mean heat flux is found very close to the 1D simulations with the same initial temperature. In contrast, the BC-2 simulations, which are more consistent with the 2D 2-zone analytical modeling, show a noticeably lower mean heat transfer (and much less stable due to the pulsating behavior).

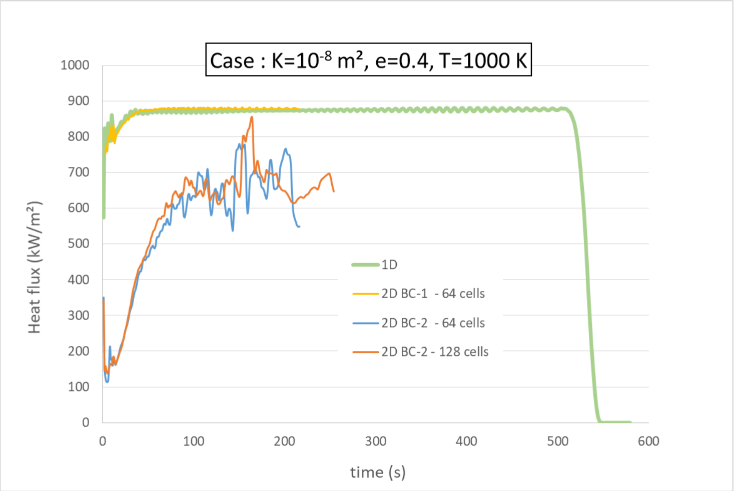

Figure 5.13 – Extracted heat flux for the 1D and 2D simulations $\kappa \sim 1 \times 10^{-8} m^2$ $(d_p = 3mm)$, P=1atm, and $T_0 = 1000K$

This lower heat transfer may be linked with the results of the 2-zone analytical model, which also predicts a lower heat flux in similar conditions. Furthermore, the approximate surface fraction of the fingers is of the order of one third. This may also be related to the results of the analytical 2-zone model where a transition of behavior was found for this order of two-phase region extent. The pulsating effect may be related to the fact that there is no preferential liquid saturation inside the fingers (black dashed lines in figure 5.5). Figure 5.11 clearly shows the deviation of a part of the produced vapor flow in-between the fingers. Note also that the advancement of the tip of the fingers is roughly of the order of 1.3 $\frac{mm}{s}$, which is consistent with the Ginsberg results, by extrapolation of figure 4.19.

The impact of the debris temperature has been rapidly investigated. Figure 5.14 plots the result of a simulation with BC-2 boundary conditions and 700 K ($\Delta T = 430K$), showing the history of water penetration. As before, there is a small number of fingers emerging. These ones are gradually merging by pair with a progressive drying of the other fingers. At the end of the simulation, only one large finger is subsisting. The fingers are penetration with a large liquid saturation, of the order of 40 %. The area of the finger ($f_{2\phi}$) is still roughly of the order of 40 %. On the other hand, the advancement of the tips of the fingers is faster, roughly of the order 3 $\frac{mm}{s}$.

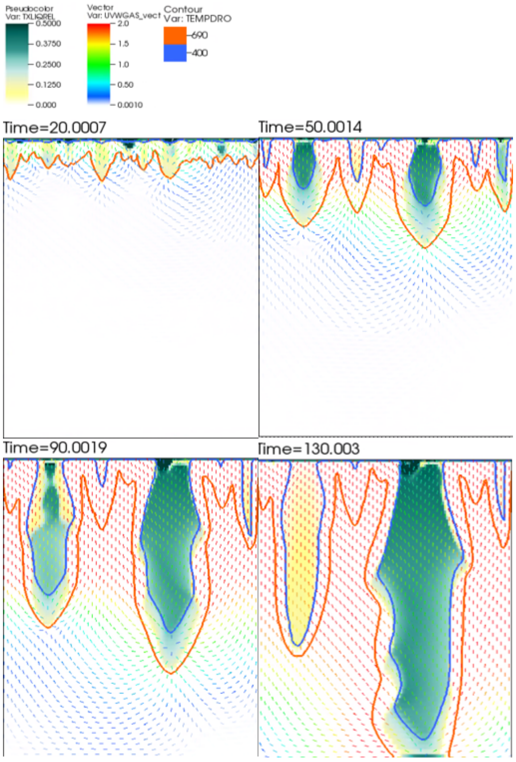

Figure 5.14 – 2D simulation of the water penetration in a debris bed with $\kappa \sim 1 \times 10^{-8} m^2$, P=1atm, and $T_0 = 700K$. Background color = liquid saturation

The extracted heat flux is shown in figure 5.15, compared with the 2D BC-2 case with T_0=1000 K. It is reminded that the heat flux in the 1D and 2D BC-1 simulations is approximately independent of the initial debris temperature. Nonetheless, this is not the case for the 2D BC-2 calculations. As can be seen, with lower temperatures, the 2D extracted heat flux tends towards the results of the 1D calculation. In other words, with a lower initial temperature of T_0, the characteristic size of the observed instabilities (width of the fingers) increases, hence the extracted heat flux increases. This trend continues until at T_0 close to saturation temperature, the instabilities disappear, and the front becomes quasi 1D.

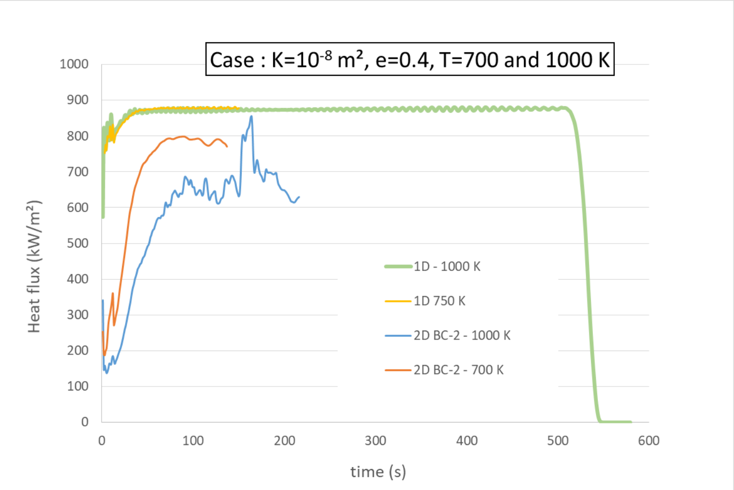

Figure 5.15 – Extracted heat flux for the 1D and 2D simulations $\kappa \sim 1 \times 10^{-8} m^2$ ($d_p = 3mm$), P=1atm, $T_0 = 700K$ and $T_0 = 1000K$

5.2.4 Simulations in the laminar range

Figure 5.16 plots the result of a simulation with the same initial conditions with the exception of the particle diameter, which was lowered from 3 to 1.6 millimeters ($\kappa = 3.10^{-9} m^2$) with the boundary conditions BC-1. In this case, the initial instabilities also merge, but the resulting wavelength is significantly smaller. The advancing water fingers seem rather coarse since, probably, the refinement of the meshing does not allow to properly capture the shape. Nevertheless, the progression is similar to the previous case. On the other hand, in figure 5.17, which plots the result of the simulations with the particle diameter of 0.9 millimeters ($\kappa = 10^{-9} m^2$), it can be seen that the growth of the instabilities is suppressed.

However, the same simulation with a reduced scale by a factor 4 shows the development of tiny fingers with a thickness of some few millimeters (figure 5.18). This is the order of magnitude of the debris size, so the consistency of the calculation is not clear.

The same calculation with $\kappa = 10^{-9} m^2$ and T_0= 1000 K was done with the initial scaling (40 cm high) and BC-2 boundary conditions, with the results shown in figure 5.18. In agreement with the findings of the laminar regime simulations using BC-1 conditions, the developed fingers are much thinner and, overall, the upper part of the domain is rapidly totally quenched, so that the behavior is almost one-dimensional. Note that the flow is very unstable close to the top boundary condition.

From these results, it can be clearly seen how the permeability drastically affects the onset of the instabilities, and the growth of the same, with lower permeabilities suppressing the instabilities, or at least making them smaller in wavelength down to the size of the debris. Furthermore, as the wavelength decreases, the effects in the quenching progression would also decrease, with the progression resembling more and more to a 1D front.

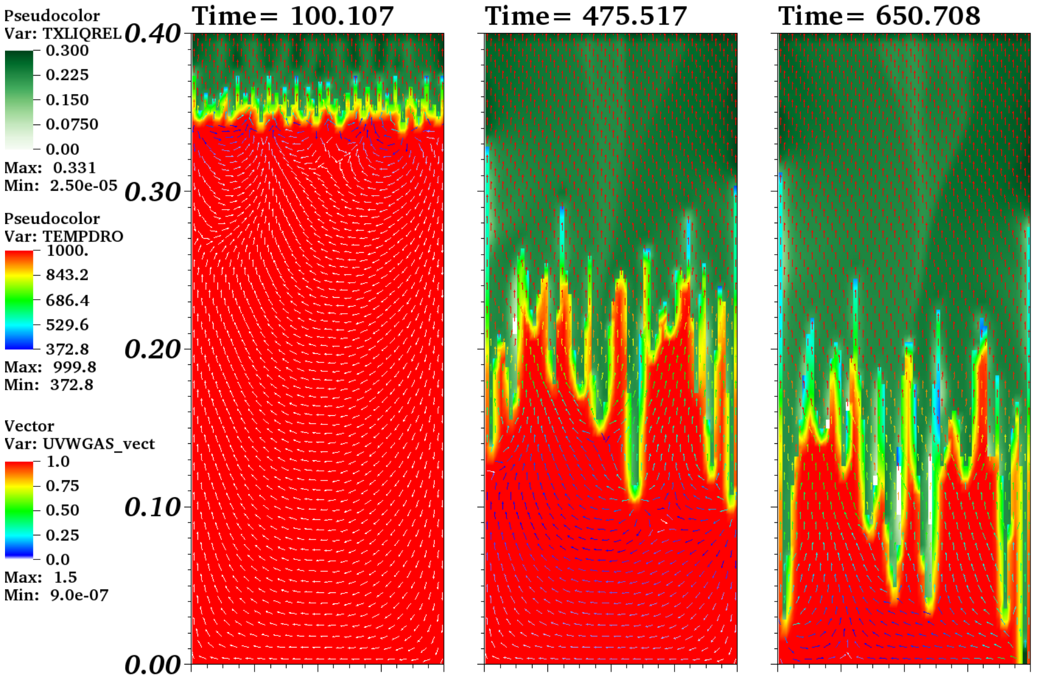

Figure 5.16 – 2D instability progression with BC-1 conditions for $\kappa \sim 3 \times 10^{-9} m^2$ ($d_p = 1.6mm$), P=1atm, and $T_0 = 1000K$ showing the configuration at three different times

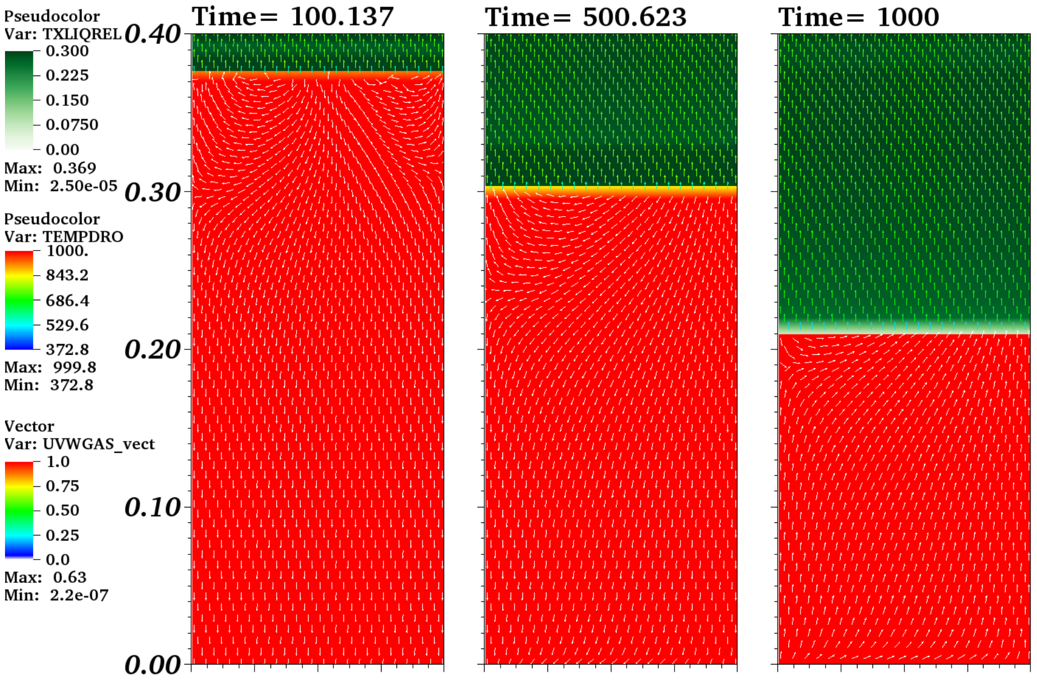

Figure 5.17 – 2D instability progression with BC-1 conditions for $\kappa \sim 1 \times 10^{-9} m^2$ ($d_p = 0.9mm$), P=1atm, and $T_0 = 1000K$ showing the configuration at three different times

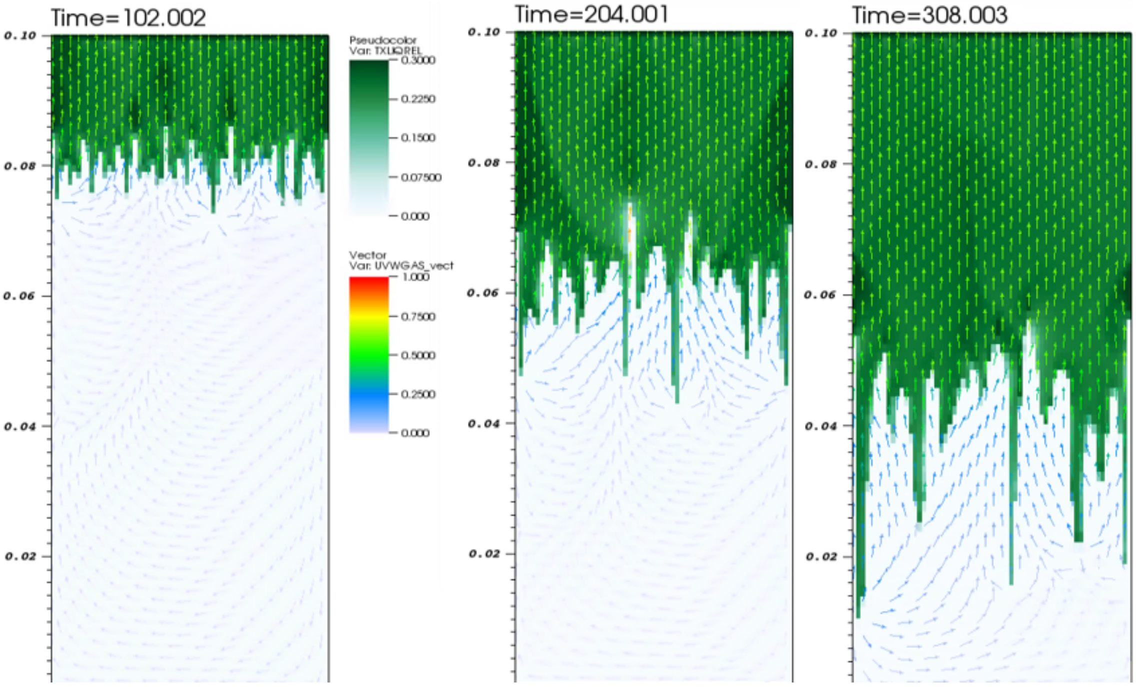

Figure 5.18 – Same calculation as figure 5.17 with a reduced scale by a factor 4.

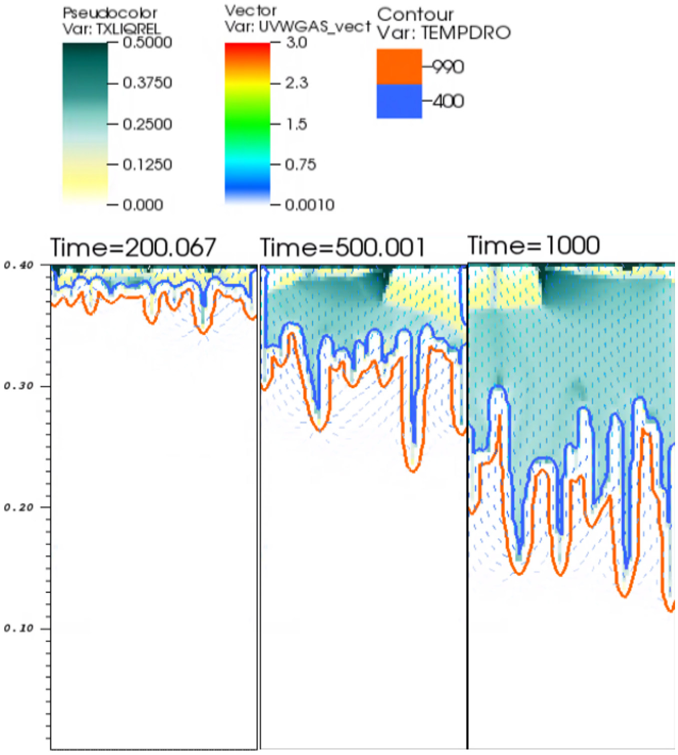

Figure 5.19 – Same calculation as figure 5.17 with the BC-2 conditions

5.2.5 Impact of the temperature heterogeneity

The results of the previous simulations show a sensitivity to both the initial conditions as well as to the boundary conditions. Recalling that the penetrating schemes presented by Cho et al. [132] and Ginsberg & Chen [131], figures 2.8 and 2.13 in section 2.1.3 are different, simulations with better estimated initial conditions were performed in order to study the source of this difference. Cho et al. presented a penetration pattern consisting of a central penetrating finger, whilst Ginsberg depicted the configuration as multiple penetrating fingers. Here Cho's experiment was simulated by introducing a temperature profile depicted in figure 5.20 with temperatures obtained from the experimental data.

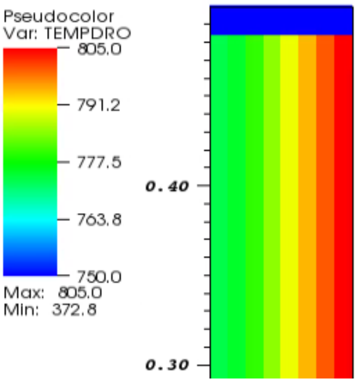

Figure 5.20 – Initial conditions for MC3D calculation of Cho experiment with a temperature gradient estimated from initial experimental conditions

The results are plotted in figure 5.21. As can be seen, it is evident that the water begins to penetrate through the cold regions, and continues without the formation of multiple finger instabilities observed in Ginsberg's experiments. In this case, the possible small perturbations are not allowed to grow, and all coalesce into a single column of penetrating water. Further calculations can be made with different temperature profiles, but it might be sufficient to point out the sensitivity of even small temperature gradients (here around 30-40 °C) to greatly impact the development of the instabilities.

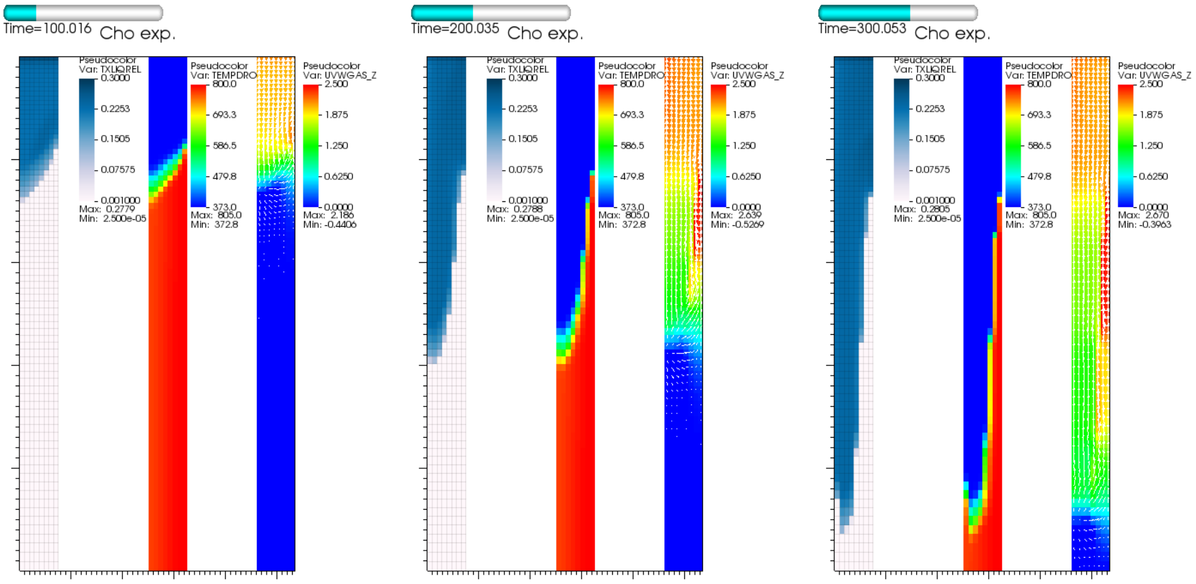

Figure 5.21 – 2D instability progression for Cho's experiment including a temperature heterogeneity showing the configuration at three different times

In general, the results of all these simulations show the sensitivity of the penetration instabilities to the permeability, the initial temperature, the temperature heterogeneity, and the boundary conditions with the overlying water pool. Whatever the case, the maximal extracted heat flux for high initial temperature is at most similar to the 1D case if the instabilities are suppressed. Nevertheless, the more realistic boundary conditions show that if the water penetration instabilities form vapor channels that extend the height of the debris bed, the extracted heat flux is lower.

5.2.6 2D effects in the SSWICS tests

In the other configuration of interest, water ingression through a fractured crust, 2D simulations were performed to study the 2D effects of the water penetration on the phenomenon.

5.2.6.1 Impact of lateral heat losses

It is reminded that the one-dimensional analysis of the SSWICS presented in section 4.3.2 tests led to conclude:

- Experimental, theoretical and simulation WI heat fluxes are consistent with the experimentally determined permeabilities for the tests where WI could be observed via a period of more or less constant heat flux.
- The duration of the plateau of WI heat flux is however, much shorter in the simulations.

- The heat transferred to the lower MgO insulation plate is re-emitted once the WI is completed, leading to the progressive decrease of the extracted heat flux.

It may then be hypothesized that the shorter heat flux plateau is due to 2D effects related to the lateral heat losses in the MgO insulator. Due to lateral heat losses, it may be anticipated that the external region is colder, and thus the water penetrates faster. This hypothesis has been tested through 2D simulations with MC3D. A major change in the modeling compared to previous cases is following the hypothesis of vertical fractures only, so that lateral mass transfer should be limited. Thus the lateral frictions have been strongly increased in order to avoid lateral convection.

Figure 5.22 illustrates the mesh and geometry used for the simulations. The red part with small porosity is not permeable to the water and simulates the MgO sidewall, and the base plate (this last is actually composed of different materials, but for simplicity is here simulated as MgO). The green part is the corium material.

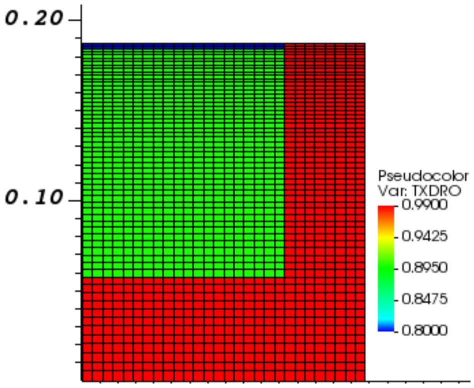

Figure 5.22 – Geometry and mesh of the 2D simulations of the SSWICS-1 test. The red part with small porosity is not permeable to the water. The green part is the corium.

The figure 5.23 shows the results of the simulation, which, in fact, does not behave exactly as expected. Due to the high conductivity of the MgO, it is seen that this zone is rapidly heated to a temperature of about 1000 K. Thus, the external region of the corium cooled down to the same temperature, which leads to a faster water progression. However, with the progression of the water, the MgO wall releases back its energy to the cooled corium, and it can be observed that, in fact, water cannot penetrate along the MgO wall. This can be deduced by recalling that no lateral fluid movement occurs so that the water-less zone close to the wall is not due to the vapor escaping. The water reaches the bottom of the test section in between the center and the wall after about 4500 s., which is a bit later than the end of the experimental heat flux plateau. After this, the energy accumulated in the basemat and the wall is gradually released.

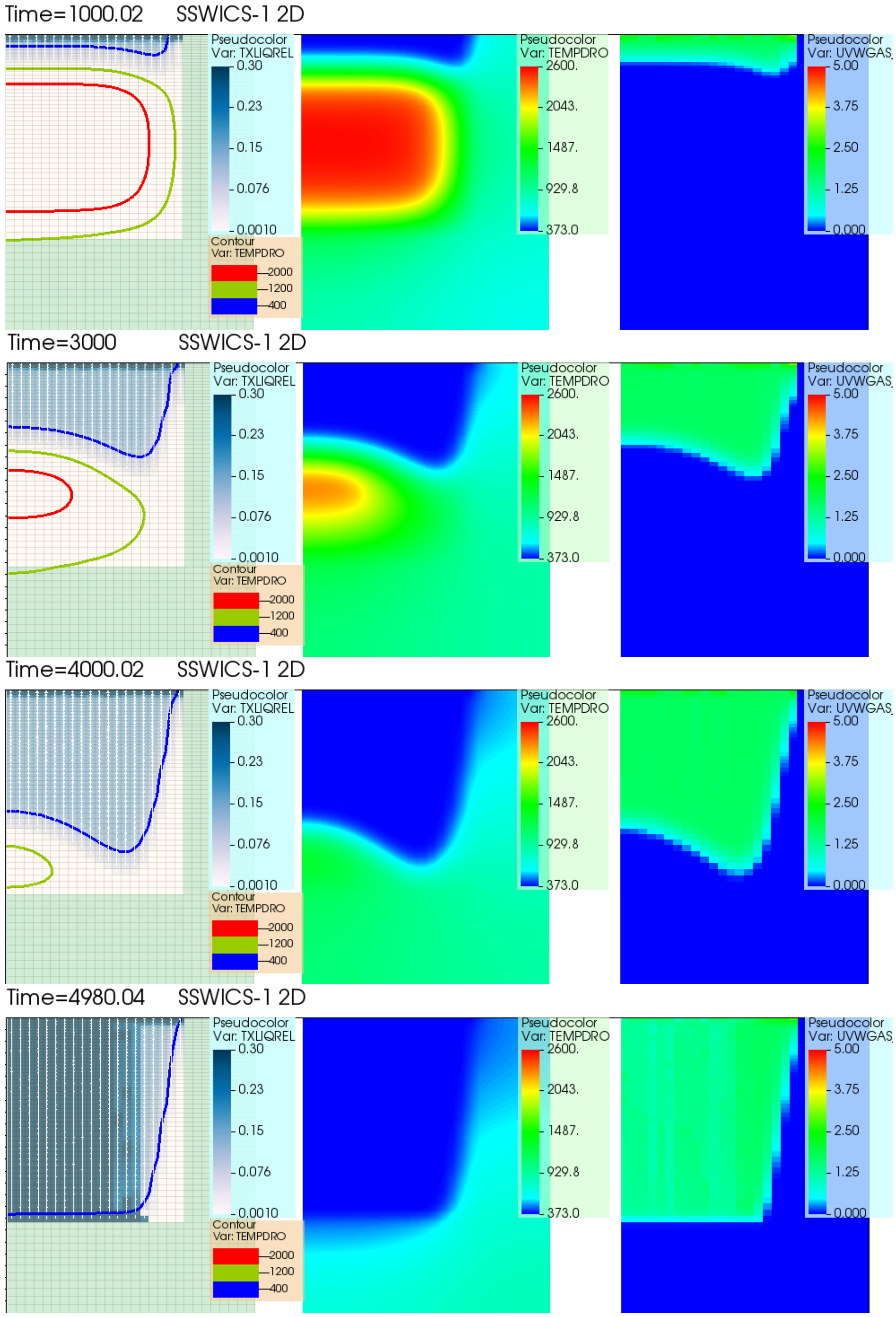

Figure 5.23 – 2D simulation of the water ingress progression for SSWICS-1 test experiment including the MgO insulator at four different times

Left: liquid volume fraction and level where T=400,1200, and T=T_{sol}= 2000 K (blue, green and red lines), with the green cells represent the MgO material; middle: temperature of the both the corium and the MgO materials; right: vapor velocity

The related heat flux is compared to the 1D simulation in figure 5.24. It is seen that a heat transfer plateau is preserved but with a slightly higher value (5-10 %), and a reduced length, due to the lateral conductive transfer of energy to the MgO wall.

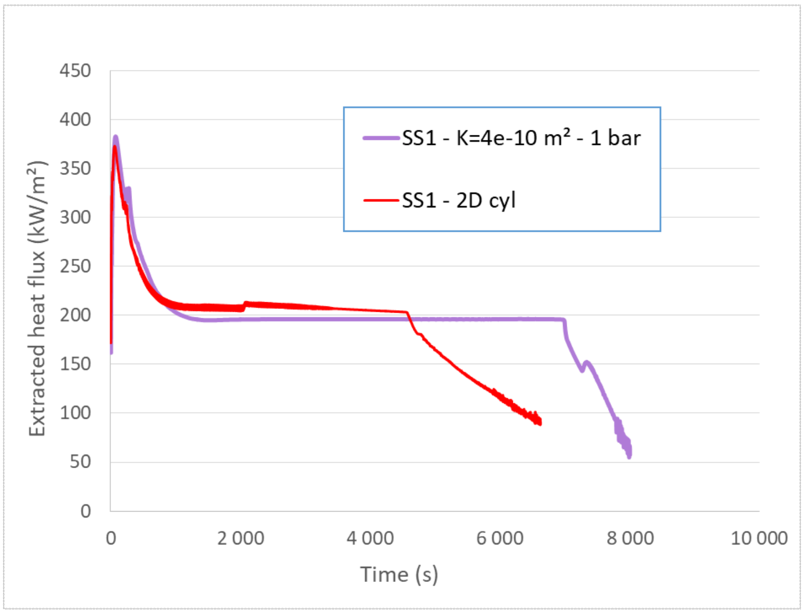

Figure 5.24 – SSWICS-1 1D versus 2D heat fluxes

Nevertheless, despite an apparently satisfactory heat flux evaluation (considering the large uncertainties), it must be reminded that the temperature measurements in the experiment are not in agreement with the simulation. Indeed, these ones clearly indicate a fast lateral complete cooling along the wall, whereas this region remains in the simulation rather hot for a long time.

5.2.6.2 Impact of heterogeneities of permeability

As the heat losses alone are not sufficient to explain the behavior of the test, notably the observed water penetration close to the regions of the wall, a second hypothesis is that the permeability is not homogeneous. In fact, the images of the corium ingot cross-sections in the publications of Lomperski and Farmer visually indicate a higher permeability in the external region. A larger cylindrical fracture close to the wall is also sometimes observed. A more important fracturing with larger permeability is probably induced by the lateral heat losses to the MgO wall.

To test this hypothesis numerically, the corium region was separated into two zones, with the second zone adjacent to the MgO sidewall initialized with a different permeability. It is reminded that only a mean permeability is measured in the experiments. Furthermore, it is also important to recall that Darcy's law leads to a flow rate proportional to the permeability. Thus, it is possible here to divide the test section in two vertical zones of surface area S_i and S_e (such that $S = S_i + S_e$) and two permeabilities κ_i and κ_e

whilst maintaining the same permeability:

$$\kappa = S_i\kappa_i + S_e\kappa_e \tag{5.16}$$

The simulation shown below was performed with $S_i = S_e = 0.5$. The permeabilities were set to $\kappa_e = 10^{-9}m^2$ and $\kappa_i = 7.10^{-11}m^2$, that is with an external region with a permeability approximately double compared to the mean experimental value, and a very small internal permeability, for which water ingression should be very difficult. In fact, the mean permeability is $\kappa_m = 5.10^{-10}m^2$, so a slightly larger than the one of the previous 2D calculations [18]. The initial conditions can be visualized in figure 5.25.

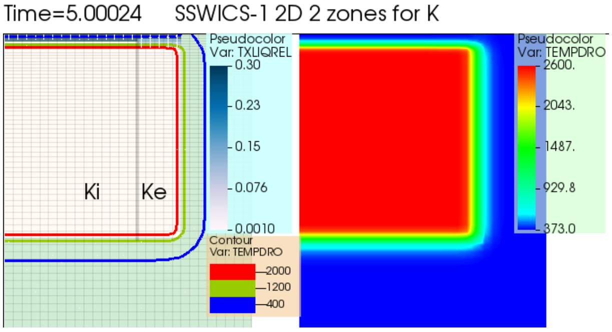

Figure 5.25 – Initial conditions for the 2D simulation of SSWICS-1 test with two zones at two different permeabilities

Legend: see figure 5.23; the vertical grey line in the left graph separates the 2 zones with permeabilities κ_i and κ_e

Figure 5.26 shows the progression of the simulation at four different times. In it, it can be clearly seen that the water penetrates mainly through the zone adjacent to the MgO sidewall, with the largest permeability. Nevertheless, as can be seen in the temperature levels in the leftmost image, a non-negligible part of the energy is transported out of the corium via conduction. This last can be confirmed with the aid of figure 5.27, which plots the extracted heat flux for the 1D and 2D simulations, where the completely flat plateau in the 1D simulations was not attained in the 2D 2-zone simulation but the tendency, before the heat flux drop, is a stabilization of the heat flux level. The plateau might not have been found due to 2D conduction effects that increase the heat extraction. Furthermore, it can be observed that the time at which the "plateau" in the 2D simulations stops (t∼4000 seconds) and a drastic decrease in heat extraction is observed, corresponds to the time of arrival of the water to the bottom of the corium as can be seen in last image in figure 5.26. This tends to indicate that, as found in the experimental results (section 3.2.1), the water mainly penetrates through the side closer to the wall. This is partly due to the fact that the wall absorbs part of the corium's energy; hence the penetration is facilitated mainly by the larger permeability but also aided by the lower temperature compared to the center of the corium. Furthermore, the approximate time of the end of the plateau found in the experimental results closely resembles the one here found in the 2D simulations.

---

[18] This is due to a small error detected lately in the elaboration of the data set. Calculations are very long, lasting more than one week, and was not redone with more precise settings, since the conclusions would in all likelihood not change.

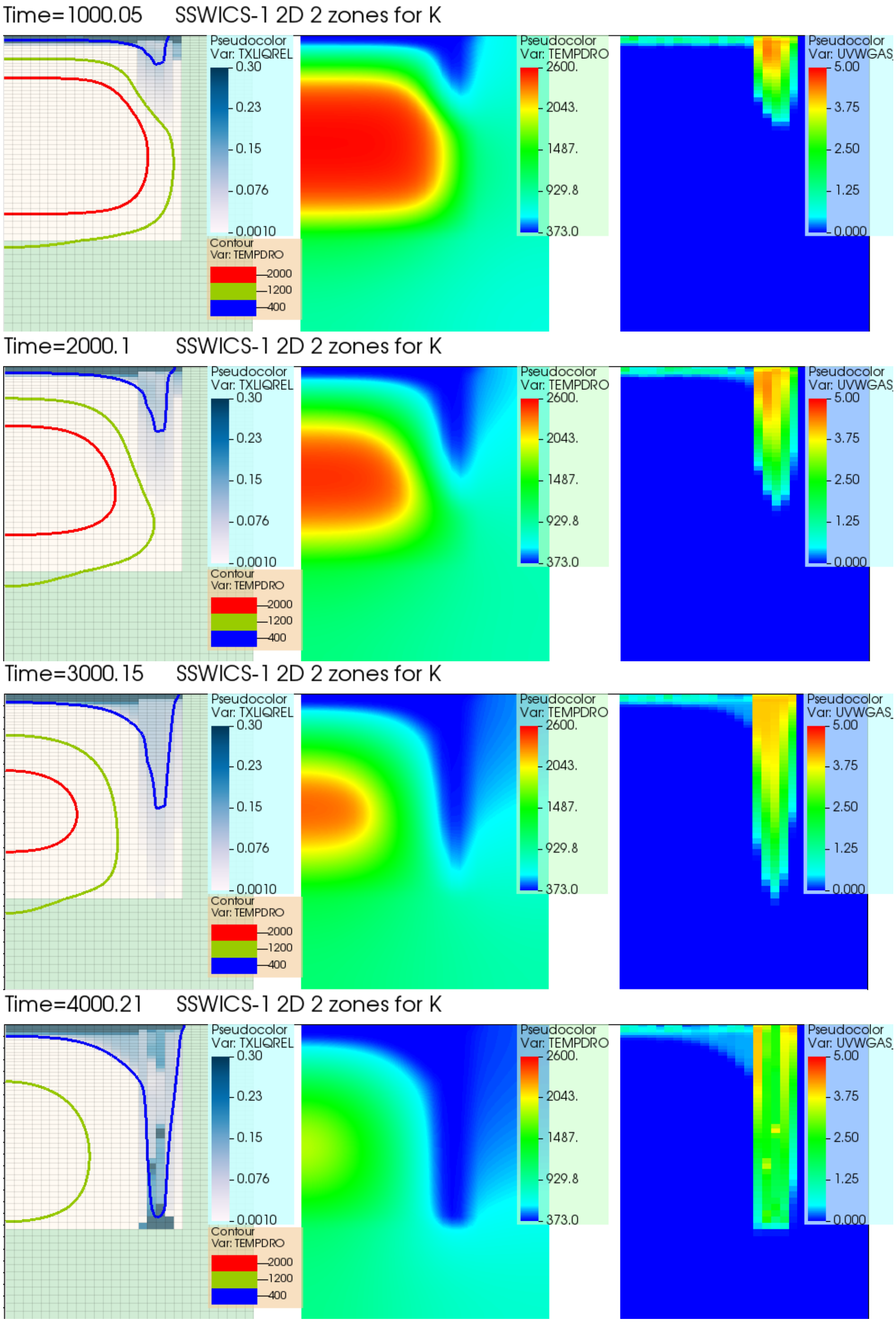

Figure 5.26 – 2D simulation of the water ingress progression for SSWICS-1 test with two different permeabilities at four different time

legend: see figure 5.23

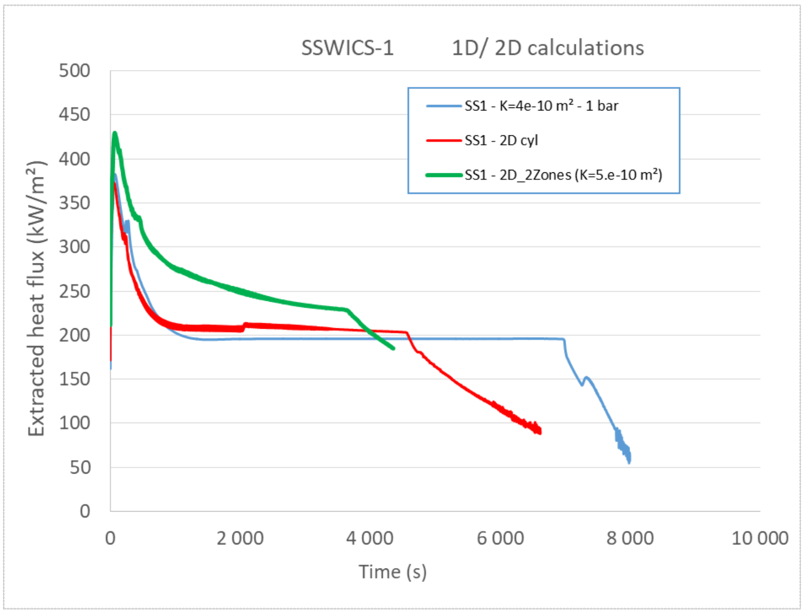

Figure 5.27 – SSWICS-1 2D simulations with two different input files

Nevertheless, looking precisely at the coolability maps in figure 5.26, it can be noted that the temperature in the immediate vicinity to the MgO wall is still not decreasing as fast as in the experiment. This may be due to fractures very closely to the wall, as can be visually intuited from the photographs of the SSWICS ingots (e.g., figure 3.14).

5.3 Conclusions

The complex nature of a two-dimensional flow into the particular corium configurations remains highly sensitive to the intrinsic characteristics of the medium and the initial conditions it is subjected to.

Although the extension of the one-dimensional model to the proposed pseudo-two-dimensional steady-state model discussed in section 5.1 remains an approximation of the configuration expected in a real scenario, it proved useful in analyzing its governing mechanics. As a result of its application, for the debris bed configuration, it was found that in the different flow regimes expected to be found in the range of permeabilities of interest, the stability of the dried zone is highly unlikely at high temperatures. Furthermore, with support of the MC3D simulations presented in section 5.2, evidence was presented that points to the instability development at lower temperatures and with larger particle diameters or permeability. This is because the penetrating water velocity with low temperatures remains higher than the characteristic velocity of the development of the instabilities. In the cases the instabilities developed, the heat flux was then found to be lower. In other words, for some particular initial conditions, and with some precise medium characteristics, the instability development needs to be considered both to be able to evaluate the extracted heat flux, as well as its stability.

On the other hand, for the fractured crusts, it is difficult to draw precise conclusions only on the bases of the preliminary simulations presented in section 5.2.6. Nevertheless, the impact of lateral heat losses in the SSWICS experiments is clear. This, in turn, highlights the importance of the fracturing mechanisms and its effects on the local permeability of the fractured medium.

Chapter 6

Conclusions and Perspectives

This work was inscribed in the context of a hypothetical nuclear severe accident with partial or extensive core meltdown. The coolability of the super-heated corium is paramount to the safety studies and design of safety countermeasures to assure the integrity of the containment of an NPP. Despite many different possibilities to cool down the corium in the case of a severe accident, the elemental, and rather natural, way is through passive gravitational water injection on the top of the corium. However, the morphology of the corium layer limits water's ability to extract heat since the outgoing generated vapor would restrict the penetrating water. In this work, the coolability of this super-heated corium was studied in two specific, expected, and observed configurations in the ex-vessel situation: particle bed, and corium pool overlaying the concrete.

Firstly, the top reflooding of a particle debris bed was explored with preliminary calculations with the multiphase flow model MC3D-PREMIX. The results of these calculations, supported by experimental evidence, showed how particular water penetration patterns developed, dependent on the initial temperature of the debris bed and its permeability. Furthermore, the results disclosed the complex two-phase flow nature of the configuration with a particular countercurrent condition. The overall volumetric presence of this competing descending and ascending fronts are dictated by the hydrodynamic characteristics of the particle bed and converge on a seeming equilibrium amid the fluid phases dependent on the frictions between them and the particle bed (mainly).

This led to the revisiting and further development of a one-dimensional analytical model. The effects of the particle diameter on the governing frictions were discussed for different flow regimes. A mixed steady-state model taking into account the governing pressure drops (viscous-inertial in the gas and viscous-gravitational in the liquid) over the range of particle diameters expected in the context of FCI and MCCI was presented. Furthermore, the model was extended and used to study the thermal stability of particle beds with the inclusion of residual power effects in an unsteady penetrating configuration. This was, in turn, used to propose two simple criteria upon which the debris bed's stability could be evaluated. First, a thermal criterion that dictates the maximal quenchable debris bed height by water percolation as a function of the particle diameter, initial temperature, and residual power. Second, a hydro-dynamical criterion that estimates the maximal corium height whose residual power could be accommodated through an overlaying already quenched debris bed also subjected to residual power. Using these criteria, it was found that for small particles and mid-high residual power, the first criterion is the limiting one, whilst for large particles, it is the second one.

A general coherence between the one-dimensional model results, the existing experimental data and the one-dimensional simulations done with a slightly modified version of MC3D (where the numerics were adjusted) was found. The one-dimensional analysis conducted to a better understanding of the essence of the two-phase countercurrent flow through the porous media:

- the flow privileges a certain vapor saturation,
- for a given mass flux, two possible solutions arise at different vapor saturation values, and
- the dryout is linked to the departure of the privileged vapor saturation by countercurrent flow limitations, and not by a progressive build-up of the void saturation tending to 1.

For the water ingression in fractured corium crust configuration, previous experimental tests were analyzed, along with the main existing models. The fracturing mechanism was quickly reviewed. A particular deficiency was found in the formulas used for calculating the corresponding permeabilities. The available models using a simplified fracturing mechanism result in the prediction of the permeability only by using a numerical parameter fit from experiments that might not be appropriately adapted to expected corium compositions in real case scenarios. In particular, the hypothesis of the Lister-Epstein model that the local permeability is a sole function of the local physical properties and conductive heat transfer appears to be incomplete. A lack of explicit consideration of specific thermophysical properties and its dependency on temperature renders the applicability of these formulas dubious at most. Furthermore, the heat flux relation used for the model lacks to account for pressure effects, mainly linked to the liquid phase, rendering the utilization of this model at high pressures problematic. The classical models related to fracturing slabs submitted to a thermal shock (from Griffith theory) were examined. Still, the high non-linearity of the terms involved, as well as the limited availability of corium's mechanical properties, complicated the analysis drastically. Nevertheless, using the SSWICS post-mortem experimental measurements of the permeability, and including specific identified relative permeability formulations, the use of the one-dimensional hydro-dynamical analytical model showed relative coherence with the extracted heat flux observed in said experiments. Furthermore, one-dimensional MC3D simulations result in acceptable agreement with both the one-dimensional model and the experimental measures.

Withal, the extension of the MC3D calculations to include residual power indeed showed a similar extracted heat flux but also showed that the stability of the configuration, regarding concrete ablation, is not given except for low residual power. In other words, under the effect of residual power, for a homogeneous configuration, a partial reflooding (water ingression) of a debris bed or fractured crust is not assured to be stable. In principle, the phenomenon is quite binary, either fully flooded, either fully dry. Nevertheless, as the involved time scales are enormous, the extent and impact of water ingression are not very clear. Models taking into account the full phenomenology and, in particular, the ablation and crust formation history are needed to evaluate the stability and evolution of the configuration correctly.

Based on experimental observations, and the preliminary calculations, the two-dimensional effects, i.e., cooling front spatial instability and temperature heterogeneities, were analyzed. Firstly, an extension of the one-dimensional model to a pseudo-two-dimensional (two one-dimensional zones, one being flooded, one being dry) steady-state analytical model was proposed with the purpose of examining the possibility of stable flows beyond the critical heat flux. Different flow regimes were analyzed, and it was found that the stability of the dried zone is highly unlikely at high temperatures.

The model was further used in complement to a numerical analysis with MC3D of the spatial stability of the two-dimensional penetrating front. In general, it was found that instability formation, or development, is favored at lower temperatures and larger particle diameters or permeability, allowing the simplification to a one-dimensional penetrating front configuration at low permeability, in particular for water ingression. In any case, the one-dimensional modeling provides a reasonable and upper value of the extracted heat flux.

Finally, two-dimensional MC3D calculations of the water ingression phenomenon in an SSWICS-like configuration were performed to analyze the border effects. A reinterpretation of the phenomenon observed in the experiments, and the results of these simulations showed the importance of the two-dimensional effects regarding heat conduction and potential permeability heterogeneity on the extracted heat flux. These simulations show an improved coherence concerning the penetration mechanism, the extracted heat flux, and the duration of the water ingression period. The influence of the temperature on the fracturing mechanism coupled with heat losses on the border of the experiment greatly influenced the permeability close to the sidewalls, hence the heat extraction. Although this is not expected in the accidental scenario, it highlights the importance of developing a better understanding of the fracture mechanisms.

Summarizing, and taking into account that the minutiae of the flow characteristics greatly depend on the configuration and evolution of the corium material, it is possible to conclude that:

- Contrary to previously analyzed and models, the assumption of an already flooded debris bed with no inclusion of the initial bed temperature is probably not representative. Hence the debris bed should not be globally considered as quenchable by nature.
- For a certain temperature range, and particle diameters, the initial bed temperature becomes the limiting factor in the stability of the layer.
- The water ingression mechanism is limited to a small range of low concrete content corium mixtures linked to relatively large permeabilities.
- Thermal shock fracturing models lack validation, particularly regarding the lack of availability of thermo-mechanical properties of corium mixtures at high temperatures.
- In a real accidental scenario, the efficiency of the water ingression mechanism would be limited to the long term coolability phase, where also the residual power needed to be extracted would be lower.
- Heterogeneous temperature and permeability distributions would have a large impact in both studied configuration.
- Two-dimensional instabilities should be taken into account for stability analysis of debris beds consisting of medium-large particles.

Having seen the importance of the heterogeneity of the corium layer to be quenched, further study of both configurations including temperature and permeability heterogeneity could prove useful in understanding the efficiency of both phenomena vis-a-vis of the coolability.

Several open questions remain, and some perspectives can be listed.

At first, the formation and initial characteristics of a debris bed, particularly its initial temperature (settling temperature of the particles), are essential for providing adequate results in the safety studies. These may be at first estimated from the FCI experiments and models. As for the problem of melt ejection during MCCI, FCI models can likely be extended. On this basis, it is nevertheless highlighted the need for experimental data such as the diameter of particles, the porosity of the medium, settling initial temperature, amongst others.

From an academic point of view, further work to study the mechanism and onset and evolution of the water fingering may be pursued with a linear, or non-linear analysis in the extended viscous and/or inertial regimes. Its dependency on the precise boundary conditions with the inclusion of residual power and a high initial temperature could prove to be useful in providing a more precise evaluation of the debris bed's capacity to extract heat.

On the other hand, the analysis of water ingression led to a better comprehension of the work needed to be performed to evaluate its efficiency correctly.

At first, the need to better characterize the fracture mechanisms in large scales (representative to accidental scenarios) with less influence from the constraints inherent to the existing experimental test section was accentuated. This might be pursued via the selection and introduction of fracture criteria, and first-order approximation of elastic material behavior coupled with the thermal hydraulics, and could, for example, be evaluated via the introductions of these criteria into the MC3D code. Furthermore, in the context of a real scenario MCCI, the question of the amount of concrete present in the crust, and its composition, takes further importance with respect to safety evaluations. The means through which the corium crust would be enriched in concrete content would greatly condition the coolability of said crust. Additionally, the impact of the temperature and said concrete content on the crust thermo-mechanical properties is equally crucial to properly evaluate not only the impact of the water ingression phenomenon but its presence altogether. Finally, the local boiling heat transfer model in the fractures could be improved for the simulations with MC3D, based for example on verified models for two-phase flows in thin channels.

Appendix A

MC3D-PREMIX modifications

It is reminded that MC3D-PREMIX is devoted to molten Fuel-Coolant Interaction. However, the code has also the capabilities to deal with situations with dense configurations, in particular debris bed. Furthermore, a specific porous media model, called MC3D-REPO, has also been developed in the frame of MC3D [180]. This MC3D-REPO application has been since then detached from the rest of the code to be autonomous, but the constitutive laws have been preserved. Since then, some improvements have been done, in particular through successive verification relative to the two-phase flow behavior and the critical heat flux in heated debris beds Raverdy et al. [181] and more recently based on the PEARL bottom flooding experiments, see e.g. Kokalj et al. [218].

All along the successive works devoted to the coolability of hot debris bed, numerous difficulties have appeared related the lack of experimental data, or large uncertainties, related to some characteristics, in particular the boiling heat transfer mechanisms and the capillary pressure. In the absence of decisive arguments, it has been decided in general to preserve the standard modeling of the code. This is the case regarding boiling heat transfers which, in FCI, are mostly under the form of film boiling. An attempt to introduce a heat transfer related to nucleate boiling has not been conclusive due to the absence of clear and decisive impact of this mechanism in the comparisons of calculations with the experiments.

It is worth to insist that the purpose of this work was to not provide a detailed verification of MC3D but rather to use the code and make some slight modifications in order to better understand the physics of water penetrating debris beds or fractured crusts. The derivation of an analytical modeling was pursued in order to provide cross-comparison and thus strengthen the conclusions. For this reason, in depth detail of the modifications done during this work are not described. The modifications made for the purpose of this work should not be introduced in the standard version of MC3D (mainly to avoid unexpected impacts on calculations not devoted).

A first important point was raised regarding the accuracy of the friction laws in the problem of water penetrating downward, due to the counter-current flow which is established. However, in fact, the classical problem of critical input power in an already cooled debris bed already induces a counter-current flow since the upstream vapor must be replaced by downstream water. The flux of water and vapor in the problem of top reflooding are not so different and there is not enough evidence to point out a possible departure out of the range of applicability of the laws. Three series of modifications were performed during this work.

In chapter 3, where preliminary analysis is presented, the situation of top reflooding posed some specific difficulties related mostly to the transport of fluid fronts. This is the reason why these calculations as considered to be preliminary. In fact, this is due to the extreme non-linearity of the frictions laws (see section section 2.3.3). As the laws do not converge when one of the fluid (liquid or gas) is vanishing, it is is necessary to impose a maximum value. To improve the behavior, the maximum value of the friction factors was reduced tenfold. Furthermore, the limits for the flow chart shown in figure 2.42 were changed. α_B was changed from 0.1 to 0.01, whilst α_D was changed from 0.9 to 0.99 with the purpose to smooth the behavior. In addition, some specific outputs were introduced that won't be commented here.

After these preliminary calculation tests, a second set of more important modifications was done and used for all the rest of the calculations presented in chapters 4 and 5.

- A first modification made to restrict the numerically high friction when the front advances between two cells was to change the way frictions are computed. In the standard model, the total frictions at a face are computed by averaging the friction values between the neighboring cells, which leads to high values when one cell has a vanishing value of one fluid, typically the case for progressing fronts. The modification consisted in evaluating the frictions directly with properties related to the faces; for the volume fractions, the "convected" volume fraction (upstream second order volume fraction) was used.

- The limitation of the friction values is computed directly by considering "minimum" volume fractions with a value of 1 %. In fact, as already underlined, it is unlikely that the constitutive laws for frictions are adequate for the situations encountered at the front in the problems investigated here. This modification has the advantage of improved readability compared to a simple cut of the final value of a friction coefficient per unit volume.

- The coolant flow map was again revised. Following the works done by Sapin and Gourbil [192], see paragraph section 2.3.1, where the film boiling heat transfer seemed to be weakly affected by a local two-phase flow, it was decided to increase the bound for the void fraction from bubbly to transition flow to 0.5.

A third set of modifications was done for the purpose of computing the case of fractured crusts.

- The computation of heat conduction (not used in debris bed calculations) was slightly revisited. The possibility to have different conductivity coefficient in different zones of the domain was introduced. For the calculations of the CCI-9 test, where bubbling leads to a mixing of the liquid phase, the possibility to increase the conduction coefficient in the liquid phase (up to the solidification temperature which is roughly set as the average between solidus and liquidus) was also introduced.

- The specific laws for relative permeabilities in fractured media by Fourard & Lenormand [190] were imposed. In this situation, the inertial frictions are not considered, due to the absence of known specific laws.

- The lateral frictions are strongly limited to avoid lateral movement of the fluids. This comes from the hypothesis that the fractures are vertical, and quite likely not communicated between each other.

Finally, the fact that the data sets must be set with great attention must be emphasized. Of particular importance are the boundary conditions and upper meshes of the debris bed. In the set of calculations in chapters 4 and 5, it was decided to avoid computation of the water flow above the debris bed (so that the limit of the domain is coincident with the limit of the debris bed). In real applications this is not possible in general. Some evaluations made in another frame with MC3D (not published) showed the relative importance of the flow structure on top the debris, in particular the convection rolls that are appearing. The experiments, particular the PEARL ones, confirm that the flow is extremely turbulent (could be even considered as "violent") with an important gas volume fraction. This may participate in the de-structuring of the debris bed that may be encountered due the entrainment of the debris with the coolant flow.

We may also at last re-highlight the question of the heat transfers for the case of fractured crusts. A more precise modeling is possible, based for example on verified models for 2-phase flows in thin channels. This would help to evaluate more precisely the role of water ingression combined with conduction.

Bibliography

[1] The World Bank, *World Bank Open Data | Data.* [Online]. Available: `https://data.worldbank.org/?type=shaded` (Cited on page 1).

[2] International Energy Agency, *Electricity Information 2018*, ser. Electricity Information. OECD, 2018, ISBN: 978-92-64-30119-1. [Online]. Available: `https://books.google.fr/books?id=9Bu3vAEACAAJ` (Cited on page 2).

[3] S.-H. Park, W.-J. Jung, T.-H. Kim, & S.-Y. T. Lee, "Can Renewable Energy Replace Nuclear Power in Korea? An Economic Valuation Analysis", en, *Nuclear Engineering and Technology*, vol. 48, no. 2, pp. 559–571, Apr. 2016, ISSN: 17385733. DOI: `10.1016/j.net.2015.12.012`. [Online]. Available: `https://linkinghub.elsevier.com/retrieve/pii/S1738573316000115` (Cited on page 2).

[4] B. K. Sovacool, "A Critical Evaluation of Nuclear Power and Renewable Electricity in Asia", en, *Journal of Contemporary Asia*, vol. 40, no. 3, pp. 369–400, Aug. 2010, ISSN: 0047-2336, 1752-7554. DOI: `10.1080/00472331003798350`. [Online]. Available: `http://www.tandfonline.com/doi/abs/10.1080/00472331003798350` (Cited on pages 2, 5).

[5] S. Hong, C. J. Bradshaw, & B. W. Brook, "Global zero-carbon energy pathways using viable mixes of nuclear and renewables", en, *Applied Energy*, vol. 143, pp. 451–459, Apr. 2015, ISSN: 03062619. DOI: `10.1016/j.apenergy.2015.01.006`. [Online]. Available: `https://linkinghub.elsevier.com/retrieve/pii/S0306261915000124` (Cited on page 2).

[6] D. S. Siqueira, J. de Almeida Meystre, M. Q. Hilário, D. H. D. Rocha, G. J. Menon, & R. J. da Silva, "Current perspectives on nuclear energy as a global climate change mitigation option", en, *Mitigation and Adaptation Strategies for Global Change*, vol. 24, no. 5, pp. 749–777, Jun. 2019, ISSN: 1381-2386, 1573-1596. DOI: `10.1007/s11027-018-9829-5`. [Online]. Available: `http://link.springer.com/10.1007/s11027-018-9829-5` (Cited on page 2).

[7] J. Parsons, J. Buongiorno, M. Corradini, & D. Petti, "A fresh look at nuclear energy", en, *Science*, vol. 363, no. 6423, pp. 105–105, Jan. 2019, ISSN: 0036-8075, 1095-9203. DOI: `10.1126/science.aaw5304`. [Online]. Available: `http://www.sciencemag.org/lookup/doi/10.1126/science.aaw5304` (Cited on pages 2, 3).

[8] B. W. Brook & C. J. A. Bradshaw, "Key role for nuclear energy in global biodiversity conservation: Biodiversity and Sustainable Energy", en, *Conservation Biology*, vol. 29, no. 3, pp. 702–712, Jun. 2015, ISSN: 08888892. DOI: `10.1111/cobi.12433`. [Online]. Available: `http://doi.wiley.com/10.1111/cobi.12433` (Cited on page 2).

[9] B. W. Brook, A. Alonso, D. A. Meneley, J. Misak, T. Blees, & J. B. van Erp, "Why nuclear energy is sustainable and has to be part of the energy mix", en, *Sustainable Materials and Technologies*, vol. 1-2, pp. 8–16, Dec. 2014, ISSN: 22149937. DOI: `10.1016/j.susmat.2014.11.001`. [Online]. Available: `https://linkinghub.elsevier.com/retrieve/pii/S2214993714000050` (Cited on page 2).

[10] B. K. Sovacool & M. V. Ramana, “Back to the Future: Small Modular Reactors, Nuclear Fantasies, and Symbolic Convergence”, en, *Science, Technology, & Human Values*, vol. 40, no. 1, pp. 96–125, 2015. DOI: `10.4324/9780367135171-3`. [Online]. Available: `https://doi.org/10.1177/0162243914542350` (Cited on page 2).

[11] T. Jin & J. Kim, “What is better for mitigating carbon emissions – Renewable energy or nuclear energy? A panel data analysis”, *Renewable and Sustainable Energy Reviews*, vol. 91, pp. 464–471, Aug. 2018, ISSN: 1364-0321. DOI: `10.1016/j.rser.2018.04.022`. [Online]. Available: `http://www.sciencedirect.com/science/article/pii/S1364032118302326` (Cited on page 2).

[12] D. Kyne & B. Bolin, “Emerging Environmental Justice Issues in Nuclear Power and Radioactive Contamination”, *International Journal of Environmental Research and Public Health*, vol. 13, no. 7, Jul. 2016, ISSN: 1661-7827. DOI: `10.3390/ijerph13070700`. [Online]. Available: `https://www.ncbi.nlm.nih.gov/pmc/articles/PMC4962241/` (Cited on page 2).

[13] R. H. Socolow & A. Glaser, “Balancing risks: nuclear energy & climate change”, en, *Daedalus*, vol. 138, no. 4, pp. 31–44, Sep. 2009, ISSN: 0011-5266, 1548-6192. DOI: `10.1162/daed.2009.138.4.31`. [Online]. Available: `http://www.mitpressjournals.org/doi/10.1162/daed.2009.138.4.31` (Cited on page 3).

[14] L. Mez, “Nuclear energy–Any solution for sustainability and climate protection?”, en, *Energy Policy*, vol. 48, pp. 56–63, Sep. 2012, ISSN: 03014215. DOI: `10.1016/j.enpol.2012.04.047`. [Online]. Available: `https://linkinghub.elsevier.com/retrieve/pii/S0301421512003527` (Cited on page 3).

[15] G. C. v. Kooten, J. Duan, & R. Lynch, “Is There a Future for Nuclear Power? Wind and Emission Reduction Targets in Fossil-Fuel Alberta”, en, *PLOS ONE*, vol. 11, no. 11, e0165822, Nov. 2016, ISSN: 1932-6203. DOI: `10.1371/journal.pone.0165822`. [Online]. Available: `https://journals.plos.org/plosone/article?id=10.1371/journal.pone.0165822` (Cited on page 3).

[16] J. Augutis, L. Martišauskas, & R. Krikštolaitis, “Energy mix optimization from an energy security perspective”, en, *Energy Conversion and Management*, vol. 90, pp. 300–314, Jan. 2015, ISSN: 01968904. DOI: `10.1016/j.enconman.2014.11.033`. [Online]. Available: `https://linkinghub.elsevier.com/retrieve/pii/S019689041400990X` (Cited on page 3).

[17] F. I. T. Petrescu, A. Apicella, R. V. V. Petrescu, S. P. Kozaitis, R. B. Bucinell, R. Aversa, & T. M. Abu-Lebdeh, “Environmental Protection through Nuclear Energy”, en, *American Journal of Applied Sciences*, vol. 13, no. 9, pp. 941–946, Sep. 2016, ISSN: 1546-9239. DOI: `10.3844/ajassp.2016.941.946`. [Online]. Available: `http://thescipub.com/abstract/10.3844/ajassp.2016.941.946` (Cited on page 3).

[18] Y. Kim, M. Kim, & W. Kim, “Effect of the Fukushima nuclear disaster on global public acceptance of nuclear energy”, en, *Energy Policy*, vol. 61, pp. 822–828, Oct. 2013, ISSN: 03014215. DOI: `10.1016/j.enpol.2013.06.107`. [Online]. Available: `https://linkinghub.elsevier.com/retrieve/pii/S0301421513006149` (Cited on page 3).

[19] S. Zhou & X. Zhang, “Nuclear energy development in China: A study of opportunities and challenges”, en, *Energy*, vol. 35, no. 11, pp. 4282–4288, Nov. 2010, ISSN: 03605442. DOI: `10.1016/j.energy.2009.04.020`. [Online]. Available: `https://linkinghub.elsevier.com/retrieve/pii/S0360544209001236` (Cited on page 3).

[20] C. Sun & X. Zhu, “Evaluating the public perceptions of nuclear power in China: Evidence from a contingent valuation survey”, en, *Energy Policy*, vol. 69, pp. 397–405, Jun. 2014, ISSN: 03014215. DOI: `10.1016/j.enpol.2014.03.011`. [Online]. Available: `https://linkinghub.elsevier.com/retrieve/pii/S030142151400158X` (Cited on page 3).

[21] J. Vira, “Geological repository for high-level nuclear waste becoming reality in Finland”, en, in *Geological Repository Systems for Safe Disposal of Spent Nuclear Fuels and Radioactive Waste*, Elsevier, 2017, pp. 645–666, ISBN: 978-0-08-100642-9. DOI: `10.1016/B978-0-08-100642-9.00023-2`. [Online]. Available: `https://linkinghub.elsevier.com/retrieve/pii/B9780081006429000232` (Cited on page 3).

[22] A. Brunnengräber, M. R. Di Nucci, A. M. Isidoro Losada, L. Mez, & M. A. Schreurs, Eds., *Nuclear waste governance, an international comparison*, de, ser. Energiepolitik und Klimaschutz = Energy policy and climate protection. Wiesbaden: Springer VS, 2015, OCLC: ocn902762152, ISBN: 978-3-658-08961-0 (Cited on page 3).

[23] J. H. Saling, A. W. Fentiman, & Y. S. Tang, Eds., *Radioactive waste management*, en, 2nd ed. New York: Taylor & Francis, 2001, ISBN: 978-1-56032-842-1 (Cited on page 3).

[24] U. E. Humphrey & M. U. Khandaker, “Viability of thorium-based nuclear fuel cycle for the next generation nuclear reactor: Issues and prospects”, *Renewable and Sustainable Energy Reviews*, vol. 97, pp. 259–275, Dec. 2018, ISSN: 1364-0321. DOI: `10.1016/j.rser.2018.08.019`. [Online]. Available: `http://www.sciencedirect.com/science/article/pii/S1364032118305951` (Cited on page 3).

[25] S. Şahin, B. Şarer, & Y. Çelik, “Utilization of nuclear waste plutonium and thorium mixed fuel in candu reactors”, en, *International Journal of Energy Research*, vol. 40, no. 14, pp. 1901–1907, 2016, ISSN: 1099-114X. DOI: `10.1002/er.3464`. [Online]. Available: `https://onlinelibrary.wiley.com/doi/abs/10.1002/er.3464` (Cited on page 3).

[26] M. Lineberry & T. Allen, “The Sodium-Cooled Fast Reactor”, *Argonne National Laboratory-West*, 2002. [Online]. Available: `http://www.ipd.anl.gov/anlpubs/2002/10/44547.pdf` (Cited on page 3).

[27] U. D. of Energy, “Sodium-Cooled fast Reactor (SFR) Technology And Safety Overview”, Washington, DC, 2015. [Online]. Available: `http://www.nrc.gov/docs/ML1504/ML15043A307.pdf` (Cited on page 3).

[28] W. F. G. van Rooijen, “Gas-Cooled Fast Reactor: A Historical Overview and Future Outlook”, p. 11, 2009. DOI: `10.1155/2009/965757`. [Online]. Available: `http://www.hindawi.com/journals/stni/2009/965757/` (Cited on page 3).

[29] M. Yetisir & W. Diamond, “GENERATION IV SUPERCRITICAL WATER-COOLED REACTOR”, 2012. [Online]. Available: `https://www.iaea.org/NuclearPower/Downloadable/Meetings/2014/2014-03-31-04-02-CM-INPRO/Gen4_SCWR.pdf` (Cited on page 3).

[30] J. Vujić, R. M. Bergmann, R. Škoda, & M. Miletić, "Small modular reactors: Simpler, safer, cheaper?", en, *Energy*, vol. 45, no. 1, pp. 288–295, Sep. 2012, ISSN: 03605442. DOI: `10.1016/j.energy.2012.01.078`. [Online]. Available: `https://linkinghub.elsevier.com/retrieve/pii/S036054421200093X` (Cited on page 3).

[31] I. A. E. Agency, "Accident analysis for nuclear power plants", International Atomic Energy Agency, Vienna, Tech. Rep. 23, 2002. [Online]. Available: `https://www-pub.iaea.org/MTCD/Publications/PDF/Pub1131_scr.pdf` (Cited on page 4).

[32] R. Avanzinelli, M. Casalini, T. Elliott, & S. Conticelli, "Carbon fluxes from subducted carbonates revealed by uranium excess at Mount Vesuvius, Italy", en, *Geology*, vol. 46, no. 3, pp. 259–262, Mar. 2018, ISSN: 0091-7613. DOI: `10.1130/G39766.1`. [Online]. Available: `https://pubs.geoscienceworld.org/gsa/geology/article/46/3/259/526076/Carbon-fluxes-from-subducted-carbonates-revealed` (Cited on page 4).

[33] R. Günther & J. Manley, "VI.— A Mural Glass Mosaic from the Imperial Roman Villa near Naples.", en, *Archaeologia*, vol. 63, pp. 99–108, 1912, ISSN: 0261-3409, 2051-3186. DOI: `10.1017/S0261340900011607`. [Online]. Available: `https://www.cambridge.org/core/product/identifier/S0261340900011607/type/journal_article` (Cited on page 4).

[34] W. B. Lewis, "The accident to the NRX reactor on December 12, 1952", English, Atomic Energy of Canada Ltd. Chalk River Project, Chalk River, Ontario (Canada), Tech. Rep. DR-32; AECL-232, Jul. 1953. [Online]. Available: `https://www.osti.gov/biblio/4379334` (Cited on page 4).

[35] J. Carter, *Why Not the Best?: the First 50 Years (p)*, en. University of Arkansas Press, 1975, Google-Books-ID: s8QrkpOEJlQC, ISBN: 978-1-61075-460-6 (Cited on page 4).

[36] R. Adams, "Did radiation dose provide protection from pancreatic cancer for President Carter?", en-US, *Atomic Insights*, May 2011. [Online]. Available: `https://atomicinsights.com/did-radiation-dose-provide-protection-from-pancreatic-cancer-for-president-carter/` (Cited on page 4).

[37] OECD, *Chernobyl: Assessment of Radiological and Health Impacts - 2002 Update of Chernobyl: Ten Years On*, en, H. Métivier, Ed. OECD Publishing, 2003. [Online]. Available: `https://www.oecd-nea.org/rp/chernobyl/` (Cited on pages 4, 7).

[38] W. G. Cross, "The Chalk River Accident in 1952", *Atomic Energy of Canada Limited (AECL)*, 1980. [Online]. Available: `http://www.nuclearfaq.ca/The_CR_Accident_in_1952_WG_Cross1980.pdf` (Cited on page 4).

[39] B. R. Sehgal, *Nuclear safety in light water reactors: severe accident phenomenology*, English. Amsterdam [etc.: Elsevier/Academic Press, 2012, OCLC: 814173028, ISBN: 978-0-12-388446-6 (Cited on pages 5, 7, 15, 23, 24, 49).

[40] U.S. Atomic Energy Commission., *Theoretical possibilities and consequences of major accidents in large nuclear power plants; a study of possible consequences if certain assumed accidents, theoretically possible but highly improbable, were to occur in large nuclear power plants.* Washington: U.S. Atomic Energy Commission, 1957. [Online]. Available: `https://catalog.hathitrust.org/Record/006172880` (Cited on page 5).

[41] J. DiNunno, F. Anderson, R. Baker, & R. Waterfield, "Calculation of Distance Factors for Power and Test Reactor Sites", en, Tech. Rep. TID-14844, 4827930, Jan. 1962, TID–14 844, 4 827 930. DOI: `10.2172/4827930`. [Online]. Available: `http://www.osti.gov/servlets/purl/4827930-j5MEIa/` (Cited on page 5).

[42] P. Tanguy, "Three decades of nuclear safety", en, *IAEA BULLETIN*, vol. 2, pp. 51–57, 1988 (Cited on page 5).

[43] N. Rasmussen, "Reactor safety study. An assessment of accident risks in U. S. commercial nuclear power plants. Executive summary: main report. [PWR and BWR]", English, Nuclear Regulatory Commission, Washington, D.C. (USA), Tech. Rep. WASH-1400-MR; NUREG-75/014-MR, Oct. 1975. DOI: `10.2172/7134131`. [Online]. Available: `https://www.osti.gov/biblio/7134131` (Cited on pages 5, 12).

[44] G. R. Corey, "A Brief Review of the Accident at Three Mile Island", en, *IAEA BULLETIN*, vol. 21, no. 5, p. 6, 1979. [Online]. Available: `https://www.iaea.org/sites/default/files/publications/magazines/bulletin/bull21-5/21502795459.pdf` (Cited on page 5).

[45] L. Högberg, "Root Causes and Impacts of Severe Accidents at Large Nuclear Power Plants", en, *AMBIO*, vol. 42, no. 3, pp. 267–284, Apr. 2013, ISSN: 0044-7447, 1654-7209. DOI: `10.1007/s13280-013-0382-x`. [Online]. Available: `http://link.springer.com/10.1007/s13280-013-0382-x` (Cited on pages 5, 7, 12).

[46] D. Marksberry, F. Gonzales, & K. Hamburger, "Three Mile Island Accident of 1979 Knowledge Management Digest, Revision 1", U.S. Nuclear Regulatory Commission, Washington, DC, Technical NUREG/KM-001, Rev. 1, Jun. 2016. [Online]. Available: `https://tmi2kml.inl.gov/Documents/Common/NUREGKM-0001,%20Revision%201%20Final.pdf` (Cited on pages 5, 6, 13).

[47] K. L. Thomsen, *Review of the TMI-2 accident evaluation and vessel investigation projects*, en, ser. Risø-R 1004. Roskilde: Risø National Laboratory, 1998, OCLC: 245704187, ISBN: 978-87-550-2346-8 (Cited on pages 5, 12).

[48] E. Tolman, P. Kuan, & J. Broughton, "TMI-2 accident scenario update", en, *Nuclear Engineering and Design*, vol. 108, no. 1-2, pp. 45–54, Jun. 1988, ISSN: 00295493. DOI: `10.1016/0029-5493(88)90055-6`. [Online]. Available: `https://linkinghub.elsevier.com/retrieve/pii/0029549388900556` (Cited on pages 5, 11).

[49] J. Rempe, M. Farmer, M. Corradini, L. Ott, R. Gauntt, & D. Powers, "Revisiting Insights from Three Mile Island Unit 2 Postaccident Examinations and Evaluations in View of the Fukushima Daiichi Accident", en, *Nuclear Science and Engineering*, vol. 172, no. 3, pp. 223–248, Nov. 2012, ISSN: 0029-5639, 1943-748X. DOI: `10.13182/NSE12-3`. [Online]. Available: `https://www.tandfonline.com/doi/full/10.13182/NSE12-3` (Cited on page 5).

[50] V. Kortov & Y. Ustyantsev, "Chernobyl accident: Causes, consequences and problems of radiation measurements", en, *Radiation Measurements*, vol. 55, pp. 12–16, Aug. 2013, ISSN: 13504487. DOI: `10.1016/j.radmeas.2012.05.015`. [Online]. Available: `https://linkinghub.elsevier.com/retrieve/pii/S1350448712001680` (Cited on page 6).

[51] L. Schou-Jensen, "The ARGOS CBRN Information System", en, p. 4, 2009 (Cited on page 7).

[52] D. Bressan, “How The Chernobyl Nuclear Plant Meltdown Formed World’s Most Dangerous Lava”, en, *Forbes*, Jun. 2019. [Online]. Available: `https://www.forbes.com/sites/davidbressan/2019/06/14/how-the-chernobyl-nuclear-plant-meltdown-formed-worlds-most-dangerous-lava-flow/` (Cited on page 7).

[53] Tokyo Electric Power Company (TEPCO), “Fukushima Nuclear Accident Analysis Report”, Tokyo Electric Power Company (TEPCO), Tokyo, Tech. Rep., Jun. 2012. [Online]. Available: `http://www.tepco.co.jp/en/press/corp-com/release/betu12_e/images/120620e0104.pdf` (Cited on page 8).

[54] C. Synolakis & U. Kânoğlu, “The Fukushima accident was preventable”, en, *Philosophical Transactions of the Royal Society A: Mathematical, Physical and Engineering Sciences*, vol. 373, no. 2053, p. 20 140 379, Oct. 2015, ISSN: 1364-503X, 1471-2962. DOI: `10.1098/rsta.2014.0379`. [Online]. Available: `https://royalsocietypublishing.org/doi/10.1098/rsta.2014.0379` (Cited on page 8).

[55] International Atomic Energy Agency, Ed., *The Fukushima Daiichi accident*, en. Vienna: International Atomic Energy Agency, 2015, ISBN: 978-92-0-107015-9 (Cited on page 8).

[56] M. Baba, “Fukushima accident: What happened?”, en, *Radiation Measurements*, vol. 55, pp. 17–21, Aug. 2013, ISSN: 13504487. DOI: `10.1016/j.radmeas.2013.01.013`. [Online]. Available: `https://linkinghub.elsevier.com/retrieve/pii/S1350448713000267` (Cited on page 8).

[57] National Academies of Sciences, Engineering, and Medicine (U.S.), Ed., *Lessons learned from the Fukushima nuclear accident for improving safety and security of U.S. nuclear plants. Phase 2*, en. Washington, D.C: National Academies Press, 2016, OCLC: ocn950978005, ISBN: 978-0-309-38888-7 (Cited on page 8).

[58] “Japan’s nuclear reactor: radioactive leaks”, en-GB, *BBC News*, Apr. 2011. [Online]. Available: `//www.bbc.co.uk/news/world-asia-pacific-12911190` (Cited on page 9).

[59] Tokyo Electric Power Company (TEPCO), *Analysis Results of Unit 2 Primary Containment Vessel Internal Investigation*, Apr. 2018. [Online]. Available: `https://photo.tepco.co.jp/en/date/2018-e/201804-e/180426-01e.html` (Cited on page 9).

[60] ——, *Fukushima Daiichi Nuclear Power Station Unit 2 Primary Containment Vessel Internal Investigation*, en, Apr. 2018. [Online]. Available: `http://www.tepco.co.jp/en/nu/fukushima-np/handouts/2018/images/handouts_180426_02-e.pdf` (Cited on page 9).

[61] International Atomic Energy Agency, *Severe accident management programmes for nuclear power plants: safety guide*, en. Vienna: International Atomic Energy Agency, 2009, OCLC: 430054623, ISBN: 978-92-0-112908-6 (Cited on page 10).

[62] Z. Domaratzki, F. R. Campbell, & R. J. Atchison, “The Nature of Reactor Accidents”, en, Tech. Rep., Jan. 1981, p. 22 (Cited on pages 10, 11).

[63] International Atomic Energy Agency, “Defining initiating eventsfor purposes ofprobabilistic safety assessment”, International Atomic Energy Agency, Vienna, Tech. Rep., Sep. 1993. [Online]. Available: `https://www-pub.iaea.org/MTCD/Publications/PDF/te_719_web.pdf` (Cited on pages 10, 11).

[64] E. D. Blandford & M. M. May, *Lessons Learned from "Lessons Learned": The Evolution of Nuclear Power Safety after Accidents and Near-Accidents*, en. Cambridge, MA: American Academy of Arts & Sciences, 2012, ISBN: 0-87724-094-9. [Online]. Available: `https://www.amacad.org/publication/lessons-learned-lessons-learned-evolution-nuclear-power-safety-after-accidents-and-near` (Cited on page 11).

[65] M. Joyce, "Chapter 14 - Nuclear Safety and Regulation", en, in *Nuclear Engineering*, M. Joyce, Ed., Butterworth-Heinemann, Jan. 2018, pp. 323–355, ISBN: 978-0-08-100962-8. DOI: `10.1016/B978-0-08-100962-8.00014-7`. [Online]. Available: `http://www.sciencedirect.com/science/article/pii/B9780081009628000147` (Cited on page 11).

[66] GPU Nuclear, *TMI-2 Clean-up Highlights Video*, en, Penn State University Libraries, Accessed in the Penn State University Libraries online Collections, 1989. [Online]. Available: `https://libraries.psu.edu/about/collections/three-mile-island-2-recovery-and-decontamination/tmi-2-clean-highlights-video` (Cited on page 12).

[67] S. Basu & T. Ginsberg, "A reassessment of the potential for an alpha-mode containment failure and a review of the current understanding of broader fuel-coolant interaction issues. Second steam explosion review group workshop", English, Nuclear Regulatory Commission, Div. of Systems Technology, Washington, DC (United States); Brookhaven National Lab., Upton, NY (United States), Tech. Rep. NUREG-1524; CONF-9506447-Summ. Aug. 1996. [Online]. Available: `https://www.osti.gov/biblio/319665` (Cited on page 12).

[68] European Commission, *In-Vessel Melt Retention Severe Accident Management Strategy for Existing and Future NPPs | IVMR Project | H2020 | CORDIS | European Commission*, 2019. [Online]. Available: `https://cordis.europa.eu/project/rcn/196923/factsheet/en` (Cited on page 13).

[69] D. Jacquemain, A. Bentaïb, H. Bonneville, G. Cénérino, IRSN, B. Clément, F. Corenwinder, M. Cranga, G. Ducros, F. Fichot, C. Journeau, V. Koundy, D. Leteinturier, D. Magallon, R. Meignen, F. Monroig, G. Nahas, F. Pichereau, E. Raimond, J.-M. Seiler, B. Tourniaire, & J.-P. Van-Dorsselaere, *Nuclear power reactor core melt accidents: current state of knowledge*, English. Les Ulis: EDP sciences, 2015, OCLC: 946645180, ISBN: 978-2-7598-1835-8. [Online]. Available: `http://www.edp-open.org/images/stories/books/fulldl/Nuclear_Power_Reactor_Core_Melt_Accidents.pdf` (Cited on pages 14, 15, 18, 21, 22, 26, 28, 50).

[70] R. Meignen, A. Bentaïb, & E. Raimond, "Evaluer les phénomènes énergétiques susceptibles de survenir en cas d'accident grave", fr, *Revue Générale Nucléaire*, no. 1, pp. 38–53, Jan. 2010, ISSN: 0335-5004. DOI: `10.1051/rgn/20101038`. [Online]. Available: `https://rgn.publications.sfen.org/articles/rgn/abs/2010/01/rgn20101p38/rgn20101p38.html` (Cited on pages 14, 15, 17, 18).

[71] J. F. Mao, J. W. Zhu, S. Y. Bao, L. J. Luo, & Z. L. Gao, "Creep and Damage Analysis of Reactor Pressure Vessel Considering Core Meltdown Scenario", en, *Procedia Engineering*, Pressure Vessel Technology: Preparing for the Future, vol. 130, pp. 1148–1161, Jan. 2015, ISSN: 1877-7058. DOI: `10.1016/j.proeng.2015.12.283`. [Online]. Available: `http://www.sciencedirect.com/science/article/pii/S1877705815041673` (Cited on pages 15, 17).

[72] B. R. Sehgal, A. Theerthan, A. Giri, A. Karbojian, H. G. Willschütz, O. Kymäläinen, S. Vandroux, J. M. Bonnet, J. M. Seiler, K. Ikkonen, R. Sairanen, S. Bhandari, M. Bürger, M. Buck, W. Widmann, J. Dienstbier, Z. Techy, P. Kostka, R. Taubner, T. Theofanous, & T. N. Dinh, "Assessment of reactor vessel integrity (ARVI)", en, *Nuclear Engineering and Design*, Mid-Term Symposium on Shared-Cost and Concerted Actions, vol. 221, no. 1, pp. 23–53, Apr. 2003, ISSN: 0029-5493. DOI: `10.1016/S0029-5493(02)00343-6`. [Online]. Available: `http://www.sciencedirect.com/science/article/pii/S0029549302003436` (Cited on pages 15, 18).

[73] X. Wang & X. Cheng, "Analysis of Focusing Effect of Light Metallic Layer in Stratified Molten Pool Under IVR-ERVC Condition", en, *Journal of Nuclear Engineering and Radiation Science*, vol. 1, no. 2, p. 021 007, Apr. 2015, ISSN: 2332-8983, 2332-8975. DOI: `10.1115/1.4029619`. [Online]. Available: `https://asmedigitalcollection.asme.org/nuclearengineering/article/doi/10.1115/1.4029619/369697/Analysis-of-Focusing-Effect-of-Light-Metallic` (Cited on page 15).

[74] V. Koundy, C. Caroli, L. Nicolas, P. Matheron, J.-M. Gentzbittel, & M. Coret, "Study of tearing behaviour of a PWR reactor pressure vessel lower head under severe accident loadings", en, *Nuclear Engineering and Design*, vol. 238, no. 9, pp. 2411–2419, Sep. 2008, ISSN: 00295493. DOI: `10.1016/j.nucengdes.2008.03.005`. [Online]. Available: `https://linkinghub.elsevier.com/retrieve/pii/S002954930800174X` (Cited on page 16).

[75] L. Humphries, T. Chu, J. Bentz, R. Simpson, C. Hanks, W. Lu, B. Antoun, C. Robino, J. Puskar, & P. Mongabure, "OECD Lower Head Failure Project Final Report", en, Sandia National Labs., Albuquerque, NM, USA, Tech. Rep., 2002, p. 570. [Online]. Available: `https://www.oecd-nea.org/nsd/docs/2002/csni-r2002-27.pdf` (Cited on page 16).

[76] L. Meyer, G. Albrecht, C. Caroli, & I. Ivanov, "Direct containment heating integral effects tests in geometries of European nuclear power plants", en, *Nuclear Engineering and Design*, vol. 239, no. 10, pp. 2070–2084, Oct. 2009, ISSN: 0029-5493. DOI: `10.1016/j.nucengdes.2009.04.016`. [Online]. Available: `http://www.sciencedirect.com/science/article/pii/S0029549309002222` (Cited on page 17).

[77] R. Meignen & T. Janin, "On the Analysis and Evaluation of Direct Containment Heating with the Multidimensional Multiphase Flow Code MC3d", en, *Science and Technology of Nuclear Installations*, vol. 2010, pp. 1–13, 2010, ISSN: 1687-6075, 1687-6083. DOI: `10.1155/2010/289792`. [Online]. Available: `http://www.hindawi.com/journals/stni/2010/289792/` (Cited on pages 17, 80).

[78] R. Meignen, S. Picchi, J. Lamome, B. Raverdy, S. Castrillon-Escobar, & G. Nicaise, "The challenge of modeling fuel coolant interaction: Part I – Premixing", *Nuclear Engineering and Design*, vol. 280, pp. 511–527, Dec. 2014, ISSN: 0029-5493. DOI: `10.1016/j.nucengdes.2014.08.029`. [Online]. Available: `http://www.sciencedirect.com/science/article/pii/S0029549314005056` (Cited on pages 18, 52).

[79] R. Meignen, B. Raverdy, M. Buck, G. Pohlner, P. Kudinov, W. Ma, C. Brayer, P. Piluso, S.-W. Hong, M. Leskovar, M. Uršič, G. Albrecht, I. Lindholm, & I. Ivanov, "Status of steam explosion understanding and modelling", en, *Annals of Nuclear Energy*, ERMSAR 2013 conference of the SARNET network, vol. 74, pp. 125–133, Dec. 2014, ISSN: 0306-4549. DOI: `10.1016/j.anucene.`

2014.07.008. [Online]. Available: `http://www.sciencedirect.com/science/article/pii/S0306454914003399` (Cited on page 18).

[80] P. Shen, W. Zhou, N. Cassiaut-Louis, C. Journeau, P. Piluso, & Y. Liao, "Corium behavior and steam explosion risks: A review of experiments", en, *Annals of Nuclear Energy*, vol. 121, pp. 162–176, Nov. 2018, ISSN: 03064549. DOI: `10.1016/j.anucene.2018.07.029`. [Online]. Available: `https://linkinghub.elsevier.com/retrieve/pii/S0306454918303785` (Cited on page 18).

[81] S. Hermsmeyer, P. Pla, & M. Sangiorgi, "Validation of ASTEC v2.0 corium jet fragmentation model using FARO experiments", en, *Nuclear Engineering and Design*, vol. 286, pp. 246–252, May 2015, ISSN: 0029-5493. DOI: `10.1016/j.nucengdes.2015.02.016`. [Online]. Available: `http://www.sciencedirect.com/science/article/pii/S0029549315000989` (Cited on page 18).

[82] J. Namiech, G. Berthoud, & N. Coutris, "Fragmentation of a molten corium jet falling into water", en, *Nuclear Engineering and Design*, vol. 229, no. 2-3, pp. 265–287, Apr. 2004, ISSN: 00295493. DOI: `10.1016/j.nucengdes.2004.01.004`. [Online]. Available: `https://linkinghub.elsevier.com/retrieve/pii/S0029549304000391` (Cited on page 18).

[83] S. J. Board, R. W. Hall, & R. S. Hall, "Detonation of fuel coolant explosions", en, *Nature*, vol. 254, no. 5498, pp. 319–321, Mar. 1975, ISSN: 1476-4687. DOI: `10.1038/254319a0`. [Online]. Available: `https://www.nature.com/articles/254319a0` (Cited on page 19).

[84] R. Meignen, P. Piluso, & N. Rimbert, "Outcomes of the French ICE project on Fuel Coolant Interaction", en, in *Proceedings of 17th International Topical Meeting on Nuclear Reactor Thermal Hydraulics (NURETH-17)*, vol. 5, Xi'an, China, Sep. 2017, pp. 2966–2982, ISBN: 978-1-5108-7262-2 (Cited on page 19).

[85] L. Viot, "Coupling and synchronisation of models in a code for severe accidents in nuclear reactors", French, PhD Thesis, Université Paris-Saclay, Oct. 2018. [Online]. Available: `https://tel.archives-ouvertes.fr/tel-01905094` (Cited on page 20).

[86] G. Xotta, G. Mazzucco, V. Salomoni, C. Majorana, & K. Willam, "Composite behavior of concrete materials under high temperatures", en, *International Journal of Solids and Structures*, vol. 64-65, pp. 86–99, Jul. 2015, ISSN: 00207683. DOI: `10.1016/j.ijsolstr.2015.03.016`. [Online]. Available: `https://linkinghub.elsevier.com/retrieve/pii/S0020768315001316` (Cited on page 21).

[87] C. Journeau & P. Piluso, "2.25 - Core Concrete Interaction", in *Comprehensive nuclear Materials*, https://doi.org/10.1016/B978-0-08-056033-5.00048-3, Oxford: Elsevier, 2012, pp. 635–654, ISBN: 9780080560274. [Online]. Available: `https://www.sciencedirect.com/science/article/pii/B9780080560335000483` (Cited on pages 21, 22).

[88] F. Paulik, J. Paulik, & M. Arnold, "Thermal decomposition of gypsum", *Thermochimica Acta*, vol. 200, no. Supplement C, pp. 195–204, 1992, ISSN: 0040-6031. DOI: `https://doi.org/10.1016/0040-6031(92)85115-C`. [Online]. Available: `http://www.sciencedirect.com/science/article/pii/004060319285115C` (Cited on page 21).

[89] OECD, "State of the Art Report on Molten Corium Concrete Interaction and Ex-Vessel Molten Core Coolability", English, OECD, State of the Art 7392, 2017, p. 363. [Online]. Available: `https://www.oecd-nea.org/nsd/pubs/2017/7392-soar-molten-corium.pdf` (Cited on pages 22, 47, 50, 51).

[90] V. Strizhov, V. Kanukova, T. Vinogradova, E. Askenov, & V. Nikulshin, "An assessment of the CORCON-MOD3 code. Part 1: Thermal-hydraulic calculations", Nuclear Regulatory Commission, Washington, DC (United States). Office of Nuclear Regulatory Research, Tech. Rep., 1996 (Cited on page 22).

[91] K. R. Robb, "Melt eruptions during molten corium concrete interactions", PhD thesis, 2011. [Online]. Available: `http://adsabs.harvard.edu/abs/2011PhDT.......133R` (Cited on page 23).

[92] S. Hermsmeyer, R. Iglesias, L. E. Herranz, B. Reer, M. Sonnenkalb, H. Nowack, A. Stefanova, E. Raimond, P. Chatelard, L. Foucher, M. Barnak, P. Matejovic, G. Pascal, M. Vela, M. Sangiorgi, P. Pla, A. Grah, M. Stručić, G. Lajtha, Z. Techy, T. Lind, M. Koch, F. Gremme, A. Bujan, & V. Sanchez, "Review of current Severe Accident Management (SAM) approaches for Nuclear Power Plants in Europe requirements", en, Joint Research Centre, Luxembourg, Scientific and Technical Research Report EUR 26967, 2014, ISBN: 978-92-79-44446-3 ISSN: 1831-9424, p. 130. DOI: `10.2790/38824`. [Online]. Available: `http://publications.jrc.ec.europa.eu/repository/bitstream/JRC93082/jrc93082_2014-12-08%20eur%20samg%20europe%20final.pdf` (Cited on page 23).

[93] Z. V. Stosic, W. Brettschuh, & U. Stoll, "Boiling water reactor with innovative safety concept: The Generation III+ SWR-1000", en, *Nuclear Engineering and Design*, vol. 238, no. 8, pp. 1863–1901, Aug. 2008, ISSN: 00295493. DOI: `10.1016/j.nucengdes.2007.12.014`. [Online]. Available: `https://linkinghub.elsevier.com/retrieve/pii/S0029549308000228` (Cited on page 24).

[94] W. Ma, Y. Yuan, & B. R. Sehgal, "In-Vessel Melt Retention of Pressurized Water Reactors: Historical Review and Future Research Needs", en, *Engineering*, vol. 2, no. 1, pp. 103–111, Mar. 2016, ISSN: 20958099. DOI: `10.1016/J.ENG.2016.01.019`. [Online]. Available: `https://linkinghub.elsevier.com/retrieve/pii/S2095809916301540` (Cited on pages 24, 25).

[95] F. Fichot & L. Carenini, *IVMR strategy and pending issues for a harmonization of safety demonstration*, Vienna, Austria, Sep. 2016 (Cited on page 24).

[96] F. Fichot, J.-M. Bonnet, & B. Chaumont, "IRSN views and perspectives on in-vessel melt retention strategy for severe accident mitigation", en, Bruxells, Belgium, Nov. 2015, p. 15. [Online]. Available: `https://www.researchgate.net/profile/Florian_Fichot/publication/291295233_IRSN_views_and_perspectives_on_in-vessel_melt_retention_strategy_for_severe_accident_mitigation/links/569f502208ae21a56425af58/IRSN-views-and-perspectives-on-in-vessel-melt-retention-strategy-for-severe-accident-mitigation.pdf` (Cited on page 24).

[97] J. H. Song, S. B. Kim, & H. D. Kim, "Unresolved Issues in Severe Accidents for Advanced Light Water Reactors", en, in *17th International Conference on Structural Mechanics in Reactor Technology 2003 (SMiRT 17)*, ser. WP01-5, vol. 4, Prague, Czech Republic: International Association for Structural Mechanics in Reactor Technology (IASMiRT), Aug. 2003, pp. 3028–3033, ISBN: 978-1-5108-1700-5. [Online]. Available: `https://repository.lib.ncsu.edu/bitstream/handle/1840.20/27447/WP01-5.pdf` (Cited on page 24).

[98] R. A. Matzie & S. E. Ritterbusch, “System 80+ TM standard plant: Design and operations overview”, English, in *Book of Extended Synopses*, Seoul, Republic of Korea: International Atomic Energy Agency, Dec. 1998, pp. 430–442. [Online]. Available: `http://inis.iaea.org/Search/search.aspx?orig_q=RN:31007062` (Cited on page 25).

[99] R. Cozeret, C. Debaudringhien, G. Cenerino, & E. Raimond, “Review of the Upgraded Severe Accident Mitigations Strategies for the Generation II PWRs in France Foreseen in the Framework of the Plant Life Extension”, en, Vienna, Austria, Jun. 2017, p. 5. [Online]. Available: `https://nucleus.iaea.org/sites/gsan/act/CN-251/papers/136-1-E._Raimond_R._Cozeret_IRSN_Gen_II_PWRS_upgrade.pdf` (Cited on page 25).

[100] A. Commandé, “Jeu de données Reacteur MEDICIS: choix et justificatifs des modèles, des donées et paramètres”, fr, IRSN, Cadarache, France, Internal technical report PSN-RES/SAG/2015-00111, Feb. 2015, p. 44 (Cited on pages 26, 27).

[101] M. Rashid, S. Rahman, R. Kulenovic, M. Bürger, & E. Laurien, “Quenching Experiments: Coolability of Debris Bed”, *Nuclear Technology*, vol. 181, no. 1, pp. 208–215, Jan. 2013, ISSN: 0029-5450. DOI: `10.13182/NT13-A15768`. [Online]. Available: `https://doi.org/10.13182/NT13-A15768` (Cited on page 28).

[102] E. Takasuo, S. Holmström, T. Kinnunen, & P. H. Pankakoski, “The COOLOCE experiments investigating the dryout power in debris beds of heap-like and cylindrical geometries”, en, *Nuclear Engineering and Design*, vol. 250, pp. 687–700, Sep. 2012, ISSN: 00295493. DOI: `10.1016/j.nucengdes.2012.06.015`. [Online]. Available: `https://linkinghub.elsevier.com/retrieve/pii/S0029549312003330` (Cited on pages 28, 35, 129).

[103] A. K. Nayak, B. R. Sehgal, & A. V. Stepanyan, “An experimental study on quenching of a radially stratified heated porous bed”, en, *Nuclear Engineering and Design*, vol. 236, no. 19-21, pp. 2189–2198, Oct. 2006, ISSN: 00295493. DOI: `10.1016/j.nucengdes.2006.03.057`. [Online]. Available: `https://linkinghub.elsevier.com/retrieve/pii/S0029549306002998` (Cited on page 28).

[104] N. E. Todreas & M. S. Kazimi, *Nuclear systems*, en. New York: Hemisphere Pub. Corp, 1990, ISBN: 0-89116-935-0 (Cited on page 28).

[105] D. Magallon, “Characteristics of corium debris bed generated in large-scale fuel-coolant interaction experiments”, en, *Nuclear Engineering and Design*, vol. 236, no. 19-21, pp. 1998–2009, Oct. 2006, ISSN: 00295493. DOI: `10.1016/j.nucengdes.2006.03.038`. [Online]. Available: `https://linkinghub.elsevier.com/retrieve/pii/S0029549306002858` (Cited on page 29).

[106] J.-H. Kim, I.-K. Park, S.-W. Hong, B.-T. Min, S.-H. Hong, J.-H. Song, & H.-D. Kim, “Steam Explosion Experiments Using Nuclear Reactor Materials in the TROI Facilities”, *Heat Transfer Engineering*, vol. 29, no. 8, pp. 748–756, Aug. 2008, ISSN: 0145-7632. DOI: `10.1080/01457630801981796`. [Online]. Available: `https://doi.org/10.1080/01457630801981796` (Cited on page 29).

[107] S. Nukiyama, “The maximum and minimum values of the heat Q transmitted from metal to boiling water under atmospheric pressure”, en, *Journal Japan Sm. Mech. Engrs*, vol. 37, pp. 367–374, 1934, ISSN: 0017-9310. DOI: `10.1016/0017-9310(66)90138-4`. [Online]. Available: `http://www.sciencedirect.com/science/article/pii/0017931066901384` (Cited on page 32).

[108] G. P. Celata & A. Mariani, *Critical Heat Flux, Post-dryout and Their Augmentation.* ENEA, RT/ERG/98/10, 1999 (Cited on page 32).

[109] R. J. Lipinski, "Model for boiling and dryout in particle beds", en, Sandia National Labs., Tech. Rep. NUREG/CR–2646, 1982. [Online]. Available: `http://inis.iaea.org/Search/search.aspx?orig_q=RN:14732098` (Cited on pages 33–35, 64, 68, 70, 71, 112, 120, 123).

[110] J. D. Gabor, J. C. Hesson, L. J. Baker, & J. C. Cassulo, "Simulation Experiments on Heat Transfer From Fast Reactor Fuel Debris", English, *Trans. Amer. Nucl. Soc. 15: No. 2, 836(Nov 1972).*, Jan. 1972. [Online]. Available: `https://www.osti.gov/biblio/4575666` (Cited on pages 33, 34).

[111] R. Trenberth & G. F. Stevens, "An experimental study of boiling heat transfer and dryout in heated particulate beds", en, UKAEA Atomic Energy Establishment, Tech. Rep. AEEW-R–1342, 1980. [Online]. Available: `http://inis.iaea.org/Search/search.aspx?orig_q=RN:12592606` (Cited on pages 33, 34).

[112] V. Dhir & I. Catton, "Dryout Heat Fluxes for Inductively Heated Particulate Beds", en, *Journal of Heat Transfer*, vol. 99, no. 2, pp. 250–256, May 1977, ISSN: 0022-1481. DOI: `10.1115/1.3450677`. [Online]. Available: `https://asmedigitalcollection.asme.org/heattransfer/article/99/2/250/382537/Dryout-Heat-Fluxes-for-Inductively-Heated` (Cited on pages 33–35).

[113] R. S. Keowen & I. Catton, "Dry out of a fluidized particle bed with internal heat generation", en, California Univ., Tech. Rep. UCLA–34P203-2, 1975. [Online]. Available: `http://inis.iaea.org/Search/search.aspx?orig_q=RN:7220336` (Cited on pages 33, 34).

[114] R. J. Lipinski & J. B. Rivard, "Debris bed heat removal models: boiling and dryout with top and bottom cooling", en, Sandia Labs., Tech. Rep. SAND–79-0091C, 1979. [Online]. Available: `http://inis.iaea.org/Search/search.aspx?orig_q=RN:11513749` (Cited on page 33).

[115] J. Rivard, "Preliminary results from initial in-pile debris bed experiments", en, in *Proceedings of the third post-accident heat removal information exchange*, Argonne National Laboratory, Nov. 1977, pp. 49–61. [Online]. Available: `https://www.osti.gov/servlets/purl/6556221` (Cited on page 33).

[116] L. Barleon, K. Thomauske, & H. Werle, "Cooling of Debris Beds", en, *Nuclear Technology*, vol. 65, no. 1, pp. 67–86, Apr. 1984, ISSN: 0029-5450, 1943-7471. DOI: `10.13182/NT84-A33374`. [Online]. Available: `https://www.tandfonline.com/doi/full/10.13182/NT84-A33374` (Cited on pages 34, 35, 124).

[117] K. Miyazaki, T. Ohama, K. Murai, S. Inoue, & N. Yamaoka, "Dryout Heat Flux for Core Debris Bed, (II): Effects of Particle Size Mixing and Coolant Flow", en, *Journal of Nuclear Science and Technology*, vol. 23, no. 9, pp. 769–778, Sep. 1986, ISSN: 0022-3131, 1881-1248. DOI: `10.1080/18811248.1986.9735054`. [Online]. Available: `http://www.tandfonline.com/doi/abs/10.1080/18811248.1986.9735054` (Cited on pages 34, 35, 124).

[118] G. Hofmann, "On the Location and Mechanisms of Dryout in Top-Fed and Bottom-Fed Particulate Beds", en, *Nuclear Technology*, vol. 65, no. 1, pp. 36–45, Apr. 1984, ISSN: 0029-5450, 1943-7471. DOI: `10.13182/NT84-A33371`. [Online]. Available: `https://www.tandfonline.com/doi/full/10.13182/NT84-A33371` (Cited on pages 34, 35, 124).

[119] M. Rashid, "Coolability of Volumetrically Heated Particle Beds", en, ISSN: 0173-6892, Dissertation PhD, Universität Stuttgart, Stuttgart, Mar. 2017. DOI: `10.18419/opus-9214`. [Online]. Available: `http://dx.doi.org/10.18419/opus-9214` (Cited on page 34).

[120] K. Hu & T. G. Theofanous, “On the measurement and mechanism of dryout in volumetrically heated coarse particle beds”, *International journal of multiphase flow*, vol. 17, no. 4, pp. 519–532, 1991. [Online]. Available: `http://www.sciencedirect.com/science/article/pii/0301932291900477` (Cited on pages 34, 64, 120).

[121] K. Miyazaki, K. Murai, T. Ohama, N. Yamaoka, & S. Inoue, “Dryout Heat Flux for Core Debris Bed, (I): Effects of System Pressure and Particle Size”, en, *Journal of Nuclear Science and Technology*, vol. 23, no. 8, pp. 702–710, Aug. 1986, ISSN: 0022-3131, 1881-1248. DOI: `10.1080/18811248.1986.9735043`. [Online]. Available: `http://www.tandfonline.com/doi/abs/10.1080/18811248.1986.9735043` (Cited on page 34).

[122] K. Atkhen & G. Berthoud, “SILFIDE experiment: Coolability in a volumetrically heated debris bed”, en, *Nuclear Engineering and Design*, vol. 236, no. 19-21, pp. 2126–2134, Oct. 2006, ISSN: 00295493. DOI: `10.1016/j.nucengdes.2006.03.061`. [Online]. Available: `http://linkinghub.elsevier.com/retrieve/pii/S0029549306002950` (Cited on pages 34, 35, 124).

[123] D. Squarer, A. T. Pieczynski, & L. E. Hochreiter, “Effect of Debris Bed Pressure, Particle Size, and Distribution on Degraded Nuclear Reactor Core Coolability”, en, *Nuclear Science and Engineering*, vol. 80, no. 1, pp. 2–13, Jan. 1982, ISSN: 0029-5639, 1943-748X. DOI: `10.13182/NSE82-A21399`. [Online]. Available: `https://www.tandfonline.com/doi/full/10.13182/NSE82-A21399` (Cited on pages 34, 35, 124).

[124] E. Takasuo, “An experimental study of the coolability of debris beds with geometry variations”, *Annals of Nuclear Energy*, vol. 92, pp. 251–261, Jun. 2016, ISSN: 0306-4549. DOI: `10.1016/j.anucene.2016.01.030`. [Online]. Available: `http://www.sciencedirect.com/science/article/pii/S0306454916300408` (Cited on pages 34, 129).

[125] L. Barleon & H. Werle, “Dependence of dryout heat flux on particle diameter for volume- and bottom-heated debris beds”, en, Kernforschungszentrum Karlsruhe G.m.b.H. (Germany, Tech. Rep. KFK–3138, 1981. [Online]. Available: `http://inis.iaea.org/Search/search.aspx?orig_q=RN:13665256` (Cited on page 35).

[126] P. Schäfer, M. Groll, & R. Kulenovic, “Basic investigations on debris cooling”, *Nuclear Engineering and Design*, Festschrift Edition Celebrating the 70th Birthday of Prof. Bal Raj Sehgal: Invited papers on - Core melt accidents in LWRs State of the art of "COOLABILITY OF POROUS DEBRIS", vol. 236, no. 19–21, pp. 2104–2116, Oct. 2006, ISSN: 0029-5493. DOI: `10.1016/j.nucengdes.2006.03.033`. [Online]. Available: `http://www.sciencedirect.com/science/article/pii/S0029549306002925` (Cited on page 35).

[127] G. Repetto, T. Garcin, S. Eymery, & F. Fichot, “Experimental program on debris reflooding (PEARL) – Results on PRELUDE facility”, en, *Nuclear Engineering and Design*, SI:NURETH-14, vol. 264, pp. 176–186, Nov. 2013, ISSN: 0029-5493. DOI: `10.1016/j.nucengdes.2012.11.024`. [Online]. Available: `http://www.sciencedirect.com/science/article/pii/S0029549313001015` (Cited on page 35).

[128] N. Chikhi & F. Fichot, “Experimental and theoretical study of large scale debris bed reflood in the PEARL facility”, en, *Nuclear Engineering and Design*, 16th International Topical Meeting on Nuclear Reactor Thermal Hydraulics, vol. 312, pp. 48–58, Feb. 2017, ISSN: 0029-5493. DOI:

`10.1016/j.nucengdes.2016.05.009`. [Online]. Available: `http://www.sciencedirect.com/science/article/pii/S0029549316301054` (Cited on pages 35, 36, 83).

[129] T. Ginsberg, J. Klein, J. Klages, C. E. Schwarz, & J. C. Chen, "Transient core-debris bed heat-removal experiments and analysis", en, Brookhaven National Lab., Tech. Rep. BNL-NUREG–31796, 1982. [Online]. Available: `http://inis.iaea.org/Search/search.aspx?orig_q=RN:14746048` (Cited on pages 37, 38, 169).

[130] T. Ginsberg, J. Klein, J. Klages, Y. Sanborn, C. E. Schwarz, J. C. Chen, & L. Wei, "An Experimental and analytical investigation of quenching of superheated debris beds under top-reflood conditions. Final report", English, Brookhaven National Lab., Upton, NY (USA), Tech. Rep. NUREG/CR-4493; BNL-NUREG-51951, Jan. 1986. [Online]. Available: `https://www.osti.gov/biblio/5912914-experimental-analytical-investigation-quenching-superheated-debris-beds-under-top-reflood-conditions-final-report` (Cited on pages 37–40, 135–137, 161).

[131] T. Ginsberg & J. C. Chen, "Quench cooling of superheated debris beds in containment during LWR core meltdown accidents", *International meeting on thermal nuclear reactor safety; Karlsruhe (Germany, F.R.)*, p. 14, 1984 (Cited on pages 40, 180).

[132] D. H. Cho, D. R. Armstrong, & S. H. Chan, "On the Pattern of Water Penetration into a Hot Particle Bed", en, *Nuclear Technology*, vol. 65, no. 1, pp. 23–31, Apr. 1984, ISSN: 0029-5450, 1943-7471. DOI: `10.13182/NT84-A33369`. [Online]. Available: `https://www.tandfonline.com/doi/full/10.13182/NT84-A33369` (Cited on pages 41, 42, 169, 180).

[133] D. H. Cho, D. R. Armstrong, L. Bova, S. H. Chan, & G. R. Thomas, "Debris bed quenching studies", en, in *Proceedings of the international meeting on thermal nuclear reactor safety*, vol. 2, Chicago, IL, USA: American Nuclear Society, 1983, pp. 987–995. [Online]. Available: `http://inis.iaea.org/Search/search.aspx?orig_q=RN:14792410` (Cited on pages 42, 43).

[134] S. Hill, "Channeling in packed columns", en, *Chemical Engineering Science*, vol. 1, no. 6, pp. 247–253, Jan. 1952, ISSN: 0009-2509. DOI: `10.1016/0009-2509(52)87017-4`. [Online]. Available: `http://www.sciencedirect.com/science/article/pii/0009250952870174` (Cited on page 44).

[135] P. G. Saffman & S. G. I. Taylor, "The penetration of a fluid into a porous medium or Hele-Shaw cell containing a more viscous liquid", *Proceedings of the Royal Society of London. Series A. Mathematical and Physical Sciences*, vol. 245, no. 1242, pp. 312–329, Jun. 1958. DOI: `10.1098/rspa.1958.0085`. [Online]. Available: `https://royalsocietypublishing.org/doi/10.1098/rspa.1958.0085` (Cited on pages 44, 171).

[136] R. L. Chuoke, P. van Meurs, & C. van der Poel, "The Instability of Slow, Immiscible, Viscous Liquid-Liquid Displacements in Permeable Media", *Petroleum Transaction, AIME*, vol. 216, pp. 188–194, Jan. 1959. [Online]. Available: `https://www.onepetro.org/general/SPE-1141-G` (Cited on page 45).

[137] G. M. Homsy, "Viscous Fingering in Porous Media", en, *Annual Review of Fluid Mechanics*, vol. 19, no. 1, pp. 271–311, 1987. DOI: `10.1146/annurev.fl.19.010187.001415`. [Online]. Available: `https://doi.org/10.1146/annurev.fl.19.010187.001415` (Cited on pages 45, 171).

[138] L. Cueto-Felgueroso & R. Juanes, "Stability analysis of a phase-field model of gravity-driven unsaturated flow through porous media", en, *Physical Review E*, vol. 79, no. 3, p. 036 301, Mar. 2009, ISSN: 1539-3755, 1550-2376. DOI: `10.1103/PhysRevE.79.036301`. [Online]. Available: `https://link.aps.org/doi/10.1103/PhysRevE.79.036301` (Cited on page 45).

[139] J. Parlange & D. Hill, "Theoretical Analysis of Wetting Front Instability in Soils", ENGLISH, *Soil Science*, vol. 122, no. 4, pp. 236–239, Oct. 1976, ISSN: 0038-075X. [Online]. Available: `insights.ovid.com` (Cited on page 45).

[140] R. J. Glass, J.-Y. Parlange, & T. S. Steenhuis, "Wetting front instability: 1. Theoretical discussion and dimensional analysis", en, *Water Resources Research*, vol. 25, no. 6, pp. 1187–1194, 1989, ISSN: 1944-7973. DOI: `10.1029/WR025i006p01187`. [Online]. Available: `https://agupubs.onlinelibrary.wiley.com/doi/abs/10.1029/WR025i006p01187` (Cited on page 45).

[141] R. Glass & M. Nicholl, "Physics of gravity fingering of immiscible fluids within porous media: An overview of current understanding and selected complicating factors", en, *Geoderma*, vol. 70, no. 2-4, pp. 133–163, Apr. 1996, ISSN: 00167061. DOI: `10.1016/0016-7061(95)00078-X`. [Online]. Available: `http://linkinghub.elsevier.com/retrieve/pii/001670619500078X` (Cited on pages 45, 47).

[142] R. J. Glass & T. S. Steenhuis, "Factors Influencing Infiltration Flow Instability and Movements of Toxics in Layered Sandy Soils", New Orleans, Dec. 1984. [Online]. Available: `https://fluidflowvisualization.sandia.gov/pdf_text/Papers%20in%20Conference%20Proceedings%20and%20Sand%20reports/1_1984_AMSE_GS.pdf` (Cited on page 46).

[143] R. J. Glass, T. S. Steenhuis, & J.-Y. Parlange, "Mechanism for Finger Persistence in Homogeneous, Unsaturated, Porous Media: Theory and Verification", en-US, *Soil Science*, vol. 148, no. 1, p. 60, Jul. 1989, ISSN: 0038-075X. [Online]. Available: `https://journals.lww.com/soilsci/Abstract/1989/07000/Mechanism_for_Finger_Persistence_in_Homogeneous,.7.aspx?Ppt=Article%7Csoilsci:1989:07000:00007%7C%7C` (Cited on page 46).

[144] D. A. DiCarlo, "Stability of gravity-driven multiphase flow in porous media: 40 Years of advancements: Stability of Multiphase Gravity-Driven Flow", en, *Water Resources Research*, vol. 49, no. 8, pp. 4531–4544, Aug. 2013, ISSN: 00431397. DOI: `10.1002/wrcr.20359`. [Online]. Available: `http://doi.wiley.com/10.1002/wrcr.20359` (Cited on pages 46, 47).

[145] L. Cueto-Felgueroso & R. Juanes, "Nonlocal Interface Dynamics and Pattern Formation in Gravity-Driven Unsaturated Flow through Porous Media", en, *Physical Review Letters*, vol. 101, no. 24, p. 244 504, Dec. 2008, ISSN: 0031-9007, 1079-7114. DOI: `10.1103/PhysRevLett.101.244504`. [Online]. Available: `https://link.aps.org/doi/10.1103/PhysRevLett.101.244504` (Cited on page 46).

[146] J. L. Nieber, "Modeling finger development and persistence in initially dry porous media", en, *Geoderma*, vol. 70, no. 2-4, pp. 207–229, Apr. 1996, ISSN: 00167061. DOI: `10.1016/0016-7061(95)00086-0`. [Online]. Available: `https://linkinghub.elsevier.com/retrieve/pii/0016706195000860` (Cited on page 46).

[147] G. A. Diment & K. K. Watson, “Stability Analysis of Water Movement in Unsaturated Porous Materials: 3. Experimental Studies”, en, *Water Resources Research*, vol. 21, no. 7, pp. 979–984, Jul. 1985, ISSN: 00431397. DOI: `10.1029/WR021i007p00979`. [Online]. Available: `http://doi.wiley.com/10.1029/WR021i007p00979` (Cited on page 47).

[148] M. F. Roche, L. Leibowitz, J. K. Fink, & L. J. Baker, “Solidus and liquidus temperatures of core-concrete mixtures”, English, Nuclear Regulatory Commission, Tech. Rep. NUREG/CR–6032, 1993. [Online]. Available: `http://inis.iaea.org/Search/search.aspx?orig_q=RN:25002007` (Cited on page 48).

[149] S. Levy, “Summary of coolability studies undertaken by ACE (Advanced Containment Experiments)/MACE (Melt Attack and Coolability Experiments)/ACEX (ACE/MACE Extension)”, California, Tech. Rep., Jan. 2002 (Cited on page 49).

[150] M. T. Farmer, S. Lomperski, D. J. Kilsdonk, & R. W. Aeschlimann, “OECD MCCI Project Final Report”, *OECD/MCCI-2005-TR06*, 2006. [Online]. Available: `http://www.ipd.anl.gov/anlpubs/2011/05/69911.pdf` (Cited on pages 49, 58).

[151] M. T. Farmer, B. Tourniaire, & K. Atkhen, “Molten Core Concrete Interaction with Early Top Flooding: Results of the CCI-8 Experiment”, en, in *Proceedings of 17th International Topical Meeting on Nuclear Reactor Thermal Hydraulics (NURETH-17)*, Xi’an, China, Sep. 2017, p. 12, ISBN: 978-1-5108-7262-2 (Cited on pages 49, 50, 52, 60).

[152] B. Tourniaire, J. Seiler, J. Bonnet, & M. Amblard, “Experimental study and modelling of liquid ejection through orifices by sparging gas”, en, *Nuclear Engineering and Design*, vol. 236, no. 19-21, pp. 2281–2295, Oct. 2006, ISSN: 00295493. DOI: `10.1016/j.nucengdes.2006.03.053`. [Online]. Available: `http://linkinghub.elsevier.com/retrieve/pii/S0029549306003098` (Cited on page 49).

[153] J. Licht, S. Lomperski, D. J. Kilsdonk, M. T. Farmer, & C. Gerardi, “Electricité de France Large Scale Core Debris Coolability Experiments:CCI-9 Data Report (DRAFT)”, Argonne National Laboratory, Illinois USA, Tech. Rep., Jun. 2017, p. 118 (Cited on pages 50, 59, 100, 101, 103).

[154] H. Alsmeyer, G. Albrecht, L. Meyer, W. Häfner, C. Journeau, M. Fischer, S. Hellman, M. Eddi, H.-J. Allelein, M. Bürger, B. Sehgal, M. Koch, Z. Alkan, J. Petrov, M. Gaune-Escard, E. Altstadt, & G. Bandini, “Ex-vessel core melt stabilization research (ECOSTAR)”, en, *Nuclear Engineering and Design*, vol. 235, no. 2-4, pp. 271–284, Feb. 2005, ISSN: 00295493. DOI: `10.1016/j.nucengdes.2004.08.040`. [Online]. Available: `https://linkinghub.elsevier.com/retrieve/pii/S0029549304003097` (Cited on page 50).

[155] R. Meignen & S. Garrier, “Résultats et interprétation de l’essai d’ICB sous eau CCI-8; Comparaison avec l’essai CCI-7”, French, Tech. Rep. PSN-RES/SAG/2015-00412, Jun. 2016, p. 61 (Cited on pages 51, 61, 98).

[156] D. Jacquemain, D. Vola, R. Meignen, J.-M. Bonnet, F. Fichot, E. Raimond, & M. Barrachin, “Past and Future R&D at IRSN on Corium Progression and Related Mitigation Strategies in a Severe Accident”, en, in *Proc. of NURETH-16*, Chicago, IL, USA, Sep. 2015, p. 19, ISBN: 978-0-89448-722-4 (Cited on page 52).

[157] C. Marchetto, “ASTEC V2.1 : MEDICIS MCCI module User’s Manual”, IRSN, Tech. Rep. PSN-RES/SAG/2015-00334, Nov. 2015 (Cited on page 52).

[158] S. Lomperski, M. Farmer, D. Kilsdonk, & B. Aeschlimann, *OECD MCCI Small-Scale Water Ingression and Crust Strength tests (SSWICS) SSWICS-1 final data report, Rev. 1 February 10, 2003.; Report, Rev. 1*, Feb. 2003 (Cited on page 53).

[159] ——, "OECD MCCI Project Small-Scale Water Ingression and Crust Strength Tests (SSWICS) SSWICS Final Report: Thermal Hydraulic Results", Argonne National Laboratory, Tech. Rep., 2005 (Cited on pages 54, 56, 58, 79).

[160] S. Lomperski & M. Farmer, "Experimental evaluation of the water ingression mechanism for corium cooling", en, *Nuclear Engineering and Design*, vol. 237, no. 9, pp. 905–917, May 2007, ISSN: 00295493. DOI: `10.1016/j.nucengdes.2006.12.009`. [Online]. Available: `http://linkinghub.elsevier.com/retrieve/pii/S0029549307000222` (Cited on pages 54, 55, 57, 58, 77, 94–97, 105, 140).

[161] J. K. Fink, "Thermophysical properties of uranium dioxide", en, *Journal of Nuclear Materials*, vol. 279, no. 1, pp. 1–18, Mar. 2000, ISSN: 0022-3115. DOI: `10.1016/S0022-3115(99)00273-1`. [Online]. Available: `http://www.sciencedirect.com/science/article/pii/S0022311599002731` (Cited on page 55).

[162] P. Combis, P. Cormont, L. Gallais, D. Hebert, L. Robin, & J.-L. Rullier, "Evaluation of the fused silica thermal conductivity by comparing infrared thermometry measurements with two-dimensional simulations", en, *Applied Physics Letters*, vol. 101, no. 21, p. 211 908, Nov. 2012, ISSN: 0003-6951, 1077-3118. DOI: `10.1063/1.4764904`. [Online]. Available: `http://aip.scitation.org/doi/10.1063/1.4764904` (Cited on page 55).

[163] A. Seibert, D. Staicu, D. Bottomley, M. Cologna, J. Boshoven, H. Hein, E. Kassim, S. Nourry, M. Ernstberger, D. Robba, & R. Konings, "Thermophysical properties of U, Zr-oxides as prototypic corium materials", en, *Journal of Nuclear Materials*, vol. 520, pp. 165–177, Jul. 2019, ISSN: 00223115. DOI: `10.1016/j.jnucmat.2019.04.019`. [Online]. Available: `https://linkinghub.elsevier.com/retrieve/pii/S0022311518315861` (Cited on page 55).

[164] L. Carenini, J.-F. Haquet, & C. Journeau, "Crust Formation and Dissolution during Corium Concrete Interaction", in *Proceedings of ICAPP 2007*, Nice, France: CEA Severe Accident Mastery experimental Laboratory (DEN/DTN/STRI/LMA), May 2007 (Cited on pages 55, 105).

[165] M. T. Farmer, R. W. Aeschlimann, N. Bremer, D. J. Kilsdonk, S. Lomperski, & S. Garrier, "Electricité de France Two-Dimensional Core Debris Coolability Experiments:CCI-8 Data Report", Argonne National Laboratory, Illinois USA, Tech. Rep., Jul. 2015, p. 118 (Cited on page 59).

[166] M. T. Farmer, D. J. Kilsdonk, R. W. Aeschlimann, S. Lomperski, & N. Bremer, "Electricité de France Two-Dimensional Core Debris Coolability Experiments: CCI-7 Data Report", Argonne National Laboratory, Illinois USA, Tech. Rep., Jun. 2014, p. 122 (Cited on pages 59, 61, 99).

[167] J. Licht, S. Lomperski, D. Kilsdonk, C. Gerardi, & M. Farmer, "Electricité de France Large Scale Core Debris Coolability Experiments: CCI-10 Data Report", Tech. Rep., 2019 (Cited on pages 59, 108, 109).

[168] A. E. Scheidegger, *The Physics of Flow Through Porous Media (3rd Edition)*, en. University of Toronto Press, 1974, ISBN: 978-1-4875-8239-5. [Online]. Available: `www.jstor.org/stable/10.3138/j.ctvfrxmtw` (Cited on page 62).

[169] K. Vafai, Ed., *Handbook of Porous Media*, en, 3rd. Boca Raton, Florida, USA: CRC Press, Jun. 2015, ISBN: 978-0-429-18434-5. DOI: `10.1201/b18614`. [Online]. Available: `https://www.taylorfrancis.com/books/9780429184345` (Cited on page 62).

[170] M. Grøva & A. Hansen, "Two-phase flow in porous media: power-law scaling of effective permeability", en, *Journal of Physics: Conference Series*, vol. 319, p. 012 009, Sep. 2011, ISSN: 1742-6596. DOI: `10.1088/1742-6596/319/1/012009`. [Online]. Available: `http://stacks.iop.org/1742-6596/319/i=1/a=012009?key=crossref.5ca32afa672e7590eaa08fc9c53a602f` (Cited on page 62).

[171] M. Hamdan, "Single-phase flow through porous channels a review of flow models and channel entry conditions", en, *Applied Mathematics and Computation*, vol. 62, no. 2-3, pp. 203–222, May 1994, ISSN: 00963003. DOI: `10.1016/0096-3003(94)90083-3`. [Online]. Available: `https://linkinghub.elsevier.com/retrieve/pii/0096300394900833` (Cited on page 62).

[172] I. F. Macdonald, M. S. El-Sayed, K. Mow, & F. A. L. Dullien, "Flow through Porous Media-the Ergun Equation Revisited", en, *Industrial & Engineering Chemistry Fundamentals*, vol. 18, no. 3, pp. 199–208, Aug. 1979, ISSN: 0196-4313, 1541-4833. DOI: `10.1021/i160071a001`. [Online]. Available: `https://pubs.acs.org/doi/abs/10.1021/i160071a001` (Cited on pages 62, 64).

[173] D. A. Nield & A. Bejan, "Mechanics of Fluid Flow Through a Porous Medium", en, in *Convection in Porous Media*, D. A. Nield & A. Bejan, Eds., 5th ed., New York, NY: Springer International Publishing, 2017, pp. 1–35, ISBN: 978-3-319-49562-0. DOI: `10.1007/978-3-319-49562-0_1`. [Online]. Available: `https://doi.org/10.1007/978-3-319-49562-0_1` (Cited on page 62).

[174] S. Whitaker, "Flow in porous media I: A theoretical derivation of Darcy's law", en, *Transport in Porous Media*, vol. 1, no. 1, pp. 3–25, 1986, ISSN: 0169-3913, 1573-1634. DOI: `10.1007/BF01036523`. [Online]. Available: `http://link.springer.com/10.1007/BF01036523` (Cited on page 62).

[175] S. M. Hassanizadeh, "Advanced Theories of Two-Phase Flow in Porous Media", en, in *Handbook of Porous Media*, 3rd, vol. Hassanizadeh, S.}, 2015, pp. 47–62, ISBN: 978-1-4398-8557-4. [Online]. Available: `https://www.taylorfrancis.com/` (Cited on page 62).

[176] R. K. Niven, "Physical insight into the Ergun and Wen & Yu equations for fluid flow in packed and fluidised beds", en, *Chemical Engineering Science*, vol. 57, no. 3, pp. 527–534, Feb. 2002, ISSN: 0009-2509. DOI: `10.1016/S0009-2509(01)00371-2`. [Online]. Available: `http://www.sciencedirect.com/science/article/pii/S0009250901003712` (Cited on page 62).

[177] W. Schmidt, "Influence of multidimensionality and interfacial friction on the coolability of fragmented corium", en, Dissertation PhD, Universität Stuttgart, 2004. [Online]. Available: `http://elib.uni-stuttgart.de/handle/11682/1664` (Cited on pages 62, 63).

[178] R. Clavier, N. Chikki, F. Fichot, & M. Quintard, "Experimental study of pressure drops in coarse particle beds", 2015. [Online]. Available: `http://oatao.univ-toulouse.fr/14294/` (Cited on page 63).

[179] T. Schulenberg & U. Müller, "An improved model for two-phase flow through beds of coarse particles", *International Journal of Multiphase Flow*, vol. 13, no. 1, pp. 87–97, Jan. 1987, ISSN: 0301-9322. DOI: `10.1016/0301-9322(87)90009-7`. [Online]. Available: `http://www.sciencedirect.com/science/article/pii/0301932287900097` (Cited on pages 63, 82).

[180] G. Berthoud, “Models and validation of particulate debris coolability with the code MC3d-REPO”, en, *Nuclear Engineering and Design*, vol. 236, no. 19-21, pp. 2135–2143, Oct. 2006, ISSN: 00295493. DOI: `10.1016/j.nucengdes.2006.03.060`. [Online]. Available: `http://linkinghub.elsevier.com/retrieve/pii/S0029549306002962` (Cited on pages 63, 65, 193).

[181] B. Raverdy, R. Meignen, L. Piar, S. Picchi, & T. Janin, “Capabilities of MC3d to investigate the coolability of corium debris beds”, en, *Nuclear Engineering and Design*, vol. 319, pp. 48–60, Aug. 2017, ISSN: 00295493. DOI: `10.1016/j.nucengdes.2017.04.005`. [Online]. Available: `http://linkinghub.elsevier.com/retrieve/pii/S0029549317301681` (Cited on pages 63, 65, 80–83, 116, 193).

[182] S. Ergun, “Fluid flow through packed columns”, *Chem. Eng. Prog.*, vol. 48, pp. 89–94, 1952. [Online]. Available: `http://dns2.asia.edu.tw/~ysho/YSHO-English/1000%20CE/PDF/Che%20Eng%20Pro48,%2089.pdf` (Cited on pages 63, 64, 112).

[183] S. Liu, A. Afacan, & J. Masliyah, “Steady incompressible laminar flow in porous media”, en, *Chemical Engineering Science*, vol. 49, no. 21, pp. 3565–3586, 1994, ISSN: 00092509. DOI: `10.1016/0009-2509(94)00168-5`. [Online]. Available: `https://linkinghub.elsevier.com/retrieve/pii/0009250994001685` (Cited on page 64).

[184] F. A. Dullien, *Porous Media*, en, 2nd ed. Elsevier/Academic Press, 1991, ISBN: 978-0-12-223651-8. DOI: `10.1016/C2009-0-26184-8`. [Online]. Available: `https://linkinghub.elsevier.com/retrieve/pii/C20090261848` (Cited on page 64).

[185] A. Davis & D. James, “Slow flow through a model fibrous porous medium”, en, *International Journal of Multiphase Flow*, vol. 22, no. 5, pp. 969–989, Sep. 1996, ISSN: 03019322. DOI: `10.1016/0301-9322(96)00017-1`. [Online]. Available: `https://linkinghub.elsevier.com/retrieve/pii/0301932296000171` (Cited on page 64).

[186] O. Rahli, L. Tadrist, M. Miscevic, & R. Santini, “Fluid Flow Through Randomly Packed Monodisperse Fibers: The Kozeny-Carman Parameter Analysis”, en, *Journal of Fluids Engineering*, vol. 119, no. 1, pp. 188–192, Mar. 1997, ISSN: 0098-2202, 1528-901X. DOI: `10.1115/1.2819107`. [Online]. Available: `https://asmedigitalcollection.asme.org/fluidsengineering/article/119/1/188/411823/Fluid-Flow-Through-Randomly-Packed-Monodisperse` (Cited on page 64).

[187] A. W. Reed, “The effect of channeling on the dryout of heated particulate beds immersed in a liquid pool”, PhD Thesis, Massachusetts Institute of Technology, 1982 (Cited on pages 64, 120, 129).

[188] M. Alemán, T. Ramamohan, & J. Slattery, “The difference between steady-state and unsteady-state relative permeabilities”, en, *Transport in Porous Media*, vol. 4, no. 5, Oct. 1989, ISSN: 0169-3913, 1573-1634. DOI: `10.1007/BF00179531`. [Online]. Available: `http://link.springer.com/10.1007/BF00179531` (Cited on page 64).

[189] R. H. Brooks, A. T. Corey, Colorado State University, & Hydrology and Water Resources Program, *Hydraulic properties of porous media*, English. Fort Collins: Colorado State University, [Hydrology & Water Resources Program, 1964, OCLC: 3441493 (Cited on page 65).

[190] M. Fourar & R. Lenormand, “A new model for two-phase flows at high velocities through porous media and fractures”, en, *Journal of Petroleum Science and Engineering*, vol. 30, no. 2, pp. 121–127, Jul. 2001, ISSN: 09204105. DOI: `10.1016/S0920-4105(01)00109-7`. [Online]. Available: `http://linkinghub.elsevier.com/retrieve/pii/S0920410501001097` (Cited on pages 65, 194).

[191] A. Chima & S. Geiger, “An Analytical Equation to Predict Gas/Water Relative Permeability Curves in Fractures.”, en, in *SPE Latin America and Caribbean Petroleum Engineering Conference*, Mexico City, Mexico: Society of Petroleum Engineers, 2012. DOI: `10.2118/152252-MS`. [Online]. Available: `http://www.onepetro.org/doi/10.2118/152252-MS` (Cited on page 65).

[192] P. Sapin, A. Gourbil, P. Duru, F. Fichot, M. Prat, & M. Quintard, “Reflooding with internal boiling of a heating model porous medium with mm-scale pores”, en, *International Journal of Heat and Mass Transfer*, vol. 99, pp. 512–520, Aug. 2016, ISSN: 0017-9310. DOI: `10.1016/j.ijheatmasstransfer.2016.04.013`. [Online]. Available: `http://www.sciencedirect.com/science/article/pii/S0017931015302957` (Cited on pages 65, 66, 194).

[193] M. Bürger, M. Buck, W. Schmidt, & W. Widmann, “Validation and application of the WABE code: Investigations of constitutive laws and 2d effects on debris coolability”, *Nuclear Engineering and Design*, Festschrift Edition Celebrating the 70th Birthday of Prof. Bal Raj Sehgal: Invited papers on - Core melt accidents in LWRs State of the art of "COOLABILITY OF POROUS DEBRIS", vol. 236, no. 19–21, pp. 2164–2188, Oct. 2006, ISSN: 0029-5493. DOI: `10.1016/j.nucengdes.2006.03.058`. [Online]. Available: `http://www.sciencedirect.com/science/article/pii/S0029549306002986` (Cited on page 65).

[194] P. Sapin, “Etude expérimentale de l’ébullition en masse dans un milieu poreux modèle”, fr, phd, May 2014. [Online]. Available: `http://ethesis.inp-toulouse.fr/archive/00002714/` (Cited on pages 66, 81).

[195] A. Gourbil, “Etude expérimentale de l’ébullition convective en milieu poreux : assèchement et flux critique”, fr, PhD thesis, Université de Toulouse, Institut National Polytechnique de Toulouse (INP Toulouse), Jun. 2017. [Online]. Available: `https://oatao.univ-toulouse.fr/18597/1/GOURBIL_Ange.pdf` (Cited on pages 66, 67, 81).

[196] J. R. Fanchi, “Measures of Rock-Fluid Interactions”, en, in *Shared Earth Modeling*, Elsevier, 2002, pp. 108–132, ISBN: 978-0-7506-7522-2. DOI: `10.1016/B978-075067522-2/50007-0`. [Online]. Available: `https://linkinghub.elsevier.com/retrieve/pii/B9780750675222500070` (Cited on page 67).

[197] M. C. Leverett, “Capillary Behavior in Porous Solids”, *Transactions of the AIME*, vol. 142, no. 01, pp. 152–169, Dec. 1941, ISSN: 0081-1696. DOI: `10.2118/941152-G`. [Online]. Available: `https://www.onepetro.org/journal-paper/SPE-941152-G` (Cited on page 67).

[198] F. A. Dullien, C. Zarcone, I. F. Macdonald, A. Collins, & R. D. Bochard, “The effects of surface roughness on the capillary pressure curves and the heights of capillary rise in glass bead packs”, en, *Journal of Colloid and Interface Science*, vol. 127, no. 2, pp. 362–372, Feb. 1989, ISSN: 00219797. DOI: `10.1016/0021-9797(89)90042-8`. [Online]. Available: `http://linkinghub.elsevier.com/retrieve/pii/0021979789900428` (Cited on pages 67, 69).

[199] M. Kaviany, *Principles of heat transfer in porous media*. en. 1995, OCLC: 1023315854, ISBN: 978-1-4612-8710-0 (Cited on page 67).

[200] K. S. Udell, “Heat transfer in porous media considering phase change and capillarity—the heat pipe effect”, en, *International Journal of Heat and Mass Transfer*, vol. 28, no. 2, pp. 485–495, Feb. 1985, ISSN: 00179310. DOI: `10.1016/0017-9310(85)90082-1`. [Online]. Available: `https://linkinghub.elsevier.com/retrieve/pii/0017931085900821` (Cited on pages 68, 124).

[201] M. T. van Genuchten, “A Closed-form Equation for Predicting the Hydraulic Conductivity of Unsaturated Soils1”, en, *Soil Science Society of America Journal*, vol. 44, no. 5, p. 892, 1980, ISSN: 0361-5995. DOI: `10.2136/sssaj1980.03615995004400050002x`. [Online]. Available: `https://www.soils.org/publications/sssaj/abstracts/44/5/SS0440050892` (Cited on page 68).

[202] S. M. Hassanizadeh & W. G. Gray, “Thermodynamic basis of capillary pressure in porous media”, en, *Water Resources Research*, vol. 29, no. 10, pp. 3389–3405, Oct. 1993, ISSN: 00431397. DOI: `10.1029/93WR01495`. [Online]. Available: `http://doi.wiley.com/10.1029/93WR01495` (Cited on page 69).

[203] H. C. Hardee & R. H. Nilson, “Natural Convection in Porous Media with Heat Generation”, en, *Nuclear Science and Engineering*, vol. 63, no. 2, pp. 119–132, Jun. 1977, ISSN: 0029-5639, 1943-748X. DOI: `10.13182/NSE77-A27015`. [Online]. Available: `https://www.tandfonline.com/doi/full/10.13182/NSE77-A27015` (Cited on page 70).

[204] S. W. Jones, M. Epstein, S. G. Bankoff, & D. R. Pedersen, “Dryout heat fluxes in particulate beds heated through the base”, *Journal of heat transfer*, vol. 106, no. 1, pp. 176–183, 1984 (Cited on page 70).

[205] M. Epstein, “Review of Water Ingression Models”, en, ACEX-TR-CD31 ACEX-TR-CD31, 2000 (Cited on pages 70, 77, 96).

[206] ——, “Dryout Heat Flux During Penetration of Water Into Solidifying Rock”, en, *Journal of Heat Transfer*, vol. 128, no. 8, p. 847, 2006, ISSN: 00221481. DOI: `10.1115/1.2227042`. [Online]. Available: `http://HeatTransfer.asmedigitalcollection.asme.org/article.aspx?articleid=1448447` (Cited on pages 70, 75, 76, 96).

[207] R. J. Lipinski, “A Coolability Model for Postaccident Nuclear Reactor Debris”, en, *Nuclear Technology*, vol. 65, no. 1, pp. 53–66, Apr. 1984, ISSN: 0029-5450, 1943-7471. DOI: `10.13182/NT84-A33373`. [Online]. Available: `https://www.tandfonline.com/doi/full/10.13182/NT84-A33373` (Cited on pages 70, 71, 122, 124).

[208] D. Leguillon, “A simple model of thermal crack pattern formation using the coupled criterion”, en, *Comptes Rendus Mécanique*, vol. 341, no. 6, pp. 538–546, Jun. 2013, ISSN: 1631-0721. DOI: `10.1016/j.crme.2013.04.002`. [Online]. Available: `http://www.sciencedirect.com/science/article/pii/S1631072113000715` (Cited on page 72).

[209] H.-A. Bahr, H.-J. Weiss, H. Maschke, & F. Meissner, “Multiple crack propagation in a strip caused by thermal shock”, en, *Theoretical and Applied Fracture Mechanics*, vol. 10, no. 3, pp. 219–226, Dec. 1988, ISSN: 01678442. DOI: `10.1016/0167-8442(88)90014-6`. [Online]. Available: `https://linkinghub.elsevier.com/retrieve/pii/0167844288900146` (Cited on page 72).

[210] H.-A. Bahr, H.-J. Weiss, U. Bahr, M. Hofmann, G. Fischer, S. Lampenscherf, & H. Balke, “Scaling behavior of thermal shock crack patterns and tunneling cracks driven by cooling or drying”, en, *Journal of the Mechanics and Physics of Solids*, vol. 58, no. 9, pp. 1411–1421, Sep. 2010, ISSN: 00225096. DOI: `10.1016/j.jmps.2010.05.005`. [Online]. Available: `https://linkinghub.elsevier.com/retrieve/pii/S0022509610000955` (Cited on pages 72, 74).

[211] L. F. Faria Ricardo, D. Leguillon, G. Parry, & A. Doitrand, “Modeling the thermal shock induced cracking in ceramics”, en, *Journal of the European Ceramic Society*, S0955221919308167, Nov. 2019, ISSN: 09552219. DOI: `10.1016/j.jeurceramsoc.2019.11.071`. [Online]. Available: `https://linkinghub.elsevier.com/retrieve/pii/S0955221919308167` (Cited on pages 72, 74).

[212] A. A. Griffith & G. I. Taylor, “VI. The phenomena of rupture and flow in solids”, *Philosophical Transactions of the Royal Society of London. Series A, Containing Papers of a Mathematical or Physical Character*, vol. 221, no. 582-593, pp. 163–198, Jan. 1921. DOI: `10.1098/rsta.1921.0006`. [Online]. Available: `https://royalsocietypublishing.org/doi/abs/10.1098/rsta.1921.0006` (Cited on page 73).

[213] S. Lomperski & M. T. Farmer, “Corium crust strength measurements”, en, *Nuclear Engineering and Design*, vol. 239, no. 11, pp. 2551–2561, Nov. 2009, ISSN: 0029-5493. DOI: `10.1016/j.nucengdes.2009.06.013`. [Online]. Available: `http://www.sciencedirect.com/science/article/pii/S0029549309003008` (Cited on page 75).

[214] J. Yang, L.-Y. Fu, W. Zhang, & Z. Wang, “Mechanical property and thermal damage factor of limestone at high temperature”, en, *International Journal of Rock Mechanics and Mining Sciences*, vol. 117, pp. 11–19, May 2019, ISSN: 1365-1609. DOI: `10.1016/j.ijrmms.2019.03.012`. [Online]. Available: `http://www.sciencedirect.com/science/article/pii/S136516091830861X` (Cited on pages 75, 97).

[215] C. R. B. Lister, “On the Penetration of Water into Hot Rock”, en, *Geophysical Journal International*, vol. 39, no. 3, pp. 465–509, Dec. 1974, ISSN: 0956-540X, 1365-246X. DOI: `10.1111/j.1365-246X.1974.tb05468.x`. [Online]. Available: `https://academic.oup.com/gji/article-lookup/doi/10.1111/j.1365-246X.1974.tb05468.x` (Cited on pages 75, 96).

[216] D. Y. Yeo & H. C. No, “Modeling crust fracture and water ingression through crust during top-flooding strategy for corium cooling”, en, *Nuclear Engineering and Design*, vol. 342, pp. 219–230, Feb. 2019, ISSN: 0029-5493. DOI: `10.1016/j.nucengdes.2018.12.004`. [Online]. Available: `http://www.sciencedirect.com/science/article/pii/S0029549318308094` (Cited on pages 79, 80).

[217] S. Vandroux-Koenig & G. Berthoud, “Modelling of a two phase momentum jet close to the breach, in the containment vessel of a liquefied gas”, en, *Journal of Loss Prevention in the Process Industries*, vol. 10, no. 1, pp. 17–29, Jan. 1997, ISSN: 09504230. DOI: `10.1016/S0950-4230(96)00038-1`. [Online]. Available: `https://linkinghub.elsevier.com/retrieve/pii/S0950423096000381` (Cited on page 80).

[218] J. Kokalj, M. Uršič, M. Leskovar, L. Piar, & R. Meignen, “Modelling of debris bed reflooding in PEARL experimental facility with MC3d code”, en, *Nuclear Engineering and Design*, vol. 330, pp. 450–462, Apr. 2018, ISSN: 0029-5493. DOI: `10.1016/j.nucengdes.2018.02.016`. [Online].

Available: http://www.sciencedirect.com/science/article/pii/S0029549318301286 (Cited on pages 83, 84, 193).

[219] S. Lomperski, M. Farmer, & S. Basu, "Experimental investigation of corium quenching at elevated pressure", en, *Nuclear Engineering and Design*, vol. 236, no. 19-21, pp. 2271–2280, Oct. 2006, ISSN: 00295493. DOI: 10.1016/j.nucengdes.2006.03.041. [Online]. Available: https://linkinghub.elsevier.com/retrieve/pii/S0029549306003062 (Cited on pages 94, 96).

[220] S. Lomperski, M. Farmer, D. Kilsdonk, & R. Aeschlimann, "OECD MCCI Project Small-Scale Water Ingression and Crust Strength Tests (SSWICS) SSWICS-13 Test Data Report: Thermal Hydraulic Results", Argonne National Laboratory, Illinois USA, Tech. Rep., Apr. 2010, p. 33 (Cited on page 103).

[221] R. Clavier, "Étude expérimentale et modélisation des pertes de pression lors du renoyage d'un lit de débris", Dissertation PhD, Institut National Polytechnique de Toulouse, Nov. 2015. [Online]. Available: http://oatao.univ-toulouse.fr/14705/ (Cited on pages 116, 129).

[222] E. Takasuo, S. Holmström, T. Kinnunen, P. H. Pankakoski, E. Hosio, & I. Lindholm, "The effect of lateral flooding on the coolability of irregular core debris beds", en, *Nuclear Engineering and Design*, vol. 241, no. 4, pp. 1196–1205, Apr. 2011, ISSN: 00295493. DOI: 10.1016/j.nucengdes.2010.04.033. [Online]. Available: http://linkinghub.elsevier.com/retrieve/pii/S0029549310003158 (Cited on page 129).

[223] A. J. Slifka, B. J. Filla, & J. M. Phelps, "Thermal Conductivity of Magnesium Oxide From Absolute, Steady-State Measurements", *Journal of Research of the National Institute of Standards and Technology*, vol. 103, no. 4, pp. 357–363, 1998, ISSN: 1044-677X. DOI: 10.6028/jres.103.021. [Online]. Available: https://www.ncbi.nlm.nih.gov/pmc/articles/PMC4887202/ (Cited on page 140).

[224] H. Kull, "Theory of the Rayleigh-Taylor instability", en, *Physics Reports*, vol. 206, no. 5, pp. 197–325, Aug. 1991, ISSN: 03701573. DOI: 10.1016/0370-1573(91)90153-D. [Online]. Available: https://linkinghub.elsevier.com/retrieve/pii/037015739190153D (Cited on page 171).

Analyse et modélisation des processus de refroidissement sous eau des lits de débris et des bains de corium en interaction avec le béton

Dans un accident grave nucléaire avec fusion du cœur, le corium surchauffé, constitué d'acier et de combustible fondu, menace le confinement si le refroidissement n'est pas assuré. Le refroidissement du corium par pénétration d'eau est étudié pour deux configurations : lit de particules et bain de corium en interaction avec le béton via une analyse approfondie des résultats expérimentaux, le développement d'un modèle analytique 1D et des simulations numériques à l'aide du logiciel MC3D. L'analyse 1D permet de proposer un modèle simplifié de pénétration de l'eau dans un milieu poreux. Le développement d'instabilités au front de pénétration est étudié à l'aide de simulations 2D avec MC3D. Le modèle analytique est ensuite étendu à une configuration à deux zones pour étudier l'impact des hétérogénéités de progression du front. Concernant les bains de corium, le mécanisme de pénétration de l'eau dans la croûte supérieure, sous l'effet de fracturation thermique, est revisité en montrant l'impact fort des effets de bords dans les essais. Dans les deux cas, le rôle de la puissance résiduelle est enfin analysé.

Mots-clés: Corium, Interaction Corium-Beton, MCFD, SSWICS, Lit debris, Water Ingression

Analysis and modeling of ex-vessel underwater cooling processes of debris bed and molten corium pool in interaction with concrete

In a severe nuclear accident with core meltdown, the superheated magma made of molten steel and fuel, called corium, threatens the integrity of the reactor vessel and later the containment building, if long-term coolability is not assured. In the ex-vessel scenario, the coolability is analyzed for two expected configurations during the Molten Corium-Concrete Interaction: particle bed, and fractured crust overlying a corium pool. The coolability of both is examined through in-depth experiments analysis, the development of an analytical model, and the modification and use of the CMFD code MC3D. One-dimensional analysis yields a proposal of a heat flux model for the water penetration. The mechanism of the water ingression phenomena in fractured crusts is revisited. Experiment analysis and calculations with MC3D show the development of front instabilities and important 2D/3D effects. The 1D is further extended a two-zone two-phase model to study the effects of the penetration front heterogeneity. In the case of an initially hot debris bed with the presence of residual power, the model shows that the extracted heat flux is less than the commonly used "dryout heat flux" criterion.

Keywords: Corium, Molten Corium-Concrete Interaction, MCFD, SSWICS, Debris bed, Water Ingression